

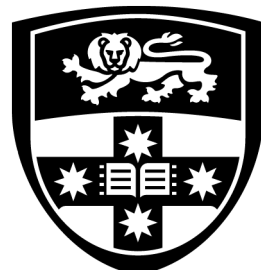


USYD

Rocketry Team

Critical Design Report For Critical Design Review

Pardalote (Widopwidop)



THE UNIVERSITY OF
SYDNEY

Executive Summary

Contents

Executive Summary	i
1 Introduction	1
2 System Architecture Overview	2
2.1 Flight Simulation	2
2.2 Propulsion - Chamber	2
2.3 Propulsion - Tank	2
2.4 Ground Support Equipment	2
2.5 Ground Control	2
2.6 Aerostructure	2
2.7 Recovery	2
3 Concept of Operations	3
4 Flight Simulation Subsystem	6
4.1 Software	6
4.2 Programming language	7
4.3 Candlebark	7
4.3.1 Hybrid Propulsion Simulation and Modelling Approach	7
4.3.2 Input configuration files	7
4.3.3 System State Initialization	7
4.3.4 Oxidiser Tank Flush Model	9
4.3.5 Feedsystem Pressure Drop Model	9
4.3.6 Injector Model	11
4.3.7 Fuel Regression Model	11
4.3.8 Grain Geometry Model	12
4.3.9 Determination of Simulation Coefficients and Efficiencies	13
4.3.10 Nozzle Flow Model	16
4.3.11 Engine Gravimetric Model	18
4.4 Candlebark Validation	19
4.4.1 Phoenix 1B	19
4.4.2 Phoenix 1A	19
4.4.3 McGill Rocketry	19
4.4.4 Waterloo Rocketry	19
4.4.5 Waratah	19
4.4.6 Wattle	19
4.4.7 Pardalote Mk1	20
4.4.8 Pardalote Mk2	22
4.5 Ironbark	22

4.5.1	Trajectory Simulation and Modelling Approach	22
4.5.2	Determination of Aerodynamic Coefficients	22
4.5.3	6-DOF Trajectory Kinematics Equations	23
4.6	Ironbark Validation	23
4.6.1	Bluewren	23
4.6.2	Rosella	23
4.6.3	Silvereye	23
4.7	Flutter	23
4.7.1	Material Properties Database	23
4.7.2	Fins	23
4.8	Pardalote MK2 Propulsion System Sizing	23
4.8.1	Sizing Prerequisites	23
4.8.2	Design Optimization Strategy	25
4.8.3	Fuel Grain Geometries	26
4.8.4	Sizing Logic	26
4.8.5	Geometry Changes Summary	26
4.8.6	Pardalote Mk2 Expected Performance Metrics	27
5	Propulsion - Chamber Subsystem	28
5.1	Engine Architecture	28
5.2	Sizing	29
5.3	Forward Closure	31
5.4	Casing	33
5.5	Injector	33
5.6	Thermal Protection System	33
5.7	Nozzle and Aft Retainment	34
5.8	Sealing System	34
5.9	Failure Mode Analysis	35
5.9.1	Forward Closure	37
5.9.2	Injector	38
5.9.3	Casing	39
5.9.4	Nozzle Insert	42
5.9.5	Nozzle	42
5.9.6	Material and Fastener Specifications	43
5.10	Ignition System	45

6 Propulsion - Tank Subsystem	45
6.1 Subsystem Overview	45
6.2 Oxidizer Tank	47
6.2.1 Vent Closure	48
6.2.2 Aft Closure	49
6.3 Main Flight Valve	50
6.3.1 Coaxial Valve	50
6.4 On-board Pneumatic System	52
6.4.1 Solenoid Valve	52
6.5 Pressure relief	53
7 Ground Support Equipment Subsystem	55
7.1 Overview	55
7.2 Launch Rail	56
7.2.1 Launch Structure	56
7.2.2 Rail System	56
7.2.3 Base Structure	57
7.2.4 Swivel Mechanism	57
7.2.5 Gin Pole	59
7.2.6 Crossbar	62
7.2.7 Winch System	62
7.2.8 Plume Deflector	66
7.2.9 Load Cell Mounting	66
7.2.10 Miscellaneous Components	67
7.2.11 Transport and Assembly	67
7.3 Ground Fill Station	67
7.3.1 Structure	67
7.3.2 Fill System	68
7.3.3 Structure	71
7.3.4 Gas Cylinder Storage	71
7.3.5 Temperature Regulation	72
7.3.6 Transport and Assembly	72
7.4 Quick Disconnect Umbilical Arm	72
7.4.1 Design Overview	72
7.4.2 Operation	75
7.4.3 Cost	75

8	Ground Control Subsystem	75
8.1	System Architecture	75
8.2	Sensing	75
8.2.1	Temperature	75
8.2.2	Pressure	76
8.2.3	Mass	76
8.2.4	Valve Position Indicators	76
8.3	Control	77
8.3.1	Valves & Motors	77
8.3.2	Igniter	77
8.3.3	Umbilical Retract	77
8.4	Data Acquisition	78
8.4.1	DAQ System	78
8.4.2	Signal Conditioning	78
8.5	Power	79
8.5.1	Electrical Umbilical	79
8.6	On-Board Logging	79
8.7	Ground Controller	79
8.7.1	Hardware	79
8.7.2	Interactive	79
8.8	Fail-safe	79
8.9	Software and Communication	79
9	Aerostructures Subsystem	85
9.1	Structure overview	85
9.2	Nose cone and boat tail	85
9.2.1	Nose cone	85
9.2.2	Boat tail	86
9.2.3	End cap	86
9.2.4	Integration design	88
9.3	Body Tubes	89
9.3.1	Mass Equations	91
9.4	Fins	91
9.4.1	Flutter	93
9.5	Bulkheads	93
9.5.1	Recovery U Bolts	93
9.5.2	Payload Bulkhead	93
9.5.3	Avionics Bulkheads	93
9.5.4	Aft Recovery Bulkhead	96
9.6	Bulkhead Optimisation	97

9.6.1	Payload Bulkhead Optimisation	97
9.6.2	Upper AV Bulkhead Optimisation	98
9.6.3	Lower AV Bulkhead Optimisation	98
9.6.4	Aft Recovery Bulkhead Optimisation	99
9.7	Avionics Bay Rods	99
9.8	Launch Rail Attachment	100
9.9	Engine Support Structure	102
9.9.1	Tank Mounting	102
9.9.2	Tank-Chamber Truss	102
9.9.3	Chamber-Truss Adapter Plate	105
9.10	External Access to Truss	106
9.11	Cover for QD Airframe Hole	106
9.12	Structural Analysis	106
9.12.1	Axial Loads	106
9.12.2	Transverse Loads	106
9.12.3	Body Tubes	110
9.12.4	Justification of Carbon Fibre Body Tube Strength Prediction	111
9.12.5	FEA of Composite Materials	112
9.12.6	Thread Shear-Out	113
9.12.7	Tube Shear from Radial Screws	113
10	Recovery Subsystem	114
10.1	Subsystem Overview	114
10.2	Parachutes	116
10.2.1	Parachute Profile	116
10.2.2	Parachute Sizing	116
10.2.3	Parachute Loading	118
10.2.4	Parachute Manufacturing	118
10.3	Parachute Deployment	120
10.3.1	Black Powder Calculations	120
10.3.2	Charge Well Sizing	121
10.4	Rigging	121
10.4.1	Shock Cords	121
10.4.2	Swivels and Quick Links	121
10.4.3	Deployment Bag	122
10.4.4	Parachute Protectors	123
10.4.5	Reefing Ring	123
10.4.6	Shock Cord Protectors	123
10.4.7	Factor of Safety	123
10.5	Avionics Bay Structure	124

10.5.1	Switch Plate	124
10.5.2	Integration Structure	124
10.5.3	Barometric Hole Sizing	127
10.5.4	Materials	127
10.6	Electronics Systems	127
10.6.1	Flight Computers	127
10.6.2	Batteries	128
10.6.3	Power Distribution Board	128
10.6.4	Wiring and Connections	129
11	Subsystem Testing	132
11.1	Flight Simulation	132
11.2	Propulsion - Chamber	132
11.3	Propulsion - Tank	132
11.4	Ground Support Equipment	132
11.5	Ground Control	132
11.6	Aerostructure	132
11.7	Recovery	143
A	Equation Derivations	145
A.1	Truss Buckling Equation	145
A.2	Tank Failure Equations	146
A.2.1	Angle Seat Valve	146
A.2.2	Thin Walled Pressure Vessel Analysis	148
A.2.3	Bolt Shear Failure	148
A.2.4	Bolt Tear-out Failure	148
A.2.5	Casing Tensile Failure	148
A.2.6	Bearing Stress Failure	148
A.3	Coaxial Valve Failure Equations and Calculations	148
A.3.1	Bolt Tension Failure Equation	149
A.3.2	External Thread Shear Equation	149
A.3.3	Internal Thread Shear Equation	149
A.3.4	Hoops Stress	150
A.4	Black Powder Calculations	150

List of Figures

1	Flight Simulation Software Ecosystem	6
2	Tank Setup	7
3	CoolProp Saturation Curve	8
4	Pressure drop model Chart	9
5	Caption	10
6	Injector Model Flow Chart	11
7	Sliver Burning Occuring	13
8	C_D Optimization	14
9	Mass Trace	15
10	Comparison between several Hybrids C_{eff}^* from ??	16
11	Hotfire Test 9 Results	19
12	Hotfire Test 9 Results	20
13	Hotfire Test 9 Results	21
14	Hotfire Test 9 Results	22
15	Enter Caption	22
16	Steady State Thrust Curve	23
17	OpenRocket Simulation Configuration	24
18	Pardalote trajectory on an N4000 motor	24
19	C^* Study	25
20	A full integrated system parametric study	26
21	Sample Fuel Grain Configurations	26
22	Expected Thrust Performance	28
23	Expected System Pressures	28
24	Expected Mass Flow Rates	28
25	Pardalote Mk2 Flight Performance	28
26	Overview of Flight Simulation Data	28
27	Pardalote Engine Architecture	29
28	Simulated Engine Thrust Curve	31
29	Simulated Tank and Chamber Pressures	31
30	Pardalote Forward Closure	32
31	Pardalote Forward Closure Section View	32
32	Pardalote Forward Closure FEA Safety Factor Results (Equivalent von-Mises Stress)	33
33	Outer Casing Temperature - Hotfire 1	41
34	Piping and Instrumentation Diagram	46
35	The Oxidizer Tank	47
36	Vent Closure	49
37	Aft Closure	49
38	Coaxial Valve Section View	50

39	Burkert 6240 Servo-Assisted Solenoid Valve	53
40	HAM-LET Spring Relief Valve	54
41	Spatial diagram for the launch rail	55
42	Launch rail CAD viewed from the side	56
43	Launch rail CAD viewed from the top	56
44	80x40 extrusions used as the rail	56
45	SKF bearing block with 50 mm inner diameter	58
46	First scenario of free body diagrams for a portion of the rail structure	59
47	Continuation of free body diagram for scenario one involving the gine pole	60
48	Second scenario of free body diagrams for a portion of the rail structure	60
49	Estimated reaction forces on the rail base, wire, gine pole and support for specific rail dimensions, given that wire is attached above halfway point of the rail	61
50	Estimated reaction forces on the rail base, wire, gine pole and support for specific rail dimensions, given that wire is attached below halfway point of the rail	61
51	Pulley subassembly	61
52	Crossbar	62
54	Winch Mount FBD	63
53	VEVOR hand winch for launch rail erection	63
55	Solved Winch Mount FBD	64
56	Solidworks Design	65
57	Truss Section Validation	65
58	Plume deflector	66
59	Load-Cell Mounting configuration	66
60	Structure CAD.	68
61	Fill System PID	69
62	Fill system CAD, front view highlighting nitrous line.	69
63	Fill system CAD, angles view highlighting both N ₂ O and air line.	70
64	Fill system CAD with nitrogen, angles view highlighting both N ₂ O and air line.	71
65	Quick Disconnect Umbilical Arm (shown detached from truss).	73
66	QD Arm gas spring	73
67	Software Systems Diagram (Simplified)	76
68	Igniter Circuit Schematic	77
69	Igniter Circuit Simulation Values from LTspice	77
70	Software Systems Diagram (Simplified)	80
71	Driver Diagram (Simplified)	81
72	ECS Systems Diagram (Simplified)	82
73	Control Systems Diagram (Simplified)	83
74	Real-time Systems Logger	84
75	Control-Systems Interface	85
76	Openrocket diagram of Pardalote.	85

77	Nose tip and retention bulkhead.	86
78	Boat tail wave drag vs Mach number for various length/diameter ratios [9]	87
79	Different endcap geometry for CFD study.	87
80	Percentage drag reduction of different endcap taper angles.	88
81	Boattail CAD crosssection	88
82	Aft airframe CAD crosssection	89
83	Body tube configuration 1 between main parachute bay and boattail.	89
84	Body tube configuration 2 between main parachute bay and boattail.	89
85	Final Body Configuration	90
86	Fin planform CFD C_d study [2]	92
87	Flutter velocity.	93
88	Payload bulkhead FEA at 33.1G recovery loading.	94
89	Flat plate top view	95
90	Flat Plate bottom view	95
91	Cut-out plate top view	95
92	Cut-out plate bottom view	95
93	Isogrid top view	95
94	Isogrid bottom view	95
95	Rosella top view	95
96	Rosella bottom view	95
97	Upper avionics bulkhead FEA for main deployment (8635 N).	96
98	Aft recovery bulkhead	97
99	FoS results for the aft recovery bulkhead FEA	97
100	FoS results comparison for Payload Bulkhead	98
101	FoS results comparison for Upper AV Bulkhead	98
102	FoS results comparison for Lower AV Bulkhead	98
103	FoS results comparison for Aft Recovery Bulkhead	99
104	FEA of aft retract mechanism.	101
105	Forward Rail Button Hardpoint	102
106	Aft Rail Button Hardpoint	102
107	The block diagram of the truss (cross-sectional view). Outer diameter is 152.4mm.	102
108	Alternate truss options considered.	103
109	Truss design and tank aft closure.	103
110	Truss strut FoS for 5kN compressive load.	104
111	Eigenvalue buckling results from ANSYS	105
112	FEA of chamber adapter plate.	105
113	FEA 2 of chamber adpater plate.	105
114	Side Profile of Launch Vehicle.	108
115	Axial force diagram.	108
116	Shear force diagram.	108

117	Bending moment diagram.	108
118	Mohr's Circle for Plane Stress.	110
119	The comparison of Glass Fibre Reinforced Polymers (GFRP) and Carbon Fibre Reinforced Polymers (CFRP) properties during the compression test conducted in [16]	111
120	Avionics Functional Diagram	115
121	Launch Vehicle Layout after Drogue and Main parachute deployment	115
122	Toroidal canopy profile.	116
123	Drogue Parachute Descent Rates against C_d	117
124	Main Parachute Descent Rates against C_d	117
125	Gore Template for Drogue (left) and Main (right)	119
126	French Seam	120
127	Rigging diagram for Drogue (Left) and Main (Right)	121
128	The packing diagrams for Drogue (Left) and Main (Right)	122
129	Packing Volume vs COTS Parachute diameter	122
130	Micro Switch Circuit	124
131	Flight Computer Switch Plate	125
132	E-match Switch Plate	125
133	Combined Switch Plate	125
134	Side Exploded View with Brackets	126
135	Front View with Brackets	126
136	PDB Mounting	126
137	Telemega Wiring Diagram	129
138	Raven 4 Wiring Diagram	129
139	GPS Tracker Wiring Diagram	129
140	Raven4, TeleMega and Featherweight GPS Tracker PDB Design	130
141	The variables that determine member cross-sectional areas	145
142	Angled-Piston Valve Cross Section	147

List of Tables

1	Concept of Operations Overview. * and ** denotes pairs of concurrent operation.	5
2	Flight Simulation Softwares	6
3	Your Table Caption	9
4	Sizing Changes Summary	26
5	Simulation Summary	27
6	Key Chamber Sizing Parameters	30
7	Caption	30
8	Sealing System Interfaces and Responsibilities	34
9	Chamber Sealing System Key Parameters	34
10	Range of Stretch and Squeeze Parameters for Chamber Sealing System	35
11	Chamber O-Ring Gland Dimensions (All dimensions in mm)	35
12	Expected and worst case operating conditions used for analysis.	35
13	Summary of the key parameters used in the FMA calculations.	36
14	Factor of Safety (FS) Table for the Combustion Chamber Components.	37
15	Temperature vs F_{ty} and F_{tu} of Al 6061-T6	41
16	Failure modes with Expected Pressure Factors of Safety (FOS).	41
17	Failure modes with Worst Case Factors of Safety (45 bar Chamber Pressure)	42
18	Summary of Carbon Graphites mechanical properties [19].	43
19	Summary of the mechanical properties of Inconel Alloy 718 [21],[22].	43
20	Summary of Aluminium Alloy T6061 mechanical properties (MIL-HDBK-5H, pg 3-257).	44
21	Summary of the key M6 Socket screw data.	44
22	Summary of the key M3 Socket screw data.	44
23	Oxidizer Tank Mass and Size	48
24	Factors of Safety for Tank Failure Modes	48
25	Oxidizer Tank O-Ring Design	48
26	Vent Closure Mass and Size	49
27	Aft Closure Mass and Size	49
28	Bolt Clamping Forces for Coaxial valve	51
29	Failure Modes and Factor of Safety of Valve Caps	51
30	O-ring sizes and properties	52
31	Coaxial Valve Advantages and Disadvantages	52
32	Cost breakdown for the fill system frame.	68
33	Quick Disconnect Umbilical Arm Cost Breakdown	75
34	Device Table	80
35	Boattail drag force for varying endcap taper angles and recess depths from Computational Fluid Dynamics (CFD) analysis.	88
36	Fin geometry.	92
37	Stability for varying windspeeds and engine performance.	92

38	AV Bulkhead Finite Element Analysis (FEA) result comparison, all 8000N loading and all new designs approx 300g mass.	96
39	Comparison of Avionics Bay Rods	100
40	Drag Coefficients and Drag of Components at Mach 0.9	107
41	Relevant Coefficients, Normal Forces and Moments of Components at Mach 0.9	107
42	Quantitative Component Analysis Values.	109
43	Tabulated values for required thread lengths.	113
44	Parachute Descent Rate Requirements	114
45	The input values for OSCALC to calculate the maximum shock load for drogue	118
46	The calculated opening shock loads for drogue parachute	118
47	The input values for OSCALC to calculate the maximum shock load for main	118
48	The calculated opening shock loads for main parachute	118
49	Parachute Material and Sizing Summary	119
50	Main Factor of Safety	123
51	Drogue Factor of Safety	123
52	Trade-off Table	127
53	Battery Configuration	128
54	Tank Failure Parameter Values	146
55	Coaxial Valve Bolt Loading Calculations	148
56	Coaxial Valve Bolt Loading Values	149
57	Coaxial Valve External Thread Shear	149
58	Coaxial Valve Internal Thread Shear	149
59	Coaxial Valve Hoops Stress Calculations and Values	150

Glossary

AoA Angle of Attack

CFD Computational Fluid Dynamics

CFRP Carbon Fibre Reinforced Polymers

FEA Finite Element Analysis

FoS Factor of Safety

g/cc grams per cubic centimetre

GFRP Glass Fibre Reinforced Polymers

gsm grams per square metre

IREC Intercollegiate Rocket Engineering Competition

LEOT Lowest Expected Operating Temperature

MEOP Maximum Expected Operating Pressure

N₂O Nitrous Oxide

SAC Spaceport America Cup

UTS Ultimate Tensile Strength

1 Introduction

This report outlines the design of Pardalote, USYD Rocketry Team's 10,000 ft, hybrid launch vehicle developed during the 2023-2024 season. The rocket has a targeted launch date in July of 2024 and utilises the Team's first hybrid engine incorporated into a launch vehicle. The project is intended to advance the Team's knowledge of hybrid launch vehicles, regarding their design and operation, such that the Team will gain the necessary experience to enter the Intercollegiate Rocket Engineering Competition (IREC) at Spaceport America Cup (SAC) in 2025.

...

2 System Architecture Overview

2.1 Flight Simulation

The Flight Simulation Subsystem overlooks all aspects in relation to the simulation and modeling of Pardalote's flight performance, including Hybrid Engine performance. The subsystem includes the development of Candlebark, in-house Hybrid Engine Performance Analysis Software, and ORHelper, Python interface for OpenRocket used to determine flight performance metrics.

2.2 Propulsion - Chamber

2.3 Propulsion - Tank

Tank Subsystem is responsible for the safe storage and movement of oxidizer within the Rocket. This includes the Oxidizer Tank, Main Flight Valve, Pressure Relief and internal plumbing. Tank is undergoing significant SRAD development in designing the Main Flight Valve and Oxidizer in-house to meet the requirements of the project, and aims to create a design knowledge base for the team moving forward.

2.4 Ground Support Equipment

This encompasses the design, manufacturing, and integration of equipment crucial for rocket preparation, launch, and recovery. Key GSE responsibilities include engineering and producing the launch rail for secure rocket vertical integration, developing the fill system for safe and efficient propellant loading, integrating ground support equipment with the rocket and launch site, and providing technical support for launch operations.

2.5 Ground Control

2.6 Aerostructure

The Aerostructures Subsystem consists of the external airframe and all interior structural components. This includes aerodynamic components such as the nosecone, body tubes, fins and boat tail as well as structural components including bulkheads, support structures and motor retention. In addition to this design and manufacturing, Aerostructures is responsible for trajectory simulation and flight analysis, in conjunction with Flight Simulation, and the modeling and simulation of components through the tools of Computational Fluid Dynamics (CFD) and Finite Element Analysis (FEA). The primary focus of the subsystem is the flight performance of the launch vehicle and the safety and reliability of design and manufacture.

2.7 Recovery

The Recovery Subsystem is responsible for the reliable and safe recovery of the rocket, that is, all stages of flight after the rocket has achieved apogee including safe landing and subsequent retrieval. The subsystem manages primary components such as the parachutes, rigging hardware and avionics required for parachute deployment. Recovery is responsible for the design and manufacturing of SRAD parachutes to better control rocket descent rates, as well as the avionics bay which encompasses all of the relevant avionics and a custom Power Distribution Board (PDB). This subsystem's target is to ensure the reliable and safe recovery of the rocket.

3 Concept of Operations

Table 1: Concept of Operations Overview. * and ** denotes pairs of concurrent operation.

Phase	Subphase	Aerostructures	Chamber	Tank	Ground Control	GSE	Recovery	Flight Simulation
T-24		Join fwd truss to aft tank	Assemble chamber components Assemble and torque bolts	Assemble Oxidizer Tank Attach plumbing and valves to truss Attach 2 post truss to aft tank	Charge Batteries Tug Test Electrical Connections Complete Integration Test	Assemble base and rail structure Keep rail structure in a horizontally re-clined position Support rail structure while horizontal Cover the assembled structure with tarp to protect against external elements and dust	Charge Batteries Fold & Pack Parachutes with attached quicklinks + swivels + protectors Attach Flight Computers to PCB Mount PCB to Battery Bay Camera mounted to Camera Bay	
Transport	State	tubes, bulkheads in pelican	pack chamber in pelican			Pack in a disassembled state	FC's + Wires on Battery Bay & Folded parachutes	
Setup	Environment Independent systems	payload frame	Check chamber fittings and threads	Inspect system for transport damage	Connect Different Ground Boxes Connect Sensors Setup Network Setup Ground Station Network Test Fill System Valve Test	Remove tarp covering the launch rail Check for level of the base and adjust jack leg stands if required Check for rail alignment and adjust if necessary Check and testing lifting and angle locking mechanisms Deploy passive cooling systems on cylinders Fully assemble fill system	Put Batteries into Battery Bay Put Batteries into Camera Bay Power + Safe	Setup weather station
Assembly	Nose Integration	Integrate payload and cameras						
	Engine Integration*	Integrate payload structure into nosecone Join adapter plate to chamber fwd closure Join adapter plate to aft truss		Attach valve wires Connect relevant GC systems Attach truss to chamber				
		Attach final truss post Insert prop assem. into carbon bodytube put the boattail end on over the chamber put in aft recovery bulkhead						
	AV Integration*						Battery Bay into AV Bay (REMOVE RBF THEN PUT BACK IN) Charge Well filling	
CT		put bulkheads onto av bay and secure screws into rods						
	Rec Integration						Attach main rigging to nose and forward AV Attach drogue rigging to AV and aft Shear pins into rocket	
Launch Preparation	Rocket on Rail					Mount rocket onto launch rail while horizontal lift rail structure up until vertical using winch Lock vertical alignment of the rail structure Use ratchet straps to secure rail structure Attach fill arm onto the quick disconnect		
	Rocket Vertical Connect Rocket			Charge Air Connect fill ubilical	Connect Data Umbilical Verify Good Data Transfer Test Flight Valve Actuation Test Vent Valve Actuation			
	Arm Rocket systems				Continuity Test Check		Remove RBF Pins (Arming Flight Computers)	
	System verification		Insert ignitor		Ignitor Arming All Readings Nominal			Calculate oxidiser fill mass
Launch Sequence	Fill			Verify MFV closed	Fill to Sim	Remove fill arm automatically once run tank is full		Final Sim
					Umbilical Retract Launch Arming Procedure			
	Ignite				Launch Post-Launch Fill Procedures			
Flight	Boost Coast Drogue Main							
Retreval**	Send team						Verify GPS coordinates Send team to retrieve rocket	
	Verify Inert				Verify Valve Open (toggle)			
	Separate Major Components	Separate rocket		Discharge Air				
Packdown**	Packdown Equipment	Ground				Return the rail structure down from vertical to horizontal position Disassemble base and rail structure Pack disassembled parts into transport vehicle Disassemble fill system		

4 Flight Simulation Subsystem

The Flight Simulation Subsystem is responsible for the simulation and analysis of all aspects relating to Pardalote's flight dynamics.

4.1 Software

The Flight Simulation subsystem oversees several softwares that handles various simulation and modelling tasks that concerns the flight dynamics of the vehicle.

Name	Purpose	Programming Language	Status
Ironbark	Trajectory and aerodynamics modelling	Python	Ongoing Development
Candlebark	Hybrid propulsion fluid and internal ballistics modelling	Python	Ongoing Development
Flutter	Fin Flutter Nastran FEA automation suite	Python	Completed
Eucalyptus	Combined rocket design environment	Java	Ongoing Development

Table 2: Flight Simulation Softwares

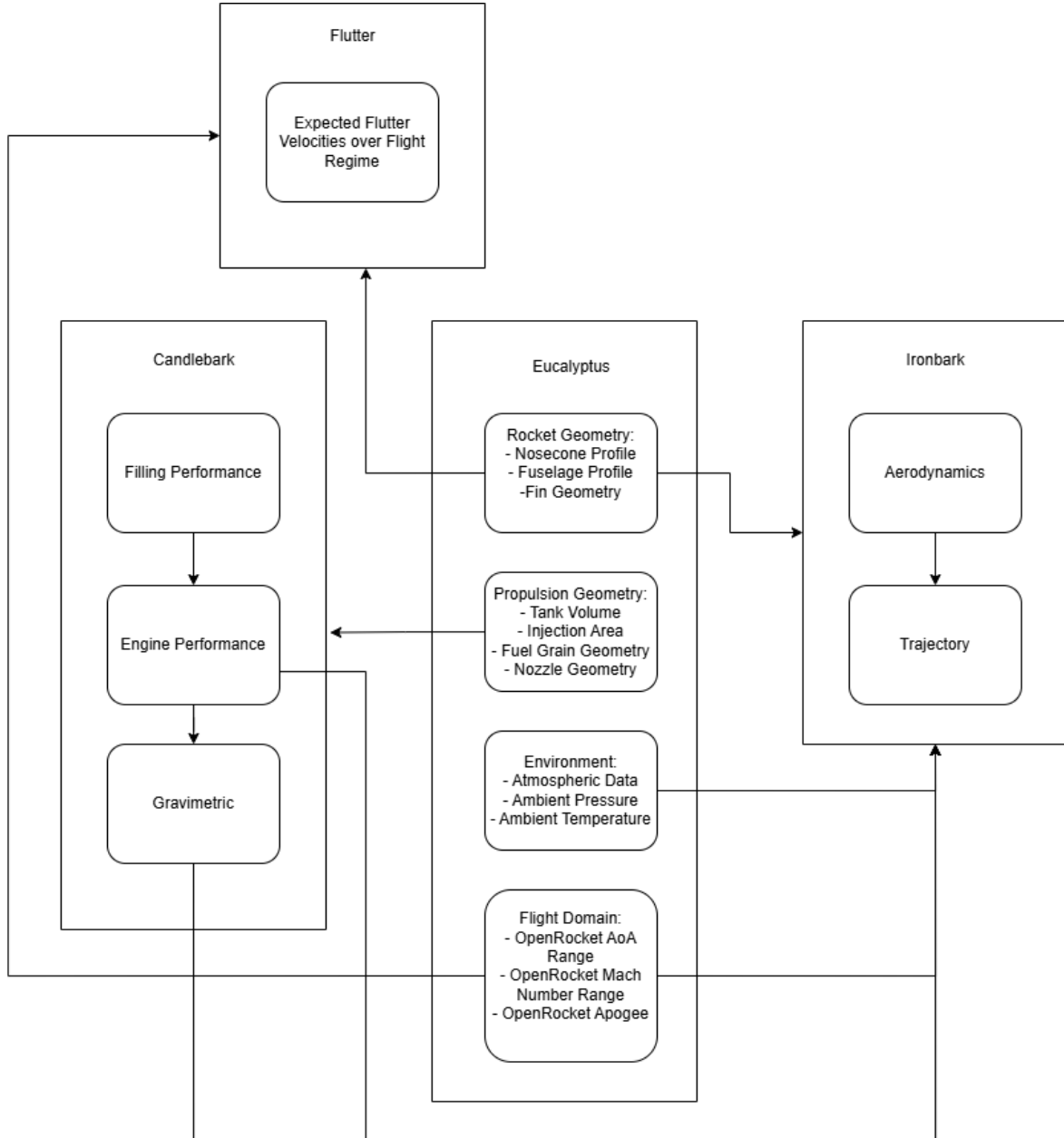


Figure 1: Flight Simulation Software Ecosystem

4.2 Programming language

Ironbark, Candlebark and Flutter are written in Python. The selection of Python and MATLAB was due to both accessibility to AMME and CS students as well as easier access to useful libraries such as RocketCEA. Eucalyptus was written in Java because it is built upon OpenRocket which is a Java application.

4.3 Candlebark

4.3.1 Hybrid Propulsion Simulation and Modelling Approach

KHoi

4.3.2 Input configuration files

Candlebark utilizes a configuration file format called Tom's Obvious, Minimal Language (TOML) to store simulation parameters. It operates based on key-pair values and is chosen due to its versatility and simplicity. A sample input file into Candlebark is attached in [APPENDIX ATACHMENT].

4.3.3 System State Initialization

Pre-simulation, Candlebark estimates the initial state of the system to define the initial state vector. The most important one is to determine the saturated state of the tank, more specifically the saturation pressure and ullage. This is calculated through the inputs on ambient temperature, oxidizer mass, and tank volume. Candlebark assumes that the tank is at equilibrium conditions with its surrounding environment and the tank casing itself. It also assumes that the gas/liquid phase is perfectly separated into two layers.

Original Ideal Gas Model

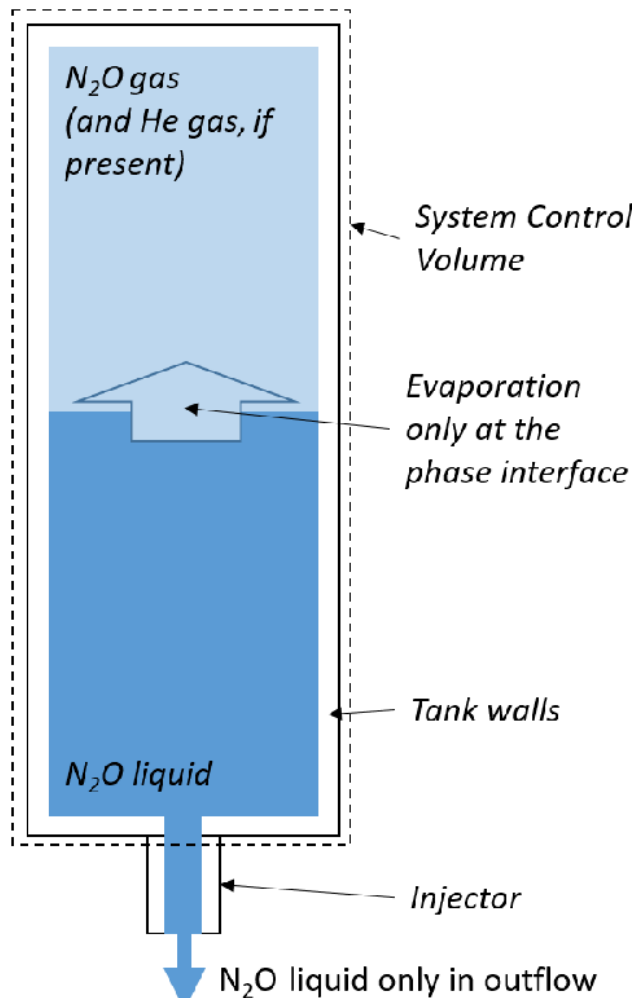


Figure 2: Tank Setup

The saturation pressure of N₂O is determined using the thermofluids library CoolProp given an input on temperature and phase.

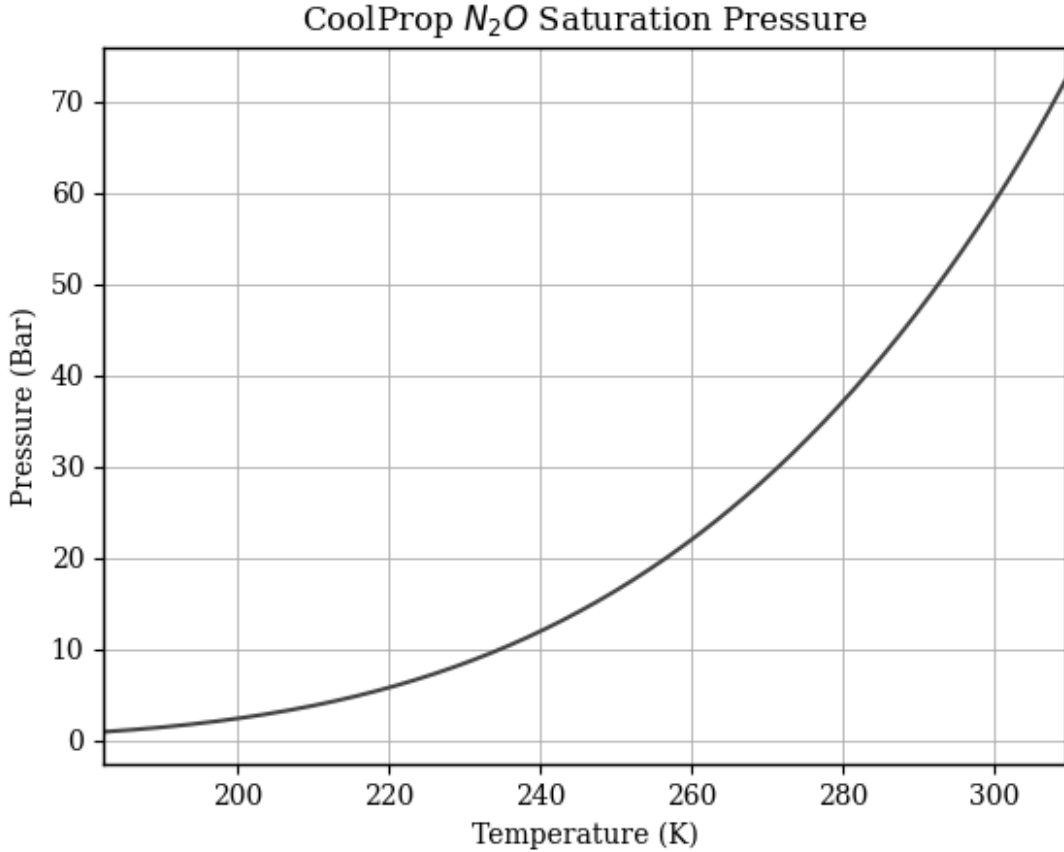


Figure 3: CoolProp Saturation Curve

If the presence of a presurrant mass is specified in the input, Candlebark can then estimate the pressure of the tank post-presurrant. This calculation is based on Dalton's Law, which dictates that the total pressure is equivalent to the sum of the partial pressures of the individual inert gasses. Hence the initial tank pressure P_{T_0} is expressed through this equation:

$$P_{T_0} = \frac{n_{o,g0} + n_{He}}{n_{o,g}} P_{\text{sat}_o}$$

To calculate the mass fractions of the liquid/vapour phase, Raoult's Law was then utilized. It is important to note that this assumes the nitrous is an ideal gas in equilibrium.

$$n_{o,l0} = \frac{\frac{m_{o0}}{M_o} RT_0 - P_{\text{sat}_o} V_T}{-P_{\text{sat}_o} \hat{V}_{o,l} + RT_0}$$

$$n_{o,g0} = \frac{P_{\text{sat}_o} \left(V_T - \hat{V}_{o,l} \frac{m_{o0}}{M_o} \right)}{-P_{\text{sat}_o} \hat{V}_{o,l} + RT_0}$$

This gives us a well-defined tank state to begin the simulation with. For downstream initial state, these were all assumed to be ambient temperature and pressure to begin with. The tank ullage can be converted

to a percentage value through relating amount of liquid moles to the molar volume of N₂O at the specific temperature:

$$\%_{\text{ullage}} = \left(1 - \frac{\hat{V}_l \times n_l}{\text{Tank Volume}}\right) * 100$$

4.3.4 Oxidiser Tank Flush Model

Candlebark's oxidiser tank flush model utilizes the Peng-Robinson non-ideal cubic equation of state in order to solve for the nitrous state properties per timestep. The governing principles and equations used to model the flushing is tabulated below:

Constraint 1	Equation
Mass Conservation	Row 1, Cell 2
Energy Conservation	Row 2, Cell 2
Flow Relation	Row 3, Cell 2
Volumetric Constraint	Row 4, Cell 2
Liquid EoS	Row 5, Cell 2
Vapour Eos	Row 6, Cell 2
Vapour-Liquid Equilibrium	jsdkjs

Table 3: Your Table Caption

4.3.5 Feedsystem Pressure Drop Model

The feedline pressure drop uses a component model for the liquid flow regime and a constant for the gaseous pressure regime. Currently only incompressible flow is supported. As oxidiser flows from the tank to the injector it's pressure drops due to friction in the plumbing system. The pressure drop due to gravity was not modeled because it would require knowing the rocket's acceleration at each point during the tank drain. This information depends on trajectory simulations, which are themselves derived from thrust curve simulations that include the effects of this pressure drop. Accounting for this would create a circular dependency, so it was excluded from the simulation.

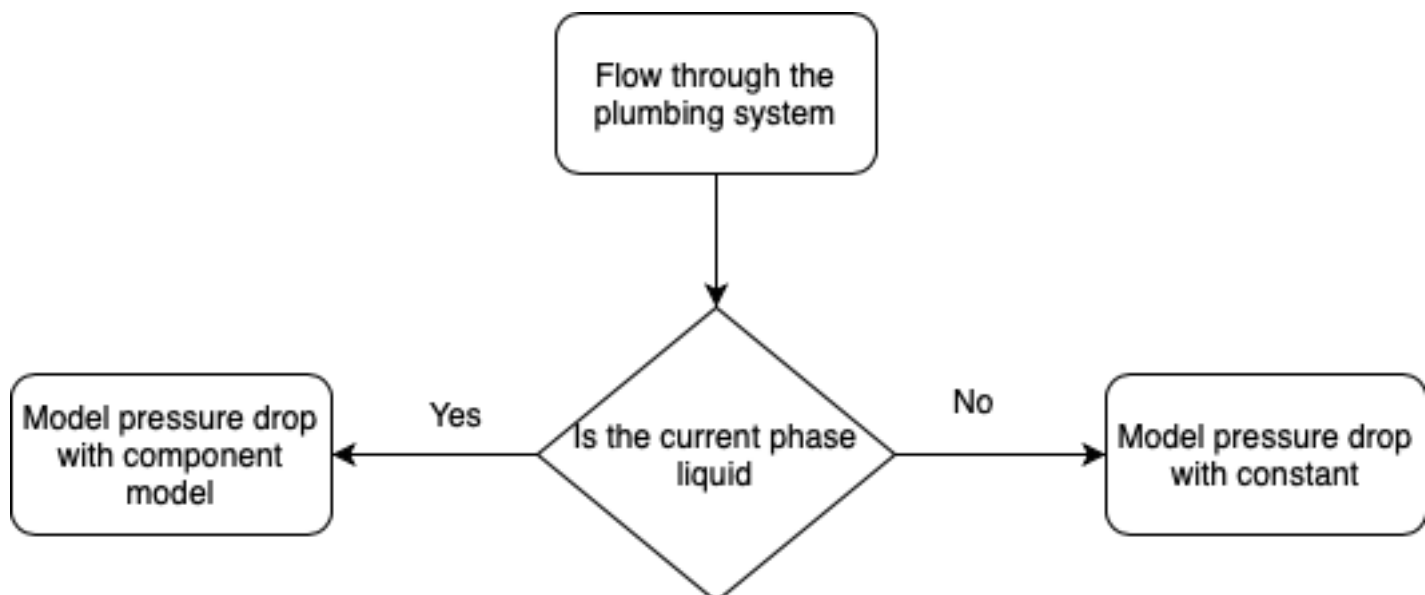


Figure 4: Pressure drop model Chart

The plumbing system consists of a pipe section, followed by an SRAD co-axial valve, and then another pipe section before the injector. Therefore, a component system was developed to model pressure drop of noncompressible fluid across pipe and a globe valve, the valve type we chose to model our valve. The total pressure drop across the plumbing system is the sum of pressure drops across each component.

Pipe A single phase model using the Darcy-Weisbach equation and the Clamond method to solve the Colebrook equation for the Darcy Friction Factor is used. The parameters are as follows.

- the density of the working fluid ρ
- the dynamic viscosity of the working fluid μ
- the mass flow rate of the working fluid m
- the diameter of the pipe d item The roughness of the pipe
- the length of the pipe l

The velocity of the fluid is calculated

$$\langle v \rangle = \frac{4 \cdot m}{\pi \cdot D^2 \cdot \rho}$$

Then the reynolds number

$$\nu = \frac{\mu}{\rho}$$

$$\text{Re} = \frac{\langle v \rangle \cdot D}{\nu}$$

Then the friction factor f_d is calculated using Clamond's method for solving the Colebrook equation.

$$\frac{1}{\sqrt{f_d}} = -2 \log_{10} \left(\frac{\varepsilon}{3.7D} + \frac{2.51}{\text{Re}\sqrt{f}} \right)$$

Finally, the head loss is calculated using the Darcy-Weisbach equation

$$\Delta P = f_D \cdot \frac{L}{D} \cdot \frac{\rho \cdot \langle v \rangle^2}{2}$$

Globe Valve The model for the globe valve is based on the model found in Crane where the loss coefficient depends on the ratio of the interior diameter of the interior pipe to the diameter of the input pipe.

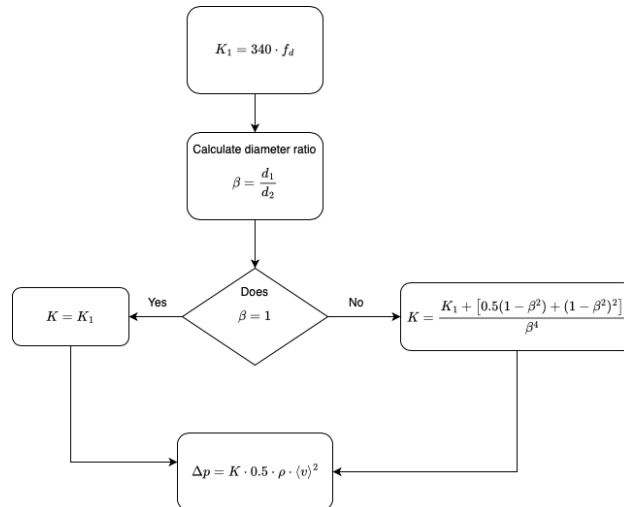


Figure 5: Caption

The friction factor is calculated using the same method as used for the pipe component.

4.3.6 Injector Model

The injector modelling comprises of a couple of different equations being interchanged depending on the current state of the system:

Single Phase Incompressible (SPI) Single Phase Compressible (SPC) Homogeneous Equilibrium Model (HEM) Dyer Model.

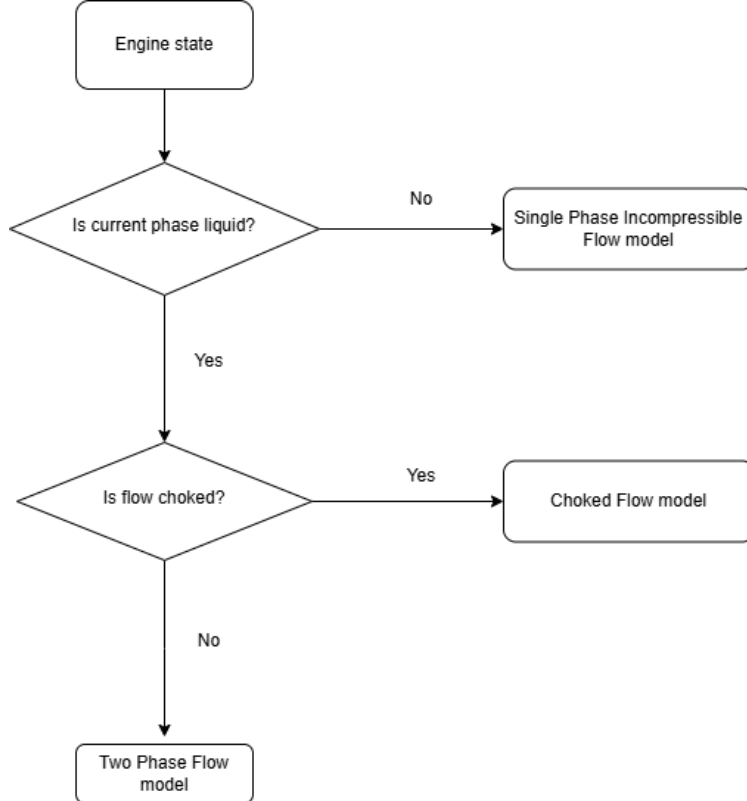


Figure 6: Injector Model Flow Chart

Single Phase Incompressible

The single phase incompressible model computes the theoretical mass flow rate based on the pressure differential between the tank pressure and chamber pressure, based upon the principles of Bernoulli's and the continuity equations. The assumptions of this model is:

- Flow is incompressible
- No frictional losses occur within the orifice
- Height remains constant within the orifice
- Uniform pressure and velocity before and after the orifice;

The equation that describes SPI is:

$$\dot{m}_{SPI} = C_D * A_{inj} * \sqrt{2\rho(P_1 - P_2)} \quad (1)$$

Single Phase Compressible

4.3.7 Fuel Regression Model

As the fuel grain reacts with the oxidiser, the fuel grain radius regresses to the edge of the chamber which is modelled by the spatially averaged Marxman regression rate:

$$\dot{r} = aG_{ox}^n \quad (2)$$

where a, n are fuel specific constants and G_{ox} is the oxidiser mass flux. For the ABS/N2O combination the constants are

- $a = 0.000127 \text{ m/s}$
- $n = 0.65$

The time derivative of the volume of the solid fuel grain is given by

$$\frac{dV}{dt} = \frac{\pi l_g}{4\Delta t} (D_{p2}^2 - D_{p1}^2) \quad (3)$$

where l_g is the grain length, D_{p1} is the previous port diameter and D_{p2} is the current port diameter:

$$D_{p2} = D_{p1} + 2\dot{r}\Delta t \quad (4)$$

The mass flow rate of the solid fuel grain is then given by

$$\dot{m}_f = \rho \frac{dV}{dt} \quad (5)$$

4.3.8 Grain Geometry Model

Candlebark currently supports the following fuel grain geometries: Circular, Star, Pseudofinocyl and wagon wheel.

Area Calculations

Simple geometries such as the circular port or triangle port's areas are calculated using their respective formulas:

$$A_{circ} = \pi * (D_{port}/2)^2 \quad (6)$$

$$A_{triangle} = 0.5 * L_{base} * L_{height} \quad (7)$$

For more complex shapes, Gauss's area formula was then implemented:

$$A = \frac{1}{2} \left| \sum_{i=1}^n (x_i y_{i+1} - y_i x_{i+1}) \right| \quad (8)$$

Perimeter Calculations

The perimeter calculations of the shape is split into two different modes, one where the shape has not encountered the fuel grain boundaries yet and where it does and sliver burning occurs.

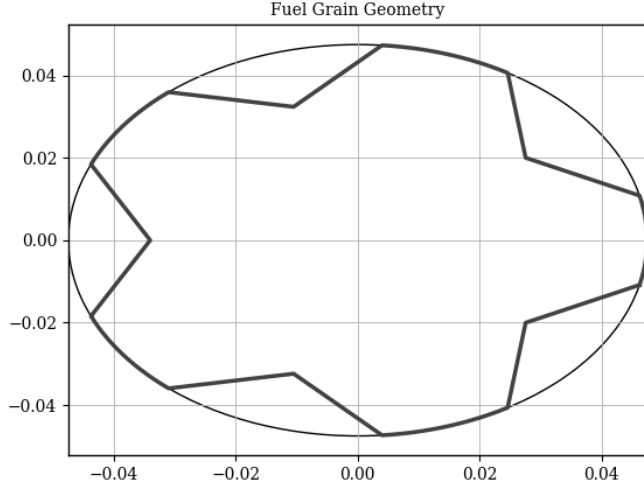


Figure 7: Sliver Burning Occuring

If the shape has not reached it's boundary yet, the perimeter is then calculated by the sum of the euclidean distance between two consecutive vertices

$$P = \sum_{i=1}^n \sqrt{(x_{i+1} - x_i)^2 + (y_{i+1} - y_i)^2} \quad (9)$$

In the case of sliver burning, the same logic still applies but with the extra constraint that the distance between (x,y) and origin $(0,0)$ must be less than the fuel grain diameter.

$$P = \sum_{\substack{i=1 \\ \sqrt{x_i^2 + y_i^2} < D_{\text{grain diameter}}}}^n \sqrt{(x_{i+1} - x_i)^2 + (y_{i+1} - y_i)^2} \quad (10)$$

Buffering Operation

The buffer operation, given a regressed distance \dot{r} , computes how the geometry of the current shape morphs every time step. The buffer logic relies on computing the Minkowski sum of a circle with a radius \dot{r} A with the current polygon B . The Minkowski sum operation adds each point in A to each point in B which results in the newly regressed geometry.

$$A + B = \{\mathbf{a} + \mathbf{b} \mid \mathbf{a} \in A, \mathbf{b} \in B\} \quad (11)$$

This logic is handled using the Python library Shapely, which handles both the buffering as well as the extraction of the perimeter of the shape.

Overlapping Operation

4.3.9 Determination of Simulation Coefficients and Efficiencies

The injector discharge coefficient (C_D) was found experimentally through a series of cold flow testing of the Pardalote injector puck. Candlebark's nonballistic simulation was used to replicate the conditions of a cold flow test, and the resulting simulation data were then compared to run tank load cell data to find an appropriate C_D .

An optimization method was then used on the data sets to find an appropriate discharge coefficient. The objective function computes the sum of squared errors between the simulated and experimental mass values, providing a measure of how well the simulation aligns with reality. The method used in the solver is the L-BFGS-B method, which is similar to the BFGS method and is used for smooth and differentiable problems

which fits the description of our use case. The main variation between BFGS and L-BFGS-B is that L-BFGS-B is designed to operate within an input constraint; this is desirable as it prevents the solver from exploring C_D values that are not realistic i.e., $C_D <= 0$, which would be anti-physical. The bounds inputted into the solver are 0.5, 0.8, which are within reasonable values of C_D from literature and the initial guess is 0.6. After 31 iterations, the solver completes with a liquid phase C_D of 0.701. The full code is included in the appendix section ???. The vapour phase C_D was then tuned manually, it is found that a value of 0.35 was sufficiently accurate.

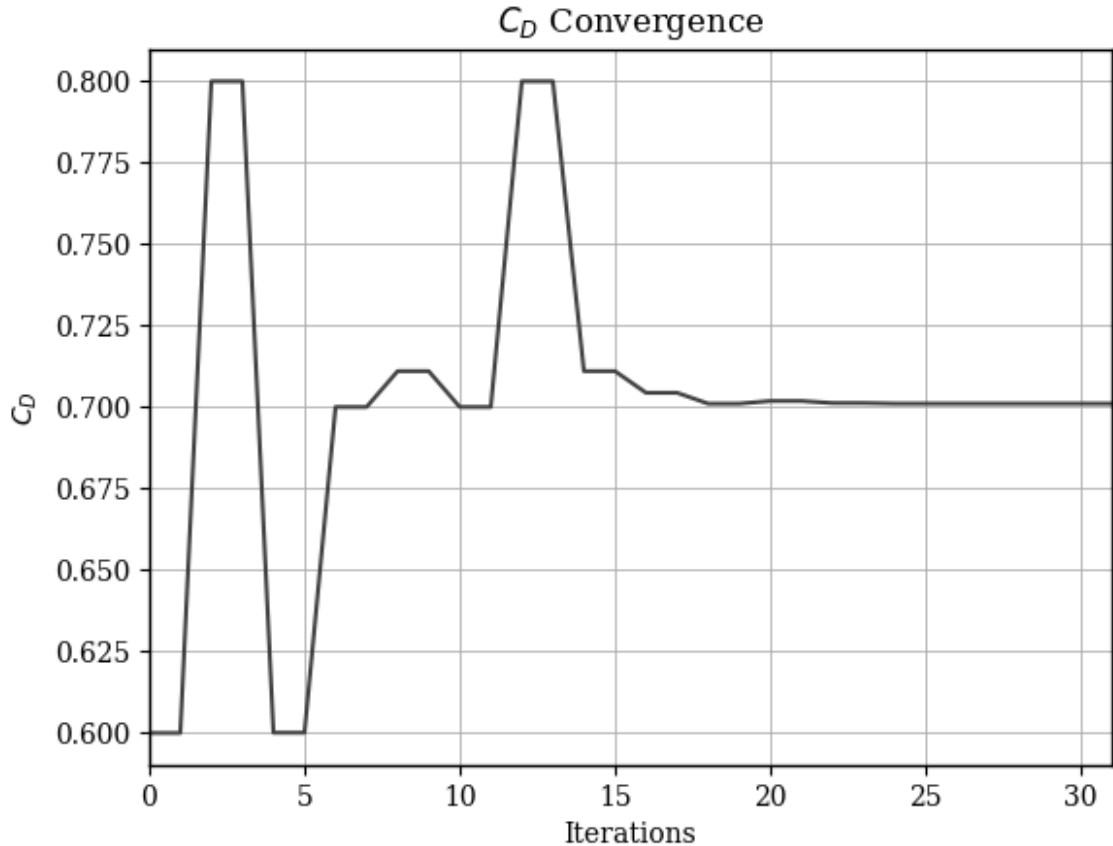


Figure 8: C_D Optimization

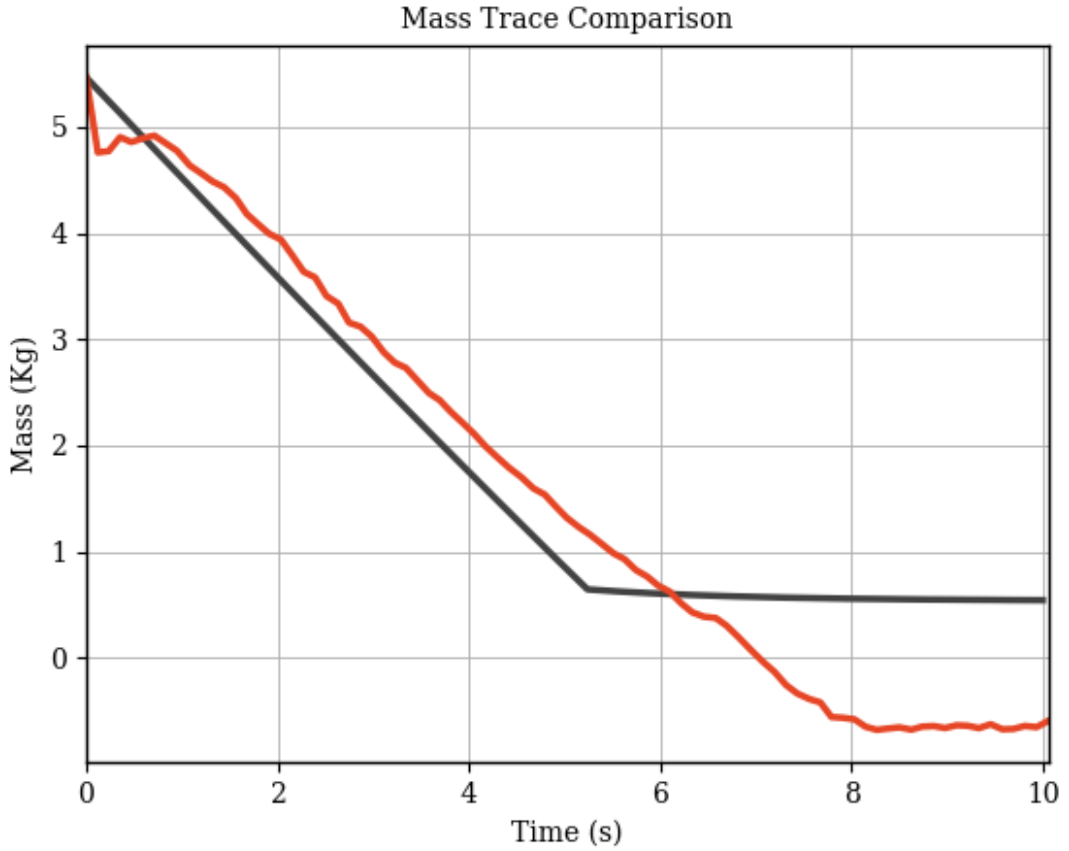


Figure 9: Mass Trace

The nozzle flow model employed by Candlebark relies on a few key coefficients and efficiencies related to the properties of the flow. The characteristic velocity C^* is defined with respect to the mass flow rate, area and pressure at the choked throat

$$C^* = \frac{P_t A_t}{\dot{m}} \quad (12)$$

This value provides a measure of the completeness of combustion, and for a given mass flow rate and area, a higher value indicates a higher chamber pressure, and hence higher thrust. We can define an efficiency factor related to this value, η_{C^*}

$$\eta_{C^*} = \frac{c_{measured}^*}{c_{ideal}^*} \quad (13)$$

This ratio compares the measured and ideal characteristic velocities usually obtained from an equilibrium combustion calculation. The value provides an indicator of combustion performance, with values closer to 1 reflecting more effective thrust generation, with propellants fully mixing and reacting within the combustion chamber. The value used in Candlebark sims is based on ??, which states that for Hybrids with no mixing element, an efficiency of 0.784 is achieved.

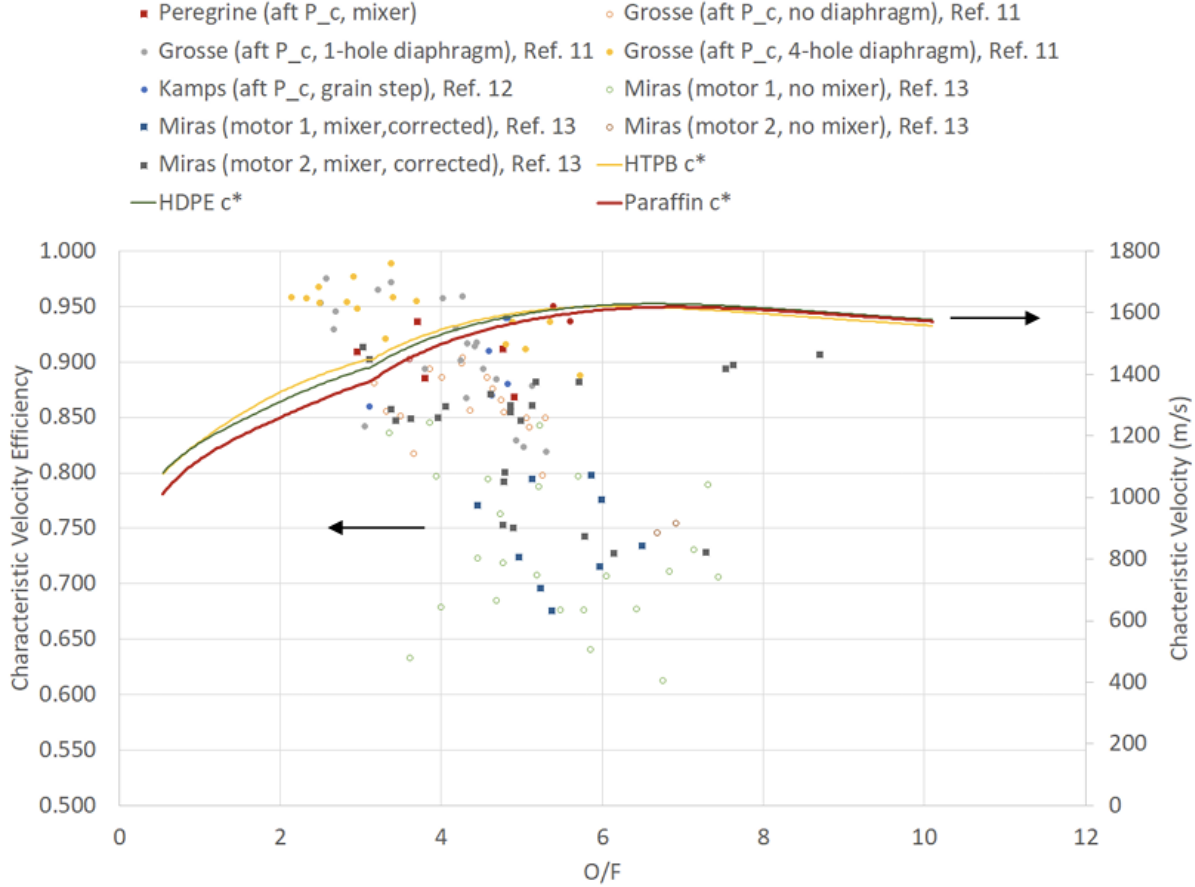


Figure 10: Comparison between several Hybrids C_{eff} from ??

Candlebark assumes that this value is constant, however literature value has demonstrated that with longer burn time systems, a shift in C_{eff} is measured. However considering Candlebark's relatively short burn time, a static value is considered sufficient.

Another measure of nozzle performance is related to the geometry of the nozzle itself, where we define an exhaust efficiency η_e proportional to the diverging angle of the nozzle. This is to account for efficiency losses due to a conical nozzle design.

$$\eta_e = \frac{1 + \cos \alpha}{2} \quad (14)$$

This effect provides a correction to the exit velocity at the nozzle, and hence the thrust output of the engine.

4.3.10 Nozzle Flow Model

The nozzle model in Candlebark assumes that the flow expands isentropically, and uses equations for a calorically perfect gas, which means that the gas has a constant specific heat capacity. Additionally the model assumes that flow across a shockwave is adiabatic, meaning there is no heat transfer across the shockwave. The exit Mach number at the nozzle M_e is determined from the expansion ratio of the nozzle geometry. Assuming choked flow, the Mach number at the nozzle throat is $M_t = 1$, meaning we can write the expansion ratio with the exit area and throat area in terms of the exit Mach number with

$$\left(\frac{A_e}{A_t} \right)^2 = \frac{1}{M_e^2} \left[\frac{2}{\gamma + 1} \left(1 + \frac{\gamma - 1}{2} M_e^2 \right) \right]^{\frac{\gamma + 1}{\gamma - 1}} \quad (15)$$

Where A_e is the exit area, A_t is the throat area, forming the expansion ratio A_e/A_t , and γ is the ratio of specific heats for the fluid. Equation 15 must be solved with a root finding method to find the exit Mach number solution, of which there are two solutions, for the subsonic and supersonic flow regimes. With the

exit Mach number, we can solve for the exit to stagnation pressure ratio

$$\frac{p_e}{p_0} = \left[1 + \frac{\gamma - 1}{2} M_e^2 \right]^{-\frac{\gamma}{\gamma-1}} \quad (16)$$

Where p_0 is the stagnation pressure from the tank reservoir and p_e is the pressure at the exit, forming the pressure ratio p_e/p_0 . This can be solved for both subsonic and supersonic flow regimes. The gas expansion creates a normal shock at the nozzle exit, with the pressure ratio across this shock given by

$$\frac{p_2}{p_1} = 1 + \frac{2\gamma}{\gamma+1} (M_1^2 - 1) \quad (17)$$

p_2/p_1 is the pressure ratio across the normal shock, and $M_1 = M_{e,sup}$ is the supersonic exit Mach number solution from Equation 15. The pressure ratio at the normal shock exit to the stagnation pressure from the reservoir ($\frac{p_e}{p_0}|_{NSE}$) can then be obtained from multiplying these pressure ratios, with

$$\frac{p_e}{p_0}|_{NSE} = \frac{p_2}{p_1} \cdot \frac{p_e}{p_0}|_{sup} \quad (18)$$

In the simulation model we define the stagnation pressure from the reservoir as the pressure in the chamber, p_c , and since the nozzle exits to the ambient atmosphere p_a , we can use the calculated pressure ratios to determine the performance of the engine. If the pressure ratio p_a/p_c is greater than the pressure ratio for a subsonic flow calculated from Equation 16, then we can determine the exit Mach number by rearranging Equation 16 to solve for M_e , where we find

$$M_e = \sqrt{\frac{2}{\gamma-1} \left[\left(\frac{p_c}{p_a} \right)^{\frac{\gamma-1}{\gamma}} - 1 \right]} \quad (19)$$

The temperature and density at the exit are then given by

$$t_e = \frac{T_c}{1 + \frac{\gamma-1}{2} M_e^2} \quad (20)$$

$$\rho_e = \left(\frac{\rho_c}{1 + \frac{\gamma-1}{2} M_e^2} \right)^{\frac{1}{\gamma-1}} \quad (21)$$

With a given nozzle efficiency η_n , and the exhaust efficiency as defined in Equation 14, the velocity at the exit is then

$$v_e = \eta_n \eta_e M_e \sqrt{\gamma R t_e} \quad (22)$$

With R the gas constant.

In the case of the pressure ratio p_a/p_c lying between the pressure ratio for the normal shock Equation 18 and the subsonic pressure ratio, the normal shockwave forms at the nozzle exit, and the exit Mach number is

$$M_e = \sqrt{\frac{(\gamma-1)M_s^2 + 2}{2\gamma M_s^2 - (\gamma-1)}} \quad (23)$$

Where M_s is the supersonic Mach number obtained from the root finding Equation 15

In each case, the mass flow rate at the exit \dot{m} is related to these flow properties, as well as the exit area A_e through

$$\dot{m} = \rho_e A_e \frac{v_e}{\eta_e} \quad (24)$$

The pressure at the front of the normal shock p_1 is related to the supersonic Mach number M_s as well as the chamber pressure p_c with

$$p_1 = \left(\frac{p_c}{1 + \frac{\gamma-1}{2} M_s^2} \right)^{\frac{\gamma+1}{2(\gamma-1)}} \quad (25)$$

The temperature at this point t_1 is related to the chamber temperature T_c through

$$t_1 = \frac{T_c}{1 + \frac{\gamma-1}{2} M_s^2} \quad (26)$$

The pressure at the exit p_e , across the shock wave is

$$p_e = p_1 \left(1 + 2(M_s^2 - 1) \frac{\gamma}{\gamma + 1} \right) \quad (27)$$

And the temperature at the exit T_e is

$$T_e = t_1 \left[1 + \frac{2\gamma}{\gamma + 1} (M_s^2 - 1) \right] \left[\frac{2 + (\gamma - 1)M_s^2}{(\gamma + 1)M_s^2} \right] \quad (28)$$

With this, the velocity at the exit v_e is

$$v_e = M_e \sqrt{\gamma R T_e} \quad (29)$$

In the case of either subsonic flow at the exit or the normal shock, the mass flow rate \dot{m} is related to the exit area A_e and the flow properties

$$\dot{m} = \rho_e A_e \frac{v_e}{\eta_e} \quad (30)$$

In the other case of supersonic flow, the mass flow rate \dot{m} is

$$\dot{m} = \frac{p_c A_t}{\eta_n C^*} \quad (31)$$

With A_t the area of the throat, η_n the nozzle efficiency and C^* is the characteristic velocity of the nozzle as discussed in the previous section. C^* is estimated in this program through the use of the RocketCEA Python library, which is a wrapper for NASA's Fortran Chemical Equilibrium with Applications (CEA) software. This is a chemical equilibrium solver that is used by Candlebark to provide the characteristic velocity of the nozzle, as well as the specific impulse of the flow. RocketCEA calls the CEA software in Python, allowing it to be used in the simulation model. The pressure at the exit is

$$\rho_e = \left(\frac{\rho_c}{1 + \frac{\gamma-1}{2} M_e^2} \right)^{\frac{1}{\gamma-1}} \quad (32)$$

And the temperature is

$$T_e = \frac{T_c}{1 + \frac{\gamma-1}{2} M_e^2} \quad (33)$$

With these properties, the velocity at the exit is then given by Equation 29. Using the flow properties, the specific impulse (I_{sp}) of the flow can be determined from RocketCEA. With these values, the overall thrust output (T) is given by

$$T = I_{sp} g \dot{m} \eta_e + (p_e - p_a) A_e \quad (34)$$

Where the exhaust efficiency correction of Equation 14 is applied.

4.3.11 Engine Gravimetric Model

The three components contributing to the engines center of gravity (CG) are the chamber, tank and nozzle. The CG of the chamber is constant, since the fuel grain burns outward in a cylindrical shape and is equal to

$$l_c = \frac{l_g}{2} + l_{post} + l_n \quad (35)$$

where l_g is the grain length, l_{post} is the length between the grain and the nozzle and l_n is the nozzle length. The tank CG is dependent on the CG's of the separate phases of the oxidiser. The CG of the liquid mass relative to the tank is calculated by dividing the liquid volume by the tank cross section area:

$$l_{N2Ol} = \frac{m_{N2Ol}}{\rho_{N2Ol} A_t} \quad (36)$$

The CG of the gaseous N₂O is

$$l_{N2Og} = \frac{l_t}{2} + l_{N2Ol} \quad (37)$$

where l_t is the length of the tank. The tank CG is then

$$l_T = \frac{l_{N2O}m_{N2O} + l_{N2Og}m_{N2Og}}{m_{N2O}} + l_f + l_{pre} + l_g + l_{post} + l_n \quad (38)$$

where l_f, l_{pre} are the feedline length and length between the tank and chamber respectively. The nozzle CG is constant at simply half the nozzle length. The engine CG is then

$$CG = \frac{l_T m_{N2O} + l_c m_c + l_n m_n}{m_{N2O} + m_c + m_n} \quad (39)$$

where m_c, m_n are the masses in the chamber and nozzle respectively.

4.4 Candlebark Validation

This is a collection of all validations that has been completed on Candlebark. All TOML configuration inputs is accessible via the appendix section.

4.4.1 Phoenix 1B

4.4.2 Phoenix 1A

4.4.3 McGill Rocketry

4.4.4 Waterloo Rocketry

4.4.5 Waratah

4.4.6 Wattle

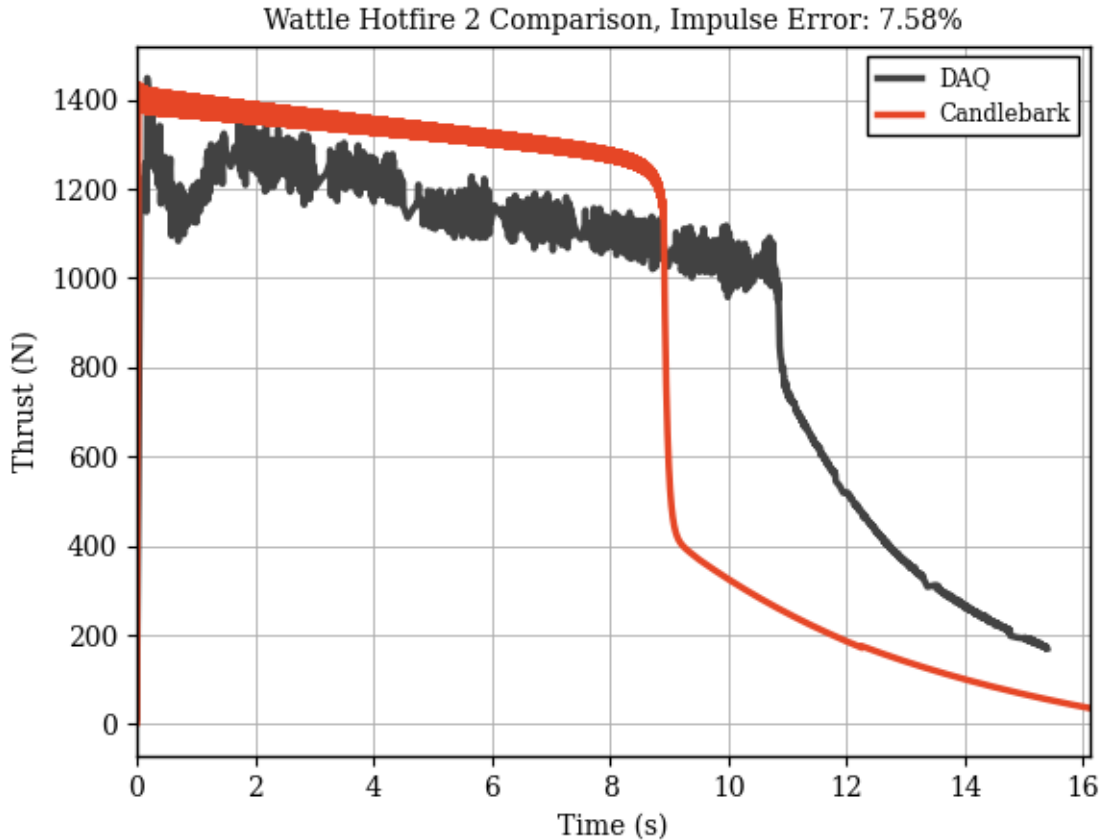


Figure 11: Hotfire Test 9 Results

4.4.7 Pardalote Mk1

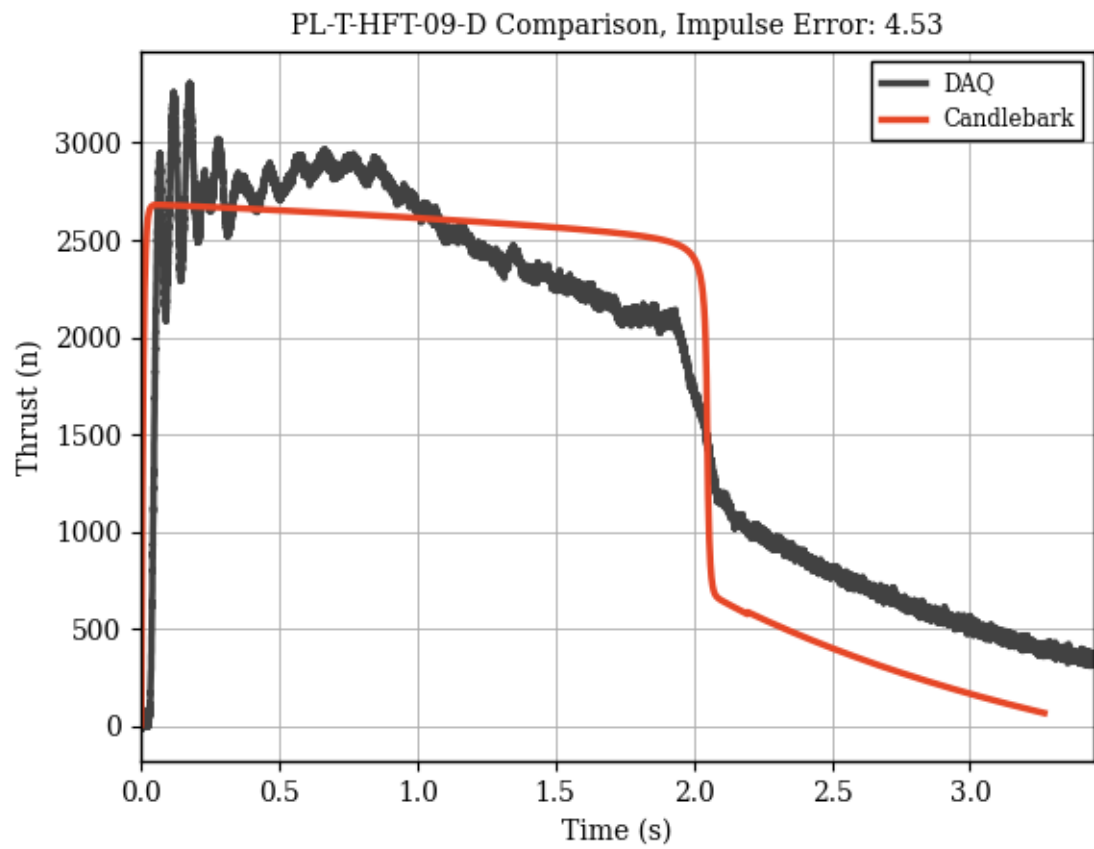


Figure 12: Hotfire Test 9 Results

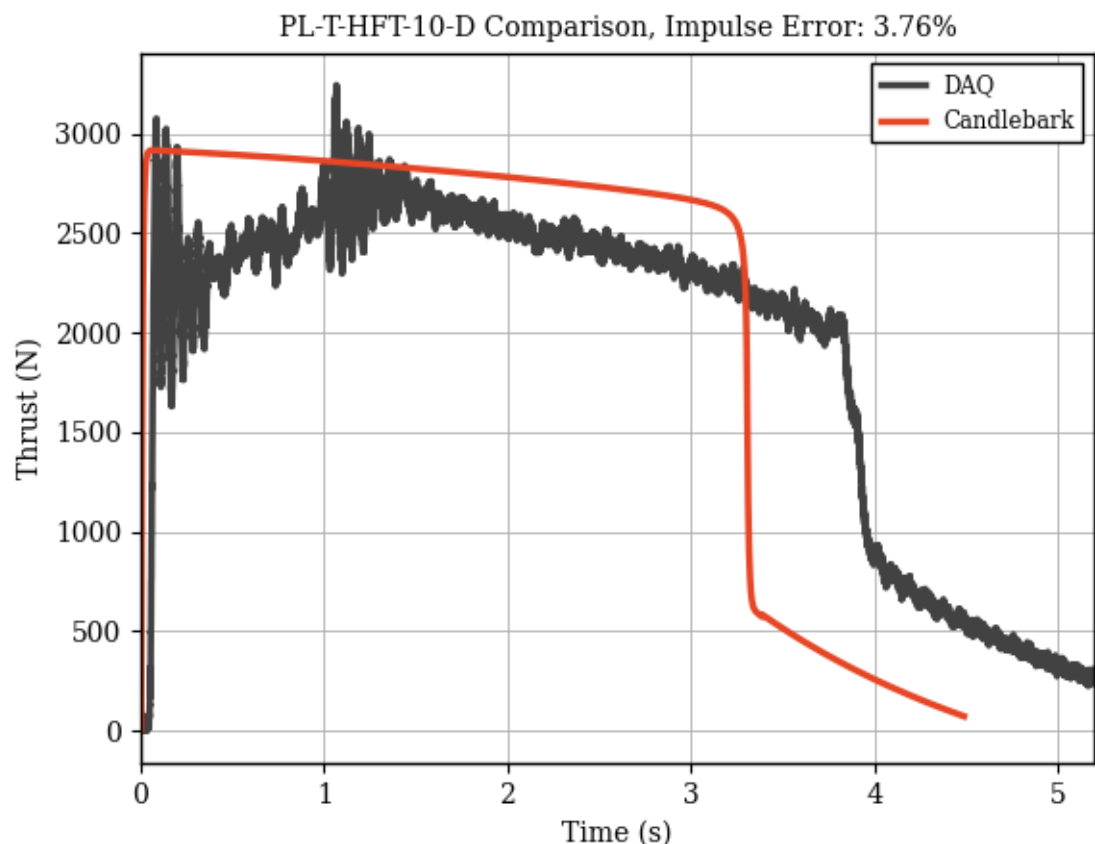


Figure 13: Hotfire Test 9 Results

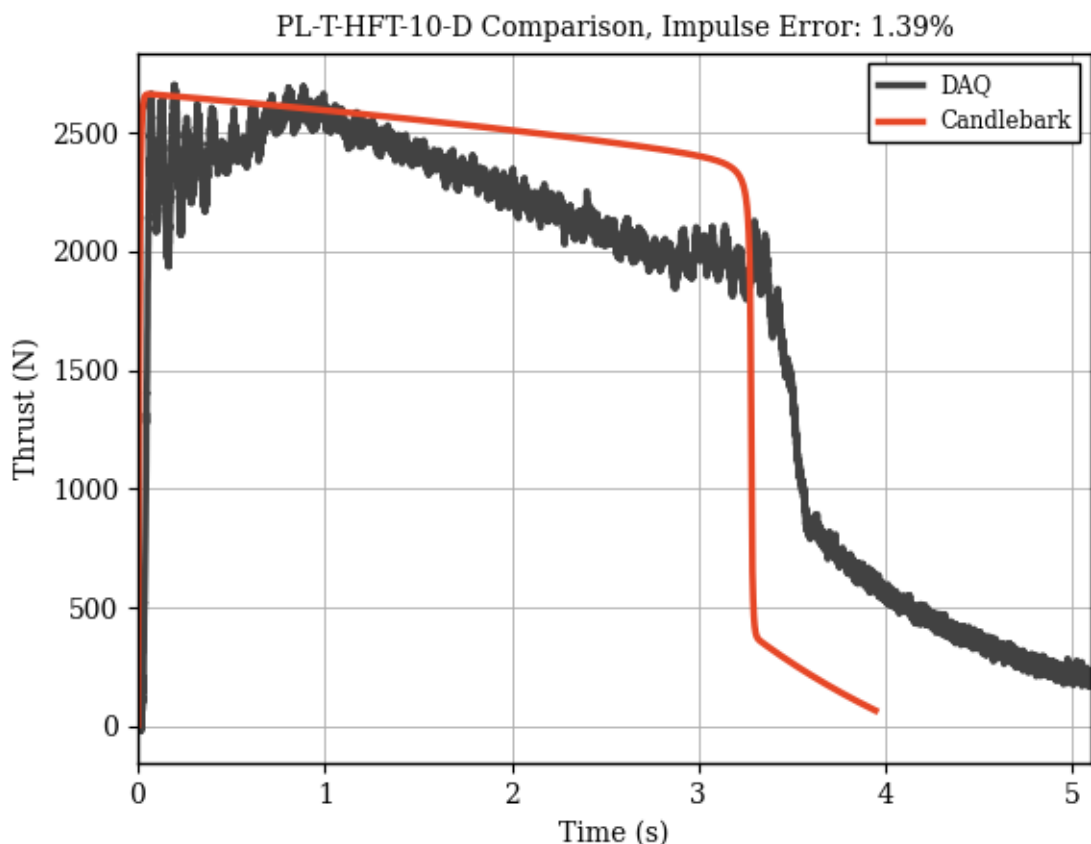


Figure 14: Hotfire Test 9 Results

4.4.8 Pardalote Mk2

4.5 Ironbark

4.5.1 Trajectory Simulation and Modelling Approach

khoi

4.5.2 Determination of Aerodynamic Coefficients

Dicky J Low Fidelity Method: Empirical Relations Medium Fidelity Method: Ironbark Panel Code

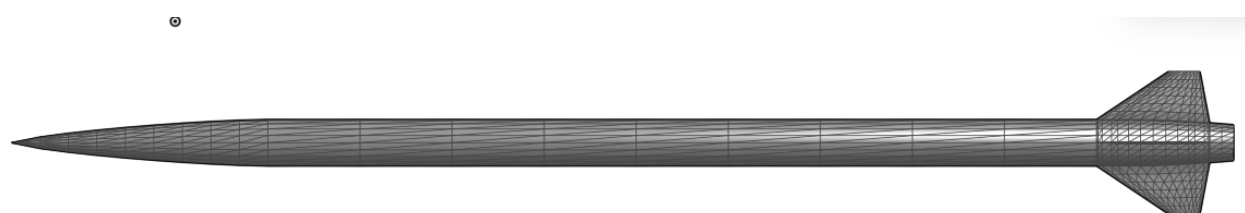


Figure 15: Enter Caption

High Fidelity Method: CFD + Wind tunnel testing

4.5.3 6-DOF Trajectory Kinematics Equations

4.6 Ironbark Validation

4.6.1 Bluewren

4.6.2 Rosella

4.6.3 Silvereye

4.7 Flutter

4.7.1 Material Properties Database

young's mod shear mod poisson ratio

Liangyu

4.7.2 Fins

4.8 Pardalote MK2 Propulsion System Sizing

4.8.1 Sizing Prerequisites

For preliminary sizing, the Pardalote Mk2 .ork file was used, as provided by the Aerostructures subsystem. It's stage mass was then overriden with the Pardalote Mk1 dry mass as a conservative estimate for the final mass for Pardalote MK2, this is based on the worst case scenario where no mass is conserved.

From this, a steady state thrust curve was estimated in order to approximate a target peak thrust and target impulse.

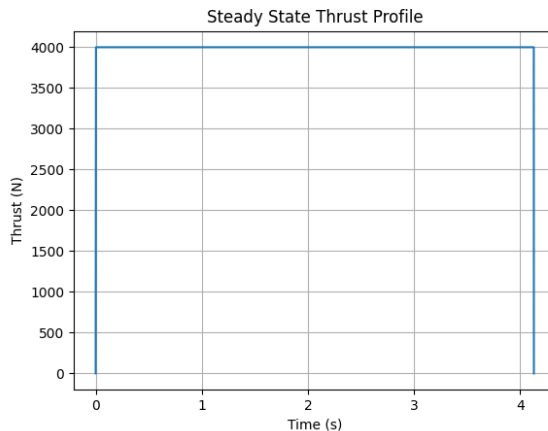


Figure 16: Steady State Thrust Curve

The steady state thrust curve then confirms that an impulse of 16500 ns is sufficient for the vehicle, assuming no mass savings occurs, would be sufficient to reach 13000 ft. With the projected Pardalote Mk2 mass, this would be an equivalent to 15000 ft. Accounting for Candlebark's known error of 6-8% and Openrocket's error of 1%, this places the vehicle's predicted apogee to be within the range of 13000 ft.

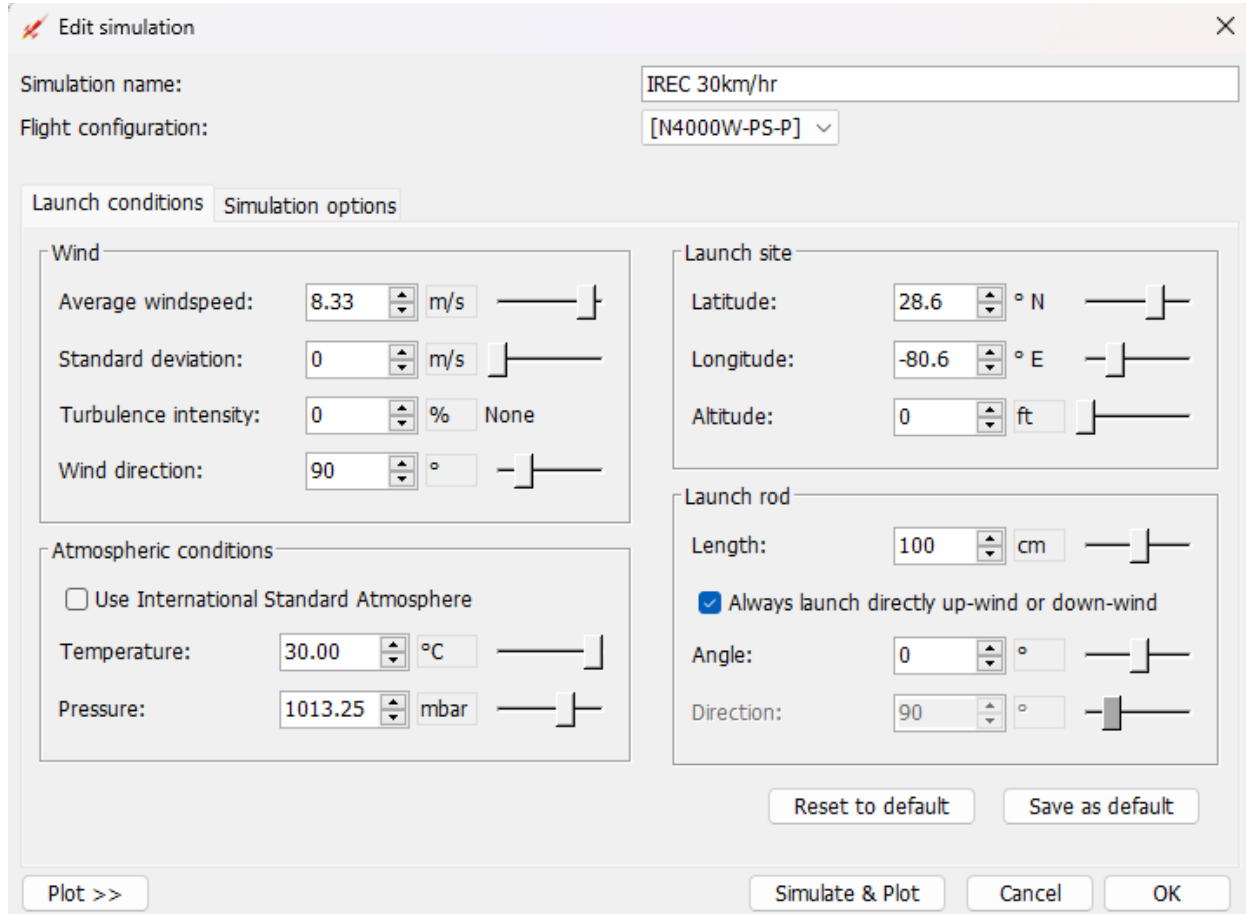


Figure 17: OpenRocket Simulation Configuration

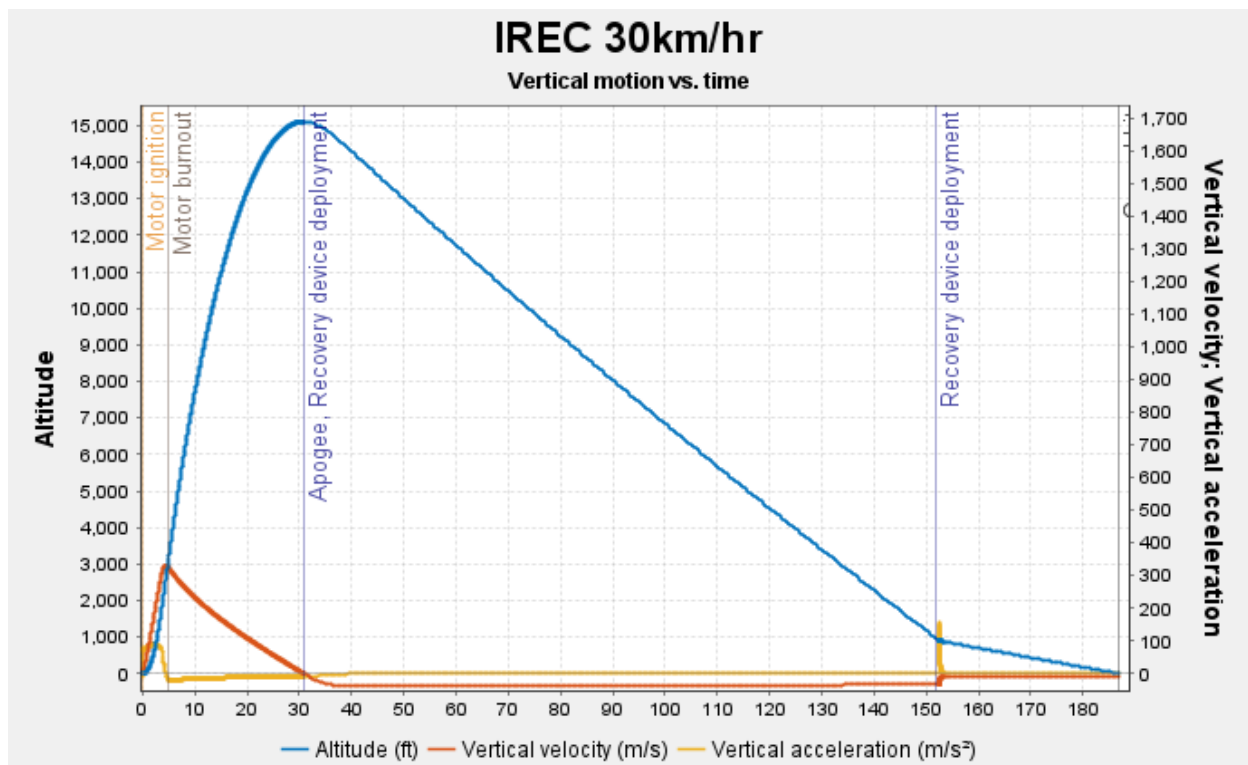


Figure 18: Pardalote trajectory on an N4000 motor

The selected design point tank pressure is 50 bar, this value was selected based on the tank pressures that the team has achieved in previous static fire tests.

The downstream pressure is then selected such that the injector pressure drop remains choked throughout the duration of the liquid burn. This is a requirement in order to reduce the effect of feed-system coupled combustion instabilities.

The target OF ratio of the system is found through an analysis of doing a sweep of OF at varying chamber pressures to compare the characteristic velocity c^* .

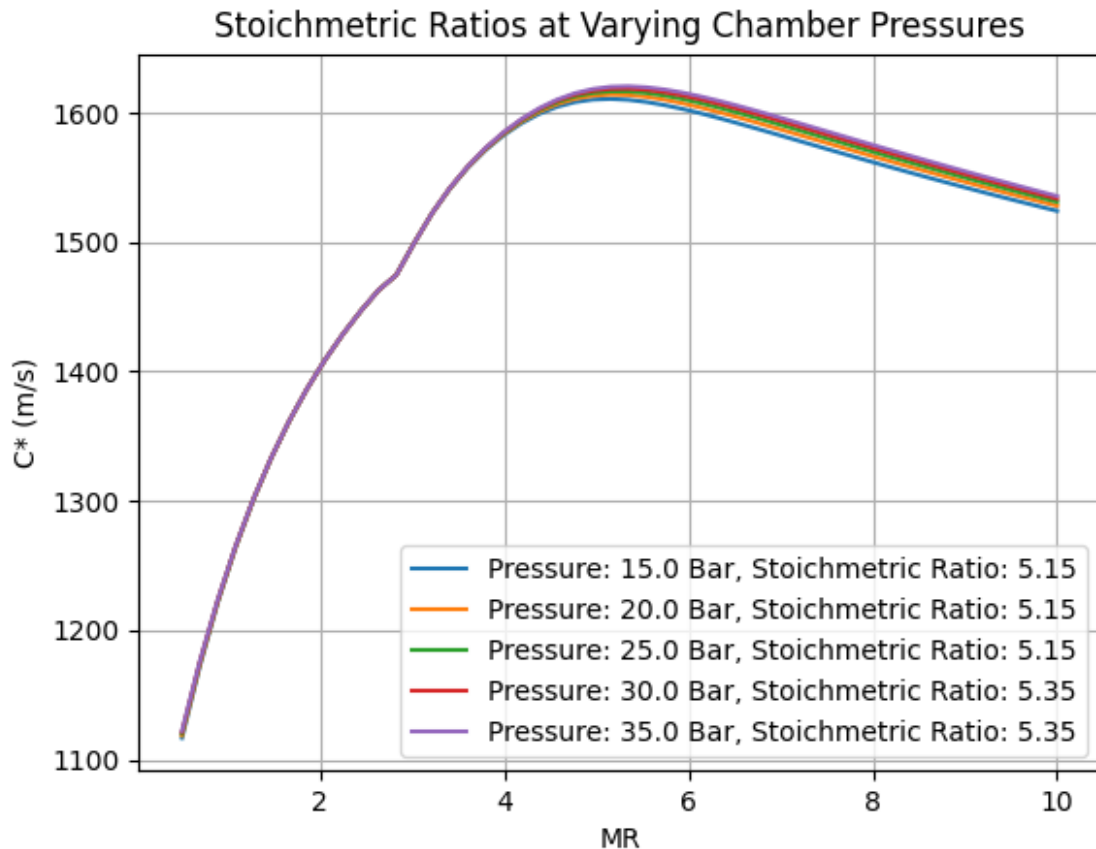


Figure 19: C^* Study

4.8.2 Design Optimization Strategy

For the purposes of preliminary sizing, OpenRocket was used as the main tool. Ironbark was not selected due to its higher order aerodynamics making it not an appropriate tool for rapid iterations. Two design optimization methods were conducted including a genetic algorithm as well as a brute force methodology method. Initially, a parametric study was completed on Pardalote's MK1 configuration to determine key sensitive variables to relevant performance as well their suggested bounds.

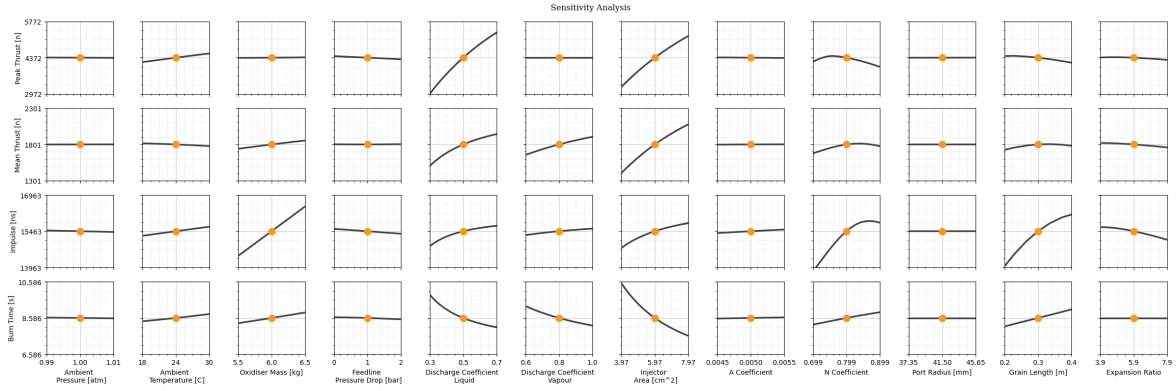


Figure 20: A full integrated system parametric study

Based on this, a solution vector z is determined to be:

$$z = \{D_{port}, A_{injector}, D_{throat}, V_{tank}, Ullage\} \quad (40)$$

4.8.3 Fuel Grain Geometries

A main challenge to be resolved with this next iteration is to improve the OF ratio during the course of engine burn. Considering that the fuel grain length will be reduced from MK1 to MK2, and that 3D printed grains have been deemed safe to operate through 3x static fire tests, more complex fuel grain geometries will be considered.

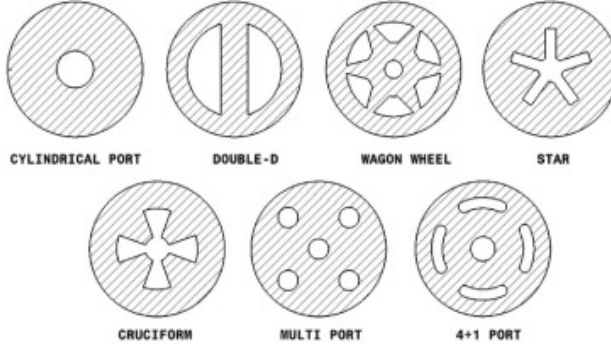


Figure 21: Sample Fuel Grain Configurations

4.8.4 Sizing Logic

4.8.5 Geometry Changes Summary

The Candlebark TOML input file for Pardalote MK2 is attached in [APPENDIX].

Component 1	Mk1 Design Point	Mk2 Design Point	% Increase
Tank Volume	7.5L	12.5L	66.6%
Injector	70mm ²	85mm ²	21.4%
Port Area	60mm	88mm	46.6%

Table 4: Sizing Changes Summary

4.8.6 Pardalote Mk2 Expected Performance Metrics

Table 5: Simulation Summary

Parameter	Value
Total Simulation Time	5.337 s
Thrust	
Peak	4480.526 N
Average	3152.122 N
Specific Impulse (Isp)	
Average	207.459 s
Total Impulse	16822.875 Ns
Average O/F Ratio	9.851
Chamber Conditions	
Average Temperature	3212.939 K
Average Pressure	1881456.14 Pa
Tank Conditions	
Average Temperature	277.469 K
Average Pressure	3347305.194 Pa
Average Regression Rate	0.000929 m/s
Average Mass Flux	22.564 kg/s.m ²
Mass Flow Rates	
Oxidizer	1.449 kg/s
Fuel	0.138 kg/s
Final Fuel Mass	0.188 kg
Final Port Diameter	0.098 m
Apogee	15803 ft
Max Velocity	359 m/s
Max acceleration	96.2 m/s ²

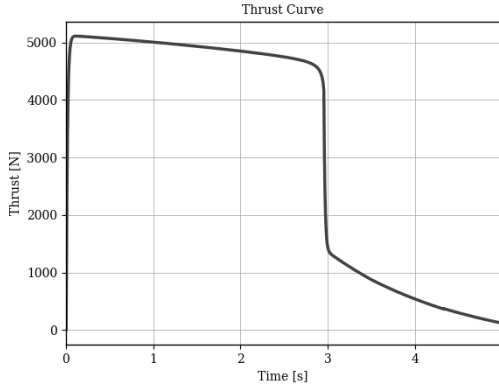


Figure 22: Expected Thrust Performance

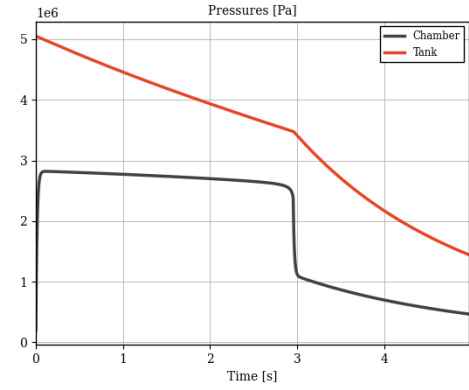


Figure 23: Expected System Pressures

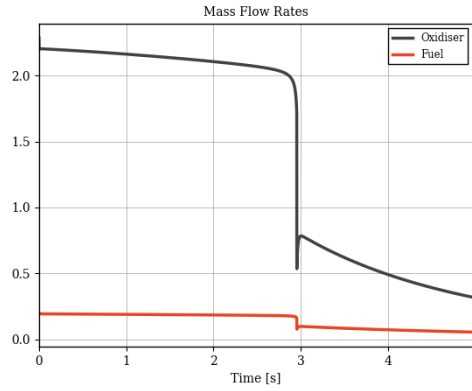


Figure 24: Expected Mass Flow Rates

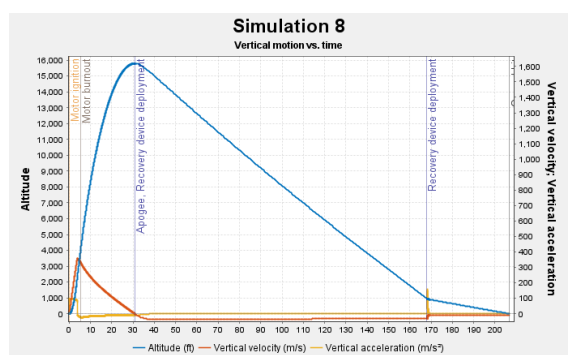


Figure 25: Pardalote Mk2 Flight Performance

Figure 26: Overview of Flight Simulation Data

5 Propulsion - Chamber Subsystem

5.1 Engine Architecture

The combustion chamber presented in this section ... [Include a short paragraph on why the chamber has been designed as it has been. What were your primary focuses in this design, what are the key features and things of note.]

The engine architecture of Pardalote is depicted in Figure 27. The Pardalote engine consists of:

- Al 6061-T6 casing, forward closure, and injector coin
- Three Paper Phenolic inserts
- ABS fuel grain
- Inconel Nozzle
- Graphite nozzle throat insert.

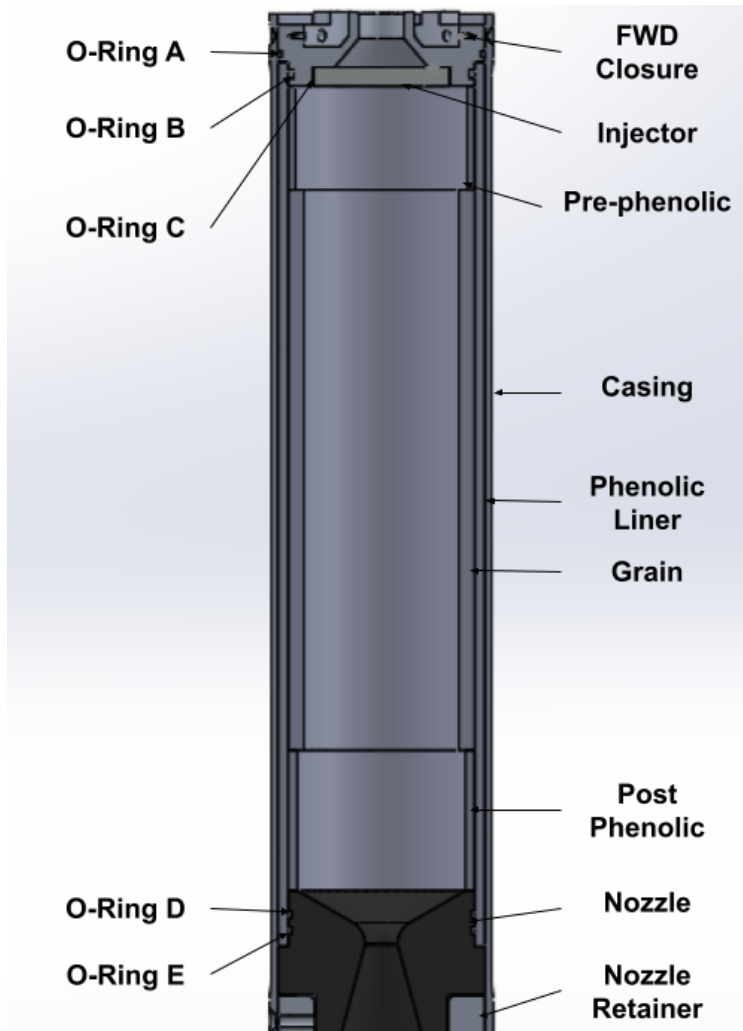


Figure 27: Pardalote Engine Architecture

5.2 Sizing

Sizing refers to the calculated dimensioning of elements utilised inside the Pardalote engine as well as the engines general g such as its' length and diameter.

The sizing for the combustion chamber has a direct correlation with the thrust potential of the engine as well as general combustion efficiency due to chamber sizing impacting the oxidiser to solid fuel ratio as well as, to an extent, the degree of atomisation of the oxidiser before combustion. Sizing also impacts the max pressures and temperatures experienced inside the chamber meaning it must be effectively designed to minimise potential part failures.

The dominant parameters that dictate the thrust curve are:

- Fuel grain port diameter
- Fuel grain length
- Nozzle throat diameter
- Total injector area
- Fuel grain outer diameter
- Mass of oxidiser and ullage

The first four parameters predominantly define the initial peak thrust. An initial sizing was undertaken using a method previously explored in xx paper [reference allens thesis] [6]. Due to the nature of the design process, the resulting design yielded a fuel grain length of over 0.6 m, which was undesirable from a rocket

stability perspective. To shorten the chamber, the 120 mm casing diameter was chosen as it was the largest diameter available from primary supplier which would fit within Pardadlo's airframe.

From this, the fuel grain outer diameter is known by estimating casing and phenolic thickness. To conserve the fuel grain mass flux during startup, the port surface area was conserved to that determined from the initial sizing in order to achieve the same peak thrust. This constrained set of equations resulted in a length of just under 250 mm and fuel grain port diameter of 83 mm . Simulating this geometry resulted in a lower than optimal oxidiser-to-fuel ratio (as per Wattle engine design analysis [reference?](#)), so to improve efficiency, a longer fuel grain of 300 mm was chosen. This added length also allows for a higher impulse, which allows for a safety margin in the event of engine underperformance. The subsequent engine parameters are outlined in Table 6, with the performance parameters with a [10-litre](#) oxidiser tank at 25 degrees ambient equilibrium shown in Table 7.

Table 6: Key Chamber Sizing Parameters

Parameter	Value	Unit
Fuel grain port diameter	83	mm
Fuel grain length	300	mm
Total injector area	60	mm^2
Fuel grain outer diameter	100	mm
Nozzle throat diameter	36	mm
Nozzle exit diameter	67.5	mm
Nozzle expansion ratio	3.5	-

Table 7: Caption

Parameter	Value	Unit
Peak Thrust	4150	N
Impulse	11,600	Ns
Liquid Burn Time	1.58	s
Total Burn Time	7.50	s
Specific Impulse	182	s
Injector Pressure Drop	41%	MPa

The simulated thrust curve and pressure are shown in Figure 28 and Figure 29 assuming an equalised tank pressure at 20 degrees. The nozzle expansion ratio is sized based of perfect expansion to atmospheric conditions with a chamber pressure of 2.65 MPa .

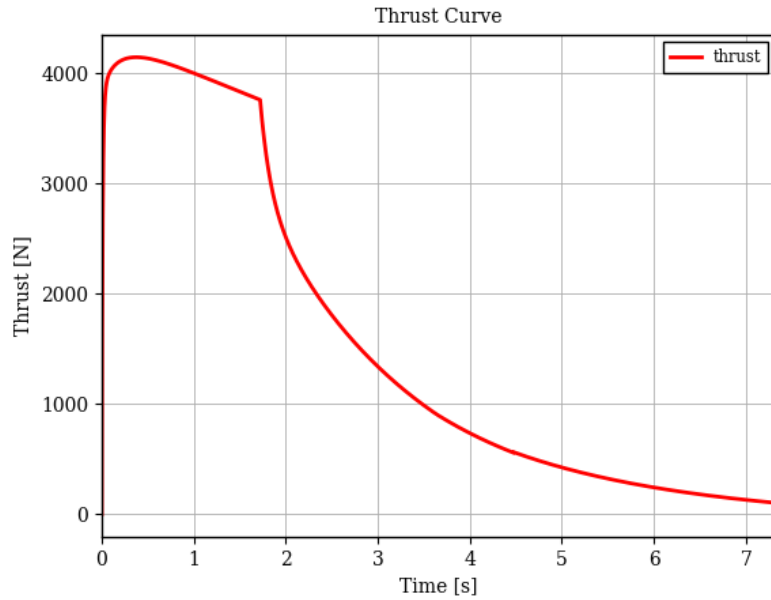


Figure 28: Simulated Engine Thrust Curve

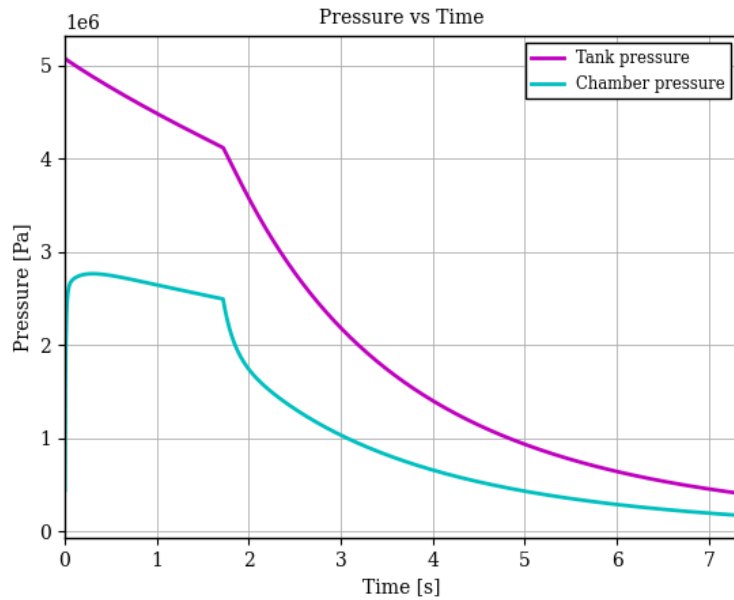


Figure 29: Simulated Tank and Chamber Pressures

5.3 Forward Closure

The Pardalote Forward Closure is responsible for holding the fore end of pressure in the chamber, as well as interfacing the engine with the Tank and Aerostructures subsystems. The Forward Closure is made of Al 6061-T651, and is depicted in Figure 30 and Figure 32.

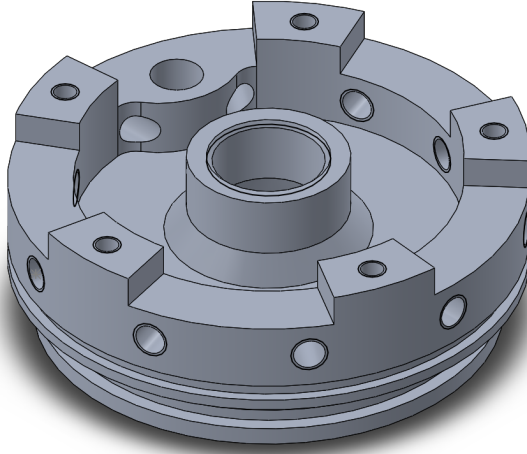


Figure 30: Pardalote Forward Closure

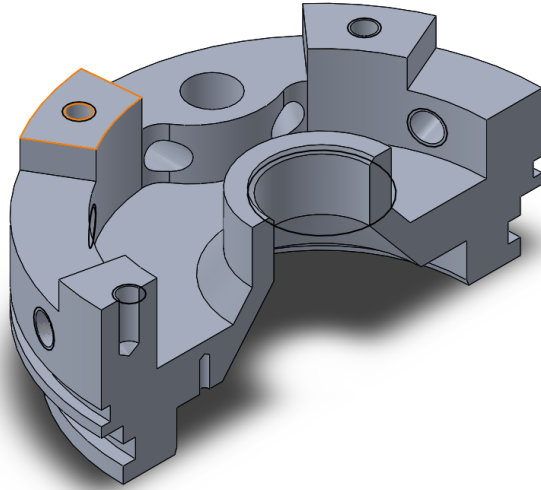


Figure 31: Pardalote Forward Closure Section View

The Forward Closure interfaces with the Oxidizer feedline via a G 3/4" BSPP port, the Chamber casing via 10 radial M6 screws, and the Aerostructures Truss-Chamber Adapter Plate via 5 axial M6 screws. The injector is retained in the forward closure with 5 axial M3 screws. The Forward Closure also houses the glands for O-rings A and C, discussed in subsection 5.8.

The upperbound diffuser angle to the injector was taken from the Waterloo 2023 hybrid rocket angle of 45 degrees [24], and the lowwerbound angle taken as 15 degrees from the Wattle hybrid rocket [29]. The diffuser angle, within these bounds, was selected as 40 degrees, based on the required space for injector integration, maximising available injector area, and minimising the forward closure height for weight reduction.

A G1/4" BSPP thread is included in the Forward Closure to interface the IFM PT5402 Pressure Transducer, such that pressure measurements in the pre-combustion chambe can be taken during operation.

FEA was performed on the Forward Closure using Ansys Mechanical to evaluate the Safety Factor of the part under the worst case load of 6 MPa during hydrostatic pressure testing. This was applied to the pressure loaded faces of the forward closure. The integration of the Forward Closure with the casing was modelled using Structural Steel pins with fixed boundary conditions on their external faces. The results of this analysis are depicted in

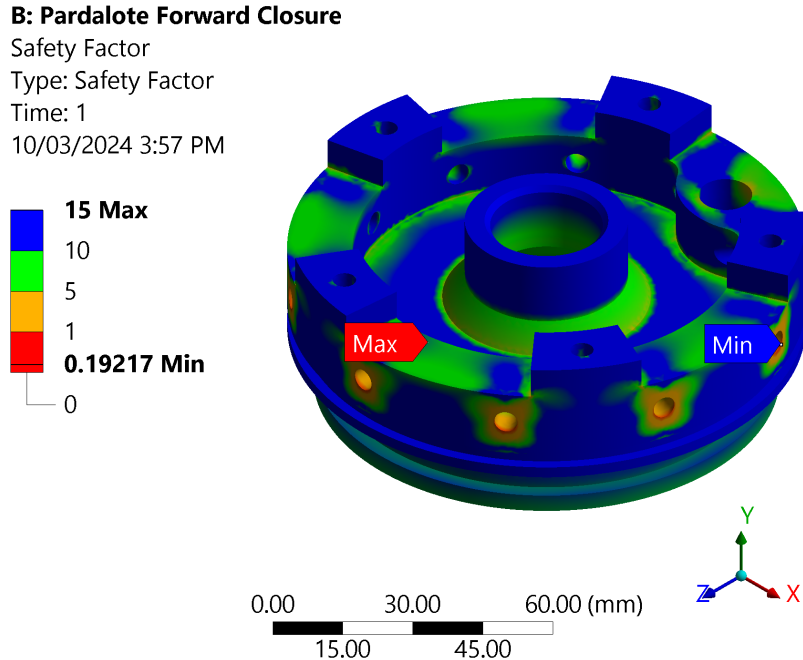


Figure 32: Pardalote Forward Closure FEA Safety Factor Results (Equivalent von-Mises Stress)

The minimum safety factor of 0.192 was neglected due to the stress concentrations of the bolt holes and boundary condition modelling. However, since all other locations in the Forward Closure satisfied a Safety Factor greater than 3, the part was considered safe for hydrostatic pressure testing.

5.4 Casing

The casing is made from aluminium 6061 tube that acts as the pressure vessel. The inner diameter is to be line-bored to achieve the required tolerancing for internal components. The forward and aft ends have radial, close-fitted countersunk holes for the forward closure and nozzle retainment. The key difference from Wattle is the reduction of wall thickness of the casing, whilst keeping thicker forward and aft ends. This allows significant weight reduction to be made, whilst bringing the hoop and longitudinal stress factors of safety more in line with the retainment failure modes. The inner diameter of the casing will be constant to allow two-way assembly and disassembly. This is a significant improvement on the Wattle design as it allows for a much easier assembly/disassembly process. The pre-combustion chamber and post-combustion chamber lengths have not been changed from the Wattle engine.

5.5 Injector

The injector design for Pardalote will directly follow from the Wattle engine injector. The same orifice length will be kept to allow for the injector to be flush with the bottom face of the forward closure. The Pardalote engine size is similar to that of the Wattle engine, therefore it is expected to see similar results in terms of the effect of engine stability as those obtained from Wattle engine testing.

5.6 Thermal Protection System

The Thermal Protection System (TPS) of Pardalote shall be responsible for keeping the temperature of the combustion chamber casing below the annealing temperature of Al 6061-T651 to fulfill **PL-R-CHA-3**.

The TPS will be three independent inserts of Paper Phenolic Tube, shown in Figure 27, sourced from AE Components [7]:

1. Pre-Combustion Chamber Insert
2. Combustion Chamber Liner
3. Post-Combustion Chamber Insert

The combustion chamber liner is sized based off dimensions from the Wattle engine [29] and the Technical University of Braunschweig's HYDRA4x engine [13], an SRAD engine with similar operating parameters to Wattle and Pardalote. From a given engine outer diameter of 140 mm and fuel grain outer diameter of 130 mm , the HYDRA4x paper phenolic liner therefore has a maximum thickness of 5 mm including the casing wall thickness. Given success of Wattle's liner thickness of 6 mm and evidence of successful engine operation with a liner thickness less than 5 mm , the liner thickness of Pardalote is selected as 5 mm .

To protect the casing from the high temperatures of the post-combustion chamber, the Pardalote Post-Combustion Chamber Insert shall be 5 mm to produce the same equivalent TPS thickness as Wattle [29] of 10 mm . Likewise, the Pardalote Pre-Combustion Chamber Insert shall be 3 mm to produce the same equivalent TPS thickness as Wattle [29] of 8 mm at the pre-combustion chamber.

5.7 Nozzle and Aft Retainment

The design for the nozzle and its retainment presented in this report is identical to that of the Wattle engine and the graphite nozzle will be lathed from a graphite round. The thickness and height of the nozzle flange will be identical to the Wattle engine. Consequently, with the same worst-case chamber pressure force, the failure modes of bearing and shear of the nozzle flange will be more conservative than Wattle, given the larger diameter. Similarly, the nozzle retainer height and thickness allow for the same bolt-to-edge distance and thread engagement as the forward closure, meaning the failure modes of bearing, shear, tension, and bolt shear will be the same as that of the forward closure.

Although this architecture has been proven to work, the solid graphite is excessively heavy. Therefore efforts will be made to complete the analysis of a design printable Inconel nozzle that houses a graphite throat. Additive manufacturing techniques will enable a relatively thinner-walled bell nozzle. Furthermore, the retainment will be able to be embedded into the Inconel as it allows for tapping, eliminating the need for a nozzle retainer. This is an area for future development.

5.8 Sealing System

The sealing system of Pardalote shall be responsible for ensuring that the injector orifices and nozzle exhaust are the only pathways for fluid flow in and out of the engine during operation to fulfil **PL-R-CHA-4**. The Sealing System consists of 5 Silicone 70 Durometer O-Rings located in Figure 27. All O-Rings are AS568 standard size male piston seals with dynamic gland dimensions. All O-rings will be sourced from Applied Industrial Technologies Australia [28]. The purpose of each O-ring is summarised in Table 8.

Table 8: Sealing System Interfaces and Responsibilities

O-Ring	Interface	Purpose
A	Casing and forward closure	Prevent top engine leakage
B	Combustion Chamber Liner and Forward Closure	Prevent fluid pathway along casing
C	Injector and Forward Closure	Prevent fluid bypass of injector orifices
D	Nozzle and Casing	Prevent fluid bypass of the nozzle
E	Nozzle and Casing	Redundant O-Ring D

The relevant dimensions of these O-Rings, their stretch and squeeze ranges, and their gland dimensions are summarised in Table 9, Table 10, and Table 11 respectively.

Table 9: Chamber Sealing System Key Parameters

O-Ring	Piston OD [mm]	Ref.	Cross Section [mm]	ID [mm]	OD [mm]
A	110	155		2.62	101.27
B	100	239		3.53	91.67
C	73	146		2.62	66.34
D	110	155		2.62	101.27
E	110	155		2.62	101.27

Table 10: Range of Stretch and Squeeze Parameters for Chamber Sealing System

O-Ring	Min. Str. %	Design Str. %	Max. Str. %	Min. Squ. %	Design Squ. %	Max. Squ. %
A	3.38	4.16	4.94	9.87	13.59	17.1
B	1.48	2.33	3.18	8.25	11.59	14.75
C	2.36	3.22	4.10	9.87	13.59	17.1
D	3.38	4.16	4.94	9.87	13.59	17.1
E	3.38	4.16	4.94	9.87	13.59	17.1

Table 11: Chamber O-Ring Gland Dimensions (All dimensions in mm)

O-Ring	C.S.	Min Gland Depth	Max Gland Depth	Min Groove Width	Max Groove Width
A	2.62	2.235	2.286	3.556	3.683
B	3.53	3.073	3.124	4.750	4.877
C	2.62	2.235	2.286	3.556	3.683
D	2.62	2.235	2.286	3.556	3.683
E	2.62	2.235	2.286	3.556	3.683

5.9 Failure Mode Analysis

The following section identifies the key failure modes of the combustion chamber and defines the parameters and calculations used to produce their associated Factor of Safety (FS). The failure modes of the combustion chamber are primarily determined by the conditions within the chamber, particularly the chamber pressure and temperature. These conditions influence the loading of the components and subsequently their factors of safety.

The operating conditions are defined in Table 12, where both the expected (E) and worst case (WC) conditions are considered. The worst case chamber pressure condition was defined as 1.5 times the expected operating condition. Whilst not possible under normal conditions this upper value was chosen as a conservative estimate. This is repeated in Table 12, where the expected upstream condition is 4 MPa and therefore the worst case upstream condition is 10 MPa , which were chosen as conservative values, although they are both not practically likely or possible.

Table 12: Expected and worst case operating conditions used for analysis.

Condition	Expected (E)	Worst Case (WC)
Upstream Pressure (MPa)	4	10
Chamber Pressure (MPa)	3.0	4.5

The associated factors of safety are calculated for each component according to their specific loading condition. The design decisions such as fastener type and placement were then sized such that the critical factor of safety was bearing failure of the casing at the nozzle retainer bolts - which is the safest mode of failure, as nozzle retainer failure minimises the potential safety concerns to the remainder of the propulsion system and launch vehicle (nozzle failure occurs at the most aft section of the rocket). The key design parameters used in the failure modes analysis are outlined in Table (13).

Table 13: Summary of the key parameters used in the FMA calculations.

Parameter	Value	Unit
FWD closure bolt depth	12	mm
Number of FWD closure bolts	10	-
FWD Closure Bolt Diameter	6	mm
Bolt to edge distance ($e/D = 1.5$)	9	mm
Injector face diameter	48	mm
Number of injector bolts	10	-
Injector Bolt Diameter	3	mm
Injector Bolt Engagement Length	6	mm
Phenolic Liner Thickness	5.5	mm
Pre-phenolic Thickness	4	mm
Post-phenolic Thickness	5	mm
Casing Thickness	4.45	mm
Casing Reduced Thickness	3.45	mm
Casing OD	120	mm
Casing Cross-Sectional Area	1615.4	mm ²
Number of Nozzle Bolts	9	-
Nozzle Bolt Hole Diameter	6	mm
Nozzle Bolt Hole Depth	12	mm

A number of materials and material properties are used in the failure modes analysis, the casing, forward closer and injector are manufactured from Aluminium 6061-T6511 while the nozzle is manufactured from PCCX3 Graphite. Finally fuel grain is manufactured from ABS and the thermal protection system is manufactured from a paper phenolic resin tubing. The specific data for materials and fasteners is summarized in Section (5.9.6)

The following subsections outline the analyses conducted for each combustion chamber component, the summary of which is presented in Table 14.

Table 14: Factor of Safety (FS) Table for the Combustion Chamber Components.

Failure Mode	Factor of Safety	
Forward Closure	E	WC
Bolt Shear Failure	5.560	3.707
Injector Thread Shear Out	6.484	2.594
Bolt Tear Out	14.327	9.552
Bolt Bearing	10.324	6.883
Injector		
Bolt Thread Shear Out	8.359	3.344
Bolt Tensile Failure	5.561	2.260
Chamber Casing		
Hoop Stress (Yield)	6.444	4.296
Hoop Stress (Ultimate)	7.733	5.155
Longitudinal Stress (Yield)	9.992	6.661
Longitudinal Stress (Ultimate)	11.990	7.993
Casing Shear Out	4.486	2.991
Casing Net Tension (Yield)	16.640	11.093
Casing Net Tension (Ultimate)	19.968	13.312
Casing Bearing	4.071	2.7
Nozzle Insert		
Thermal compression Failure	11.214	7.476
Nozzle		
Bolt Shear Failure	5.212	3.475
Nozzle Bolt Tear Out	28.025	18.683
Graphite Nozzle Tear Out	7.933	7.933
Nozzle Bearing Failure	14.013	9.342

5.9.1 Forward Closure

The forward closure interfaces with the chamber, TPS liner and injector. It has 10 radial tapped holes and 10 axial tapped holes for securing the injector. The forward closure also acts as the primary interface between the combustion chamber and the fluids truss structure (Main Flight Valve), transferring the nitrous oxide from the tank to the chamber, resulting in the following failure modes:

- Bolt Shear Failure
- Bolt Tear-Out Failure
- Bolt Bearing Failure
- Injector Thread Shear Out

Bolt Shear Failure

The bolt shear failure is calculated as a function of the internal chamber pressure, pressure area, and the subsequent loading per bolt. The pressure area can be expressed as the area exposed by the bottom face of the closure minus the ID of the pre-combustion chamber lining.

$$A_{FWD} = \frac{\pi}{4} D_{pre}^2$$

The force per bolt is then calculated from the pressure area, chamber pressure, and the number of bolts, which evaluates to $2356.2N$ and $3534.3N$ for the expected and worst-case conditions respectively. The factor of safety is obtained from the shear loading capacity of the M6 bolts used (specifications outlined in table (??)), where the factor of safety in this case is defined as $FS = F_{max}/F_{load}$. This results in a factor of safety of 5.560 and 3.707 for the expected and worst case conditions respectively.

Bolt Tear Out Failure

The tear-out failure mode is defined as the tear-out of the material supporting the bolt, which in this case acts along the depth of the bolt holes. The shear area is defined as the plane parallel to the axis of the bolt

holes and parallel to the axis of the chamber (on both sides of the bolt hole). This results in the following equation:

$$A_{shear} = 2D_{bolt}(b_{depth} - \frac{D_{bolt}}{2})$$

Then the stress σ_{tear} is defined as $\sigma_{tear} = F_{bolt}/A_{shear}$, the factor of safety can then be calculated using the yield strength of the material (see Table 20 for material specifications):

$$FS = \frac{\sigma_{yield}}{\sigma_{tear}}$$

This function evaluates to a factor of safety of 14.327 and 9.552 for the expected and worst-case conditions respectively.

Bolt Bearing Failure

The next failure mode considered is a bearing failure, which is the result of the deformation of the material supporting the bolt. This failure mode is governed by the area of the rectangular cross-section of the bolt hole and the loading of each bolt. The area considered is defined by the relation:

$$A_{bear} = td_{bolt}$$

Where t is the bolt hole depth and d_{bolt} is the bolt hole diameter. The shear stress is then calculated by the loading per unit area, $\sigma_{bear} = F/A_{bear}$, which resulted in a factor of safety of 10.324 and 6.993 for both expected and worst case conditions.

Injector Thread Shear Out

The final failure mode considered for the forward closure was the thread shear out of the injector bolts, where the external threads are stripped or damaged during operation. The stress area considered for this failure mode is outlined by ISO 898, which defines the stress area as the cylinder formed by the thread engagement length (L_e) and the pitch diameter of the external thread.

$$A_{th} = \frac{1}{2}\pi d_p L_e$$

In this case, the pitch diameter of the external threads is 2.675 mm, assuming a normal fit tolerance (6g). From this value and an engagement length of 6 mm, the shear area was calculated as 25.211 mm^2 . Then the shear stress is taken as the loading per unit area for each bolt. It should be noted that the conditions used in this calculation assume an expected upstream pressure of 4 MPa and a worst-case pressure of 10 MPa. During operation the net pressure is a product of the pressure difference across the injector, or the difference in pressure between the tank and the chamber, however in this case only the upstream pressure was used to obtain a conservative estimate. Following the shear stress calculation, the factor of safety can be determined using the shear stress of the material, which for aluminum T6061 is 186.165 MPa [15]. Using this value the respective factors of safety for both conditions are 6.484 and 2.594.

5.9.2 Injector

The failure modes of the injector consist of:

- Bolt Tensile Failure
- Bolt Thread Shear Failure

These failure modes are primarily caused by the upstream pressure, chamber pressure and sizing of the specific components. The calculations for each of these failure modes will be outlined in this section, including relevant parameters and assumptions.

Bolt Tensile Failure

The bolt tensile failure mode is a failure of any of the 10x M3 bolts retaining the injector puck into the forward closure. These bolts are loaded in tension due to the pressure difference across the injector, in this analysis the upstream pressure was taken as the net pressure acting on the component. The stress area

(A_s) for the tensile loading is taken as the minor diameter, also known as the area of the shank subtracting the threaded area. This value is less than the shank area for a typical bolt and as a result will always have a lower strength, for this reason, the factor of safety for the shank area will not be considered.

For a standard metric M3 bolt, the minor diameter is 2.459 mm, resulting in a stress area of 5.1030 mm^2 . From this, the tensile stress is taken as the loading per bolt divided by the stress area. The factor of safety is then a product of the tensile strength of the material and the tensile stress. These calculations resulted in a factor of safety (for the yield strength) of 5.651 and 2.260 for the expected and worst-case upstream conditions, which are 4 MPa and 10 MPa .

Bolt Thread Shear Failure

The bolt thread shear failure was calculated using the same equations as the forward closure external thread failure, where the shear area is defined as:

$$A_{th} = \frac{1}{2}\pi d_p L_e$$

The engagement length (L_e) is 6 mm and the pitch diameter (d_p) is 2.675 mm, the shear stress is then calculated as $\sigma_{th} = F_{bolt}/A_{th}$. From this the factor of safety was obtained as 8.359 and 3.344 for the expected and worst-case conditions respectively.

5.9.3 Casing

The failure modes of the combustion chamber casing consist of:

- Hoop Stress Failure
- Longitudinal Stress Failure
- Shear Out Failure
- Net Tension Failure
- Bearing Failure
- Plastic Deformation from High Temperatures

These failure modes come as a result of the chamber acting as a thin-walled pressure vessel possessing a cylindrical geometry. The steps used to calculate the associated factor of safety for each of these failure modes are outlined in this section.

Hoop and Longitudinal Stress Failure

Pressure within the chamber results in a loading of the thin walls of the casing and this stress has two components; hoop stress and longitudinal stress. The hoop stress is the component of loading around the circumference and longitudinal stress is the axial component. Each of these component stresses can be defined as:

$$\sigma_h = \frac{Pd}{2t}$$

$$\sigma_l = \frac{Pd}{4t}$$

Where σ_h and σ_l are the hoop and longitudinal stresses respectively and t is the wall thickness. From these equations, the factors of safety for both the yield and ultimate strength were calculated whereby the FS is defined:

$$FS = \frac{\sigma_{tension}}{\sigma_{load}}$$

Where σ_{load} is the hoop or longitudinal stress. From this, the hoop failure mode yield factor of safety was 7.733 and 5.155 for the expected and worst-case conditions respectively. Similarly, the Longitudinal failure mode yield factor of safety was calculated as 9.992 and 6.661.

Casing Shear Out

The casing shear-out failure mode considers the failure of the material supporting the forward closure or nozzle bolts. This failure mode considers the stress area as the shear plane defined by the bolt depth, diameter, and distance to-edge on both sides of the bolt. Mathematically this shear area is defined as:

$$A_{tear} = 2t(L_{te} - 0.5d_{bolt})$$

This area is defined from the edge of the bolt hole, rather than the full area; this provides a conservative estimate that simplifies the effect of the curved surface of the bolt's circumference. From this equation, the shear stress was calculated as $\sigma_{tear} = F_{bolt}/A_{tear}$, which results in a factor of safety of 4.486 and 2.991 for the expected and worst case conditions.

Net Tension Failure

A net tension failure is the failure of the material between bolt holes, specifically due to the tension applied by the bolts to the chamber. The addition of a radial bolt pattern in the combustion chambers' design results in a reduction in the cross-sectional area of the casing, this results in a concentration of the load that can fail if not accounted for. This new area is defined as:

$$A_{net} = A_{cross} - A_{bolts} = \frac{\pi}{4}(OD^2 - ID^2) - ntd_{bolt}$$

Where n is the number of bolts, t is the wall thickness and d_{bolt} is the bolt diameter. The loading in this instance is the pressure force applied to the ID of the forward closure, which was taken as the ID of the phenolic liner. Then the stress is defined as:

$$\sigma_{net} = \frac{F}{A_{net}} = \frac{P\pi ID_{liner}^2}{4A_{net}}$$

This results in a factor of safety of 16.640 for the expected conditions and 11.093 for the worst case.

Bearing Failure

The next failure mode considered was the bearing failure, which was calculated using the same method as the FWD Closure, where the bearing area is: $A_{bear} = d_{bolt}t$. This is then combined with the loading per bolt to obtain a bearing stress for the casing, which resulted in a factor of safety 4.071 and 2.7 for the expected and worst-case conditions respectively.

It should be noted that a buckling failure mode was not considered for the casing, or any component, as it is most relevant to a thin structural member under compression.

High Temperatures: From the first hot fire of the Pardalote engine, it was noted by the Pirtek thermal indicator stickers that the casing reached a temperature of approximately 177C at the nozzle end.

From the hot-fire, the outer casing at the post-combustion end experienced temperatures between 100 and 180C for ≈ 1000 s or 17 minutes, as shown in 33 - indicating that post-hotfire, the graphite nozzle continued to conduct heat to the chamber casing. As the casing material, Al 6061-T6 will experience plastic deformation at 200C, this presents major concerns in regards to further engine tests with the following configurations:

- Higher Tank Pressure
- Nozzle with Reduced Throat Diameter

Both configurations result in increased chamber pressure and hence higher temperature of combustion in the chamber. This presents an issue with preserving the integrity of the Al 6061-T6 casing and ensuring failure modes are still accounted for. As indicated from graphs from [MIL-HANDBOOK], following 30 minutes of exposure to a temperature of 200C, the material properties of Al 6061-T6 change as follows:

For the configurations to result in a higher chamber temperature mentioned above, only a minimal increase to the aft casing temperature is expected. Thus, calculations are re-performed for an aft casing temperature of 200C to re-assess the factor of safety for the outlined failure modes.

The factor of safety calculated with the new material properties following exposure to 200C temperature for 30 mins is displayed in the table below:

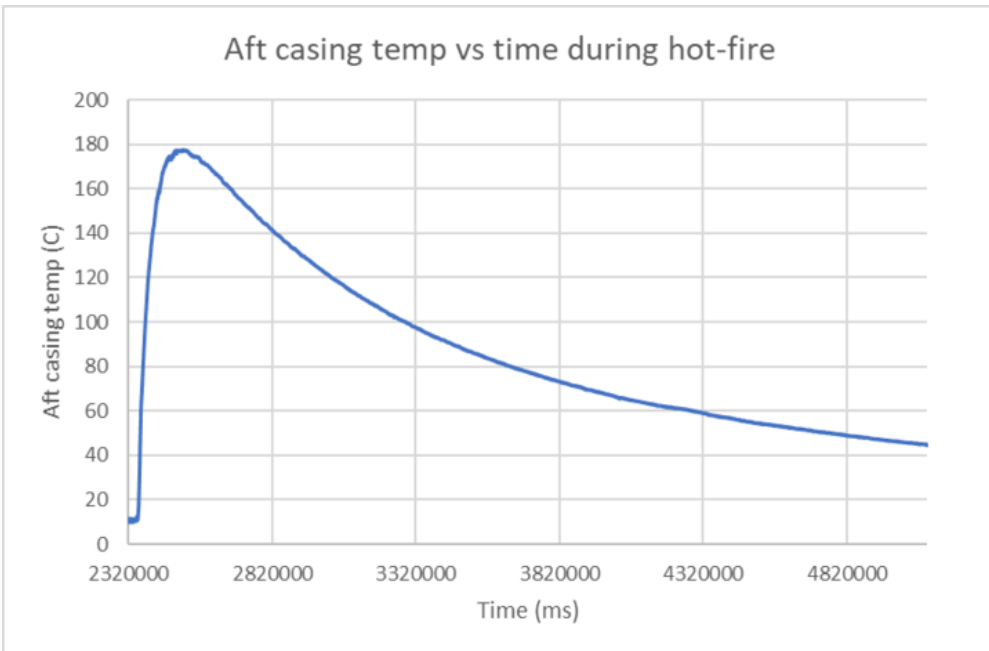


Figure 33: Outer Casing Temperature - Hotfire 1

Temperature (°C)	Fraction F_{tu}	F_{tu} (MPa)	Fraction F_{ty}	F_{ty}
25	1.00	310	1.00	276
100	0.90	279	0.91	251.2
200	0.66	204.6	0.71	195.96
250	0.46	142.6	0.5	138
300	0.26	80.6	0.24	66.24

Table 15: Temperature vs F_{ty} and F_{tu} of Al 6061-T6

Failure Mode	Yield Expected FOS	Ult Expected FOS
Chamber Hoop Stress	5.233	5.463
Chamber Longitudinal Stress	8.114	8.471
Body Tube Shear Out	8.142	NA
Body Tube Net Tension	13.51	14.10
Body Tube Bearing	4.071	NA
Body Tube Buckling	7.39×10^7	
Chamber Hoop Stress (Reduced OD)	4.057	4.236
Chamber Longitudinal Stress (Reduced OD)	8.114	8.471
Nozzle Retainer Thread Shear (Tear Out)		

Table 16: Failure modes with Expected Pressure Factors of Safety (FOS).

Thus, as seen from tables 16 and 17, the factor of safety for all casing failure modes remains to be over 2 - meeting the system requirements. As a result it can be concluded that improving system performance and hence a predicted chamber temperature increase from simulations will not catastrophically impact the casing.

Failure Mode	Yield Worst Case FOS	Ult Worst Case FOS
Chamber Hoop Stress	3.488	3.642
Chamber Longitudinal Stress	5.409	5.648
Body Tube Shear Out	5.428	NA
Body Tube Net Tension	9.008	9.405
Body Tube Bearing	2.7	NA
Body Tube Buckling	NA	NA
Chamber Hoop Stress (Reduced OD)	2.705	2.824
Chamber Longitudinal Stress (Reduced OD)	5.409	5.648
Nozzle Retainer Thread Shear (Tear Out)		

Table 17: Failure modes with Worst Case Factors of Safety (45 bar Chamber Pressure)

5.9.4 Nozzle Insert

The nozzle insert consists of a single graphite component that creates the throat of the nozzle. The purpose of this component is to withstand the majority of the thermal stresses induced by the combustion chamber exiting the nozzle. This results in its key failure mode ultimately being determined by the stresses due to thermal expansion, this can be estimated as the sum of the thermal expansion stress generated by the two different materials. The thermal stress of a member can be estimated by considering its change in length due to a temperature difference, mathematically this can be defined as:

$$dl = \alpha l_0 dT$$

Where α is the thermal expansion coefficient, l_0 is the initial length and dT is the change in temperature. Simplifying the inconel and graphite as two linear beams along their radius, the stress can be related using the materials Young's modulus, where:

$$E = \frac{\sigma}{\epsilon} = \frac{F/A}{dl/l_0}$$

Rearranging for the stress and substituting the above results in the relation:

$$\sigma_{dT} = E \alpha dT$$

This relation can then be used to sum to associated stress from each material, where $\sigma_{net} = \sigma_{dT,1} + \sigma_{dT,2}$. Expanding this relation produces an equation that represents the total thermal stress, in terms of the material properties and change in temperature.

$$\sigma_{net} = E_{in} \alpha_{in} dT + E_G \alpha_G dT = dT(E_{in} \alpha_{in} + E_G \alpha_G)$$

Then a factor of safety can be determined through comparing the net thermal stress to the max compressive stress of the weakest material, which in this case is graphite. This results in a factor of safety of 11.21 and 7.48 for the expected and worst case conditions respectively, where the compressive strength of graphite was taken as 345 MPa [19].

5.9.5 Nozzle

The nozzle is the final component considered in the combustion chambers failure mode analysis. The nozzle is manufactured via PCCX3 graphite. The failure modes of the nozzle consist of:

- Bolt Shear Failure
- Bolt Tear Out
- Bearing Failure

Bolt Shear Failure

The bolt shear failure mode is determined through considering the average loading of each bolt and the bolts properties (outlined in section 5.9.6). The pressure area was taken as the nozzle inner diameter minus the throat, this results in an area of 7539.82 mm^2 , Then the pressure force is taken as $F = PA$. Then the factor of safety can be calculated from the force per bolt, as each M6 screw has a shear capacity of 13.10% kN, this results in a factor of safety of 5.212 and 3.475 for the expected and worst-case conditions. This results in the bolt shear failure acting as the critical failure mode whilst also maintaining the design requirement by remaining above a minimum FS of 2.

Bolt Tear-Out Failure

The bolt tear-out is taken as a function of the bolt depth and distance to-edge, this can be expressed in the same way as the forward closure:

more relevant to the updated nozzle design

$$A_{tear} = 2t(L_{te} - 0.5d_{bolt})$$

In this case, the edge distance is the distance from the centre of the bolt to the top surface of the nozzle. From this equation, using M6 screws and a depth of 15mm the yield factor of safety was calculated as 28.025 for the expected conditions and 18.693 for the worst case.

Bolt Bearing Failure

The final failure mode for the nozzle is the bolt bearing, which is calculated with the same method outlined for the forward closure and casing, where $A_{bear} = d_{bolt}t$. From this, the bearing area was calculated and then the stress was taken as $\sigma_{bear} = F/A_{bear}$. Then the factor of safety was calculated using the yield strength of the material, which resulted in a FS of 14.013 and 9.342 for the expected and worst-case conditions respectively.

5.9.6 Material and Fastener Specifications

This section outlines the specifications obtained for the fasteners and materials used, it also specifically references fasteners from Hobson Engineering. The materials used in the combustion chamber consist of Aluminium T6061, Inconel 718, Graphite and Paper Phenolic. The properties of which, are listed in the tables below.

Table 18: Summary of Carbon Graphites mechanical properties [19].

Property	Value	SI unit
Density	1830	kg/m^3
Compressive strength	345	MPa
Shear Modulus	11.5	GPa
Tensile Strength	76	MPa
Thermal Expansion Coefficient	0.6	$10^{-6}/K$

Table 19: Summary of the mechanical properties of Inconel Alloy 718 [21],[22].

Property	Value	SI unit
Density	8190	kg/m^3
Ultimate Tensile Strength	1375	MPa
Yield Tensile Strength	1100	MPa
Coefficient of Thermal Expansion	13	$10^{-6}/K$
Young's Modulus	211	MPa

Table 20: Summary of Aluminium Alloy T6061 mechanical properties (MIL-HDBK-5H, pg 3-257).

Property	Value	SI unit
F _{tu}	289.58	MPa
F _{ty}	241.317	MPa
F _{cy}	234.422	MPa
F _{su}	186.158	MPa
Poisson's Ratio	0.33	
Elasticity (E)	6.83E+04	MPa
Compressive strength	250	MPa

The fasteners were sized and obtained from Hobsons engineering and the technical data they provide. There are two fasteners used in the combustion chamber, for the forward and aft closure and for the injector respectively:

- M6 socket screw csk (Class 12.9)
- M3 socket screw csk (316 stainless A/4)

Both of these fasteners are countersunk socket screws manufactured to a class 12.9 strength standard. The M6 socket screws tensile strength was approximated from data available from Hobsons outlining the strength of a class 12.9 bolt [12]. The shear strength was also given from Hobsons, It was taken from the socket head cap screw data sheet [11], These assumptions result in the screw properties:

Table 21: Summary of the key M6 Socket screw data.

Property	Value	SI Unit
Screw Type	Socket screw	-
Drive Type	Hex	-
Hobson Stock Code	SCSOFCM060016	-
Size	M6	-
Finish	ZINC FLAKE SILVER	-
Length	12 / 16	mm
Specification	DIN 7991 / CLASS 012.9	-
Thread	M6-1.00 x Fully Threaded	-
Shear Strength	13.10	kN
Tensile Strength	44.65	kN

The length of these screws are sized such that they have a 11.5mm depth and pass through 4.5mm of the casing. The M3 screws mechanical properties were determined from estimations of Hobson breaking strength data for different materials [10] The M3 tensile strength was approximated from the strength of head cap screws provided by Hobsons [11]. The shear capacity of these bolts were obtained from the breaking strengths document, assuming a 50% reduction from tensile to shear [17] and taking the yield strength as 60% of the breaking strength. This provided a shear capacity that could be used along with the engagement length and depth to provide a factor of safety.

Table 22: Summary of the key M3 Socket screw data.

Property	Value	SI Unit
Screw Type	Socket screw	-
Drive Type	Hex	-
Hobson Stock Code	SC16PCM030016	-
Size	M3	-
Finish	316 Stainless Steel	-
Length	16	mm
Specification	ISO 10642 / A4	-
Thread	M3-0.50 x Fully Threaded	-
Tensile Strength	4.09	kN
Yield Shear Stress	240	MPa

5.10 Ignition System

The ignition system is responsible for initiating combustion. The ignition system is split into two different elements, an initiation device and a heating element. The initiation device consists of dual E-matches provided by FOTI International and is responsible for starting the heating element, once commanded by the control system. The heating element, hereinafter referred to as the igniter, produces the high-temperature flame to begin combustion.

There are two different configurations, a pre-installed and a post-installed igniter. This refers to when the igniter is placed during assembly, with a post-installed igniter placed in the chamber once the rocket is vertical on the rail. Special care must be taken when a pre-installed igniter is used, limiting the personnel around the chamber and ensuring PPE is worn. Another limitation of a pre-installed igniter is the inability to swap out igniters without partially disassembling the airframe and chamber. An igniter disk may also prevent nitrous from flowing out of the chamber in the event of an abort. A post-installed igniter requires a support rod to hold the igniter or E-match in place when vertical. This can be overcome using a thin cardboard tube.

The chosen igniter ... [details]). The igniter is aimed to still be burning as the main valve opens, as to aid combustion and reduce the risk of a flameout.

A series of igniter tests are to be conducted on ABS grain samples to ensure the reliability of the igniter, regardless of configuration. **Further information can be found in Section X (testing section).**

6 Propulsion - Tank Subsystem

6.1 Subsystem Overview

The Propulsion - Tank Subsystem is responsible for the safe storage and movement of oxidiser with the rocket during all stages of operation. **Nitrous Oxide (N_2O) has been selected as the oxidiser used ... [because...]** within the Rocket. The subsystem is designed in consideration for a Maximum Expected Operating Pressure (MEOP) of 6 MPa and a Lowest Expected Operating Temperature (LEOT) of -30 C.

The Piping and Instrumentation Diagram seen below in Figure 34 outlines the layout and components required for oxidiser control and supply to the engine.

Pardalote Tank CDR P&ID

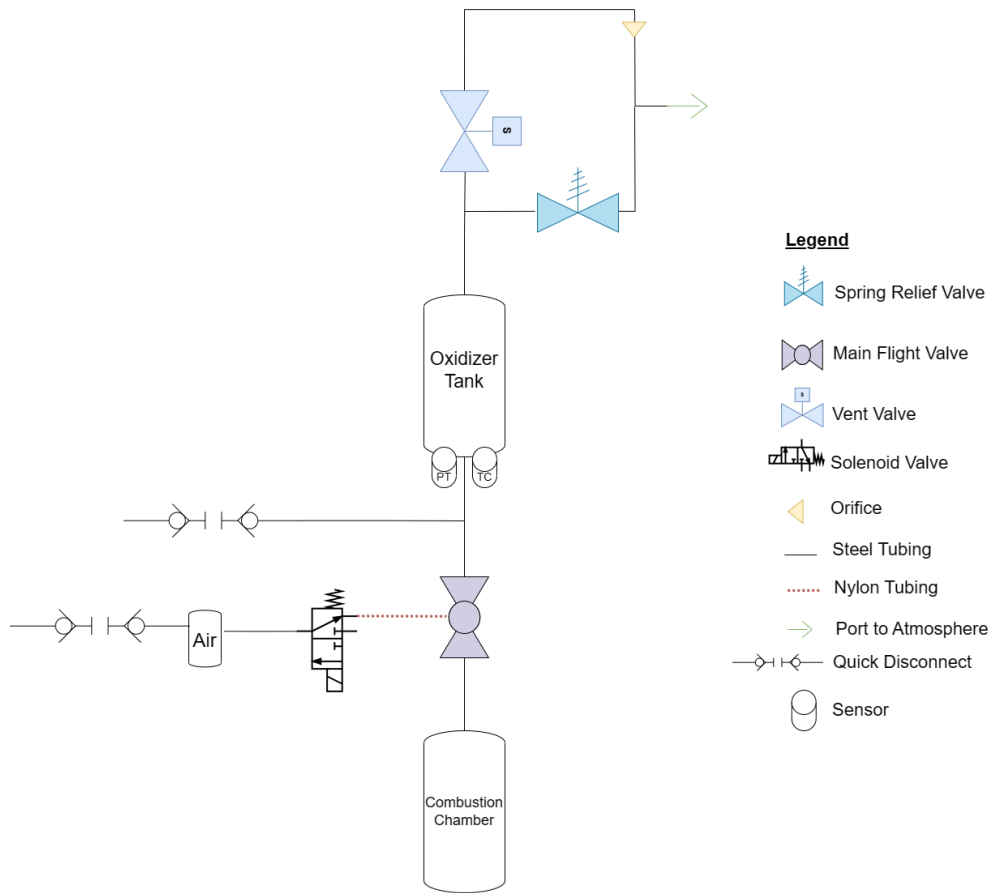


Figure 34: Piping and Instrumentation Diagram

The subsystem has three states:

1. Fill
2. Hold
3. Fire/Dump

Fill In Fill, the Main Flight Valve is closed and the Vent Valve is opened. The Main Flight Valve is controlled by the on-board pneumatic system consisting of an air-supply and solenoid valve. Liquid N₂O flows from the fill quick disconnect and into the oxidiser tank. The filling mechanism is the balance between the mass flow of gaseous N₂O boiling off and escaping through the vent valve, and the liquid N₂O entering. The Orifice diameter may be changed to increase or decrease the fill rate.

Fill-Testing will be conducted to experimentally fine tune the filling process and form an expected fill time at nominal conditions. The Fill state ends once desired Oxidiser mass is achieved and the Fill Valve in Ground Support Equipment is closed 7.

Hold In Hold, the Vent Valve is closed and the Fill Quick Disconnect is disconnected. N₂O is now safely stored on-board the rocket. Pressure

To prevent over-pressurization a Spring Relief Valve is included on the vent line above the Oxidizer Tank.

Fire/Dump In Fire/Dump, the Main Flight Valve is actuated open by the pneumatic system. Oxidizer flows from the Oxidizer Tank, through the valve to the Combustion Chamber. The Vent Valve remains closed.

6.2 Oxidizer Tank

The oxidizer tank is responsible for the storage of oxidizer in the rocket. It is a tube and radial closure design. The tube is turned from an aluminium 6061-T6511 extruded tube. The ends of the tube will remain the full wall-thickness for increased resistance against bearing and tear out failure with the closures. Each end has 14 radial M6 countersunk holes.



Figure 35: The Oxidizer Tank

For the desired minimum tank wall thickness, the hoop stress must be evaluated. Given that the tank has a wall thickness of no more than one 10th of its radius we can make the assumption that it is a thin walled cylinder. A wall thickness of 4.33mm is required for a factor of safety of 2.5 and is appropriate to contain the stress in the thin sections of the tank. A.2.2

$$t = \frac{P * D_{in}}{2\sigma_\theta - P} \quad (41)$$

Mass (g)	Diameter (mm)	Length (mm)
3631g	152.4	645

Table 23: Oxidizer Tank Mass and Size

For the bolted connections between the tank and the closures there are four main failure modes that can occur: bolt shear failure, bolt tear-out failure, tensile failure, and bearing stress failure.

Bolt shear stress occurs when the bolts used to hold the closure into the tank break due to the force applied perpendicular to the axis of the fastener. The closure-tank connection uses 14 m6 bolts. A.2.3

Bolt tear-out is the failure in which the bolts tear through the end of the casing. It is most likely to occur in designs in which the fastener holes are very close to the edge of the casing, or when the casing wall is relatively thin. For this reason the tank is broadened to a thickness of 9.53mm at both ends. A.2.4

Casing tensile failure occurs when the portion of the aluminium casing between the fastener holes is stretched beyond its breaking point. Given that only 14 relatively small bolts are used, this failure mode is the least concerning. A.2.5

Bearing failure occurs when the force of the bolts pushing against the edges of their holes causes the casing material to fail in compression. It is likely to occur in designs with a small number of bolts of relatively small diameter, or, again, when the casing wall is relatively thin. The thicker walls at the end also help to protect against this failure mode. A.2.6

Failure Mode	Factor of Safety
Bolt Shear Failure	2.77
Bolt Tear-out	4.91
Casing Tensile Failure	8.33
Bearing Stress Failure	3.05

Table 24: Factors of Safety for Tank Failure Modes

The Oxidizer Tank is sealed through the use of 4x Silicone O-Rings; two on each closure with one a redundant backup. The O-Rings form a static seal between the Closures and Tank tube. 70 Durometer Silicone was chosen as it is chemically inert with Nitrous Oxide and has a minimum operational temperature of -60C, sufficient for the potential -30C temperatures seen in the previous Wattle project [26]. O-Rings were sized using the Parker O-Ring Handbook as a static seal [23] with modified groove geometry to improve squeeze. The designed size and O-Ring properties can be seen in Table 25 below.

O Ring	Size	Fit	Squeeze %	Stretch %	Gland Fill %	Quantity
A	G130-S7	Static	19.4	1.1	75.5	4

Table 25: Oxidizer Tank O-Ring Design

All O-Rings in the Propulsion-Tank section are greased with LOX-8 oxygen-safe Grease for lubrication and to promote minor swelling for increased sealing [3].

6.2.1 Vent Closure

The vent closure is responsible for sealing the top of the oxidizer tank whilst allowing the oxidizer to vent as needed. 14 Radial m6 screws surround the closure and bolt through the side of the tank, supporting the closure in shear. Below these bolts are two grooves that hold in the O-rings to seal the tank against the pressure. Two O-rings are used for redundancy. This closure has 12 tabs each with an m3 threaded hole to connect to the body tube. There are two 1/4 inch BSPP fitting at the top of the closure which will connect to the vent valve. Both the vent and aft closures will also be machined from 6061-T6511 aluminium round stock.

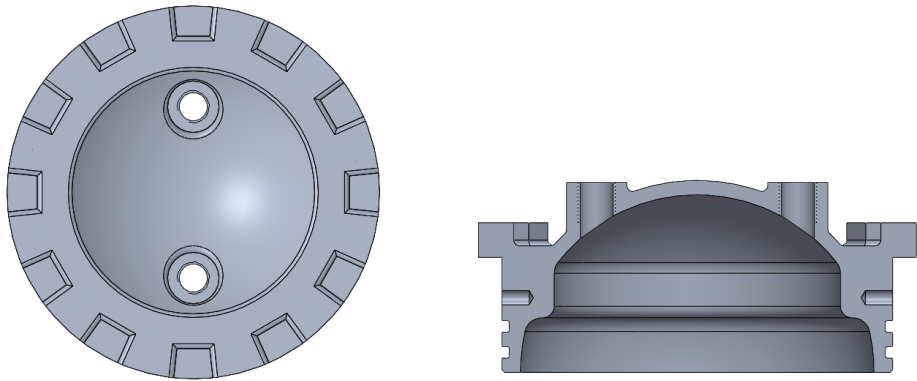


Figure 36: Vent Closure

Mass (g)	Diameter (mm)	Length (mm)
805	152.4	66

Table 26: Vent Closure Mass and Size

6.2.2 Aft Closure

The aft closure connects to the oxidizer tank using the same sealing system as the vent closure, with radial bolts and two O-rings. There is one 1/2" BSPP main port which connects to the run valve and two 1/4" BSPP sensor ports to each side. These connect to a thermocouple and a pressure transducer to monitor the tank conditions. There are 3 small, and 3 large tabs on the bottom face which interface with the truss system below. Each of the large tabs has two m5 threaded holes to bolt to the truss.

Mass (g)	Diameter (mm)	Length (mm)
905	152.4	77.5

Table 27: Aft Closure Mass and Size

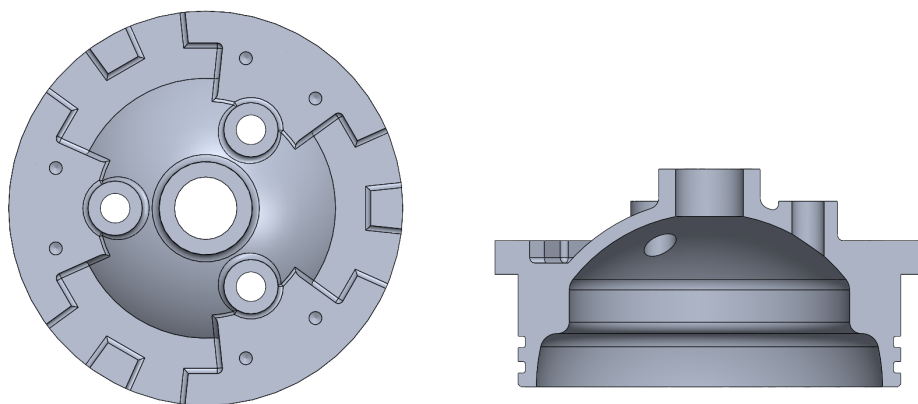


Figure 37: Aft Closure

6.3 Main Flight Valve

Pardalote's Main Flight Valve is responsible for the control of Nitrous Oxide from the Oxidizer Tank to the combustion chamber. The design requires fast actuation (PL-R-TNK-4) and a compact layout to be fitted within the 6 inch diameter of the airframe. Pneumatic control has been selected to provide fast and powerful actuation with the ability to return to a normal state in the case of loss of power. As the fuselage diameter limits volume for a traditional COTS actuator and ball valve, the proposed design instead incorporate a SRAD actuation system into the body of the valve itself.

Valve design is non-trivial and a completely new area of research for URT. As such, careful planning and research are required, along with proper testing of the manufactured design.

6.3.1 Coaxial Valve

The coaxial valve actuates linearly to provide a compact design, simplistic installation and provide coaxial flow, reaching a maximum diameter of 96mm by 140mm in length and weighs 1.4kg. The valve comes in five separate parts (see figure 38), with the body housing the sleeve and sealed off by two caps with M3 Bolts. Nitrous Oxide flow comes through the inlet from the top, travels around the piston head and through the sleeve. Initially in an open state, a local solenoid provides air pressure of 8 bar into the pneumatic intake. This provides a force of 1645N upon the sleeve outer rim, pushing the piston head onto the valve seat, sealing the valve. The force of nitrous oxide acting on the head to open is 1176N. A local solenoid then exhausts the air and in turn allow the spring to force the valve to an open state, allowing nitrous oxide to flow. This will remain in an open state until all nitrous oxide is exhausted. The spring is custom made from a supplier, providing an extra force of 100N to open the valve when there is power or air loss.

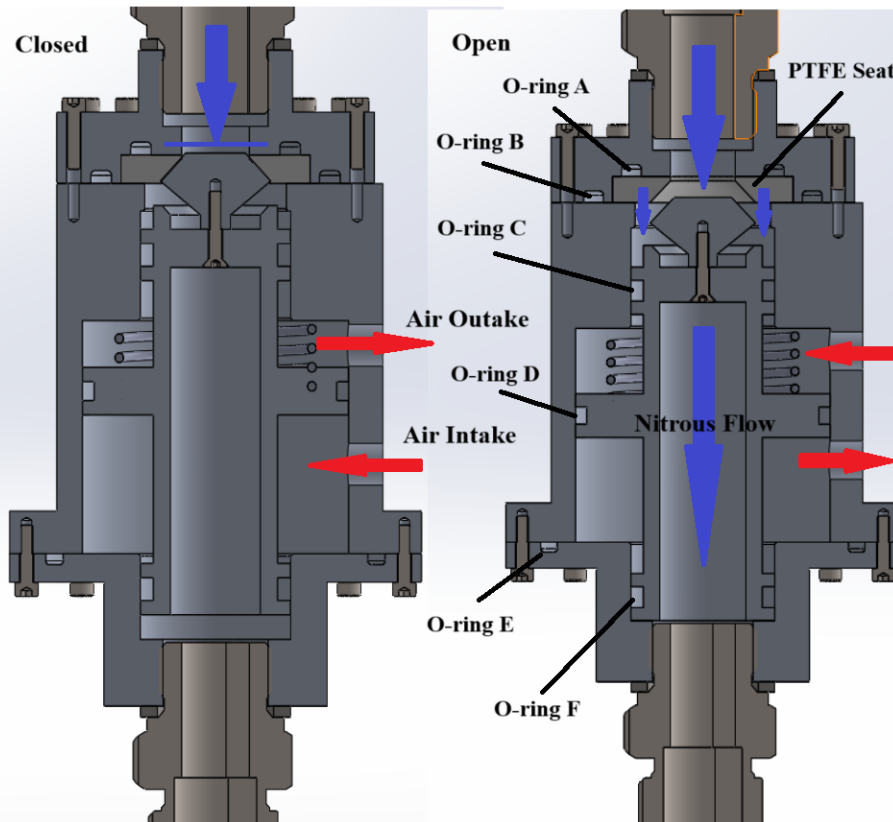


Figure 38: Coaxial Valve Section View

When closed, the piston head rests upon the valve seat and compressed by the inlet cap. The valve seat is a machined PTFE sealant with a three-quarter inch inner diameter. PTFE is chosen due to its machinability and works well in cold conditions. In addition, PTFE has low elasticity, lowering the risk of deformation under pressurised conditions. This prevents any nitrous oxide flow when the piston head pushes against the PTFE. The head of the piston is chamfered as to provide the best flow rate while also ensuring maximum surface area contact between the head and the PTFE valve seat for sealing. If the PTFE seat deforms under

operation, the chamfered head will still maintain contact and can push further into the seat if required.

The coaxial valve uses material Al 6061-T6511 due to its chemical resistance and high strength to weight ratio, ensuring the valve to meet standards of a high pressure vessel. Wall thickness are ensured to be high, primarily for the sleeve part the endures nitrous oxide pressure and so Hoop stress calculations confirm the safety of the pressure vessel. A strong clamping force is required to seal the vessel on either side, requiring 14 M3 socket head cap screws on the inlet cap and 8 M3 socket head cap screws on the outlet cap (see table 28. As this design is entirely student research and manufactured, testing the validity of this pressure vessel is required. The valve will undergo an actuation test to test the mechanism of the valve, hydrostatic testing to prove the valves ability to withstand 60 bar of pressure, and a cold flow to test the actuation ability when 60 bar of pressure is present.

Table 28: Bolt Clamping Forces for Coaxial valve

Flange	O-ring Compression Force (N)	N2O Force (N)	Number of Bolts	Load per Bolt (N)
Inlet	751	4271	14	394
Outlet	383	660.84	8	214

As the valve is a pressure vessel, the sealing produces excessive forces upon the bolts that clamp the assembly together. The bolts can fail and fracture in two ways; bolt tension failure and thread shear failure.

Bolt tension failure occurs due to the tensional force applied by the cap that pulls the bolt out, potentially snapping on the bolts neck. This is minimised by thread depth and increasing the number of bolts required. 98

Thread shear failure occurs through the shearing between the internal and external threads, where snapping of said threads could occur. For this section, both the internal thread of the aluminium valve body and the external thread of the bolt are considered. Again, thread depth is a key influence in design the factor of safety. 99 100

Table 29: Failure Modes and Factor of Safety of Valve Caps

Failure Mode	Inlet Cap F.O.S	Outlet Cap F.O.S
Bolt Tension Failure	7.15	13.16
Internal Thread Shear	17.6	32.4
External Thread Shear	93.3	172

The thickness of the sleeve is primarily driven by Hoops stress, which determines the stress exerted upon the material given the pressure within the pressure vessel. With a wall thickness of 6mm, the yield factor of safety is 29.1. 101

O-rings are required to seal the valve to prevent escape of gas and liquids involved. The valve dimensions are primarily based off the o-ring sizes available from AB Seals [26] using squeeze, stretch and gland fill formulas. Silicone material was chosen due to its cold flexibility down to -59 °C and availability of the material. For face seal o-rings, 20% - 30% squeeze range is ensured to maintain a proper seal, where stretch is the amount of deformation the o-ring undergoes upon sealing. The dynamic o-rings are ensured to be within a 12% - 16% as to maximise sealing between nitrous oxide pressure and air pressure. Similarly for stretch, defined as the difference in diameters for the o-ring and groove, the values must fall within the range of 1% - 5%. The chosen o-ring dimensions and their calculations [4] can be found in table 30.

$$\%Squeeze = \frac{W_0 + W_c}{W_0}$$

$$\%Stretch = \frac{D_{groove} - D_{ID}}{D_{ID}}$$

$$\%GlandFill = \frac{O-ring_C S_Area}{Groove_C S_Area}$$

Table 30: O-ring sizes and properties

O-ring	Size	Fit	Squeeze %	Stretch %	Gland Fill %
A	P030-S7	Face Seal	22.9	1	74.2
B	P048-S7	Face Seal	22.9	1.68	74.2
C	P028-S7	Dynamic	14.3	4.48	66.8
D	G055-S7	Dynamic	12.9	4	69.9
E	G070-S7	Face Seal	25.8	2.3	82
F	P028-S7	Dynamic	14.3	4.48	66.8

Table 31: Coaxial Valve Advantages and Disadvantages

Advantages	Disadvantages
Coaxial Flow	Complex parts
Nitrous keeps valve open	Expansion of Nitrous
Linear and compact	

6.4 On-board Pneumatic System

The requirements of the on-board pneumatic system is to hold pressurised air for valve actuation, be capable of being filled with ease via the quick disconnect and be able to hold enough air for at least 1 valve actuation.

The system provides pneumatic actuation to the valves using a 38g CO_2 cartridge acting as an on-board air reservoir and will require a flat gasket to seal between the surface of the cartridge and manifold. The 38g CO_2 cartridge has a volume of 60 ml which will sufficiently store the air when the coaxial valve is closed.

Pressure (MPa)	Temperature (K)	Density (kg/m ³)	Mass (g)
0.8	298.15	9.6	0.58

A Pirtek quick disconnect will be threaded into a custom manifold which will be used to provide a convenient junction point for distributing the air. Since the quick disconnect closes upon disconnection, this absolves us of the need for check valves. The manifold will be constructed out of 6061 Aluminium alloy primarily for its cost effectiveness and a low density of $2.7g/cm^3$, reducing the weight that is on-board. Also, due to the fact low pressure air is being used, the propensity for it to wear and tear will not be much of a concern. The system includes M3 holes for mounting to the truss of the rocket.

The pneumatic system is capable of operating for approximately 3 valve actuations for the angle seat valve. This was calculated by summing both the volume of the pneumatic intake when the valve is opened and closed.

6.4.1 Solenoid Valve

A solenoid valve allows control of airflow into the flight valves remotely. For both versions of the valve, a 4/2 port solenoid is used as to provide source of air to the chosen inlet and simultaneously vent air. Pneutech supplies 4 port solenoids with a 1/8" port size from their MAC series with associated dimensions 56mm x 27.5mm x 62mm.

The valve is powered by 24V DC current supplied by the GC power umbilical. The valve will impose a normal position onto the main flight valve, when no power is provided the main flight valve will stay in an "open" position. When power is given, the flight valve will remain in a "closed" position.

6.5 Pressure relief

The Vent Valve is a Servo-Assisted Solenoid Valve which is used to vent N₂O gas during filling. It is electrically actuated requiring a 24VDC input. It has G 1/4" female ports. The valve has a maximum pressure rating of 100 bar and a minimum operating temperature of -40C. The selected valve can be seen in Figure 39 below.



Figure 39: Burkert 6240 Servo-Assisted Solenoid Valve

A requirement in both IREC and FAR-OUT (PL-R-TNK-2.3) is the inclusion of a pressure relief device, to prevent over-pressurisation of the Oxidizer Tank. This is done with a HAM-LET Spring Relief Valve set to 75 bar.



Figure 40: HAM-LET Spring Relief Valve

7 Ground Support Equipment Subsystem

7.1 Overview

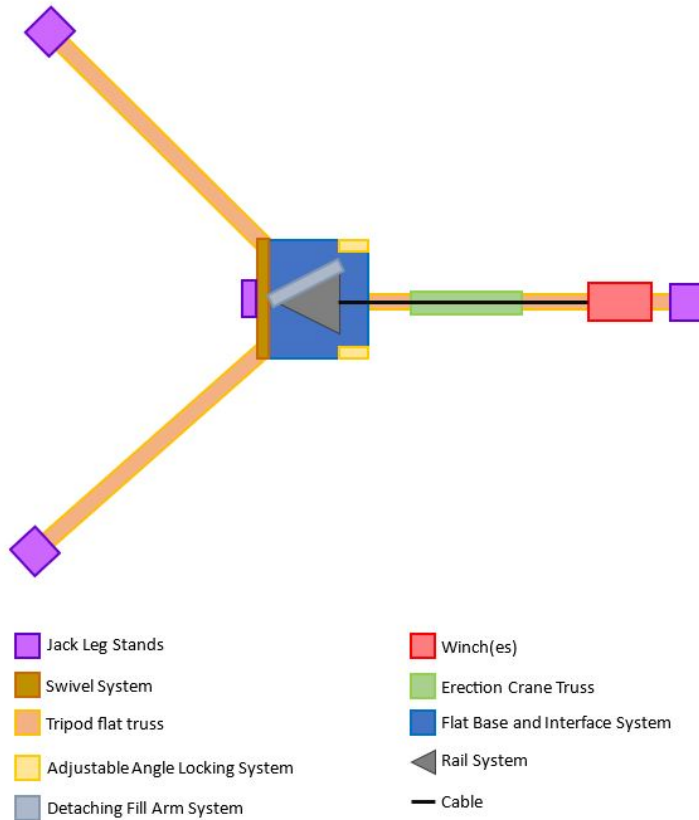


Figure 41: Spatial diagram for the launch rail

Due to the high mass of the Pardalote launch vehicle and the thrust limitations of hybrid propulsion systems, a launch tower spanning 10+m is required. This tall span necessitates a wider and more rigid base structure. This launch tower is designed for future Team launches and must be transportable to the United States, resulting in requirements of modality and minimal mass. Furthermore, it has to come with an alignment mechanism that allows it to be lifted from a horizontal position and brought down from a vertical position for rocket mounting and launch.

7.2 Launch Rail

7.2.1 Launch Structure

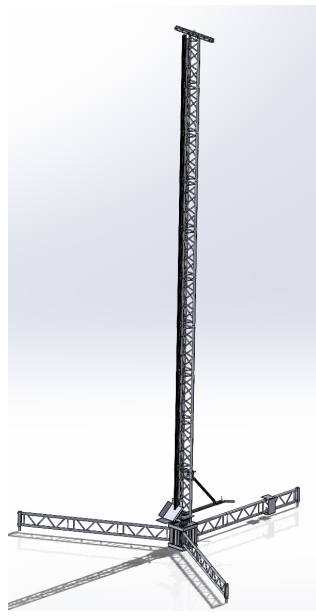


Figure 42: Launch rail CAD viewed from the side



Figure 43: Launch rail CAD viewed from the top

Figures 42 and 43 shows a proposed launch rail structure that will be used for pardalote onwards. The overall structure will cover an approximate square area with sides of 4-5 m long. The adjustable height of the bottom of the extrusion rail from the ground will be slightly less than 1 m and with a default extrusion rail length of 10 m, the overall height of the rail structure would tower approximately 11 m. If several meters-long adjustments to the rail need to be made, the structure would increase in height in 1 m increments as 1 m extrusions and tri-trusses are used.

7.2.2 Rail System



Figure 44: 80x40 extrusions used as the rail

1 m tri-trusses and 1 m 80x40 T-profile extrusions will primarily make up the vertical rail system where the rocket will be mounted onto as shown in figure 44. Instead of using butt fasteners to connect the extrusions together which makes alignment of the previous launch rail more difficult, plates can be used which will

ease the alignment process. However, T nuts will still be needed for the bolting process and so instead of using plates, using long T nuts which can span between two extrusions for alignment. Furthermore, defects on the extrusion surfaces either due to manufacturing or external factors when handling them may prevent perfect alignment, which is not a problem if long T nuts are used.

The extrusions will be attached to the tri-trusses via a series of aluminium G-clamps, ensuring that the extrusion is located and facing angularly between two flat trusses as shown in figures 42 and 43. The bottom end of the tri-truss will be connected to a base plate using conical connectors and pins.

The mass per length of the 80x40 extrusion and tri-truss is 4.138 kg/m and 5 kg/m respectively. The G-clamps each have a mass of 0.73 kg. For the default height of 10 m and accounting for the conical connectors and other fasteners, this would give an approximate mass of 120 kg. The extension of the rail by 1 m would increase this mass by roughly 10 kg.

7.2.3 Base Structure

Considerations were made in regards to have a quadpod structure instead of a tripod one for an increased base stability. However, based on the alignment of the flat-trusses with respect to the mounted rocket, several issues arise. Firstly, if a flat truss was in line with the rocket, the winch can be placed at the leg across it, however the plume shield should be designed to prevent the rocket from damaging the flat truss during the engine combustion. In a reclined position of the rail, the rail should be positioned higher from the ground to ensure there is enough clearance for mounting the rocket as the flat truss is now located below the rail.

If the rocket was located in between the flat truss, similar to the tripod structure, these issues would be mitigated. Although, a new issue arises with the placement of the crane and winch. If the crane and winch was located at only one of the legs, the angle the cable makes with respect to the direction of erection makes it inefficient as the cable needs a higher tension to pull the rail up. If the crane and winch was located in between the flat trusses, a more complicated structure has to be made, incorporating the flat trusses, so that the crane and winch is fixed in place which is much more difficult to design and assemble. If the winch was somehow placed on the ground instead, a structure has to be designed and fixed and or weighted on the ground to prevent the winch from being pulled up from pulling the rail up which is highly dependent on ground conditions. If the two cranks and winches were used, one on each flat truss, the tension load will be shared across two cables. This will also pose as a safety feature of the rail where if one cable fails and snaps, there will still be another wire to hold up the rail. However, this would also mean an increase in the number of parts needed for the rail structure.

Another proposal is that the interfaces would be made out of rectangular hollow sections (RHS) which are cut and welded together to create a pre-assembled structured. This reduces the need to assemble the interfaces and can be ready in a shorter amount of time. With shorter RHS used, the interfaces can be made to be smaller than the ones using extrusions and so will reduce spatial occupation during transportation when in an assembled state. Furthermore, since most of the rail structure load is applied onto the interfaces via the swivels, they need to be strong enough and have adequate factor of safety to hold the structure up. RHS would be stronger than extrusions due to being made out of steel compared to the aluminium of the extrusions.

7.2.4 Swivel Mechanism

Bottom plate

The bottom plate attaches to the base box and the lower bearing blocks of the swivel. The plate is a square with two rectangular cutouts in the lower corners. The cutouts allow for the outer bearing blocks on the top plate to pass cleanly. The plate is machined out of 10mm aluminium plate.

8 m12 clearance holes are aligned with matching holes in the base box to be secured using bolts. 2 of these bolts also pass through the bearing blocks and secure it to both the top plate and the base box. These 2 holes are matched with two more m12 clearance holes that will secure the other connection of the bearing blocks.

Four m8 clearance hole are positioned in the middle of the plate. These are to allow the angle blocks to be attached.

Bolted connections are used throughout the base assemble as they are modular and replaceable. In the event of failure or wear, there is a smaller chance that critical components will be damaged and replacement

components will be easier to facilitate.

Risers

4 risers are used to ensure clearance not only of the grease nipple that protrudes from the bearing blocks, but also the bolts that secure them. There are 4 20mm thick risers and 2 10mm thick risers all made of aluminum. These risers are simple plates that have clearance holes allowing them to be easily bolted down.

Swivel

A few considerations were made for how the swivel mechanism design. A series of 80x40 heavy duty hinges, weighing 1.02 kg each, was considered to attach the base plate onto the rectangular base, allowing the rail structure to rotate between a horizontally reclined position for mounting and a vertically inclined position for launch as shown in figure ???. Given that the hinges are rated to take on lateral and shear loads of up to 1500 N with movement, this means that they could theoretically hold slightly more than 150 kg of mass each. Based on fig 49, an expected reaction force of 2600 N will act on the rail base, the minimum number of swivels needed would be two. However, due to the swivel mechanism being a highly structural part that would pose a very high risk when failure occurs, a factor of safety of at least two would mean a swivel count of at least four. Depending on the decision on increasing the rail height, the number of swivels may increase to withstand higher weight forces.

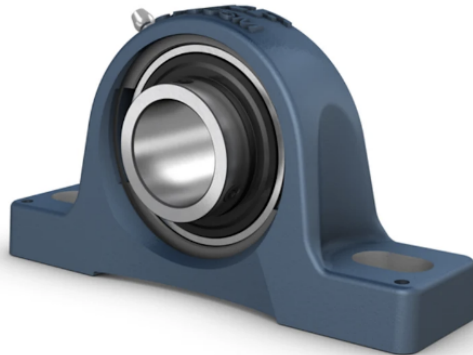


Figure 45: SKF bearing block with 50 mm inner diameter

Another contender for the swivel mechanism is a series of bearing blocks. A set of two bearing blocks will be attached to both the rail base and the tri-truss plate. A steel shaft will be fed through the bearing blocks, attaching the tri-truss base plate to the quadrilateral interface and keeping them in a pre-assembled state. The main advantage of bearings is that they are generally able to take on higher loads. The shaft also helps align the bearing blocks and even if there is a small misalignment, the angular tolerances of the bearings and bearing blocks would still allow for smooth rotations. The only issue would be higher mass and cost of components from both the bearing blocks and the shaft compared to swivels.

Angle Blocks

The adjustable angle blocks allow us to fulfill the requirement of aiming the launch rail at multiple angles to the horizontal. The usual operation case is a flat block that simply allows the rail to rest upon it and rise straight up normal to the ground. However, if required it can be substituted with a block where the top face is angled. The top plate will then rest on this angled face and correspondingly the rail will be tilted. Multiple sets of these blocks will allow the rail to be aimed at 90°, 87° or 84°.

To resist any tension forces, these blocks are threaded and bolted on both sides to the top and bottom plates. However the function of resisting these forces is also shared with the ratchets and the wires, enabling the launch rail to exist stably even when not exactly vertical.

Top Plate

The top plate connects to the tri truss above and the swivel below. The load cell is also mounted on the top plate so as to be close to the bottom of the rail. Multiple elements are identical to the bottom plate. It has the same attachment points to the bearing blocks and the angle blocks as well as similar cutouts. The connection to the truss comes in the form of three half conical connectors that are bolted down. The plate

was bought from a commercial supplier and then modified to suit our needs so that the holes for the conical connectors would be aligned optimally.

The top plate also serves as the connection point for the gin pole and correspondingly has holes drilled and aligned.

7.2.5 Gin Pole

The gin pole serves as a way to redirect the pulling force of the winch to make the force curve more optimal. The gin pole itself is a two part member consisting of two 1m lengths connected by two plates in the central joint. Each section is 35mm x 65mm steel pregal RHS as the pole needs to be able to attach under the lowest part of the truss. No aluminium hollow sections were found that were suitable in size and strength so steel was chosen due to the loads that the pole undergoes.

The pole is bolted to the top plate with four M10 bolts and to the truss by an additional support member. The support member attaches to two hinges. One is mounted on a plate attached to the truss and the other attaches to the connector plates in the middle of the gin pole. This support arm is used to provide additional support against buckling.

The connector plates attached to each length with four M8 bolts leading to a total of 8 M8 connecting the member together. The attachment point for the support member is located through the connector plates so as to avoid any stress concentration at the bottom of the plate and to take advantage of the added rigidity.

In order to determine the most efficient position on the rail where the crank wire will be attached to, calculations of the tension force on the wire have to be made to ensure the least amount of tension possible. Two possible scenarios were identified for the rail as it is lifted and descended as shown in figures 46, 47 and 48:

- Scenario 1 - Wire still in contact of the rail at lower launch rail angles.
- Scenario 2 - Wire no longer in contact with the rail at higher launch rail angles.

The expressions for the reactions in x-direction, reaction in y-direction and reaction resultant forces, as well as the tension force were obtained. With the equations for each force, the forces are calculated for all rail angles with the horizontal from 0 to 90 degrees as shown in figures 46, 47 and 48:

Wire Attachment

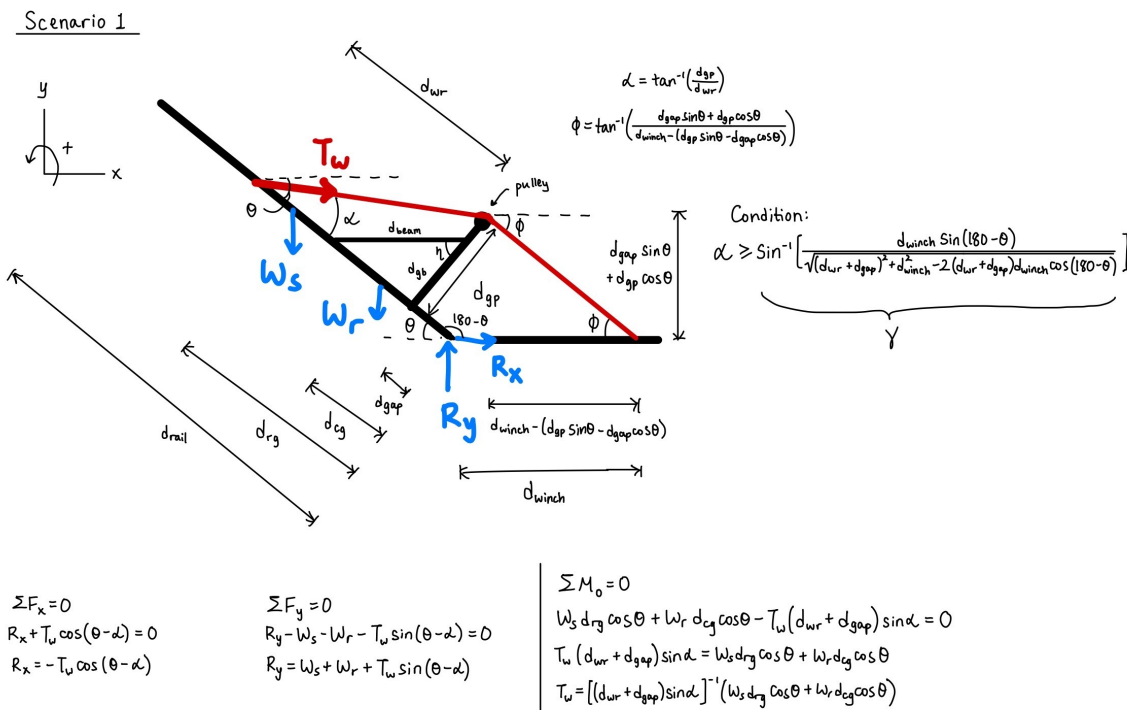
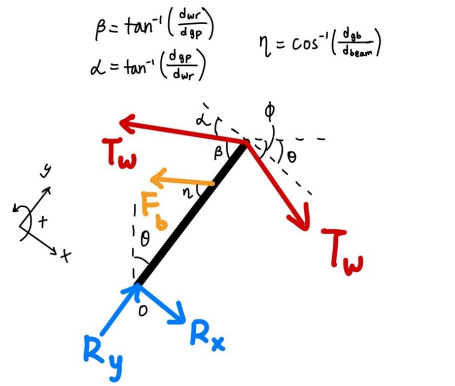


Figure 46: First scenario of free body diagrams for a portion of the rail structure



$$\sum M_o = 0$$

$$T_w d_{gp} \cos \alpha - T_w d_{gp} \cos(\phi - \theta) + F_b d_{gb} \sin \eta = 0$$

$$F_b d_{gb} \sin \eta = T_w d_{gp} [\cos(\phi - \theta) - \cos \alpha]$$

$$F_b = (d_{gb} \sin \eta)^{-1} \{ T_w d_{gp} [\cos(\phi - \theta) - \cos \alpha] \}$$

$$\begin{cases} \sum F_x = 0 \\ R_x + T_w \cos(\phi - \theta) - T_w \cos \alpha - F_b \sin \eta = 0 \\ R_x = T_w \cos \alpha - T_w \cos(\phi - \theta) + F_b \sin \eta \\ \sum F_y = 0 \\ R_y - T_w \sin(\phi - \theta) - T_w \sin \alpha - F_b \cos \eta = 0 \\ R_y = T_w \sin(\phi - \theta) + T_w \sin \alpha + F_b \cos \eta \end{cases}$$

Figure 47: Continuation of free body diagram for scenario one involving the gine pole

Scenario 2

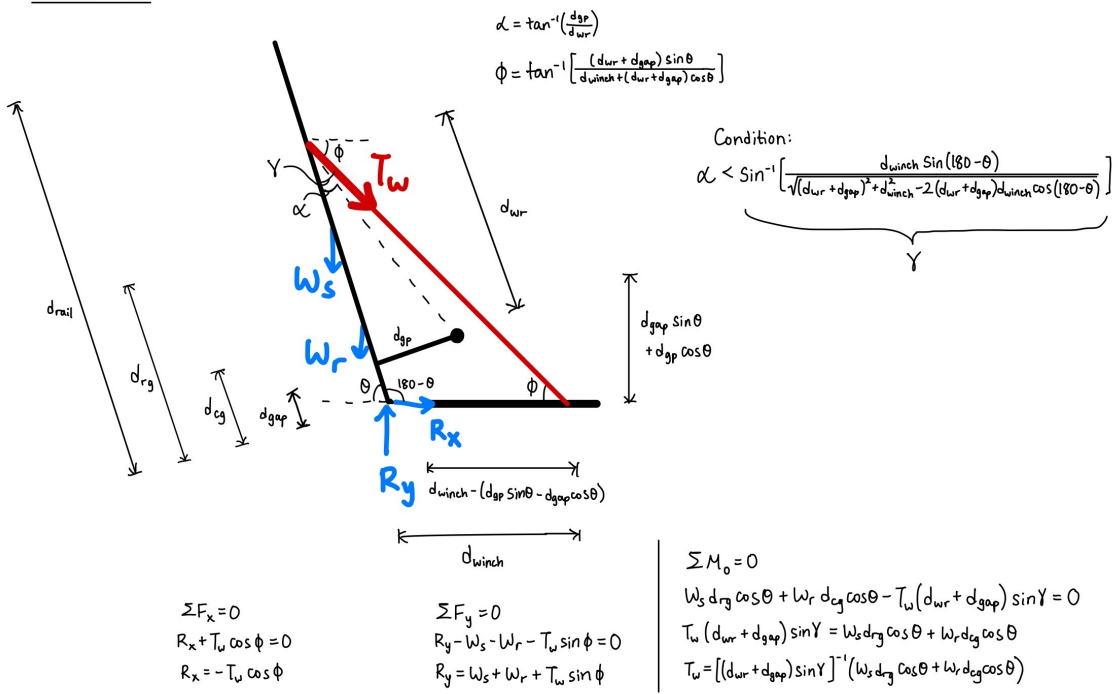


Figure 48: Second scenario of free body diagrams for a portion of the rail structure

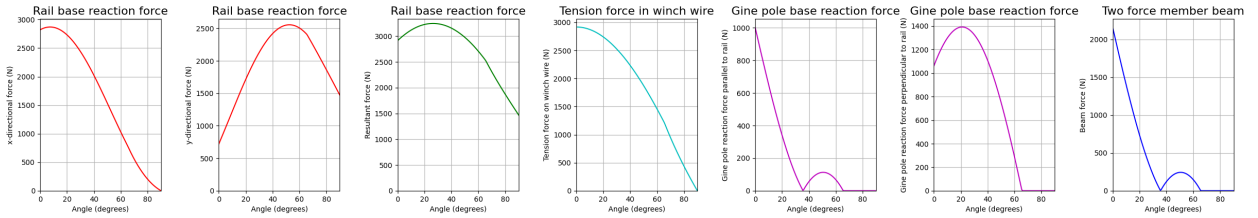


Figure 49: Estimated reaction forces on the rail base, wire, gine pole and support for specific rail dimensions, given that wire is attached above halfway point of the rail

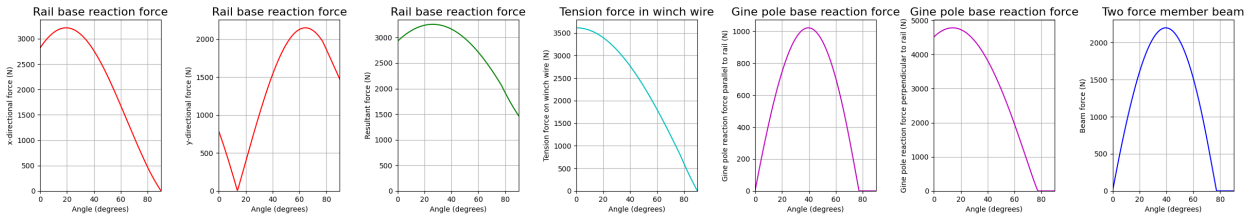


Figure 50: Estimated reaction forces on the rail base, wire, gine pole and support for specific rail dimensions, given that wire is attached below halfway point of the rail

Based on calculations and plots of the reaction forces at the rail base and wire tension force, attaching the wire above the halfway point of the rail, 10 m in this case, will yield similar maximum rail base resultant reaction force but significantly different tension force on the wire and gine pole reaction force. This reduces the possible range on the rail where the wire should be attached on to be between the halfway point (5 m) and the upper point (10 m).

Pulley



Figure 51: Pulley subassembly

The rail wire will be fed through the pulley at the top end of the gine pole. Two bent 3mm thick metal sheets will be attached to straight 10mm thick metal plates via M8 rivets. These assembled steel pieces will then be attached to the gine pole via M8 bolts which would allow for the pulley to be mounted in between them using a M10 bolt as shown in figure 51. A stainless steel pulley with a bronze bush was selected, which has a diameter of 50 mm and thickness of 20 mm.

Pulley Attachment

7.2.6 Crossbar



Figure 52: Crossbar

Building upon the foundational design principles of its predecessors, the Enhanced Crossbar represents a significant advancement in structural support. Carefully engineered to accommodate the increased scale and complexity of the new erection mechanism, this critical component serves as the pivotal anchor point for the entire system. Designed to withstand substantial forces, the crossbar integrates a robust platform for the secure attachment of four ratchet straps, three tensioning wires, and a lifting cable, ensuring optimal stability and control during the erection process and launch.

The Crossbar is constructed using 76x76mm Aluminum SHS with a thickness of 6.35mm to ensure optimal strength and weight efficiency. Key attributes include a central frame featuring integrated attachment points with eight M12 Eye-Bolts. Additionally, it incorporates two half-couplers for attachment to the launch rail truss. The cutouts are engineered to allow easy access to the interior nuts with a spanner. The half-couplers feature larger cutouts because they are attached to the truss before being bolted to the crossbar, requiring tightening from the inside.

Tensioning wires

Two extra tensioning wires will be connected from the crossbar to the flat truss legs. With the winch wire, this will provide tension force with the launch rail from all three sides. The purpose of these wires is to provide internal rigidity and support to the structure, helping to support against deflection from the wind, or in the case that the launch rail is positioned at an angle. Pre fixed wires have been chosen for this role as they are more reliable and less susceptible to failure compared to cutting and adding hardware ourselves. These wires will be attached to an eyebolt on each flat truss leg and tensioned using a turnbuckle.

Ratchets

Four ratchet straps support the launch rail from the outer eyebolts on the crossbar and attach to stakes driven into the ground. The ratchets provide tension to the launch rail and help it resist any wind forces or imbalances. When tensioned, they will provide structural support to the length rail. Whereas the wires help to fix the vertical rail to the legs, the straps will help fix the rail to the ground. Four 2500kg, 16m, ratchet straps have been chosen as they will provide more than enough tension while also being able to be fixed a good distance away.

7.2.7 Winch System

Winch Selection

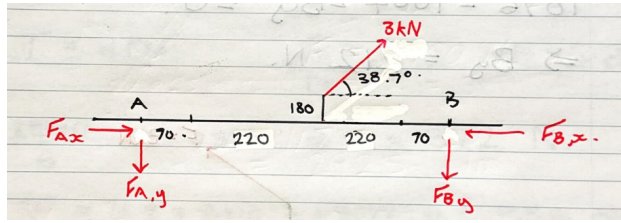


Figure 54: Winch Mount FBD



Figure 53: VEVOR hand winch for launch rail erection

The winch selected is a VEVOR hand winch as is shown in figure 53. This winch was selected for several reasons. Its working load capacity of 1587.5kg gives a high factor of safety (approximately 5) given our expected pull of around 3kN. The two-way ratchet enables both draw as well as letting the winch wire out under tension. It was picked over an electric winch due to the advantage of not needing power, and having control over winch speed. This control over the winch speed reduces the risk of overtensioning the winch wire and causing damage to the rail structure. The polyester rope has a length of 10m, meaning that the hook at no point passes through the pulley of the 2m tall gin pole. At the end of this rope is a length of steel wire which connects to the crossbar at the top of the launch rail using dee shackles and wire rope thimbles and grips for securement. An additional length of steel wire 10.5m long will attach onto the end of the

Winch Mount

Winch mounting plate to interface the winch with the flat truss section of the launch rail leg and provide a point of attachment.

The mounting plate will be attached to the upper section of the leg truss through the use of JD-Sound aluminium G-clamps.

The M10 bolt of the G-clamps will be slotted through a 12 mm pre-drilled hole on the plate and bolted in place.

Force calculations were conducted with the following assumptions:

- The mounting plate is placed 2.5 m from the launch rail base
- The tension force of the strap acts at the centre of the mounting plate
- Maximum tension force is 3000 N when vertical based on gin pole calculations

See below:

$$\theta = \tan^{-1} \left(\frac{2}{2.5} \right) = 38.7^\circ$$

$$F_x = 30000 \cos 38.7 = 2341N$$

$$F_y = 30000 \sin 38.7 = 1876N$$

$$F_{Ax} = F_{Bx} = \frac{2341}{2} = 1170N$$

$$\Sigma F_y = 0 : 1876 - F_{Ay} - F_{By} = 0$$

$$\Sigma M_B = 0 : 0.58F_{Ay} - 0.180 \times 2341 - 1876 \times 0.29 = 0$$

$$\Rightarrow F_{Ay} = 1664N$$

$$\Rightarrow F_{By} = 212N$$

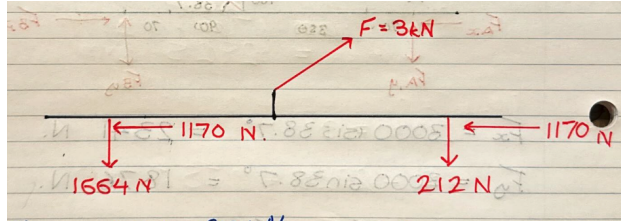


Figure 55: Solved Winch Mount FBD

Clamps are rated to 981 N normal force. Based on this and a factor of safety of 2, 4 clamps behind the winch and at least 1 (ideally 2 for redundancy) in front is sufficient.

Friction of the clamps resists the shear force. Coefficient of static friction between aluminium - aluminium is 1.05

To calculate resisting static friction the clamping force of the G-clamp bolts was considered:

$$F_x \overline{N = \mu R \Rightarrow \frac{2340}{6} = 1.05 RR = 372N}$$

Where N is the number of clamps which we take to be 6 based on above reasoning.

$$T = cDF$$

$$c = 0.2$$

$$D = 8 \times 10^{-3}$$

$$T = 0.2 \times 8 \times 10^{-3} \times 372 = 0.595Nm$$

Considering a factor of safety of 2, we have a tightening torque of 1.2 Nm. This is the minimum torque that the clamps must be tightened with to resist the horizontal shear forces generated.

1.2 Nm is a very small amount so just the reaction force is sufficient at generating the necessary static friction. The clamps will be tightened by hand with wing nuts which will be more than 1.2 Nm of torque and hence more than sufficient.

Therefore 6 clamps is sufficient at resisting the necessary loads and our limiting factor here is the normal reaction force, not horizontal shearing.

The plate used will likely be 10 mm aluminium. Its strength should be significantly greater than the forces being considered here and is not an issue.

Due to the large friction generated, and the self-correcting tension of the cable, the question of the mount rotating around the tubular section of the truss is not being considered as an issue.

The following design was made where the shaded box is the footprint of the winch. The right of the image is the direction of the launch rail.

The position of the clamps was determined by physically measuring the flat truss section. If the center of the mounting plate is placed over the center of the 1 m truss section in the upright orientation shown below there will be sufficient room for the clamps as indicated.

Note that the truss must be in the orientation with the internal members attaching at the centre of the section.

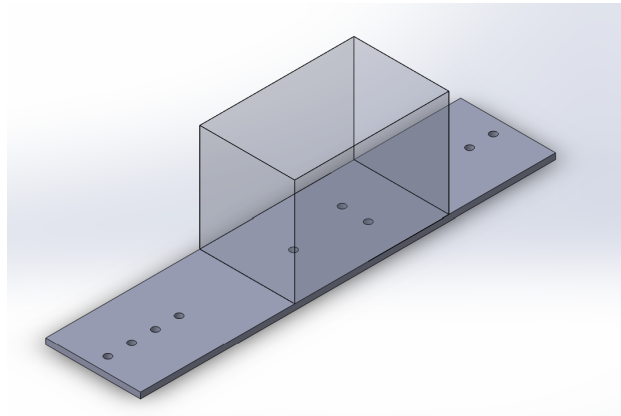


Figure 56: Solidworks Design



Figure 57: Truss Section Validation

7.2.8 Plume Deflector

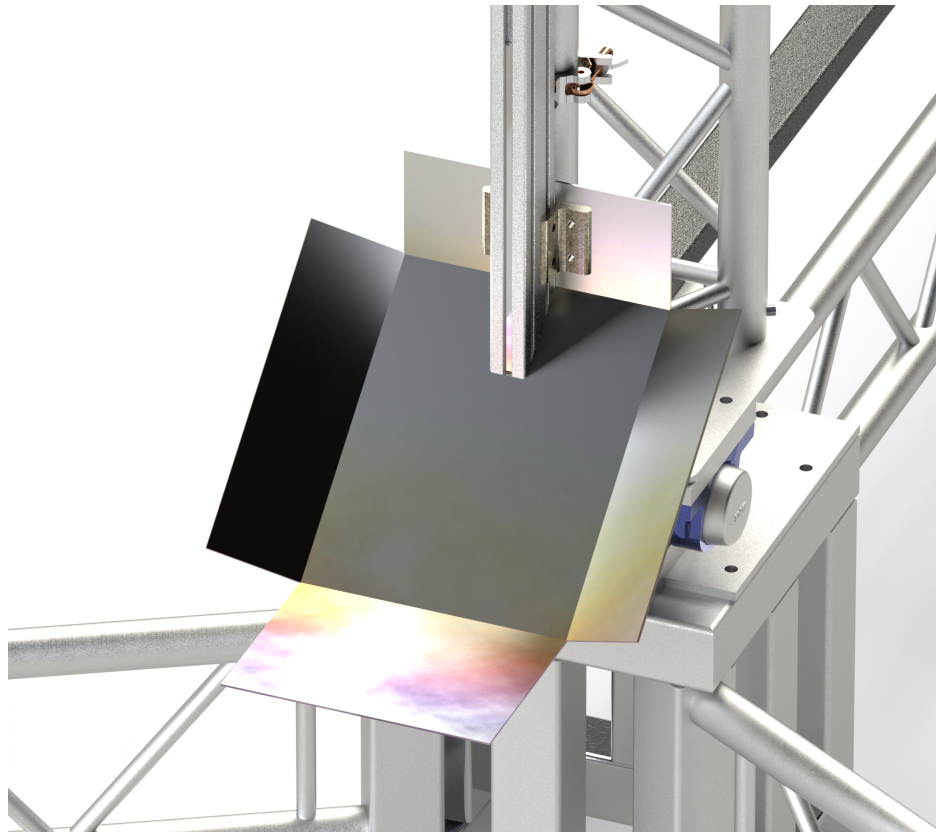


Figure 58: Plume deflector

The plume deflector will be made out of a thin steel sheet which will be laser cut and bent into a scoop shaped plate as shown in figure 58. The material selected is 316 Stainless Steel for its good mechanical properties and heat resistance, ensuring the plume deflector can withstand the high thrust and temperatures of the exhaust gas. Moreover, 316 Stainless Steel has strong corrosion resistance without using a zinc coating which would degrade under high temperatures.

7.2.9 Load Cell Mounting

Load Cell Selection

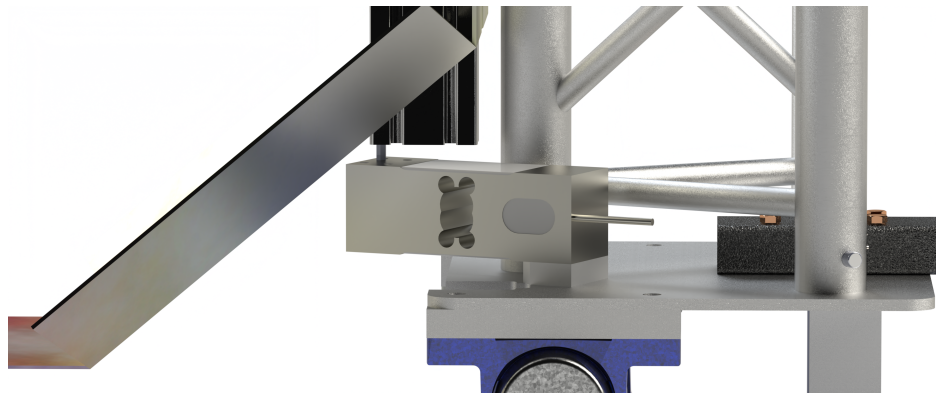


Figure 59: Load-Cell Mounting configuration

A DACELL CB2 load cell with a 250kgf rating will be installed on the rail base plate of the launch tower. This setup ensures precise measurement of the vehicle's mass and protection by the plume deflector, thereby promoting reusability. To measure the vehicle's mass, the lower rail button of the rocket will be positioned

on an extended T-nut, the load cell is then properly aligned so that the T-nut sits directly on top of it. Four M8 bolts are used to fasten the spacer block and load cell to the base plate.

Spacer Plate An essential part is the 16mm spacer block, which is used to ensure clearance between the Load Cell and the base box when the launch tower is in a horizontal position. A chamfer is incorporated into the boxed shape to give extra clearance from the swivel's bolts.

7.2.10 Miscellaneous Components

Stands After assembly of most of the launch rail, the rail structure has to adopt a horizontal alignment before the rocket gets mounted onto it. due to the immense weight of the rail structure, prolonged exposure of the swivel system may lead to fatigue due to large moments. The use of support stands at the end and along the rail structure reduces the load burden on the swivel mechanism in preparation for launch.

Cameras

Cameras may be set up on the rail structure to allow for multiple angle shots of the rocket before and during launch. These positions may include:

- Top of rail structure - viewing down on docked rocket.
- One of the two tripod legs without the lifting mechanism - recording the initial stages of rocket launch.

7.2.11 Transport and Assembly

Due to dimensional constraints for ground transportation and shipment to the US, All trusses and the extrusion-based rail will be disassembled into 1 m sections for transport. However, interface made out of welded RHS parts would have to be transported in the state it is in.

During assembly, the first to be assembled would be the flat trusses and the interfaces that make up the base of the rail structure. The tri-trusses, base plate and the 80x40 extrusions that make up the rail will be assembled in a horizontal position with the help of supports to hold up the tri-trusses. Alignment of the rail will be tested while the set of extrusions are facing towards the ground. Swivels will be used to connect the base plate to the interfaces before assembling the erection crane system. A test lift of the rail will be done prior to launch to ensure everything works as intended, bringing it back down right after and covering the entire rail structure from as much outside interference as possible with tarps.

7.3 Ground Fill Station

The ground fill system is required to be transportable as one component and portable over short distances. For this to work, the entire fluids system should be condensed into a small box that can be deposited at the launch site, with connection easily and quickly attached from fluid bottles and to the rocket.

7.3.1 Structure

For the fluids system housing, a rectangular prism, with a welded RHS frame, covered with steel sheeting will be used. This design is simple and cheap, while providing a rigid structure for mounting, and adding mass so that the fill system has less of a tendency to move when placed down. The RHS frame will be made from 50mm x 50mm x 1.6mm RHS, assembled in a 300mm x 400mm x 500mm frame. The frame will utilise 3mm galvanised steel sheets as the mounting surfaces of the fluids components, and will encapsulate all sides of the prism so that exposure to the elements for the fluids components is limited. Holes will be cut on certain panels so that needle valves, pressure gauges and attachment fittings are all accessible from outside the box. The front and top surfaces (which nominally do not mount components) will be made from detachable semi-transparent acrylic, to that the inside of the box can be viewed without having to open the the box.

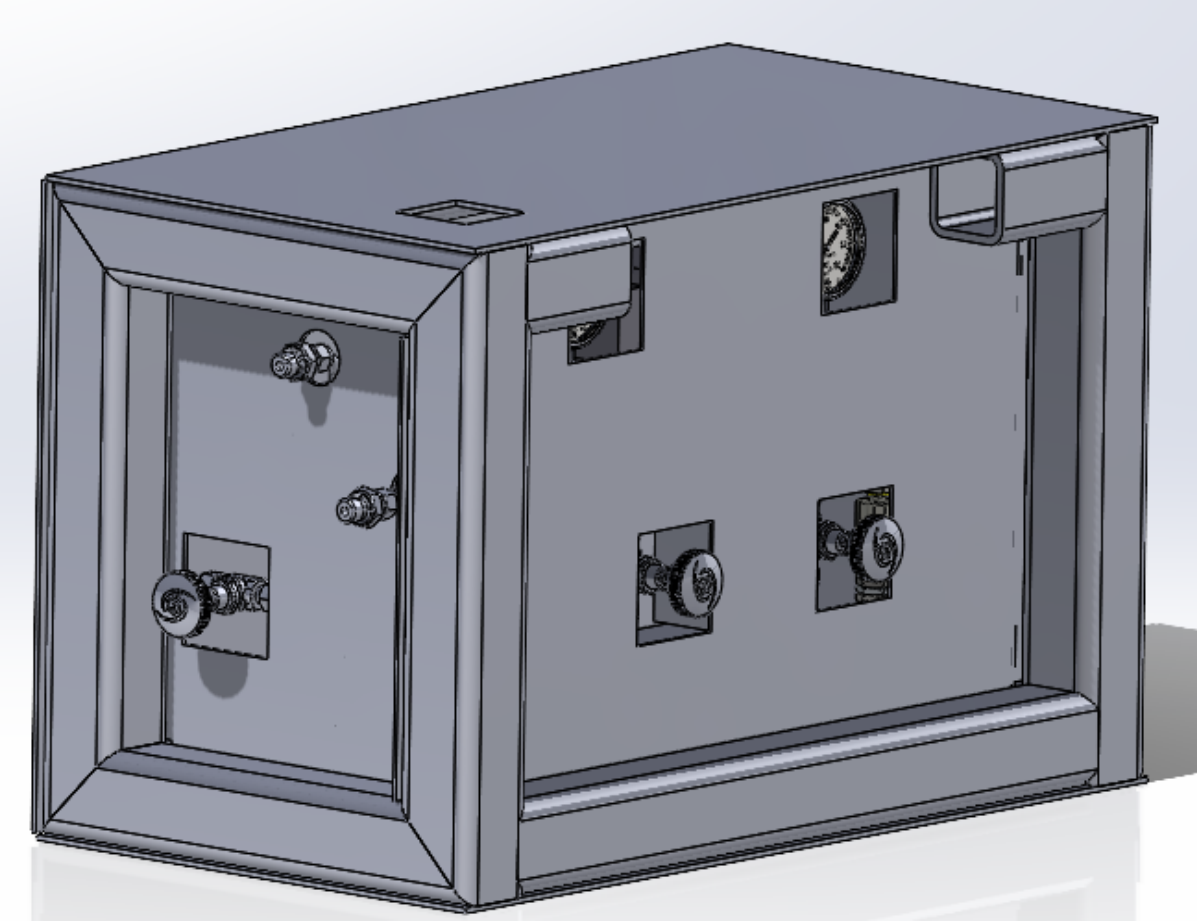


Figure 60: Structure CAD.

Component	Material	Amount	Cost
RHS Frame	Steel RHS (50mm x 50mm x 1.6mm)	4800mm	\$57.50
Mounting Surfaces	3mm Thick Galvanised Steel Sheet	0.94m ²	\$144.00
Transparent Front Panels	Clear Acrylic	0.32m ²	\$51.00

Table 32: Cost breakdown for the fill system frame.

7.3.2 Fill System

The purpose of the fill system is to be able to supply the quick disconnect with nitrous oxide, which is connected to the rocket when filling. Since the quick disconnect closes when disconnected from the rocket, the fill system needs a way to manually vent the system post-fire, or if the rocket is disconnected. Figure 60 shows the P&ID for the fill system, with a optional T-connection where nitrogen can be introduced for testing purging.

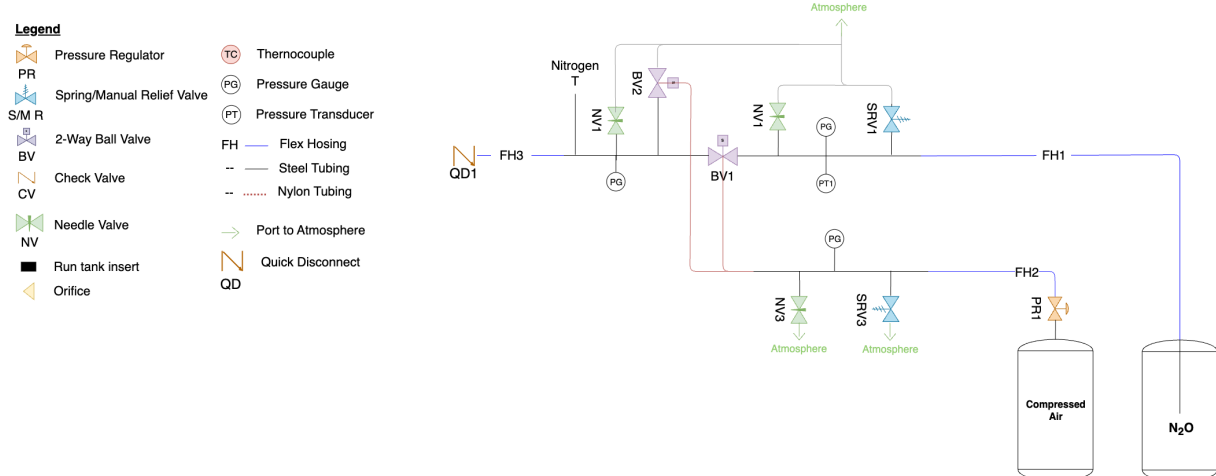


Figure 61: Fill System PID

Nitrous Line

The nitrous line has a pressure gauge, pressure transducer, spring relief valve and needle valve between the fill valve (BV1) and the bottle. The needle valve is there for when the system is required to be manually depressurised, in the event of a remote valve actuation failure. The pressure gauge provides the system pressure at the fill system, allowing knowledge of whether the system is pressurised, if someone is at the fill station. The spring relief valve prevents the line from overpressurising (set to a pressure limit of 100 bar), which is required as per SAC rules, and generally improves safety.

The line between the quick disconnect, fill valve (BV1) and the vent valve (BV2) only has a pressure gauge and a needle valve as that line does not have direct access to a fluid bottle, thus it doesn't require a remote pressure value, or a spring relief safety system. If the fill valve is open and the line is supplied nitrous oxide, PT1 and SRV1 will provide the required safety mechanisms for a pressurised nitrous line.

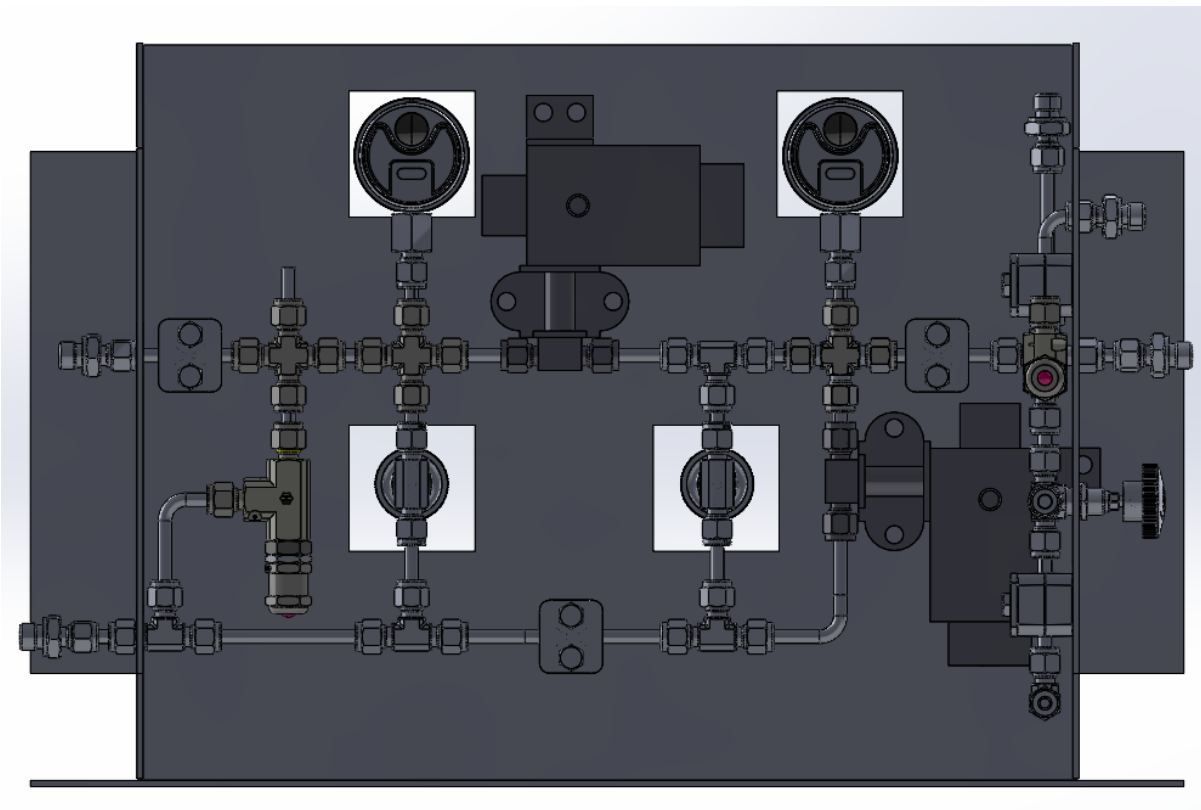


Figure 62: Fill system CAD, front view highlighting nitrous line.

Air Line

The air line is used to provide compressed air to the pneumatic ball valves on the nitrous line, as well as providing air to fill the compressed air storage on the tank subsystem. The air line does not require a pressure transducer, but the other safety features exist. Compressed air also incorporates a pressure regulator, which ensures the pressure of air in the line is kept to around 5 bar. The needle valve is used as both the method for manual depressurisation, as well as being a manual supply of air to tank.

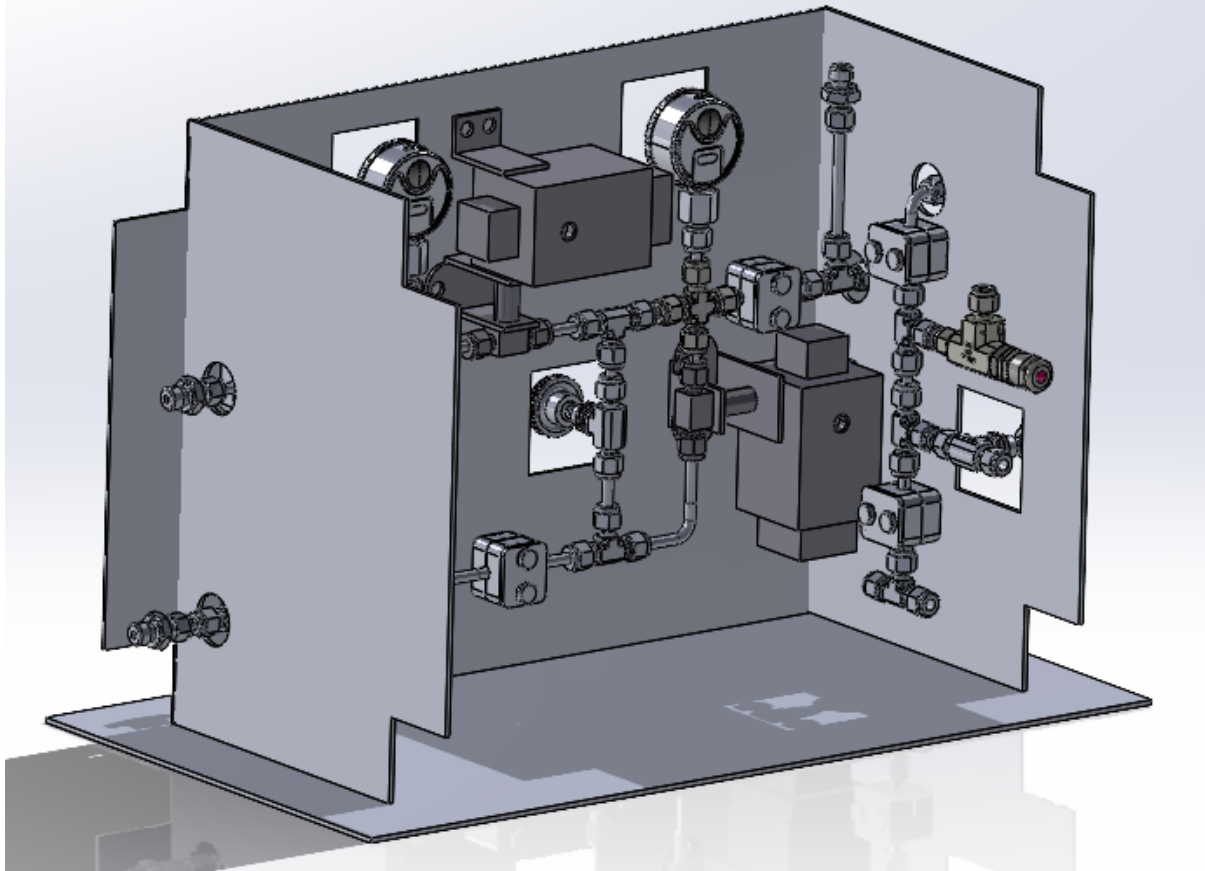


Figure 63: Fill system CAD, angles view highlighting both N₂O and air line.

System Operation

Ball valves 1 and 2 are both pneumatically actuated ball valves, sourced from . BV1 feeds nitrous from the bottle to the quick disconnect, while BV2 allows the fill system to vent the system remotely. When filling, the quick disconnect would be connected to the rocket, and BV1 would be open until the tank mass reaches the required value. Once full, BV1 would close, and the quick disconnect would get disconnected. Following this, the nitrous bottle is manually closed, and then BV2 and BV1 is opened to vent the system of remaining nitrous.

Nitrogen Extension

Nitrogen is used to purge the system of nitrous, which is generally required if the fill system is not out in the open in a ventilated area. Purging the system with nitrogen greater reduces the amount of nitrous that remains around the testing area. During testing, the fill system will require nitrogen to both purge the system post-test, and to be used to extinguish engine flames. However, nitrogen is not required during a launch.

When testing, the top acrylic panel is replaced with a nitrogen board, that connects to the nitrogen line, as well as connecting the nitrogen vent line to the fill system vent line.

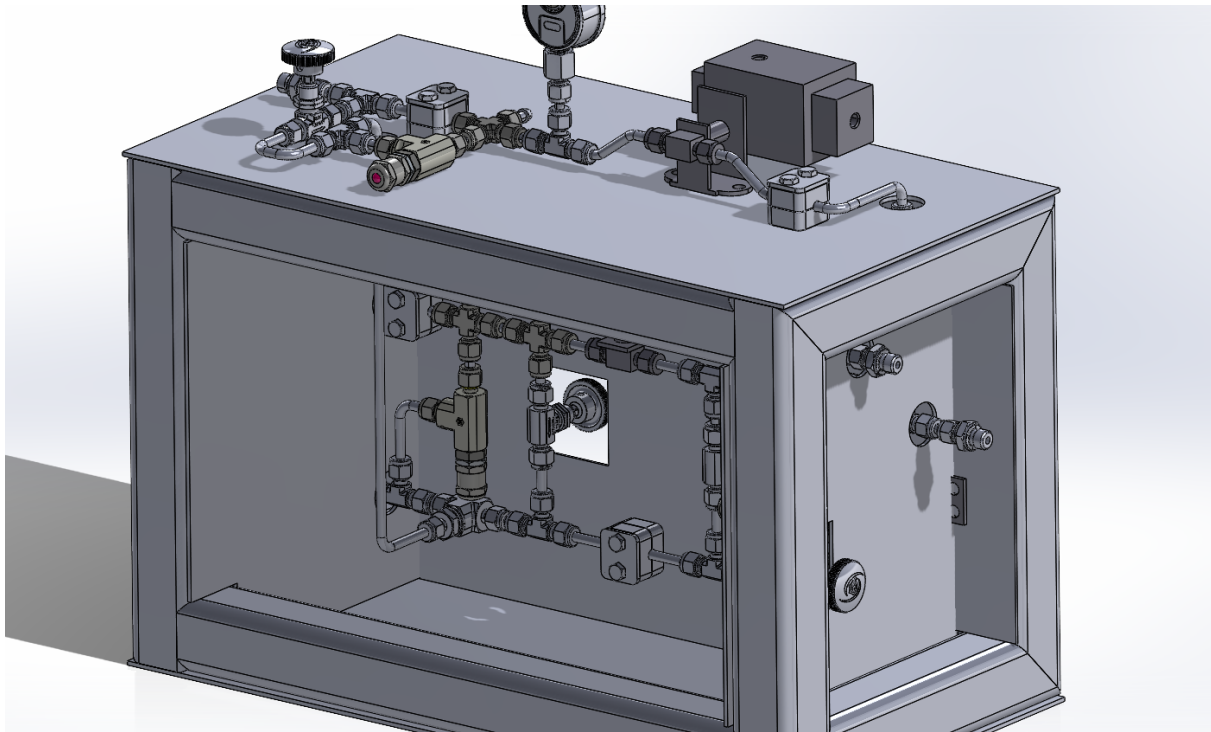


Figure 64: Fill system CAD with nitrogen, angles view highlighting both N₂O and air line.

Interfacing

Rivnuts on everything.

7.3.3 Structure

Instead of having the entire fill system to be assembly onto a large stack, it can be assembled onto multiple stacks of much smaller sizes to increase the compactability factor. An extrusion-based compartment will house the stacks and have wheels attached to the base of the compartment. This lifts the entire fill system compartment above the ground and allows for mobility. The stacks will slide along the aligned slot of the extrusions above and below and then secured in place after accessing them. Assuming dimensions of 300x200x600 mm for the compartment frame and 300 x 200 mm in size, the total length of extrusions, accounting for the wheels and fasteners, would yield a total mass of approximately 20 kg.

7.3.4 Gas Cylinder Storage

A separate housing will be made for the three G-size gas cylinders, one each for nitrogen, nitrous and air. A plate acting as the base of the compartment will allow the cylinders to sit in the housing. Due to the large mass of each cylinder, there is no need for continuous mobility of the cylinders. A steel cage made from welded steel rods and a base plate will allow for the cylinder to be slid into the housing from opening. The cylinders have an approximate diameter and height of 230 mm and 1580 mm respectively, allowing for the design of a compartment with a square cross-section and height roughly spanning 1.5 m from the base of the cylinders. Accounting the wheels, plate and fasteners, the total mass of the housings for all three cylinders will be approximately 20 kg.

Securement

To prevent chances of the stacks from being removed from the compartment, LetLocks can be used to secure them in place. Another alternative is to use long narrow plates or extrusions that locks the stacks in the compartment. This method will require the use of fasteners such as T nuts and bolts in order to work.

For the gas cylinders, simply one side of the housing will be extrusion-free for each gas cylinder, allowing for easier installation of the cylinders into the housing. The extrusions that were intended to be on that open side will then be secured back in place to keep the cylinders from falling out.

Load Cell

Siemens SIWAREX WL260 SP-S AA compression load cells will be under each of the gas cylinders to ensure that the mass of gas in the cylinders is known. Single point design load cells will be used due to their simplicity and lower cost.

7.3.5 Temperature Regulation

After considering both active and passive methods of cooling, a passive cooling jacket would seem like the most suitable option for maintaining internal cylinder temperatures. This reduces the reliance on an electrical source which is highly restricted in SAC to non-generator-based sources. A CO₂ cylinder dedicated to making dry ice can be supplied. Powder-like dry ice made can then be placed inside the cooling jacket, in contact with the cylinder, and cool it down hours before launch.

7.3.6 Transport and Assembly

Since the compartments take up a considerable amount of space, they need to be disassembled for transportation. Both the fill system and gas cylinder compartments can be disassembled into single extrusions and parts, grouping the parts of each compartment separately as to not mix them up.

There are two approaches when it comes to the fill system on the stacks. The first approach is to have the entire fill system in an assembled state on the stacks except for any tubing or parts between the stacks. This reduces the time needed for setting up the fill system, although at the cost of a more delicate system during transport. Parts that are sensitive to impurities and require connections made in clean environments will not be subjected to harsher conditions on field as there will be access to more equipment to deal with any contamination. The other approach is to have the fill system off the stack and disassembled into individual or joined parts. While this will consume more time for assembly, this allows the parts to be stored in safer containers for transport. By having the more sensitive connections between parts already joined together, this reduces risks of contamination. Another issue with transporting the stacks with components mounted to them is vibrating these components during transit. These vibrations could damage components and cause leaks in the system.

These concerns demand further evaluation and testing, but currently the easiest and most time-effective method of system transportation is to have the housing disassembled, but transport each stack assembled. This will save time, and reduce the risk of contamination, as well as avoiding having to assemble on launch day which runs the risk of having several system leaks. Concerns involving vibration can be mitigated by transportation method, by storing the stacks in foam or another viable material.

7.4 Quick Disconnect Umbilical Arm

The Quick Disconnect Umbilical Arm ("QD Arm") remotely and automatically disconnects the fill system from the rocket prior to launch. Such an apparatus is necessary to comply with a 600 meter exclusion radius around filled rockets imposed by Spaceport America Cup regulations.

7.4.1 Design Overview

The load bearing components of the QD Arm consist entirely of COTS components while the end effector is SRAD. From base to tip, the QD Arm consists of a truss clamp, a swing mechanism, two arm elements, and an end effector as primary subassemblies. A primary design consideration has been for adjustability using variable angle connectors and adjustable positions. This allows for an optimal pose to be set based on the current conditions. There exist alternative designs for a Quick Disconnect system, however the design and layout of SRAD components used on the Pardalote rocket presents many difficulties. Specifically, the position and orientation of the quick disconnect male connector inside the SRAD Pardalote tank would cause interference with the rocket fins for many designs. Thus, an arm design is favorable.

Truss clamp. The truss clamp assembly contains two truss clamps and a section of 4040-lite aluminum extrusion. The clamps firmly attach the extrusion to the truss at a position and angle that can be easily changed during assembly of the ground support equipment. This allows a great deal of flexibility and versatility independent of changes to other systems. The clamps are rated to 100kg, which exceeds the reasonable expectation for mass of QD Arm design, thus they are suitable to support the QD Arm.

Swing mechanism. The swing mechanism includes two dynamic pivot joints and a gas spring. Attached to the extrusion of the truss clamp assembly are the parallel pivot joints which provide a connection for the rest of the arm. The parallel pivot joints are described as dynamic, referring to their freedom to change

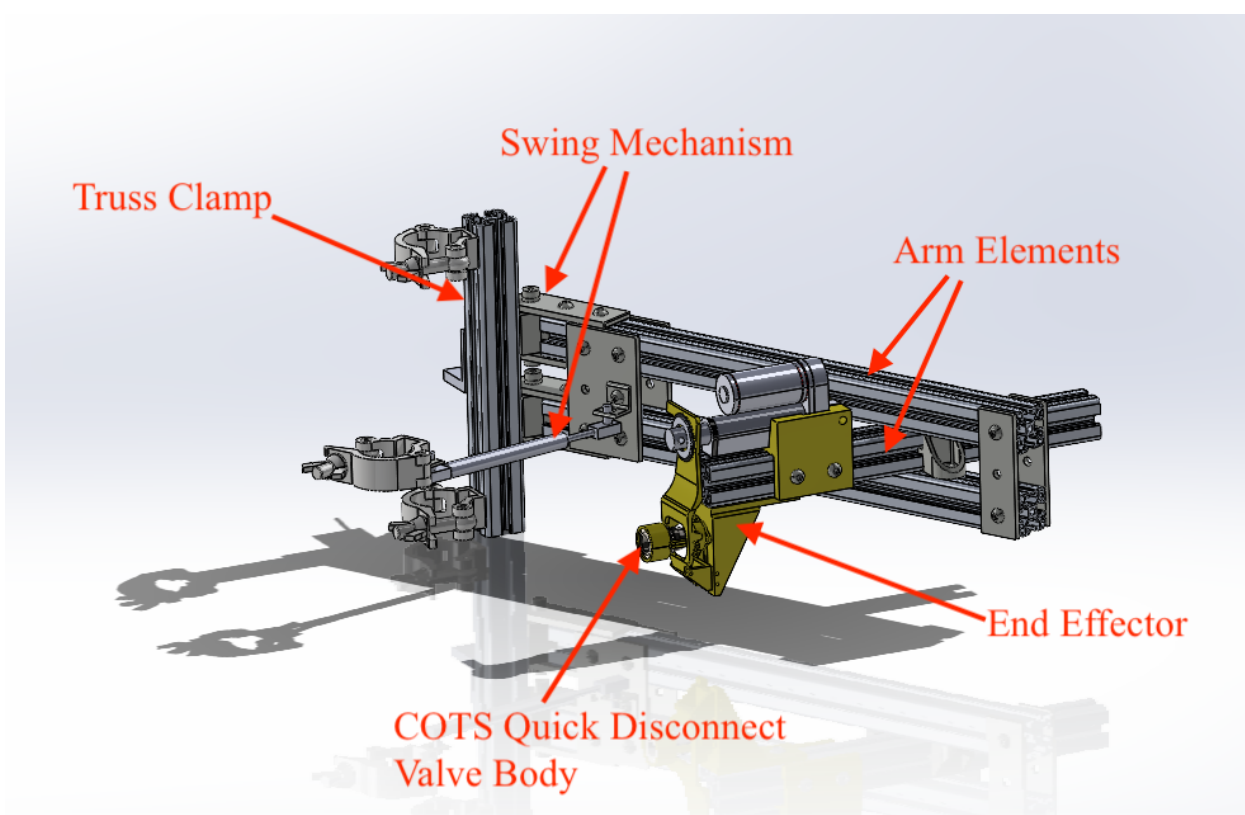


Figure 65: Quick Disconnect Umbilical Arm (shown detached from truss).

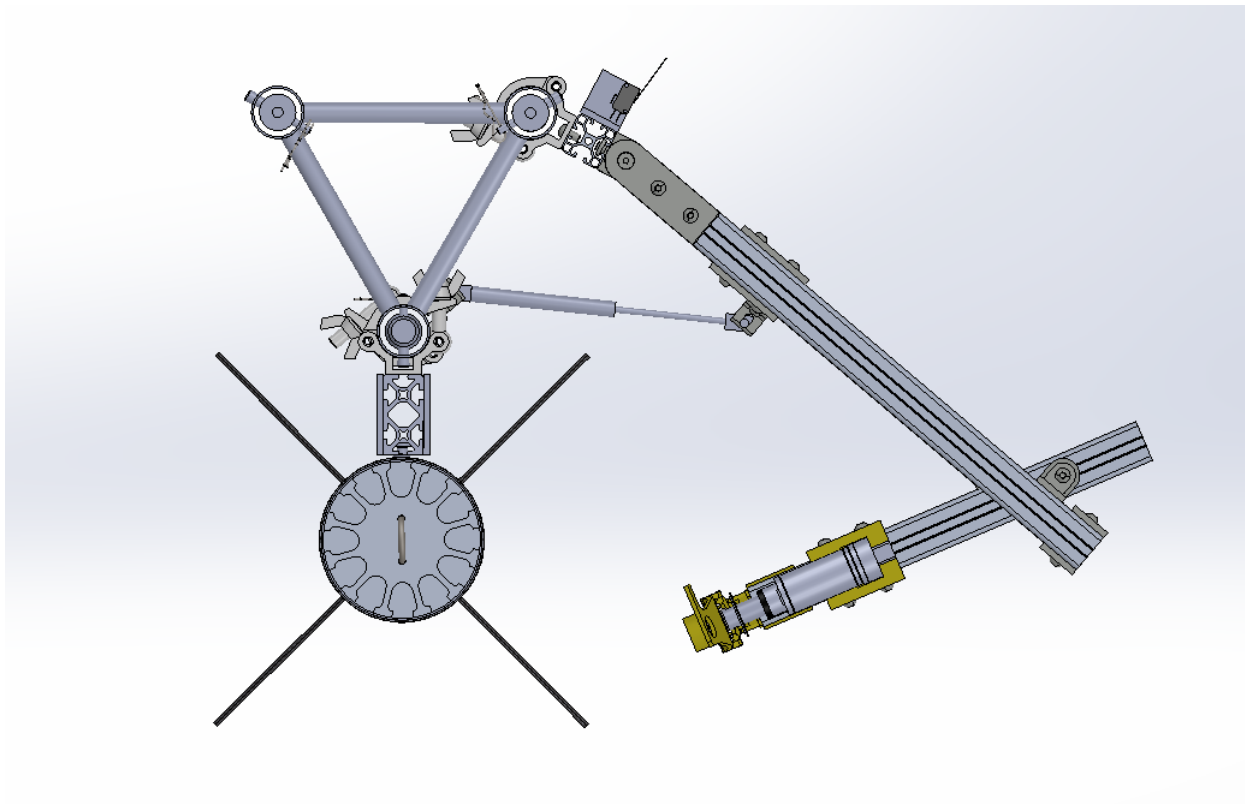


Figure 66: QD Arm gas spring

angle arbitrarily after they have been fixed in position. The pivot joints are used upon activation of the QD Arm to provide the actual "swinging" action that separates the arm from the rocket prior to launch. Two pivot joints are used in parallel to attach to the arm for reasons of stiffness and weight distribution. A single pivot joint was initially tested however issues were identified with the weight of the arm, and friction and stiffness. The dual-pivot design appears to sufficiently avoid these issues. The pivot joints can be freely moved up or down on the truss clamp extrusion to adjust the height of the arm.

A force to enable the "swinging" action of the arm is provided by a gas spring attached between the launch rail truss and the proximal arm element (see section below on arm elements). Several alternatives were considered in the design, such as driving the rotation of the arm using an electric motor and using a hanging weight to pull the arm away from the rocket. The motor design was not chosen as it is possible that the motor would be driven before the quick disconnect valve is completely detached, therefore potentially applying a large force to the internal fluids system of the rocket. The hanging weight was also not chosen as with the current QD Arm geometry there is only a very small moment arm and it is difficult to increase this easily. A gas spring is therefore used as it provides a larger moment arm than other methods considered (such as using a deadweight and spring) and can be purchased with the desired force, length, and other characteristics. The gas spring must apply enough force to separate the end effector from the rocket, and to cause a moment sufficient to swing the arm away from the rocket. Through testing it was found that the QD Arm actuates with a moment of 9.94 Nm applied. With an intended mounting point 0.350m from the pivot point on the arm, the selected gas spring of 80N force is able to provide a moment of 28 Nm, thus there is an acceptable safety factor of 2.8. The length of the gas spring was selected by inspection of the CAD and physical measurement of the assembled arm during testing. A selection of gas springs available for purchase was assessed and a spring with an extended length of 280mm and stroke of 107mm was selected as it is able to fit within the available space when compressed and can actuate the arm suitably clear of the rocket when extended.

Also included in the swing mechanism is a limit switch to verify QD Arm clearance from the rocket at launch time. Although pad box cameras will be used to visually monitor the rocket on the launch rail until launch time, it is desirable to have additional confirmation of clearance based on the actual arm position in case of camera feed failure. The limit switch can be seen near the top right corner of the truss at the top of Figure 66. It is located such that it is triggered when the QD Arm is in a position clear from the rocket, indicating that it is safe to launch.

Arm Elements. The arm elements are named "proximal" and "distal" depending on their mounting position relative to the launch rail truss. The proximal element is connected directly to the dynamic pivot joints. It consists of two parallel aluminium extrusions that are each mounted to separate pivot joints at a specified distance apart. This distance is 40mm, or the height of a 4040 aluminium extrusion. The use of two extrusions is to improve arm stiffness and distribute the weight load of the arm across two joints for improved performance. Mounting brackets are present on each side of the arm and at each end to maintain the correct distance between each extrusion and to improve rigidity. The distal element is connected to the proximal element and holds the end effector on one end. Variable angle clamps are used to hold the proximal and distal elements together and the distal element is effectively "sandwiched" between the two extrusions of the proximal element, preventing rotation of the distal element. The arm elements are set into an optimal pose with the variable angle clamps as the orientation of the distal element as well as its mounting position along the proximal element may be adjusted.

End effector. The end effector performs the physical disconnection of the fuel system from the rocket at time of launch. This is achieved by using an SRAD mechanism to actuate a COTS quick disconnect valve. The COTS valve consists of two paired parts, a plug located inside the rocket and a body located in the QD end effector. The plug is inserted into the body to connect the fill system and to disconnect a "sleeve" on the plug body is pulled back, allowing the two halves to separate and therefore disconnect. The end effector mechanism performs this sleeve actuation. A simple lever mechanism is used for the actuation, which is actuated with an electronic 12V linear actuator. Actuation of the linear actuator is controlled by a LabJack device located externally at the base station. The LabJack supplies a 12V potential to the linear actuator during operation of the arm. The end effector can be seen in figure XYZ.

The end effector includes a limit switch to prevent overactuation of the lever mechanism. The stroke of the linear actuator is longer than the actuation distance of the lever arm, therefore there is a risk that the linear actuator will overactuate and damage the lever arm. The hardware limit switch is used to electrically disconnect the linear actuator from the supplied power to prevent actuation beyond the intended stopping point.

Table 33: Quick Disconnect Umbilical Arm Cost Breakdown

Part	Purpose	Quantity	Cost
4040 Lite Extrusion 300mm	Truss clamp	1	XXX
4040 Lite Extrusion 550mm	Arm elements	1	XXX
4040 Lite Extrusion 400mm	Arm elements	1	XXX
Dynamic Pivot Joint	Swing mechanism	2	XXX
Gas Spring	Swing mechanism	1	XXX
Angle Clamp Block	Arm elements	3	XXX
Quick Disconnect Valve	End effector	1	XXX
Linear Actuator	End effector	1	XXX

need to see details about material and manufacturing of the end effector

the acutation time of the linear actuator is something that can be tested and reliably repeated with software, i'm not sure overactuation is something that needs to be overly worried about, especially as it is not flight critical. what is flight critical however, is that the entire arm assembly is clear away from the rocket, so it would be highly benefical to use a limit switch on the angle between the truss clamp assembly and the proximal arm, such that the limit switch being held down for x amount of time could confirm that the entire arm assembly was clear away from the rocket and safe for launch

7.4.2 Operation

As late as reasonably possible prior to launch, the QD Arm shall be "activated", which refers to performing the disconnection and actuation to clear the fill line from the rocket's launch trajectory. The activation process for the QD Arm is as follows.

1. The QD Arm activation button is pushed at the launch controller.
2. 12V is supplied to the linear actuator for a **predetermined length of time**, causing it to actuate.
3. The end effector disconnects the quick disconnect valve from the rocket.
4. The gas spring swings the arm clear of the rocket's launch trajectory.

QD Arm activation is controlled by a button located on the primary control panel at the launch controller. This button is only operated by instruction from the launch director and is only to be operated when specified by official launch preparation checklist.

7.4.3 Cost

The complete cost breakdown of the QD Arm is shown in the following table.

8 Ground Control Subsystem

8.1 System Architecture

8.2 Sensing

8.2.1 Temperature

Type T Mineral Insulated Thermocouples supplied by TCDirect will be used for all in-line temperature measurements. The chosen configuration includes a 1.5 x 150mm probe, a 321 Stainless Steel Sheath and a standard miniature flat pin plug for connection. It has a measurement range of -185-260C.

They will be connected to the fluids system with a 1.5mm x 1/4" Compression Fittings. Threads are available in BSPT or NPT from TCDirect and BSPP from RS Components.

They will be connected to the DAQ system with a standard miniature flat pin thermocouple connector panel.

Surface temperature measurements will be made with Type T Self Adhesive Patch Thermocouples.

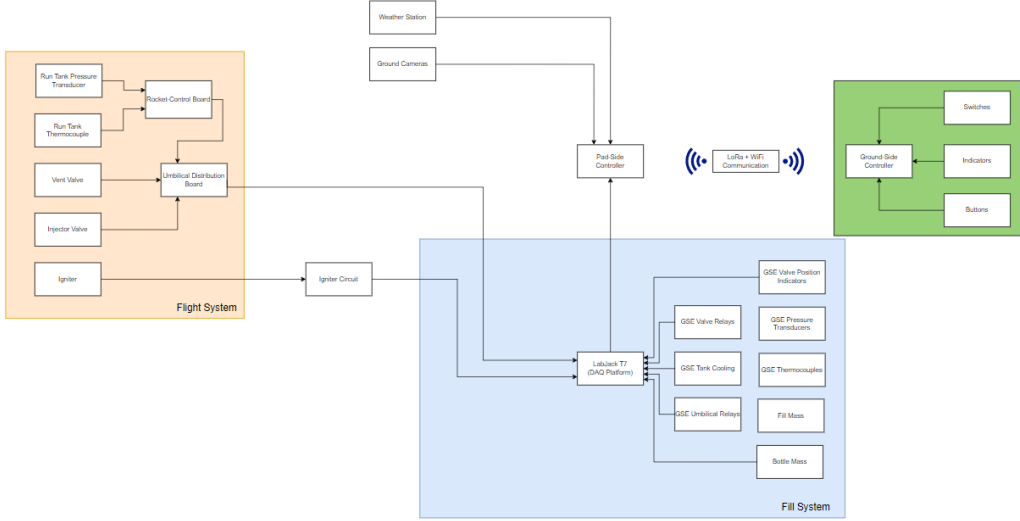


Figure 67: Software Systems Diagram (Simplified)

8.2.2 Pressure

The selected pressure transducer is the ifm PT5402. It's a relative pressure transducer with a nominal measurement range of 0-100bar, and a maximum pressure rating of 250 bar. The compatible medium temperature range is from -40-90C so it is suitable for use within the nitrous fluid lines.

Similarly, the ifm PT5404 (0-10bar) will be used to measure the pressure of the on-board air tank to ensure there is sufficient on-board pressure to actuate the electro-pneumatic ball valves.

Electrical characteristics of these pressure transducers include an operating input voltage of 8.5-36VDC and an analogue output current range of 4-20mA. The decision was made to switch from the previous voltage-based 0-10V output used on Wattle to a 4-20mA current-based output to improve noise over long runs, the ability to diagnose no signal faults and for a simplified two-wire loop wiring solution.

The electrical connector is an A-type M12 circular connector. This will be connected to the Ground Control System with pre-terminated M12-to-M12 jumper cables.

The accompanying process connection is an external G 1/4 thread. This will be sealed with a first-party gasket from ifm (FKM -30-200C/EPDM -40-130C). For compatibility with lower temperatures, it could also be sealed with a -45C PR14/E80 profile ring from Global O-ring and Seal.

8.2.3 Mass

Due to the fill-load-cell being placed on the rocket platform rail where the rocket will compress said load cell while not being perfectly aligned, a single point load cell is preferable resulting in greater flexibility if the design of the launch platform and thus positioning between the rocket and load cell has to change.

The Siemens SIWAREX WL260 SP-S AA Load Cell family has been chosen brand recognition, low price point, 3m default cable length.

It is a family of single-point load cells with a maximum platform size of 400x400mm. They are designed for use as platform scales and come in rated loads of 3,5,10,20,50 and 100kg. They are 6-wire load cells with a characteristic output of $2\pm 0.2 \text{ mV/V}$ and a combined error of $\pm 0.02\%$.

The fill-mass load cell will be the 100kg Siemens 7MH5102-3AD00.

The tank-mass load cell will be the 50kg Siemens 7MH5102-2PD00.

8.2.4 Valve Position Indicators

This will be a COTS part purchased from Pirtek. It is a simple limit switch that produces a digital output that can be read directly by the LabJack.

8.3 Control

8.3.1 Valves & Motors

There will be (x) valves for the Fluids Board, 2 valves on the rocket, 2 umbilical retract motors, and a Igniter for a total of (x) required relays. They will be controlled remotely and connected via the LabJack RB12 Relay Board and Opto22 G4ODC5 Relay Modules. The selected relays are Solid State Relays rated for an output voltage range of 5-60VDC with a supply current of 3A at 45C. Alternatively, the Grayhill 70G-ODC5 are also available with an output voltage range of 3-60VDC and a supply current of 3.5A at 25C.

8.3.2 Igniter

The Igniter circuit serves as a continuity tester designed around an NPN transistor, a resistor, an e-match (Igniter), and an indicator LED. The NPN transistor, such as the BC549CG is used for checking the continuity. The circuit such as shown in the figure 68 is designed using Altium Designer.

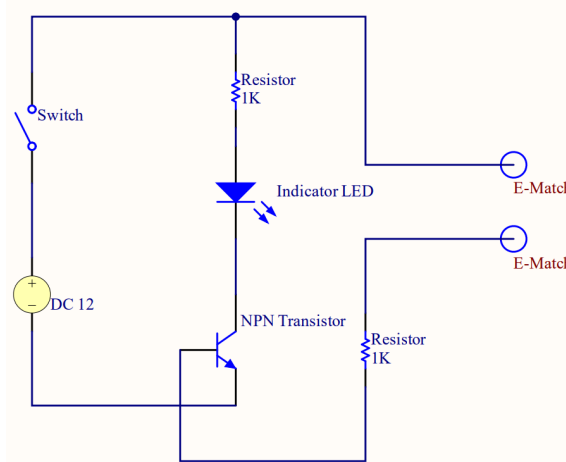


Figure 68: Igniter Circuit Schematic

During the operation of the circuit, when the switch is pressed, the E-Match is powered, enabling current to flow through it. The resistor in conjunction with the e-match forms a voltage divider, and if the E-Match has continuity, the voltage at the base of the NPN transistor becomes sufficient to turn it on, that also turns on the indicating LED.



Figure 69: Igniter Circuit Simulation Values from LTspice

The figure 69 shows the simulation using LTspice, the current that is being passed through the Igniter and the indicating LED, this confirms the continuity of the E-Match. The resistor in that is connected with the E-Match serves a protective function by limiting the current through the e-match, ensuring safety and preventing damage due to excessive current by providing the required voltage.

8.3.3 Umbilical Retract

The Umbilical Retract hardware will be designed by the GSE subsystem and connected/controlled by GC hardware and software. The retract will consist of several motors for both the articulating arm and quick-disconnect valve that can be driven either by two relays on the relay board in a H-Bridge configuration or

through communication with an external motor controller board via I2C/SPI/UART which are all officially supported protocols by LabJack.

The linear actuators used by the GSE retract mechanism are electrically specified to be 12V (x)A. They will be connected to the Ground Control system in an identical manner to the ball valves via the LabJack RB12 Relay Board and a singular Relay Module. This will limit the actuators to uni-directional movement unless two relays are used per actuator. Thus upon initial insertion of the retract, the coil of the linear actuator must be de-energised before being later armed for retract.

A fly-back diode will also be connected to the linear actuator to prevent damage to the relay modules. This will be done within the pad-side Ground Control box by connecting a diode in parallel to the connector via a Component Terminal Block.

8.4 Data Acquisition

8.4.1 DAQ System

The DAQ System used will be a single LabJack T7 in conjunction with several first-party add-on boards. This was decided with the justification that the team had used this system prior on Wattle and thus was familiar with it and had the capability to iteratively test software without purchasing new hardware. Additionally, the price to performance for this solution is significantly better than the next best competitor.

The following add-on boards will be used.

- RB12 Relay Board
- CB37 Terminal Board
- LJTICK-InAmp
- LJTICK-CurrentShunt

ADC Bandwidth The LabJack T7 has the capability to conduct measurements in command-response mode at varying Resolution Indexes. By adjusting the Resolution Index we form a trade-off between the Effective Resolution of our measurements and the sample time it takes for each measurement. Where generally, as you require greater resolution and/or gain per sample, the sample time increases.

For the Load Cell's, our minimum required measurement resolution is calculated to be $201\mu V$ and thus with a resolution index setting of 4 (equal to an Effective Resolution of $112\mu V$) we have a sample time of 0.09ms/sample.

For the Pressure Transducers, our minimum required measurement resolution is calculated to be $9.45mV$ and thus can be resolved with the minimum resolution index of 1 (equal to an Effective Resolution of $316\mu V$).

Assuming we utilize the higher of the two required resolution indexes (4), have a USB overhead of 0.7ms, and a total of 5 sensors. We can then calculate to have a total Command-Response Time of 1.15ms. This results in a sample speed of 173Hz for each of the 5 sensors. Under the Nyquist criterion this should allow for us to characterize any frequency dependent event at 87Hz or lower.

$$CRT(ms) = \text{overhead} + (\#AINs \times \text{AIN Sample Time})$$

$$\begin{aligned} & 0.002 * 2.5 * 0.0002 * 201 \\ & (2.36 - 0.47) * 0.005 \end{aligned}$$

8.4.2 Signal Conditioning

The LJTICK-InAmp is a first-party add-on board that combines an Analog Devices AD623 Instrumentation Amplifier with a LT1461 2.5V Voltage Reference. This allows it to take differential measurements with a maximum configured gain of 201 (although higher gains can be achieved with custom resistor combinations) and a highly stable voltage reference for ratio-metric sensors. We plan on using this board to connect both load cells to the LabJack. Although the LabJack T7 has a more accurate built-in InAmp, the acquisition speed in Command-Response mode decreases substantially when the gain is set to be greater than 1. Thus a per-channel amplification solution will be used instead.

The LJTick-CurrentShunt will be used to convert the 4-20mA current loop signal into a 0.47-2.36V output to be read by the LabJack. Alternatively, a precision 250Ω resistor on a custom PCB could also be used to save on cost (\$65 per unit for the LJTick-CurrentShunt).

The 4-20mA current loop signal will be converted to a 0-10V output with a custom PCB. This PCB will include a low-dropout regulator (LDO) to help minimise the switching noise from the upstream switching power supply. The output of this supply is then used to drive the sensor before being shunted by a 500Ω resistor. By measuring the voltage drop across the resistor we can expect a corresponding linear output range of 2-10V using Ohm's Law. This is within the LabJack typical input range of -10.6 to 10.1V.

8.5 Power

On-Ground Power will be delivered by a 120/240V COTS

The sensors and valves will be powered off independent 24V power supplies to reduce the effect of switching noise from the solenoids.

8.5.1 Electrical Umbilical

There will be two electrical umbilicals connected to the rocket upon take-off and disconnecting due to vertical force upon the rocket leaving the rail. This cable will be

8.6 On-Board Logging

8.7 Ground Controller

8.7.1 Hardware

8.7.2 Interactive

Similar to Wattle, the Pardalote Launch Controller will utilize solely industry standard 22mm Panel Mount Push Buttons and Key Switches where possible. A combination of Push Buttons and Key Switches will be used to control all ground procedures safely including but not limited to filling, arming, and launching.

edit: All key switches on the Ground Controller shall be randomly keyed and retaining. In situations where procedural safety requirements dictate that two independent keys should always be together they will be connected with a suitable metal keyring. For example, the pad-side GSE system should never be able to be disarmed/armed while the ground controller GSE keyswitch is armed, thus by connecting these two keys and ensuring the ground controller has a retaining key switch we can ensure that this will not happen.

8.8 Fail-safe

(With the intentional avoidance of the usage of the word "Emergency Stop/E-Stop".)

The GC system must ensure that all systems fail into a safely approachable state (PL-R-GRC-2.1). Under the IREC DTEG the failsafe mechanism shall provide automatic venting of oxidiser in the even of power or communication loss during fill. For the first case - the loss of power - the GC system will automatically vent due to the normally-open specification of all ball valves within the GSE system. For the second case, we intend to implement a software (xxx ??) solution.

In the case of unrecoverable software/kernel faults or hardware issues there is also an in-built hardware watchdog timer on the Raspberry Pi. This will be enabled and set to the maximum time length of 15 seconds. After this time, the Raspberry Pi will reboot and initialise all software back to its default "safe" state.

8.9 Software and Communication

The software component of the DAQ system will follow the following requirements.

There must be software on both the pad and mission control hardware units, each must be homogenous higher-order units. They must share a common core library and be individually exportable, with the mission control providing a web socket export service which can be consumed by any listener.

The software will only be featured on the pad and control,

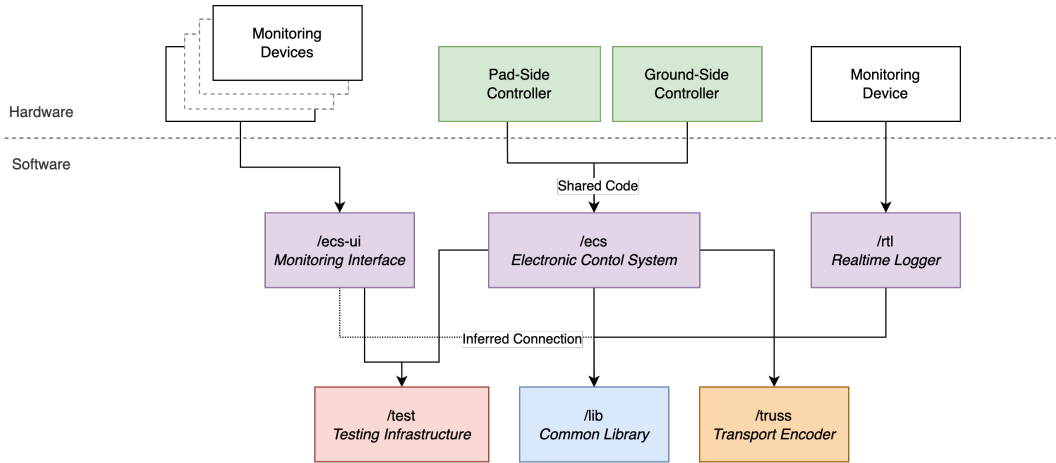


Figure 70: Software Systems Diagram (Simplified)

Location	Export Services	Hardware Devices	Injections	Chip
Station-Centered	WS, Split & Aggregate CSV	Pad_LORA, Cameras_WIFI	Buttons	RP2040
Pad-Centered	Split & Aggregate CSV	LJM Binding	LoRA	RP2040

Table 34: Device Table

Above, we see the following;

Agnostic Components

- Both will be compiled to the same platform
- Both shall be placed in different physical locations, with variable functionality
- Both have a generic data export system
- Both have bindings to hardware devices
- Both have interactive device functionality.

Variant Components

- Station (Mission-Control) software will be listening to a LoRA signal over SPI, whilst the Pad software listens to the LabJack components through our open-source binding, ljm-rs.
- The Pad software will listen to LoRA emulated buttons, not physical GPIO pins seen on the Station software.

Structure

The control systems are structured as seen in 73. Of which, as seen in 70, both controllers (in green), share a common code segment. As they both require the same tick-based control system. The software practices into both are as such.

Both control units follow a ‘driver-based’ approach to device I/O. Such that, the ground-side controller is running the same code to read a sensor as the pad-side controller, just with different drivers. This is generic upon both actionable items (i.e. Relays), and observable items (i.e. Sensors).

This is formatted as follows:

```
struct SensorModule<SensorType, SensorReading>;
struct RelayModule<RelayType, RelayReading>;
```

These fall under **layers 3 and 4** of figure 71. They are separate implementations of the generic module driver.

For something to be readable, writable or both, it must implement the highest-generic ‘Interface’ (alias. Driver) trait. This is a trait implemented by both the Sensor Module and Relay Module. It lives adjacent to the Generic Module Driver.

Furthermore, all sensors are laid out at compile time. This means, we have a static relationship between a key (representing the item's placement in hardware), and a 'StaticItem', such as a Static Sensor or Static Relay.

A static item is one without **Hydration**. This means, after compiling, we have the sensors in program memory, as a static representation of how to obtain our sensor, what we can do with it, and special properties pertaining to its variant, i.e. units of measurements, conversions, etc.

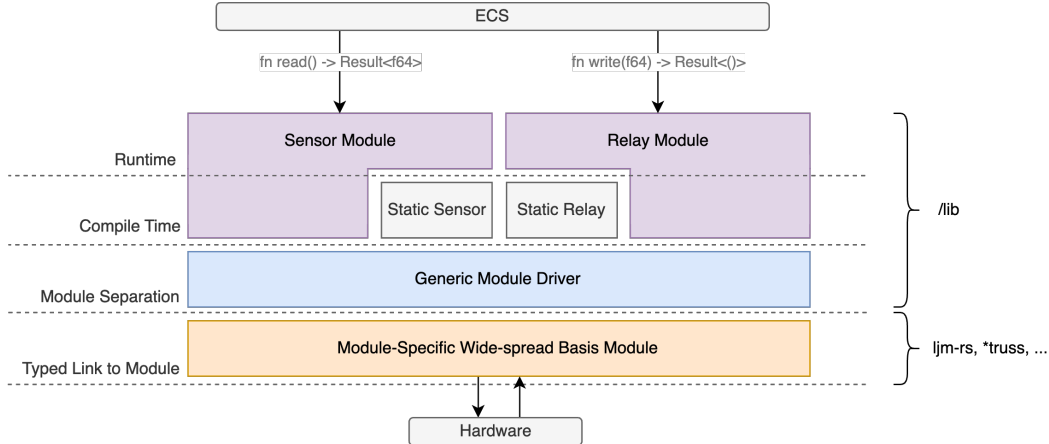


Figure 71: Driver Diagram (Simplified)

This can be seen above, as the 'Static Sensor' and 'Static Relay' modules. They live at level 3, inside the '/lib' folder. They have an associated driver which lives at the same level, which it becomes absorbed by the module parent at runtime, as it converts into a working sensor/relay.

At level 2, we have the **Generic Module Driver**, an example of one can be seen in DAQ, as the **LabJackModule <T,F>**. This is a generic module implementation (binding / driver), which stores items specific to its lower level basis module.

For LabJack, these include but are not limited to: *ModbusName*, *ModbusAddress*, *ModbusResolution*, *HandleID*, *ModuleType*, ...

Thus, this becomes extendable, as we can swap the generic module driver, on a per-item basis.

The lowest level, **level 1**, contains the code for the item itself. For example, our labjack driver, 'ljm-rs', contains a series of Rust-to-C bindings for all LJM functions we require. This component simply provides a uniform and typed way to write our generic module driver from.

System Architecture

The system is structured as seen in 72. We can see that 'ecs' (the controller software) is split into three main subsystems. The first is the input thread. This is a separate thread, forked off of the main thread which handles reading from hardware devices through primarily GPIO, the current use-case, these are read from the Raspberry Pi - where we utilise the rppal crate to read from the buttons and arming switches. These share a state mutex, so they can invoke 'Core Tasks' as seen in the scheduler subsystem.

The second being our system thread. This handles data ingest and exporting. Primarily, we collect through our collector which manages the driver crates such as 'ljmrs', in order to collect data from the LabJacks.

In exporting, we have two primary export types, these are entirely generic and so other methods can be added in the future if necessary.

The first being CSV, this is an export service which saves data locally to the device, and is the primary source of truth for data that is later stored and sent to other teams for post-run analysis.

The other being over WebSocket. Such that any listening device can listen over the network by establishing itself as a WebSocket peer, upon doing so it'll receive real-time data on the systems sensors. This is the data that is received by monitoring devices in 73 under the 'WebSocket' label.

The last thread is our primary, or main thread, which handles our scheduler. This handles our priority queue for tasks. This is not a standard, weighted task queue but simply does not execute an ephemeral

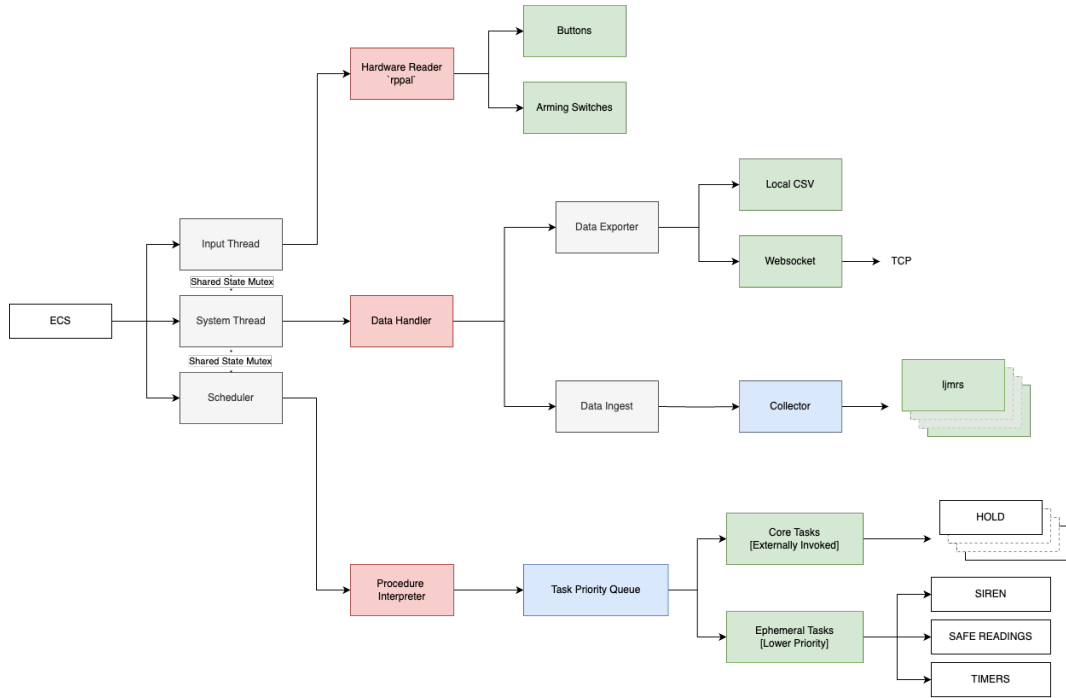


Figure 72: ECS Systems Diagram (Simplified)

task if there is a core task available, and will execute the core task instead, as the priority of a core task is infinitely higher than an ephemeral task.

An ephemeral task is one which handles something non-critical or long-running about the system. For example, the ‘SIREN’ task handles turning on and off the siren based on the arming state of the system. This means we do not have to hard-code such behaviour in the other parts of the system, and thus makes it a very easily modifiable and manageable attribute.

Similarly to the siren task, the timer task handles starting and stopping automated timers, which indicate how long the system has been in a particular state. For example, when a line is pressurised, the task will handle starting the timer for the pressurisation as long as it meets certain conditions, such as being at an elevated state for multiple ticks, then providing the start time of when it first entered the elevated state, and thus this timer can be shown visually on the GUI.

Network Transport

As seen in 73, the network setup follows a two staged approach, with the use of Wi-Fi (TCP over Wi-Fi signal) for non-critical components that are of no importance to the operation of the rocket critically. All critical components are routed under a custom, SAC compliant LoRa signal. This is operated through a firmware layer on both the ground and pad side controllers, utilising homogenous receivers, communicated internally through the SPI protocol. More about the signal at 8.9.

In order to maximise both security and simplicity, the design features a uni-composite signal structure, meaning each direction carries **only one type of signal**. This being, the ground side controller is only permitted to send commands to the pad-side controller, and the pad controller only data to the ground station.

Control

Control is structured in the following way as to completely minimise the risk of actions occurring that are not supposed to do so.

This means, we must parse our own program and validate it. As a result this warrants the implementation of an interpreter. Such that there are a series of fixed commands, for example, in our ‘fire’ procedure we have a procedure structure like the following simplified code.

```
fn spawn(&self) -> VecDeque<ProcedureItem> {
    let mut vec = VecDeque::new();
```

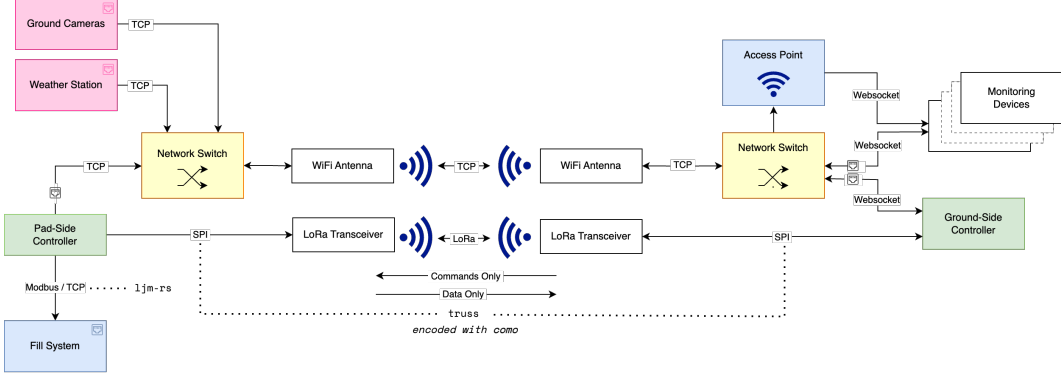


Figure 73: Control Systems Diagram (Simplified)

```
// ...
// Open E-Match 1
vec.push_back(ProcedureItem::Action(open_match!("em1")));

// Wait 3s.
vec.push_back(ProcedureItem::Condition(
    ProcedureConditional::DurationPassed(3_000),
));

// Close E-Match 1
vec.push_back(ProcedureItem::Action(close_match!("em1")));
// ...

}
```

Most notably, a procedure is not executed in-line but rather **described** inline, and executed out-of-line. This means we do not have a repeatability fault, where code is not written the same way, as we know that if we can test the ‘DurationPassed’ sub-condition, then every time it is used, it will behave the same way.

As an added benefit, we can employ grammar rulings to specify our procedures, and convert these grammar rulings into a specified vector of procedure items as seen above, without having to write a scripting and interpreting language for that as well.

Thus, it provides us with a solid middle ground, giving us enough flexibility to make procedures as detailed as we need, without relying on the quality of code used to describe the procedure.

Signal / Communication

The signal is encoded under the ‘como’ format, abbreviated for the COntrol MOdule protocol. It features a 3 byte header length addition, security through AES encryption, auto-reconnection support, packet segmentation and acknowledgement support. This protocol is intended to be lightweight, to provide minimal overhead in sending messages, whilst allowing for redundancy checks, packet identification, segmentation, and minor security in the event of malicious intent.

This encoding method is going to run on **truss**. It will encode the structure into a bitfield of undecided format. This bitfield is to be sent over the intended format of transmission. Most likely, through an SPI lane from the controlling device, to a LoRA transmission module, which will be picked up by a LoRA transceiver on the other end, which will be similarly decoded into a packet object and handled by **truss**. For reference, in the current implementation, the RFM95 module has a corresponding low-level driver implemented through our proprietary ‘rmf9x-rs’ module, which abstracts the hardware into simpler methods for use by **truss**.

COTS/SRAD Selections

Computational components selected are commercial. Such that no high-speed hardware has been developed internally.

The selected microcontrollers to be running this software stack are two identical Raspberry Pi 4’s. The connection diagram for these to other system components can be found in 73.

Visualisation

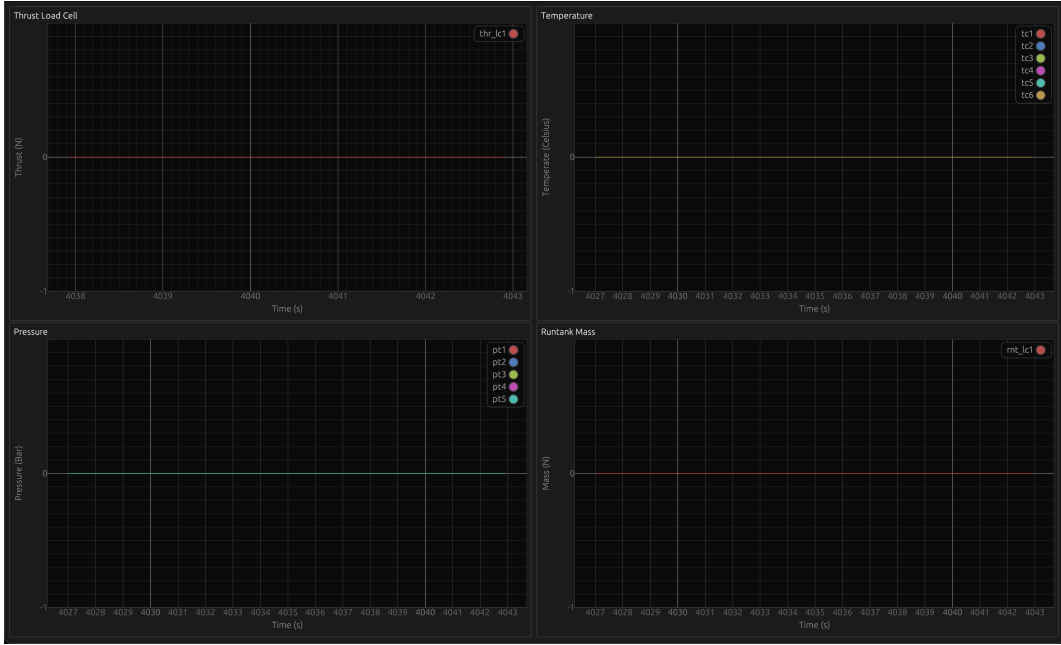


Figure 74: Real-time Systems Logger

Visualisation of components is a critical requirement for a high-functioning data acquisition software.

This comes in the form of two components.

- Control Systems Interface
- Real-time Logging

Both the CSI, outlined in 75, and seen as code in `/visuals/ecs-ui`, and the RTL, outlined in 74, seen in `/visuals/rtl` are designed to be realtime, concurrent systems that outline the systems' state at any point in time.

A valid point of argument may arise as to the reasoning behind two individual systems to log information. The reasons are three-fold.

- **Expansion and Knowledge**

By building two, individual systems, we can understand the standpoint of a simpler yet higher-performance native desktop application of `rtl`, needing little in the way of development but with a highly-extendable interface to userapp `ecs-ui`, and `ecs-ui` itself, as a quick and easy yet clean and easy-to-read interface.

Thus, we have the ability to grow `rtl` to meet our needs, whilst having `ecs-ui` as a standpoint for members unfamiliar with the low-level nature of `rtl`, an easier window into DAQ software design.

- **Robustness**

By having two systems, we eliminate one failure mode, that of `blind-failure`, where a single point of visibility into a system can result in an unknown failure position, as if one UI was to go down, the other would still report the current reported values, such that if both go down it is with almost absolute certainty that we know the hardware itself has failed, and not a UI component.

- **Performance**

By splitting the components apart, each platform can focus on their task solely. This increases the level of performance, particularly due to the approach taken. The Web-based system is event-driven, and so will update less frequently, holding against repainting when values haven't changed. This enables the application to run well on lower-end hardware, such as team-members viewing the application during a launch. Where `rtl` does between 60 and 120 repaints per second, thus achieving no paint-delay, but suffering from a higher performance hit.

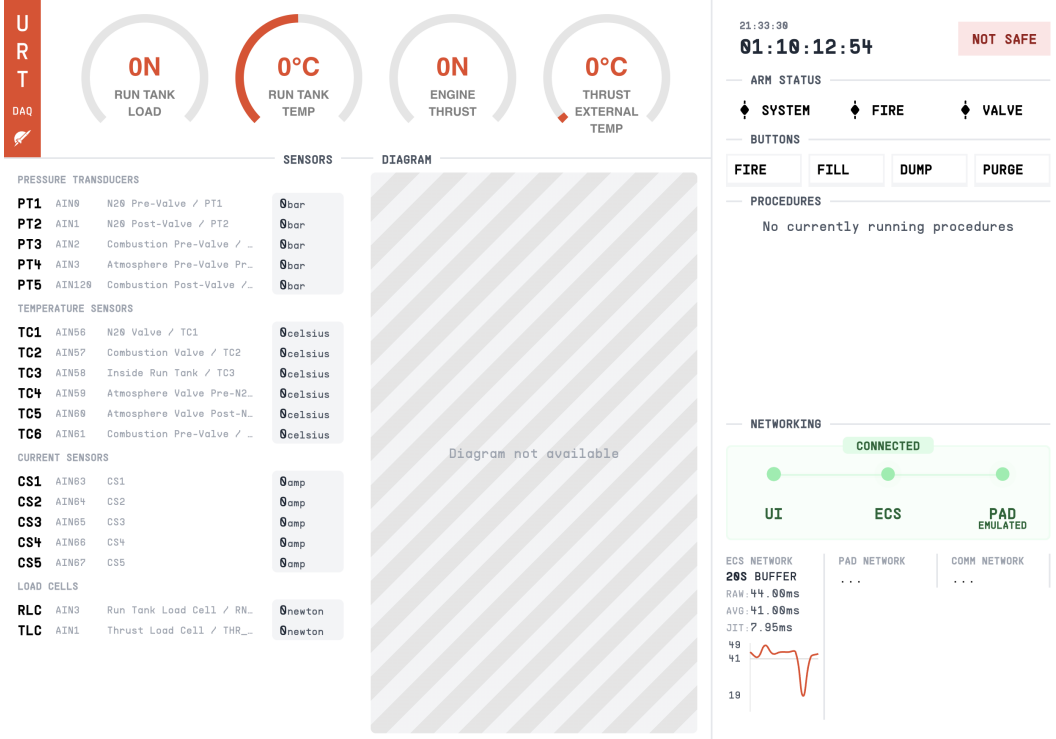


Figure 75: Control-Systems Interface

9 Aerostructures Subsystem

9.1 Structure overview

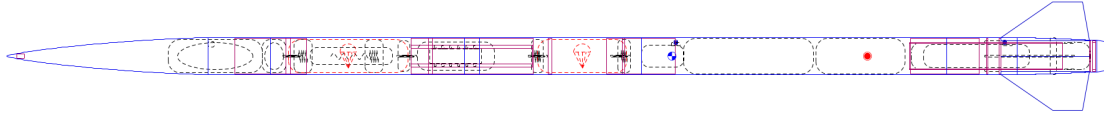


Figure 76: Openrocket diagram of Pardalote.

Pardalote's configuration is a center, dual separation recovery vehicle housing the payload bay in the nosecone. This configuration was chosen over a top deployment launch vehicle as it avoids a bulkhead with an epoxied nose cone. Incorporating an epoxy joint decreases both the ease of maintenance and testing of the structure (PL-R-SYS-8.1,8.2). The payload bulkhead also acts as the nose cone attachment for the shock cord. The airframe of Pardalote will be a mixture of carbon fibre and fibre glass. This means that the airframe is Radio Frequency (RF) transparent, which allows greater flexibility when incorporating telemetry systems and live video feed. The oxidiser tank and combustion chamber are connected via a truss frame that allows the entire propulsion system to be integrated external to the airframe to reduce integration complexity. The airframe design is shown in Figure 76.

9.2 Nose cone and boat tail

9.2.1 Nose cone

The nose cone is a Von Karman profile with a 5.5 fineness ratio. This was chosen primarily since the mold was manufactured for Rosella, and thus the re-use of it saves significant costs. The nose tip will be manufactured from Al-6061 T6 with an internal retaining bulkhead, a design which has been used extensively by URT on previous projects (Figure 77).

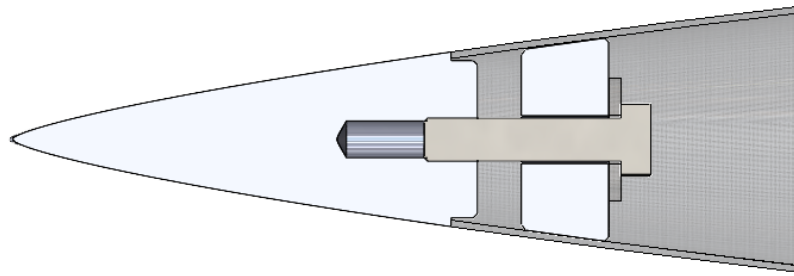


Figure 77: Nose tip and retention bulkhead.

9.2.2 Boat tail

The aft of the airframe can be tapered to reduce the diameter at the base of the airframe. This is beneficial by reducing wake drag. The boat tail will be made using the same profile as the nose cone, but reversed and cut shorter, with the reduced diameter of the boat tail composite as 135mm, which was chosen as the minimum diameter that could accommodate a 120mm chamber diameter and additional hardware to secure the endcap, as outlined below. The apogee gain achieved by incorporating a boat tail is approximately 800 ft compared to a straight-cut end.

The boat tail taper achieved by the composite airframe can be further extended through the addition of an endcap. The benefits include: reduced cross sectional area to reduce base drag; provide protection for composite airframe and nozzle upon landing; and to serve as a redundant aft retainer for the combustion chamber. However, the disadvantage is that simulation accuracy is reduced since the recessed cavity ‘behind’ the endcap cannot be modelled by the Openrocket simulation software. To determine the magnitude of drag reduction offered by an endcap, literature was consulted and CFD studies performed.

At low subsonic speeds, the greatest reduction in wake drag occurs at taper angle of about 19 degrees (Figure 78). However, in practice, angles greater than 9-10 degrees can result in drastic increases in drag resulting from flow separation at sharper angles [20]. Further, a tube diameter to boat tail diameter ratio greater than 0.85 delivers negligible drag reduction [25]. The optimal boat tail for subsonic travel is approximately a 0.85 diameter ratio and 1.2 length/diameter ratio (Figure 78). A common issue with a boat tail is that they shift the center of pressure forward resulting in reduced stability. However, the airframe length of this design is sufficient that this does not pose a significant concern, in fact, it is desirable since the length of Pardalote is such that over-stability is a major concern.

9.2.3 End cap

To determine the geometry of the boattail endcap, CFD was used to quantify the drag reduction benefits of different designs. The CFD was of a 2D cross section of the boattail from the leading edge of the fins afterwards, and the fins were ignored. To properly compare results, the drag without an endcap was first calculated as a baseline to compare with designs, to determine the effect of the endcap itself. Four designs were considered: one with a taper angle of 3.6 degrees which is tangential to the boat tail; and one with an 8 degree taper (so 4.4 degree sharp transition angle at the endcap-boat tail interface); and both of these with both deep (30mm) and shallow (15mm) recesses. The results of the CFD are presented in Table 35, along side the total vehicle drag derived from Openrocket (ORK). The percentage drag reduction afforded by an endcap is shown in Figure 80.

Based on the results from the CFD analysis, an endcap with a taper angle of 8 degrees and a deep recess has been chosen due to its highest percentage drag reduction compared to other designs for Mach 0.3 to 0.9, with a 7-9% reduction in drag force across the entire flight regime of Pardalote.

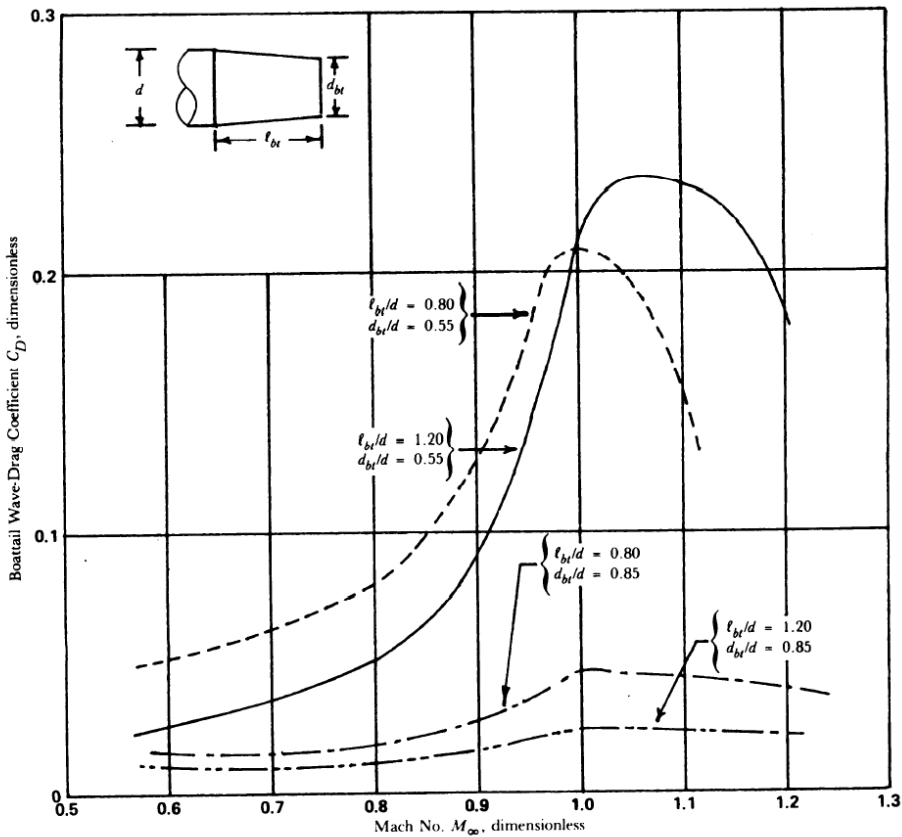


Figure 5-121. Subsonic/Transonic Boattail Wave Drag vs Mach Number for Various Length-to-Diameter Ratios (Ref. 81)

Figure 78: Boat tail wave drag vs Mach number for various length/diameter ratios [9]

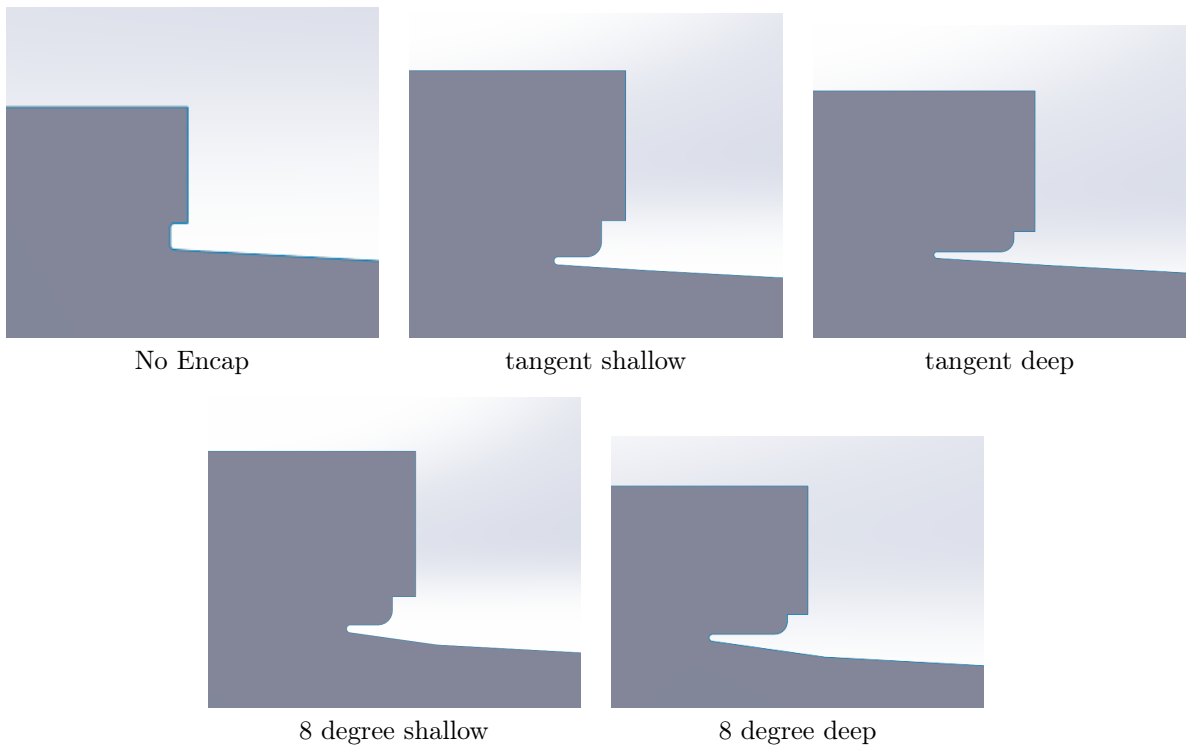


Figure 79: Different endcap geometry for CFD study.

Mach Num	Drag Force (N)					
	Total vehicle drag ORK data	Boattail drag	CFD data			
		No Endcap	8° deep	3.6° deep	8° shallow	3.6° shallow
0.3	42.88	-17.036	-13.819	-17.490	-14.504	-16.593
0.5	114.76	-49.426	-37.114	-47.959	-39.129	-45.214
0.7	224.08	-90.185	-70.961	-94.462	-74.964	-88.070
0.9	418.00	-154.14	-118.07	-168.97	-124.62	-150.44

Table 35: Boattail drag force for varying endcap taper angles and recess depths from CFD analysis.

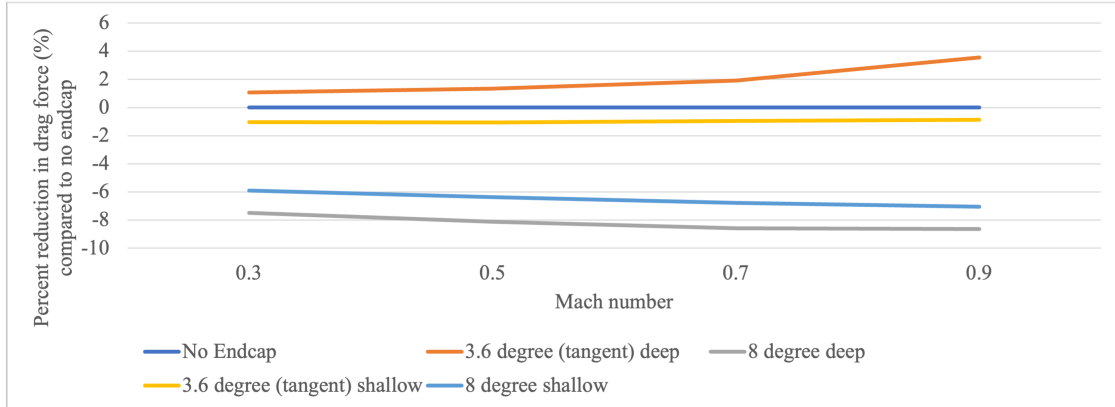


Figure 80: Percentage drag reduction of different endcap taper angles.

9.2.4 Integration design

The composite boat tail will taper from 155mm to 135mm OD over 268mm length, and the endcap will further taper to 120mm diameter. Due to the constraints imposed by the combustion chamber position, the endcap cannot be secured to the airframe by countersunk M3 screws through the airframe and into an aluminium ring bonded to the boattail. Instead, the endcap will have 6 screws, that align with the length of the rocket, that attach it to the aluminium retaining ring bonded into the boattail. Figure 81 shows the assembled boattail endcap.

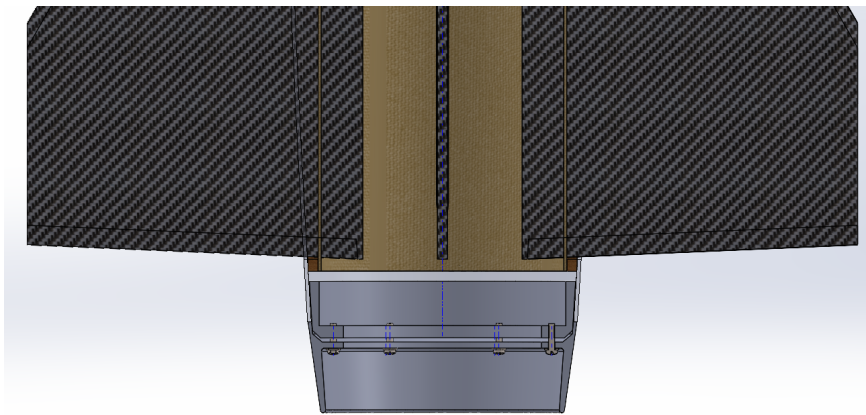


Figure 81: Boattail CAD crosssection

The boat tail will slide over the combustion chamber through the inclusion of a internal tube to align with the chamber (Figure 82). This tube is nominally non-structural. There was consideration towards using a fiberglass composite tube manufactured by the team, however the glass-transition-temperature of Ampreg-31 epoxy used to manufacture the tube is 59 degrees Celsius, so it is essential for the external surface of the combustion chamber to remain below this temperature. Since this couldn't be ensured at that stage, the use of high temperature resistant phenolic resins was considered as an alternative. This raised concerning risks, as they typically have a class 1 chemical hazard classification (GHS) for carcinogenicity, specific

organ toxicity; and class 2 GHS for skin and eye irritation, and reproductive damage. For these reasons, it was decided that phenolic resins would not be used. The final chosen design is to use a commercially sourced paper phenolic tube with an ID of 120.60 mm and a wall thickness of 1.7 mm. The wall thickness was conservatively chosen by comparing with commercial paper phenolic motor alignment tubes, which typically have wall thickness between 1.2 and 1.6 mm.

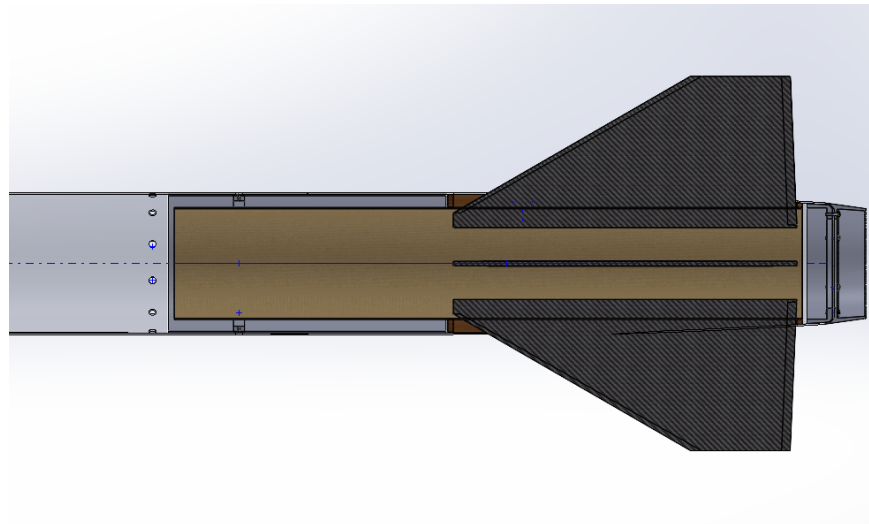


Figure 82: Aft airframe CAD crosssection

9.3 Body Tubes

There are 3 main body tubes in the Pardalote airframe: forward; center; and aft (Figure 76). The forward tube is located between the nose cone and the AV bay, and is used to house the main parachute. Near the forward edge of the tube are two 12.5 mm diameter holes for the onboard cameras. The center tube is located aft of the AV bay and couples to the aft tube above the tank. From here, the aft tube runs the length of the tank and connects to the boattail.

A major consideration was how the body tubes would be coupled around the run tank. Several possible configurations were considered, as shown in Figure 83 and Figure 84, where blue indicates internal components, black is body tubes, and yellow is coupler tubes.

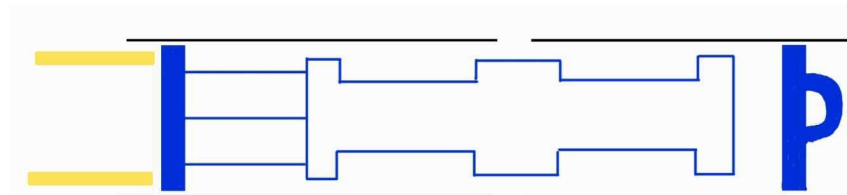


Figure 83: Body tube configuration 1 between main parachute bay and boattail.

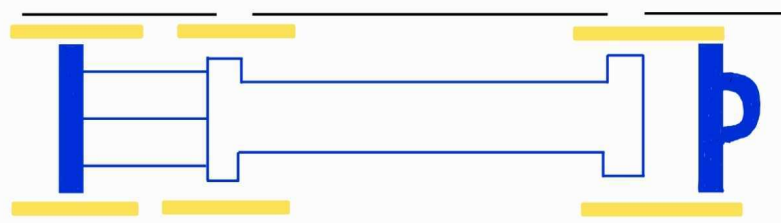


Figure 84: Body tube configuration 2 between main parachute bay and boattail.



Figure 85: Final Body Configuration

Configuration 1 relies on the tank itself being used as a coupler, where the central section of the tank has a 6" diameter to center the tubes. The advantage of this design is that the tank is much longer than a standard coupler, so provides a greater moment arm to resist in-flight forces. The second design does not use the tank as a coupler, rather, there are two composite couplers immediately on each end of the tank that connect with shorter pieces of body tube. This second design is advantageous in that it removes the dependence on the tank as a structural component, and is 400g lighter than option 1. A third design was chosen as the final design: the center tube connects the AV bay to a coupler above the tank. This coupler is bonded to the center tube, and connected to the aft tube using 12 M3 radial screws into the forward tank closure. By using a carbon fiber tube (which can be made longer than a fiberglass tube due to manufacturing restrictions), the aft tube spans from the forward tank closure to where it couples with the boat tail. The coupler is bonded to the aft tube and attached to the boat tail using 12 M3 radial screws into the aft truss ring.

Axial loading and bending moment calculations result in a margin of safety for a 5-layer fiberglass tube of 1.14, and a 6-layer fiberglass tube of 1.33 (subsection 9.12). Since the maximum bending moment is experienced over the interval between the AV bay and boat tail, the center and aft tubes benefit from being made of carbon fiber rather than fiberglass. The fiberglass body and coupler tubes will be made of fiberglass-epoxy resin composite with 5 layers of 8HS 301 gsm fiberglass fabric with a desired 60/40 fibre to resin ratio, and the carbon fiber tubes with 5 layers to match the same thickness as the fiberglass tubes for a continuous outer diameter of the airframe.

The decision to use carbon fiber for the longer aft tube is also constrained by availability of materials. Structural fiberglass fabric is not available in widths greater than 1.27 m. An alternative option considered was to use fiberglass sleeve, as this could be used to make a continuous tube of infinite length. However, the 45 degree bi-axial fiber orientation of sleeve fabric is not desirable, as the fibers are subject to the greater resultant of hoop and longitudinal stresses. Two different options for carbon fiber fabric were considered based on availability, which are both 3K 2x2 Twill. The first is a standard weave 'Mitsubishi fabric', resulting in 200 gsm and 0.28mm thickness, whereas the Dowaksa A-38 'high density' fabric has an additional pick per 10cm, resulting in 240 gsm and 0.32mm thickness. The high density fabric has been chosen. An additional contributing factor in this decision was that detailed technical data sheets exist for the Dowaksa A-38 fabric, however not for the Mitsubishi fabric. The slight increase in cost and mass of the high density fabric (an additional \$11 per meter and 97g/meter of tube) was considered acceptable given the increase in strength and the availability of accurate technical data.

Coupler tubes that do not slide during flight will extend 1 caliber either side of the joint, whereas the two coupling joints on the AV bay that slide during flight for parachute deployment will extend 1.5 body calibers either side of the joint to increase rigidity. An additional advantage of longer coupling joints is the future-proofing of the design for SAC rules that have indicated a desire to mandate the coupler lengths used here.

Post-curing of composite components was considered as an option to increase the strength of the body tubes without increasing weight. The compressive strength of Ampreg 31 epoxy increases from 40 to 73 MPa if post cured at 70 degrees Celsius for 5 hours or 50 degrees Celsius for 16 hours. Such a significant increase could result in less layers of fiberglass fabric required for the same strength which would result in large weight savings. However, there is insufficient time available in the schedule for this project to further pursue this, so it will remain open as a consideration for future projects.

9.3.1 Mass Equations

The general equation for the mass of a body tube of 5 layers is as follows:

$$m_{tube} = \rho_{FG} \cdot \left(\frac{1}{4} \cdot \pi \cdot (OD - ID)^2 \cdot L \right) \quad (42)$$

where:

- ρ_{FG} is the density of fiberglass (1.74 g/cm³ from Rosella)
- OD is the outer diameter of the tube (15.6 cm for the body tube and 15.3 cm for the coupler tube)
- ID is the inner diameter of the tube (15.3 cm for the body tube and 15 cm for the coupler tube)
- L is the length of the tube.

Thus, substituting these values into Equation 42 gives an equation for the mass of a body tube as a function of its length:

$$m_{body} = 1.74 \cdot \left(\frac{1}{4} \cdot \pi \cdot (15.6 - 15.3)^2 \cdot L \right) \quad (43)$$

And similarly, the equation for the mass of a coupler tube:

$$m_{coupler} = 1.74 \cdot \left(\frac{1}{4} \cdot \pi \cdot (15.3 - 15)^2 \cdot L \right) \quad (44)$$

9.4 Fins

The fins must ensure a minimum stability margin of 1.5 calibers immediately off the rail with a required speed of at least 31.5 m/s. During flight, stability must be maintained within the range of 1.5 to 6 calibres (system requirement PL-R-AER-3.2, PL-R-AER-3.3). Further, to ensure the airframe can be transported in a Pelican case, the semispan of the fins shall not be greater than 180mm. The fin root chord will align with the Von Karmen profile of the boat tail.

Although a symmetrical NACA profile renders the least drag in the subsonic regime, a chamfered leading and trailing edge resulting in a hex profile will be used to reduce manufacturing complexity for minimal increase in interference drag at low subsonic speeds. The advantage of a hex profile is that it offers significantly reduced drag in high-transonic, which RASAero models estimates Pardalote to achieve. It also future-proofs the boat tail and fin assembly for potential re-use in Pardalote Mk.2 that may have different flight characteristics. A non-symmetrical trapezoidal fin is the chosen design due to the lower drag compared to alternate options (Figure 86). A forward swept trailing edge will be used to reduce chance of damage upon landing. The fin will be manufactured from carbon fiber plate. The exact fin planform will depend on the as-yet-unchosen thrust curve and will be designed to meet the stability criterion, however a long root chord is desired to increase fin rigidity.

The fin design is integrated into the contour of the boat tail to increase the stability and performance of the launch vehicle by increasing the moment arm to the CG. Fin dams made of 6mm plywood will be used to secure the fins to the airframe. The depth of fin contained within the fin dam is 15mm at the leading edge and 5mm at the aft edge.

The maximum permissible semi-span that will fit within the chosen transport cases is 183 mm (based on a 370 mm square), hence accounting for the thickness of the fins plus contingency, the semi-span is limited to 170 mm.

The chosen fin geometry is given in Table 36. The effectiveness of the chosen geometry is evaluated in Table 37, where the N1600 engine corresponds to a worst-case 40 Bar fill, and the N1866 engine corresponds to a best-case 55 Bar fill to encapsulate the range of engine performance that can be reasonably expected. The system requirements for this project call for stability shall be greater than 1.5 body calipers for sustained winds of up to 20 km/h (PL-R-AER-3.4), which is satisfied by the chosen geometry. The requirements state the vehicle should be capable of launching in 32 km/h sustained winds (PL-R-AER-3.5), however this requirement is not met in its entirety, with the stability off the rail is 1.22 body calipers for 30 km/h wind. At 25 km/h sustained wind, the off-rail stability is 1.55, which meets the requirements. Note that although requirement PL-R-AER-3.1 (off-rail velocity should be greater than 30.5 m/s) is not met in the worse-case scenario, the stability has been demonstrated to be sufficient and safe for successful flight. Further, the maximum stability during flight is kept below 6 to ensure the airframe is not over-stable (PL-R-AER-3.3).

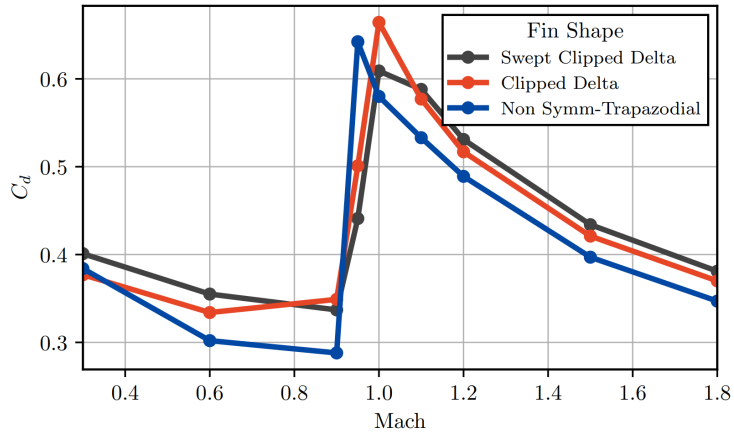


Figure 86: Fin planform CFD C_d study [2]

Parameter	Value	Unit
Root Chord	377	mm
Tip Chord	177	mm
Semi-span	170	mm
Leading edge sweep angle	43.8	degrees

Table 36: Fin geometry.

Motor	Off-rail Velocity (m/s)	Windspeed (km/h)	Off-rail stability (body calipers)	Maximum in-flight stability (body calipers)
N1600	27.9	0	4.87	5.73
		10	3.06	5.73
		20	1.95	5.73
		25	1.55	5.73
		30	1.22	5.73
N1866	34.4	0	4.87	5.75
		10	3.35	5.75
		20	2.33	5.75
		30	1.61	5.75

Table 37: Stability for varying windspeeds and engine performance.

9.4.1 Flutter

Flutter is an aeroelastic phenomenon that can compromise the strength of the fins. The thickness of the fins is calculated such that the flutter velocity is at least 50% higher than the flight velocity. The aeroelastic characteristics of the fins have been analysed using Nastran and the flutter divergence velocity plotted in Figure 87.

- material properties came from where?? - what code? - what solver/equations?

Figure 87: Flutter velocity.

9.5 Bulkheads

The maximum expected recovery loading is 33.1G, and all bulkheads have been designed to withstand consequent loadings at this acceleration.

9.5.1 Recovery U Bolts

Stainless steel M6 U-bolts with a 40mm diameter will be used to attach the shock cords to the bulkheads. Previous testing showed that the M6 U-bolts have an elastic limit of approx. 9 kN, and a failure limit of 16 kN, which is well above the expected flight loads.

The maximum expected loading on a single U bolt is on the Upper Avionics bulkhead, which experiences a force of 8634.7 N during main deployment (subsubsection 9.5.3). Grade 8.8 M6 nuts are capable of withstanding 11.6 kN of tensile force and are commonly available and thus this shall be the minimum grade of nut used to attach the U bolts to the bulkheads [27].

9.5.2 Payload Bulkhead

The payload bulkhead will be made of Al 6061-T6 due to its high strength-to-weight ratio and ease of availability and manufacture. The payload bulkhead must support the weight of the nosecone (1.27kg) and payload frame (4kg) during recovery loading. The resulting loads are therefore:

$$F_{\text{nosecone}} = (2.48)(33.1)(9.81) = 805 \text{ N (shear)} \quad (45)$$

$$F_{\text{payload frame}} = (4)(33.1)(9.81) = 1299 \text{ N (tension)} \quad (46)$$

The U-bolt holes are considered as fixed supports for FEA analysis, where a converged mesh size of 0.9mm was used. A minimum FoS of 5 is achieved (Figure 88). The localized lower FoS around screw holes is result of inaccurate boundary condition modeling around the screws, such that experts have asserted “don’t get your hopes up that any idealization method will get you even close to the true stress state around a bolted hole” [14]. In light of this, and by considering previous experimental results and comparing to FEA, the localised stress concentrations around the screw holes have been ignored in this simulation and all other FEA in this document. The bulkhead mass is 380g.

9.5.3 Avionics Bulkheads

The upper and lower bulkheads hold the same attachments (charge wells, barrier blocks, etc) yet are subject to the different loading cases to each other, and the loading cases are different for the drogue and main parachute deployment. The avionics bulkheads enclose and seal the avionics bay, and require mounting infrastructure for; two avionics rods, an M6 U-bolt, a primary and secondary charge well, a cable gland, and 2 barrier blocks. The AV rods are used to connect the upper and lower bulkheads together. The dimensional constraints of the avionics bulkheads are: a section of outer diameter 152.4mm (6in) to fit within the body tubes and rest of the lip of the avionics coupler tube, and section of outer diameter 149.4mm (5.88in) to fit within the avionics coupler tube to concentrically align the bulkhead. The primary design objective of the avionics bulkheads is to withstand shock loads applied to the U-bolts during parachute deployment, and to transfer the loads through the AV rods. Both bulkheads experience loads during the drogue and main parachute deployment, but as the main deployment causes a greater deceleration of the descending rocket, the forces exerted on the bulkheads are higher and main deployment is the case used to conduct analysis of the bulkheads. In the ideal case, the load during drogue deployment is zero as the deployment event nominally occurs at zero velocity at apogee.

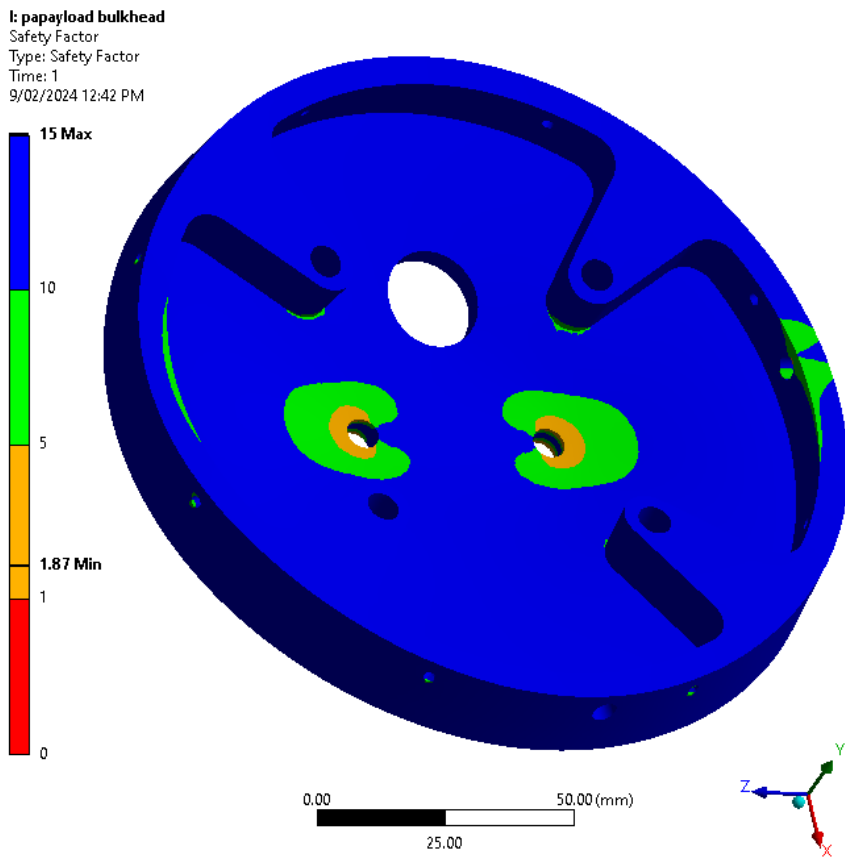


Figure 88: Payload bulkhead FEA at 33.1G recovery loading.

The critical load case for an avionics bulkhead occurs immediately after main deployment, when the shock cords achieve tension and the weight of the AV Bay and the aft assembly oppose the force applied through the U-Bolt on the upper AV bulkhead.

The forces applied to the avionics bulkheads come from the parachute deployment causing the deceleration of the descending rocket. Newton's second law $F = ma$ is used to find the force applied to the bulkhead. During main deployment, the mass acting upon the AV bay does not include the nose cone and the parachute/rigging itself. The mass aft of the AV bay is 23796 g, and the mass of the AV bay is 2796 g (masses from ork v1.6). As a result of the different loading conditions, the upper avionics bulkhead would be required to be thicker than the lower one to maintain the same minimum FoS. However, for ease of design and manufacturing and since the weight gain is minimal, both bulkheads will be 12mm in thickness, which is conservative for the lower avionics bulkhead.

$$\begin{aligned}
 F_{\text{Upper}} &= ma \\
 &= (23796 + 2796)/1000 \times 33.1g \\
 &= 8634.7N \\
 F_{\text{Lower}} &= ma \\
 &= (23796)/1000 \times 33.1g \\
 &= 7726.8N
 \end{aligned}$$

Design Comparison Multiple initial designs were considered for Pardalote's avionics bulkheads, which are shown below.

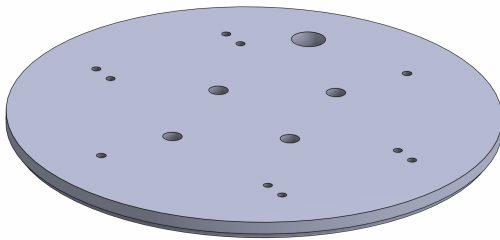


Figure 89: Flat plate top view

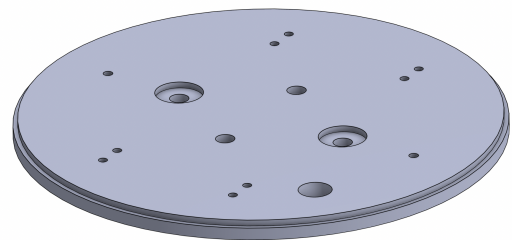


Figure 90: Flat Plate bottom view

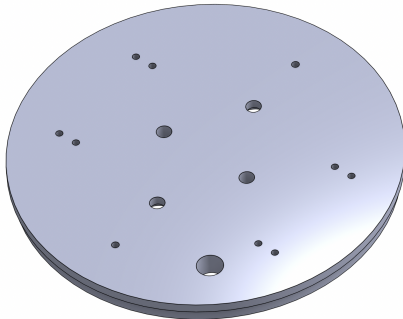


Figure 91: Cut-out plate top view



Figure 92: Cut-out plate bottom view

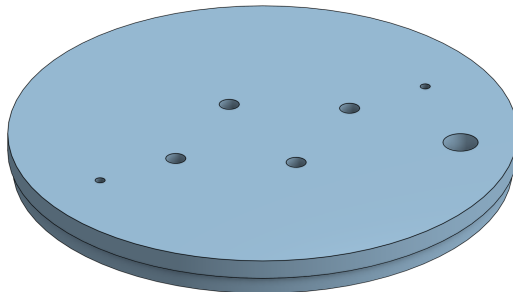


Figure 93: Isogrid top view

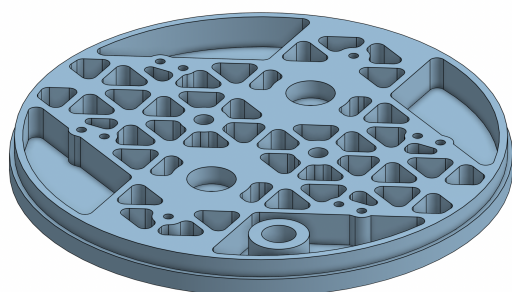


Figure 94: Isogrid bottom view

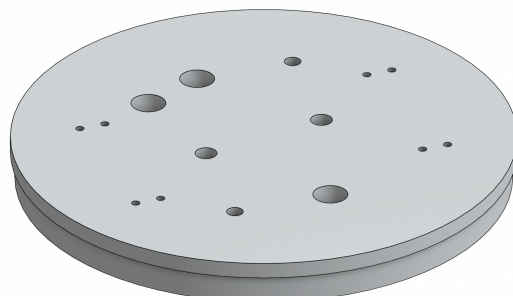


Figure 95: Rosella top view

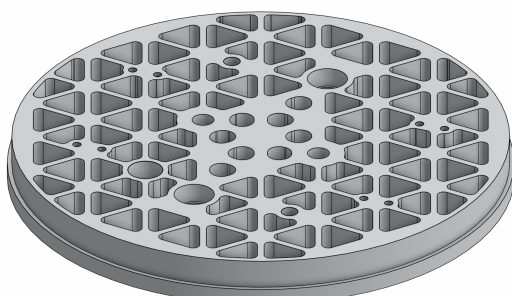


Figure 96: Rosella bottom view

The comparison of these designs takes into account strength under tensile load, weight, and ease of manufacturing. For FEA, a force load of 8000N was used in both directions, away from the AV Bay on the coupler lip, and towards the AV Bay on the U-Bolt washers. In order to compare these different designs accurately, an attempt was made to adjust the thickness of each new bulkhead until the mass is near 300 grams. From this comparison, a design can be chosen and thickness adjustments can be made to that design.

if required. Please note that the FoS results presented in Table 38 include the stress concentrations around the screw boundary conditions, which as previously discussed are not indicative of the true minimum FoS.

Table 38: AV Bulkhead FEA result comparison, all 8000N loading and all new designs approx 300g mass.

Design	Mass (g)	Max Stress (MPa)	Min Yield	FoS	Min Ultimate	FoS
Flat Plate	288	342	-		0.90788	
Cut-Out	292	169	1.5723		1.8993	
Isogrid	319	230	1.1246		1.3585	
Rosella	445	178	1.4548		1.7573	

Based on these FEA results in Table 38, the best performing design is the cut-out plate, so this is the chosen design. This design is also significantly advantageous over the isogrid design since the manufacturing complexity is greatly reduced. The FEA results for the final design are shown in Figure 97 with a minimum FoS of 5.2 in the main structure. The mass is 334g. Both charge wells have been positioned on one side of the bulkhead with a camera placed on the opposite side to increase the distance between them to reduce chance of the camera lens getting damaged/foggy/dirty from the deployment charge.

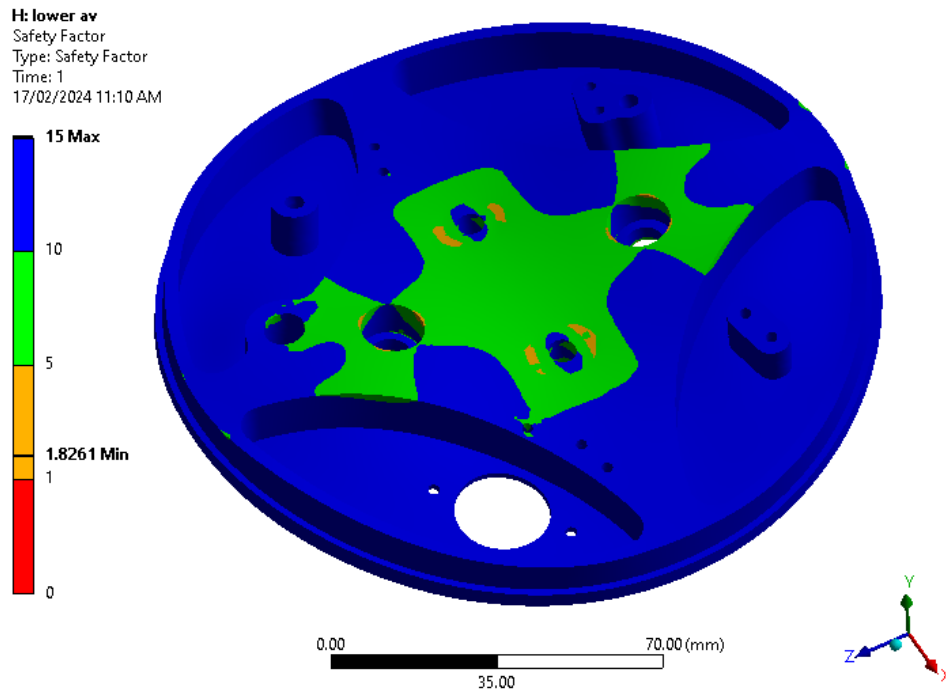


Figure 97: Upper avionics bulkhead FEA for main deployment (8635 N).

9.5.4 Aft Recovery Bulkhead

The aft recovery bulkhead is designed to transfer the forces from the parachutes to the aft airframe of the rocket. It is required to securely connect with aft body tube and support a U-bolt, to which the parachutes will be attached. The design of the aft recovery bulkhead is illustrated in Figure 98. The bulkhead is a flat plate with radial gussets for reinforcement, which was determined to be more mass efficient than a flat plate. The thread depth of the radial holes is 10mm, which is at least 2 diameters to ensure sufficient thread engagement to reduce the risk of thread pullout. The bulkhead will be manufactured from Al6061-T6 due to its ease of availability, relatively low cost, and sufficient strength. A 40mm diameter stainless steel M6 U-bolt will connect the parachute rigging to the bulkhead.

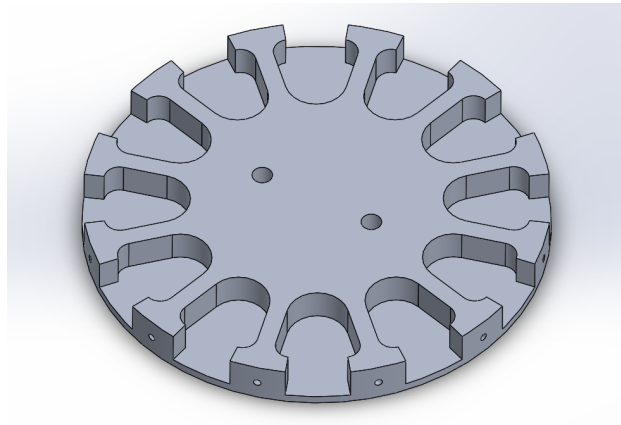


Figure 98: Aft recovery bulkhead

need new fea without button mounts FEA was used to verify the design of the aft recovery bulkhead to support a recovery loading of 7144N on the central U-bolt (the aft airframe with a mass of 22kg multiplied by an acceleration of 33.1G). Using a converged mesh size of 0.8mm, the results are shown in Figure 99 and show the minimum factor of safety is 4.0. Lower safety factors around screw holes are an artifact of the simulation boundary conditions.

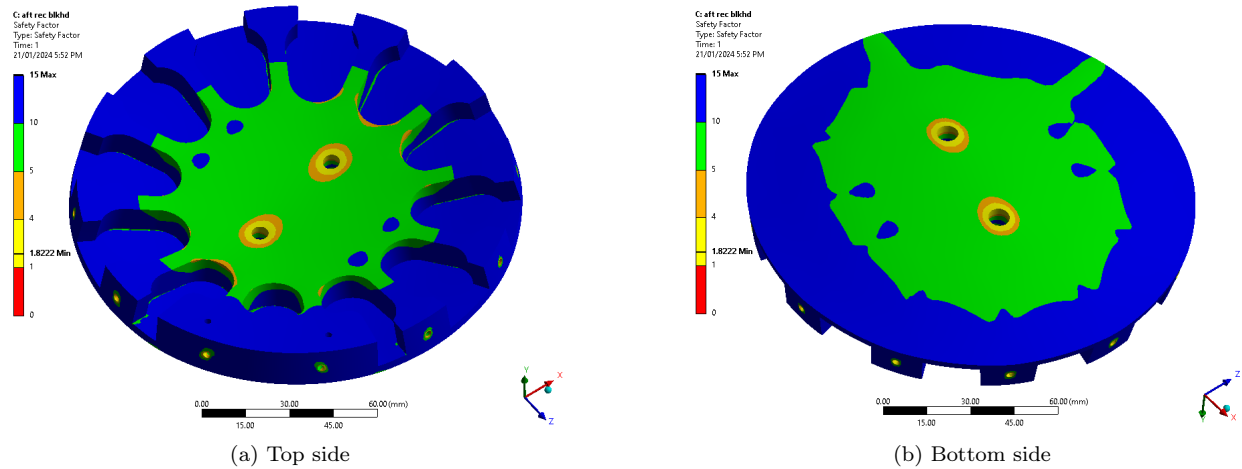


Figure 99: FoS results for the aft recovery bulkhead FEA

9.6 Bulkhead Optimisation

Bulkhead optimisation is implemented to reduced overall weight, while keeping its FoS at a respective value so that it will not fail throughout the launch and recovery process. This is an important and necessary step in order to allowing the rocket to be able to reach a higher altitude as it requires less fuel and propulsive force.

9.6.1 Payload Bulkhead Optimisation

The payload bulkhead is the first to have its weight reduced, looking at Figure 88, there is some unnecessary joining metal from the edge of the bulkhead so that is removed. Applying this change, Figure 100 below shows that the minimum FoS is seen to be 2.4396, when compared to its optimised, a reduction to 2.1084 is seen. This is still acceptable as the bulkhead will be able to withstand 2x its necessary force, while having less metal, making it lighter and more optimal.

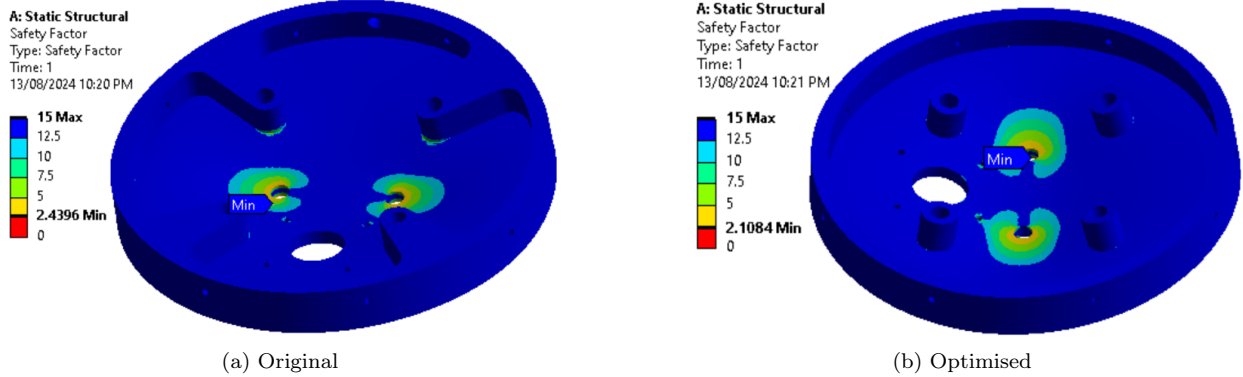


Figure 100: FoS results comparison for Payload Bulkhead

9.6.2 Upper AV Bulkhead Optimisation

Analysing the upper AV bulkhead seen in figure 101, it is seen there is no significant change in the FoS with the changes made. It is noticeable that changes seen in the optimised figure, the edges of the bulkhead attached to the outer rim are removed as they serve no purpose in the ability to resist load. This is backed by the minimal change in FoS seen with the removal of the extra material.

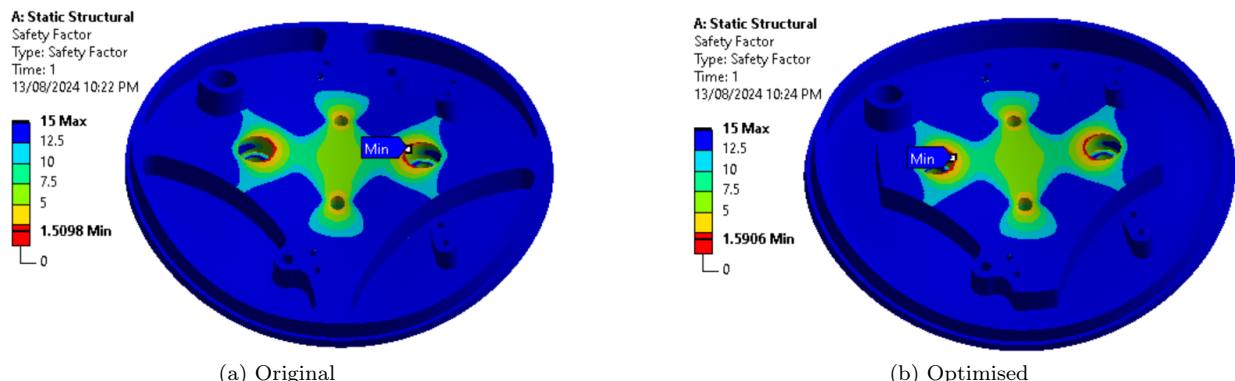


Figure 101: FoS results comparison for Upper AV Bulkhead

9.6.3 Lower AV Bulkhead Optimisation

The same can be said with the Lower Av Bulkheads, seen in figure 102. The FoS is seen to change very little while optimising weight and cutting out a large portion of the unnecessary material. The original FoS is 1.6873 which changes to 1.6858 showing its minimal loss of safety is a reduction of weight.

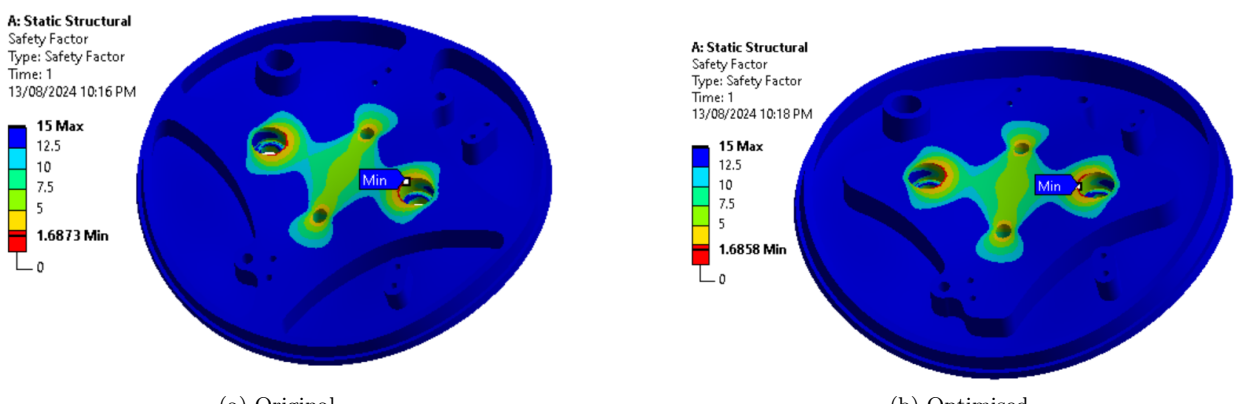


Figure 102: FoS results comparison for Lower AV Bulkhead

9.6.4 Aft Recovery Bulkhead Optimisation

The Aft Recovery Bulkhead has in depth analysis in figure 99 at its original design. Figure 103 below shows 2 iterative designs on potential optimised bulkheads. As seen, V1 has more supports and a wider frame, allowing for a great FoS of 1.2506 as opposed to V2 with only a 1.0404. V2 will be lighter, so it would be a toss between lighter or more stable, for something as important as the Aft Recover, it may require V1. Both of these are compared to its original FoS of 1.8222, showing the cut down in material takes away larger safety, but still effectively will work.

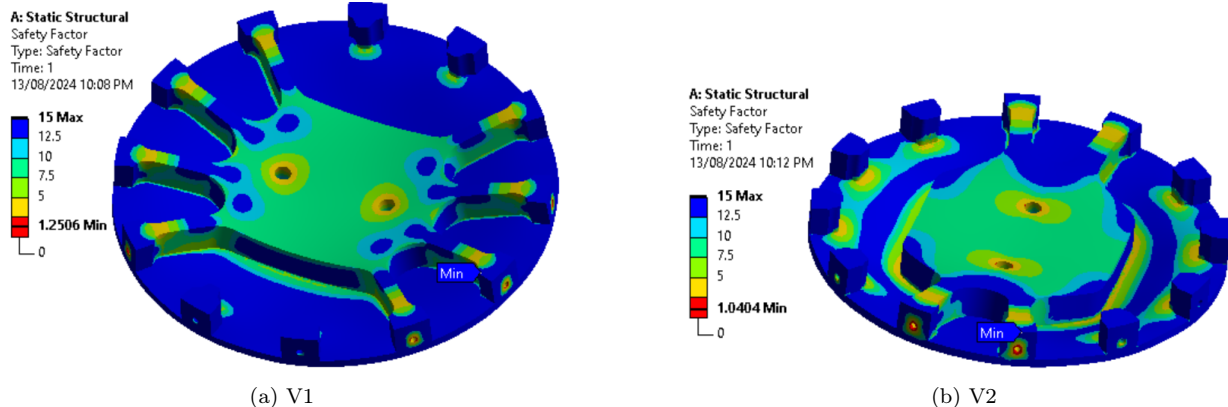


Figure 103: FoS results comparison for Aft Recovery Bulkhead

9.7 Avionics Bay Rods

The Avionics Bay Rods must be able to withstand both parachute deployment loads and hold the two avionics bulkheads together against the Avionics Coupler tube. 3 different designs were considered for the avionics bay rods: aluminum tube, aluminum solid rod, and carbon fibre tube with aluminum inserts. Carbon fibre tube has a large weight advantage over solid aluminum tube, but has a point of failure at the epoxy bond to a metal insert, and we were not able to do sufficient testing of this joint strength to be sure it would survive deployment loads. The advantage that solid rod has over tubing is that we are not limited to commercially available ID sizes, and can drill a hole to fit the bolt size we choose. For the solid bar option, we will use M8x1.25 bolts, as they offer high enough strength to be confident in not experiencing thread shear out, but allow the tube section around the bolt to be thicker, therefore creating a higher cross sectional area to resist stress.

In order to find the most suitable dimension of the tube, multiple ID were tested through research and calculations. The dimensions of the OD is set to 12.7mm, where the ID test dimensions were, 8mm, 9mm, 10mm, 11mm and 12mm. It is noted, the 11mm and 12mm ID will require an increased OD as the FoS will be too small and the tube will be to weak, this value is 15.88mm. The maximum force (F) applied to the AV Rods used in calculations is 8634.7N. The material selection included, Al-2024, Al-5052, Al-6061, Al-7050 and Al-7075. Each Aluminium Alloy provides its own respective benefit to suit the need for the AV rod. The yield strength (σ_y) used for Al-2024 is 441MPa, Al-5052 is 193MPa, Al-6061 is 276 MPa, Al-7050 is 469MPa and for Al-7075 it is 503 MPa. The FoS is calculated as follows:

$$CSA = \pi \left(\left(\frac{OD}{2} \right)^2 - \left(\frac{ID}{2} \right)^2 \right)$$

$$\sigma = \frac{F}{CSA}$$

$$FoS = \frac{\sigma_y}{\sigma}$$

As the M8 bolt has been selected, a comparison in Table 39 below shows the different Aluminium stock available to be selected as a tube and solid rod, displaying their respective cross-sectional area (CSA), Factor of Safety (FoS) and mass.

Table 39: Comparison of Avionics Bay Rods

Material	OD (mm)	ID (mm)	σ_y (MPa)	Max Force (N)	CSA (mm ²)	FoS (1 Rod)	Mass (g) (1 Rod)
2024 Tube M8	12.7	8	441	8634.7	76.41	3.90	110.61
2024 Solid Bar M8	12.7	8	441	8634.7	76.41	3.90	183.37
5052 Tube M8	12.7	8	193	8634.7	76.41	1.71	106.63
5052 Solid Bar M8	12.7	8	193	8635.7	76.41	1.71	176.77
6061 Tube M8	12.7	8	276	8635.7	76.41	2.44	107.43
6061 Solid Bar M8	12.7	8	276	8635.7	76.41	2.44	178.09
7050 Tube M8	12.7	8	469	8635.7	76.41	4.15	112.60
7050 Solid Bar M8	12.7	8	469	8635.7	76.41	4.15	186.67
7075 Tube M8	12.7	8	503	8635.7	76.41	4.45	111.80
7075 Solid Bar M8	12.7	8	503	8635.7	76.41	4.45	185.35

The best option is the 6061 tube with M8 screws, with a sufficient FoS as well as a relatively low mass. It is also the most readily available and cost efficient. To manufacture the tube option is only available in the UK or USA, and thus the cost is approximately \$62 per 6ft rod. The 5052 tube is also a potential option, however repeated it has a worse FoS at the expense of being \approx 1g lighter. With the need to cut down weight, a tube option is the best route to take. There is little availability in Australia, meaning the rods will need to be outsourced from the US. Two rods will be used, and each individual rod has a FoS of 2.44 for tensile failure in the worst case that a single rod carries the entire load. The thread length required for no shear out at each screw (with FoS 3) was calculated to be 21mm (subsubsection 9.12.6).

The maximum available thread length on a standard M8 screw is 35 mm of full thread, which results in a usable length of 31 mm since the bulkhead is 4 mm thick due to the counterbore. Hence there is sufficient thread length on standard screws to meet the required minimum length for no thread shear out.

The battery bay will be secured to the AV rods by shaft collars that are placed around the rods. Previous projects have used 12mm AV rods so new collars will be required to accommodate the 12.7 mm diameter. These can be purchased or made by team members since they are a relatively simple component.

9.8 Launch Rail Attachment

There will be two rail buttons to support the airframe on the launch rail. The forward button will be mounted to the tank vent closure, which is approximately **2.3** body calipers forward of the CG. **Originally, the design involved the forward button to be mounted to the aft recovery bulkhead, which is approximately 4 body calipers forward of the CG, however, it was moved roughly 10 inches aftward.** The CG is located within the span of the run tank, and there is insufficient wall thickness in the tank to mount the rail button to the tank wall. The rail button will be forward of the tank to increase the moment arm around the CG. The aft button will be located between the fins just before the boat tail taper begins. (Figure 76).

Retractable rail guides (retracts) may be used to reduce form drag by retracting the rail button into the airframe after rail departure. The retracts must be able to support the full mass of the launch vehicle in both shear and tension (requirement PD-R-AER-4.4, PD-R-AER-4.5). There are both advantages and disadvantages to using retracts:

Benefits:

1. Slight drag reduction
2. Ensures knowledge of complicated system remains within the current team. A CAD design and IREC report are not sufficient sources of knowledge because they skim over the flaws of the design.
3. Use in this airframe will prove the design will work for a heavier rocket, which is important foundation work if they are to be considered for Pardalote V2.
4. Openrocket includes rail button drag however no data as to accuracy of it.
5. The retract design is flight proven.

Disadvantages:

1. Additional 10g of mass per button compared to conventional hardpoint, however this is a negligible mass and the airframe is not mass optimised.
2. The spindle could jam out and affect sim accuracy, openrocket now sims rail buttons but no data as to how accurate that is.

It has been decided that despite the disadvantages being outnumbered by the advantages, the disadvantages are far too significant to ignore, and provide enough reason not to pursue the retract design for launch rail attachment. Since it is unknown how much drag would be reduced without the rail button drag, it's logical to prevent over-complication of the design. **delete the below two paragraphs? not doing retracts**

The primary constraint on the design is available radial distance, which is 15mm for the aft retract. The design is fundamentally similar to the design previously used by URT, however slightly modified to fit within a smaller radial distance (15mm compared to 16.8mm). The rail buttons will be COTS 1515 buttons and will be counterbored to reduce their depth. The rail button is mounted to a spindle, made of Al 7075 T6, since the greater strength is required compared to Al 6061 due to the reduced thickness. The hardpoint is Al 6061 T6. The fore hardpoint is attached to the aft recovery bulkhead with 2 M3 screws, and the aft hardpoint is attached directly to the airframe by 2 M3 screws and tinnerman washers.

The design of the retract mechanism has been validated to support the wet launch mass on a single retract. The results of a combined loading of 47kg in shear and 23.5kg in tension are shown in Figure 104

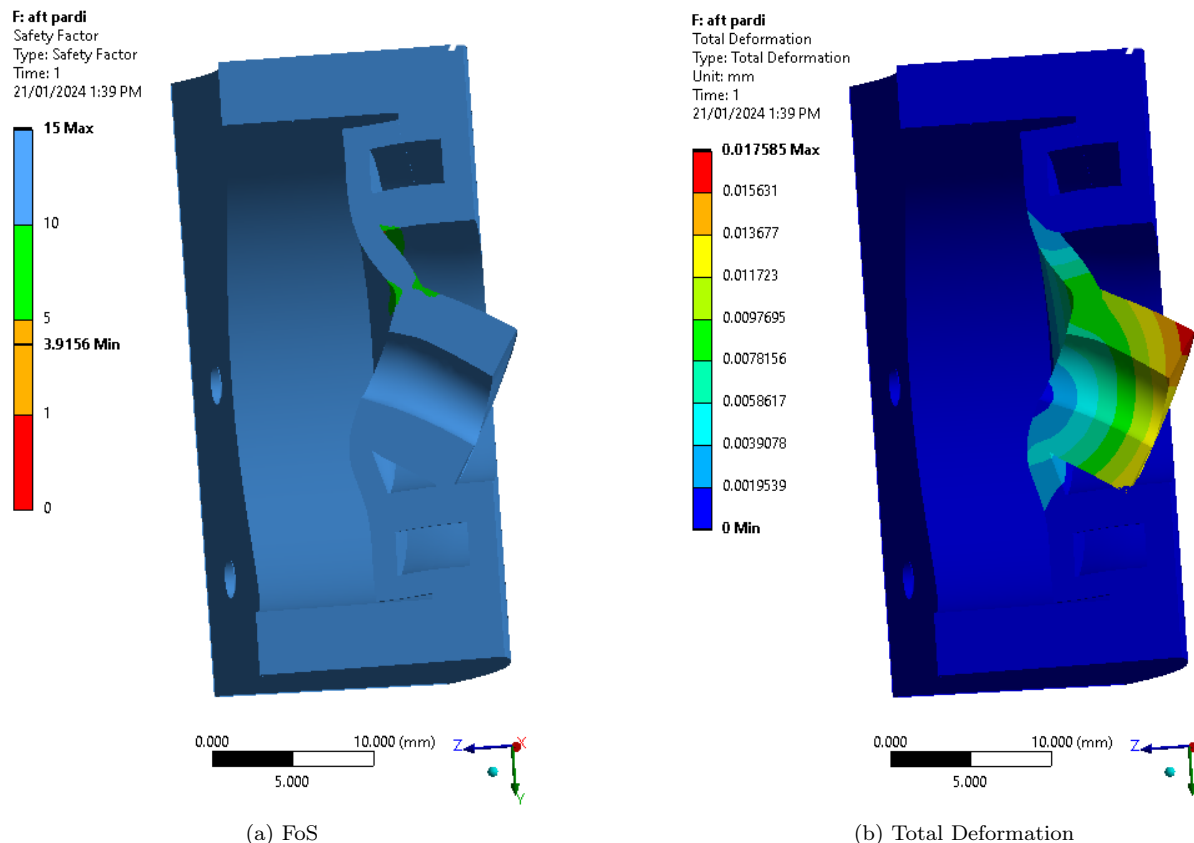


Figure 104: FEA of aft retract mechanism.

Unfortunately, the project director and chief engineer ruled that the minimal risk of the retracts was unacceptable and could not be used in the final design. **does that sentence sound petty?** Hence, the chosen design is a static mounted rail button on aluminium hardpoints. The fore and aft hardpoint designs are presented in Figures 105 and 106. The fore hardpoint is attached to the tank vent closure with 4 M3 screws, as well as attached directly to the airframe with 2 M3 screws. The aft hardpoint is attached directly to the airframe in between the fins by 4 M3 screws and tinnerman washers.

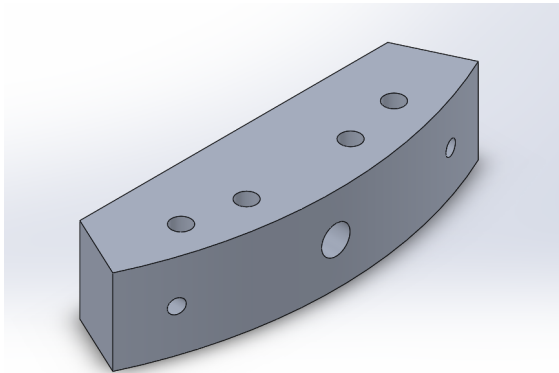


Figure 105: Forward Rail Button Hardpoint

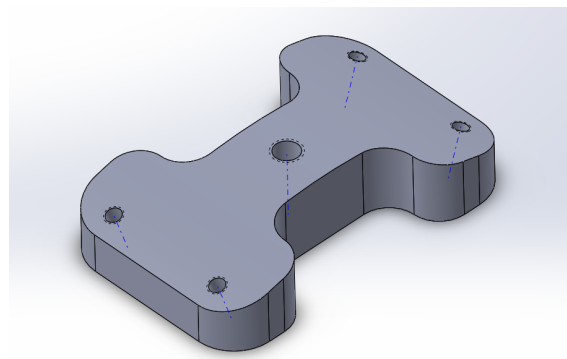


Figure 106: Aft Rail Button Hardpoint

9.9 Engine Support Structure

9.9.1 Tank Mounting

The tank (serving as a coupler) will be mounted to the airframe with 12 radial M3 screws on the forward closure and 12 M3 radial screws on the aft closure, as well as being secured to the truss frame below it with 6 M6 longitudinal screws.

9.9.2 Tank-Chamber Truss

The tank-chamber truss provides structural support against the thrust force and bending moments resulting from the tank and the chamber, as well as any torsional moments that may arise during flight. Several designs were considered based on a series of arbitrary loading conditions. The truss will be sufficiently strong to transfer the thrust loading to the airframe through the aft tank closure in the case that the lower truss ring doesn't transfer the load due to tolerances in the Tinnerman washers. The layout of the truss is shown in Figure 107. For compatibility with the body tubes, the truss has an outer diameter of 149mm to match the internal diameter of the boat tail coupler. The members in the truss will need to be sufficiently thick to incorporate mounting holes for any brackets etc. required by the fluids systems.

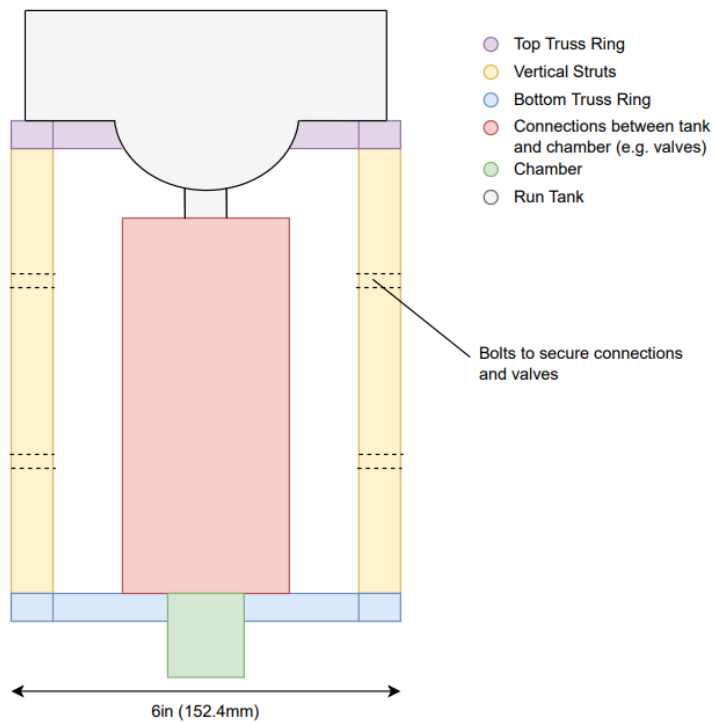


Figure 107: The block diagram of the truss (cross-sectional view). Outer diameter is 152.4mm.

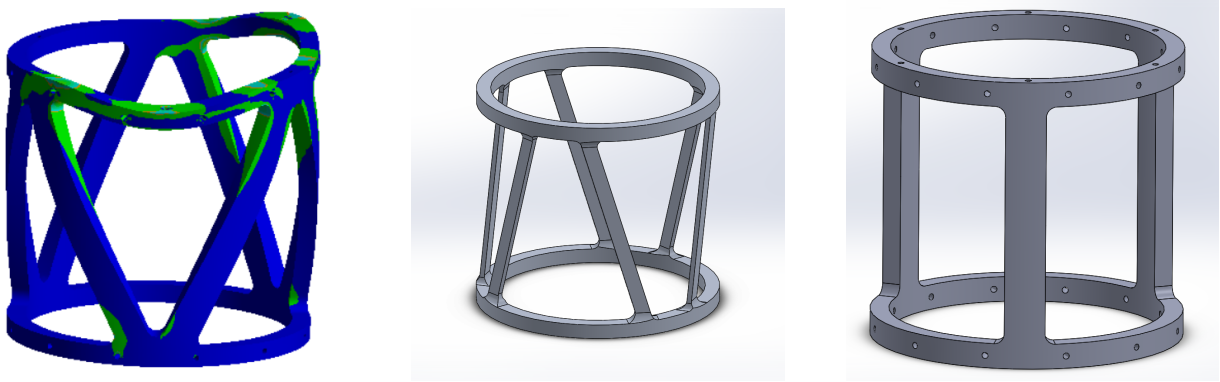


Figure 108: Alternate truss options considered.

Figure 108 shows the different designs that were considered, from left to right: diagonal members that curve with the truss ring; diagonal members that connect without curving; and straight vertical members. Due to the minimal torsional loads experienced by the truss (only during integration and assembly) the diagonal member designs were rejected. The lack of accessibility to inside the frame and additional manufacturing complexity are also disadvantages of the diagonal member designs. The chosen design is a straight membered truss with 3 struts (Figure 109). Three struts were chosen rather than a higher number because it improves the clearance angles for assembly, and each strut is thicker and thus has higher buckling FoS compared to the use of four struts.

The struts are designed to attach to the aft tank closure with 2 M6 screws per strut. Similarly, 2 M6 screws are also used to attach the other end of the strut to the chamber adapter plate at the aft of the truss. The complete truss assembly is shown in Figure 109. The advantage of bolted connections between the struts and other components is that one of the struts can be left off during integration for improved access, and installed after the fluids systems are fitted.

The truss strut has a cross section of 279.30 mm^2 , but all 3 struts have slight variations in their hole arrangements, and thus all 3 struts were checked individually using FEA. When subject to 1667 N compression, the minimum compression FoS was 1.5773 and the buckling FoS was 16.707. In the case that the worst case scenario that the full 5 kN thrust load is transferred through one strut, the compressive FoS is 1.1031, and buckling FoS is 5.570. Each strut is manufactured from Al 6060 T5 due to its ease of availability and machinability, and each member has a mass of 334 g. Note that the minimum FoS shown in Figure 110 is a result of stress concentrations around bolts, and can be ignored.

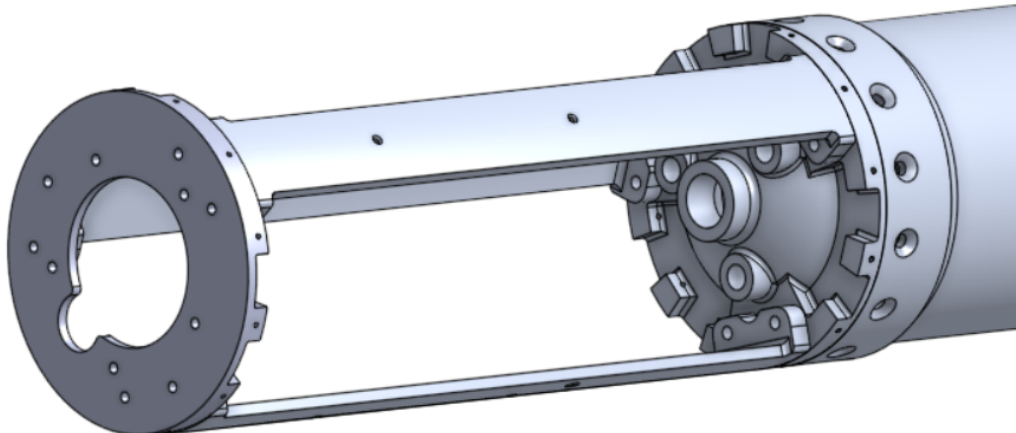


Figure 109: Truss design and tank aft closure.

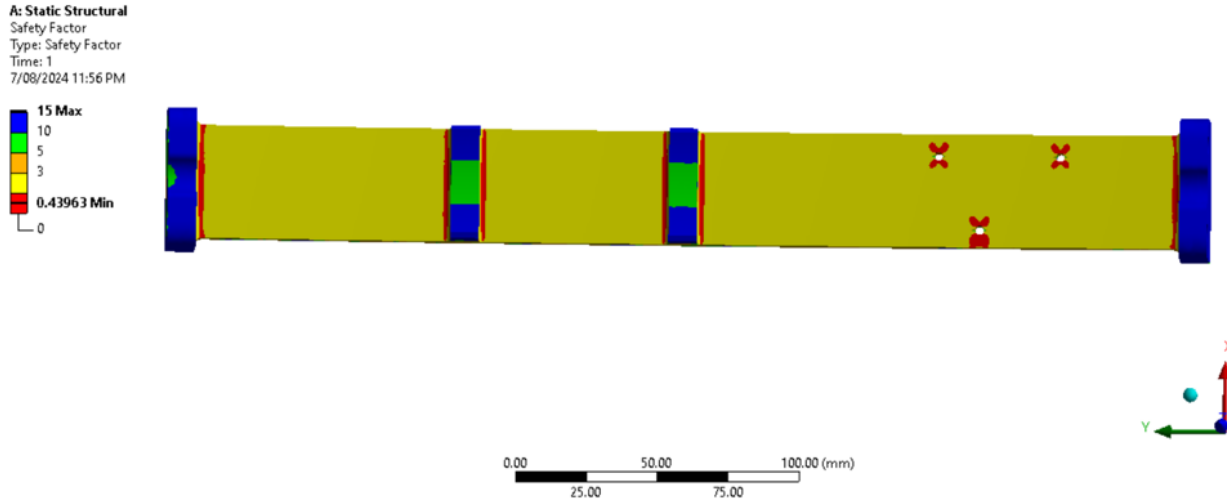


Figure 110: Truss strut FoS for 5kN compressive load.

Expected max force on chamber beams: 5kN

$$P_{CR} = \frac{\pi^2 EI}{(KL)^2} \quad (47)$$

Because the cross-sectional area of the truss features arcs, standard moment of inertia formulas cannot be used without heavy calculation. Therefore, we use the moment of inertia value given in Solidworks, which is able to accurately calculate the I_{xx} of the truss strut. Given parameters:

$$\begin{aligned} E &= 69 \text{ GPa} = 69 \times 10^9 \text{ Pa} \\ I_{xx} &= 1218.01 \text{ mm}^4 = 1218.01 \times 10^{-12} \text{ m}^4 \\ L &= 380 \text{ mm} = 380 \times 10^{-3} \text{ m} \\ K &= 0.5 \text{ (both ends of beams fixed)} \end{aligned}$$

Substituting E , I , K , and L into the critical load formula:

$$P_{cr} = \frac{\pi^2 EI}{(KL)^2}$$

$$P_{cr} = \frac{\pi^2 \times 69 \times 10^9 \times 1218.01 \times 10^{-12}}{(0.5 \times 380 \times 10^{-3})^2} \approx 22978.65 \text{ N}$$

Thus, the critical buckling force is approximately 22979 N.

Therefore,

$$FOS = \frac{22979}{5000} \approx 4.6$$

This is an underestimation from the critical force provided by eigenvalue buckling in Ansys FEA, which gives a minimum critical load of 27850.57 N in strut 3 shown in Figure 111.

This simulation was run with 1667 N compressive force, but due to the nature of linear load multipliers, this force ends up being arbitrary in the final calculation. Given the load multiplier of 16.707, the critical load is:

$$P_{CR} = \lambda_i F_{perturb} = 16.707 \times 1667 = 27860.57 \text{ N} \quad (48)$$

This gives buckling FoS values of:

$$FoS_{1667N} = \frac{27850.57}{1667} = 16.707 \quad (49)$$

$$FoS_{5000N} = \frac{27850.57}{5000} = 5.570 \quad (50)$$

B: Eigenvalue Buckling
 Total Deformation
 Type: Total Deformation
 Load Multiplier (Linear): 16.707
 Unit: mm
 8/08/2024 12:01 AM

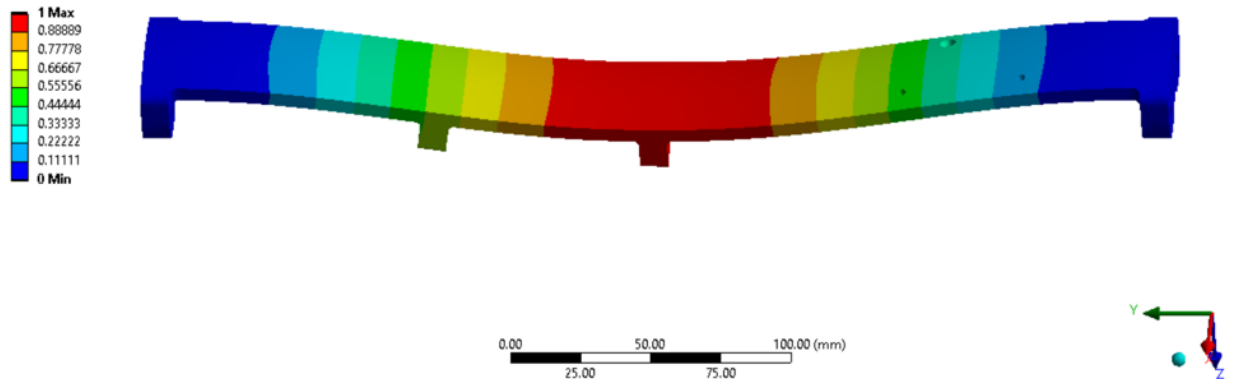


Figure 111: Eigenvalue buckling results from ANSYS

9.9.3 Chamber-Truss Adapter Plate

An adapter plate is needed to transfer the thrust force from the forward closure of the chamber to the truss struts. The plate also serves as the primary point to transfer thrust loads to the airframe, with 12 M3 radial screws connecting to the airframe. The FEA results for a 5kN thrust loading completely transferred to the M3 radial screws is shown in Figure 112, and the thrust completely transferred to the truss is shown in Figure 113. Like the truss, the minimum FoS occurs at stress concentrations near bolts, so these spots can be disregarded.

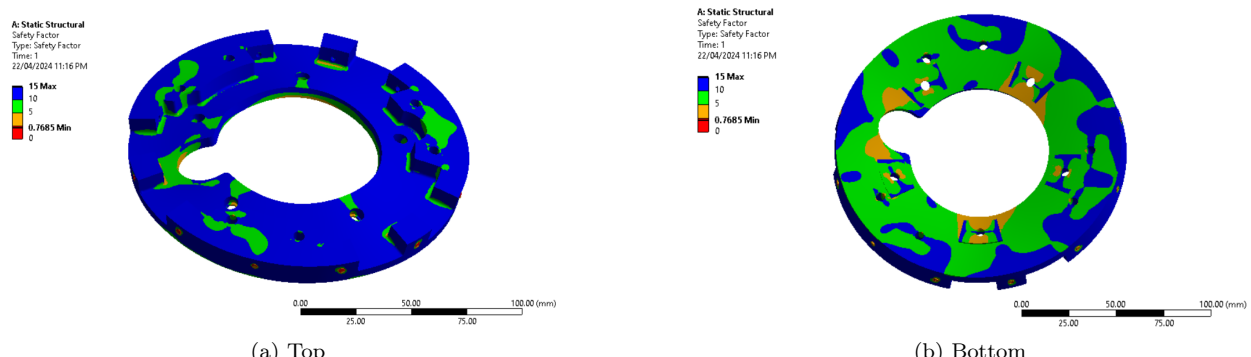


Figure 112: FEA of chamber adapter plate.

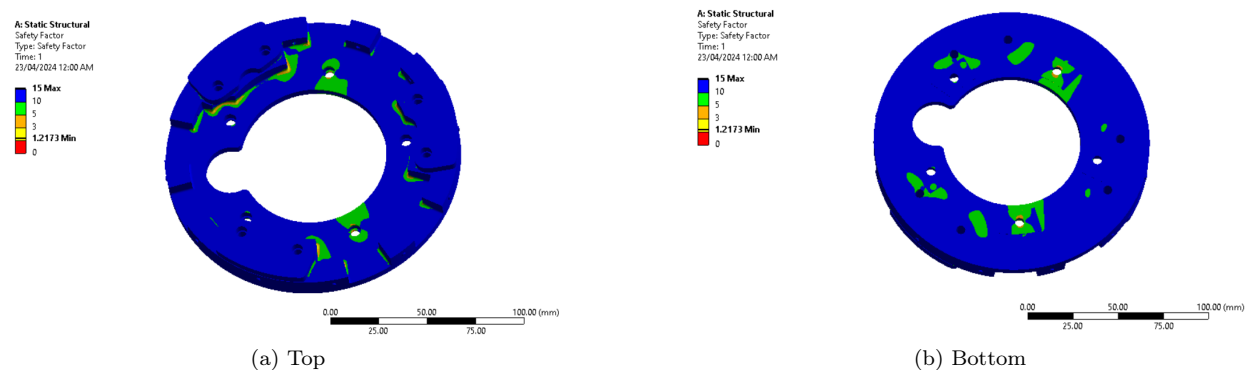


Figure 113: FEA 2 of chamber adpater plate.

9.10 External Access to Truss

A removable access panel for the truss was considered in order to facilitate easy repairs to any leaks that may occur in the components in the truss, or to recharge the air reservoir. This would remove the need to disassemble a significant portion of the rocket (which would include a section of the tank, the entire truss and sections of the chamber) to complete any repairs. However, it was decided that a removable panel was not needed, for the following reasons:

1. The complete fluids assembly is assembled outside the airframe, and can thus be tested for leaks before integration.
2. The air reservoir contains enough air for multiple valve actuations so should not require refilling.
3. A removable panel may reduce the strength of the airframe.

9.11 Cover for QD Airframe Hole

Izaak write this, gist is I don't think its worth it. I think it has more risk than the retracts for similarly negligible drag reduction, and since retracts weren't allowed, I can't see this being allowed.

9.12 Structural Analysis

The conducted load analysis makes use of appropriate assumptions while wholly reflecting the structural composition of the launch vehicle. Simplifications in the analysis are compensated by applying relevant factors of safety to calculations. This accounts for inaccuracies from incomplete modelling, manufacturing tolerances and uncertainties, load approximations and environmental variations. The launch vehicle must exhibit a minimum Factor of Safety (FoS) of 1.5 to ensure structural integrity across all flight phases:

$$\text{Design Load} = \text{FoS} \times \text{Load} \quad (51)$$

The Margin of Safety (MoS) may then be calculated:

$$\text{MoS} = \frac{\text{Failure Load}}{\text{Design Load}} - 1 \quad (52)$$

The Failure Load is dictated by material properties. Fittings must satisfy an additional FoS of 1.15 due to variation in actual stress conditions once installed into the surrounding structure. These values are consistent with that used in aerospace applications [5],[8]. Using conservative values such as maximum dynamic pressure, mach number, etc. in calculations further ensures that loads are not underestimated and retain the appropriate FoS.

9.12.1 Axial Loads

OpenRocket utilises the Barrowman equations by decomposing the external components of the launch vehicle to determine relevant parameters such as drag coefficient. The side profile is shown in Figure 114. A conservative value for dynamic pressure may be calculated using maximum density and velocity. The resulting drag forces contributed by each component may then be determined, shown in Table 40:

$$q = \frac{1}{2} \rho V^2 = 183.4 \text{ kPa} \quad (53)$$

$$D = C_D q S \quad (54)$$

The maximum anticipated thrust of the Pardalote engine is 5000 N, acting at the chamber-adapter plate of the launch vehicle. Components along the length of the airframe experience variation in drag. The axial forces experienced across the launch vehicle are represented in Figure 115.

9.12.2 Transverse Loads

Transverse loads on the launch vehicle have been analysed through the contribution of a gust load at 30.0 m/s (98.4 ft/s). The gust will result in shearing around the centre of pressure to create a bending moment

Table 40: Drag Coefficients and Drag of Components at Mach 0.9

Component	C_D	Drag (N)
Nose Cone	0.027629212	30.605
Nose Cone Ext	0.013009545	14.411
FWD Tube	0.044614415	49.420
Switch Band	0.003117382	3.453
Center Tube	0.026523883	29.381
AFT Tube	0.068765623	76.173
Fins	0.028549424	31.625
Fin Can	0.129772948	143.752
Total	0.342	378.821

and induce a non-zero Angle of Attack (AoA). The magnitude of the AoA is dependent on axial velocity:

$$\alpha = \arctan\left(\frac{v}{V}\right) = \arctan\left(\frac{30}{0.9 \times 343}\right) = 5.599^\circ \quad (55)$$

Table 41: Relevant Coefficients, Normal Forces and Moments of Components at Mach 0.9

Component	C_{Na}	C_N	Normal (N)	M_{cg} (Nm)
Nose Cone	2.518363125	0.264	292.131	-718.758
Nose Cone Ext	0.247601027	0.026	28.722	-59.411
FWD Tube	0.849318241	0.089	98.521	-145.959
Switch Band	0.059330812	0.006	6.882	-6.849
Center Tube	0.50454549	0.053	58.527	-40.589
AFT Tube	1.308080899	0.137	151.738	41.955
Fins	12.20605382	1.278	1415.905	1955.365
Fin Can	-0.21559176	-0.023	-25.009	-34.537
Total	17.478	1.830	2027.418	991.217

The contributing normal forces and moments from the center of gravity at each station are dependent on their normal coefficients found from OpenRocket and the maximum angle of attack. These values are displayed in Table 41, calculated from the following relationships:

$$C_N = C_{Na}\alpha \quad (56)$$

$$N = C_N q A \quad (57)$$

$$M_{cg} = N(x_i - x_{cg}) \quad (58)$$

The lateral acceleration contributed by the gust load is then dependent on the sum of normal forces and mass of the launch vehicle:

$$a_{lat} = \frac{\sum N}{\sum m} = 43.61 \text{m/s}^2 \quad (59)$$

The angular acceleration may also be calculated through the sum of moments and inertia at each station:

$$\ddot{\alpha} = \frac{\sum M_{cg}}{\sum I} = 20.30 \text{rad/s}^2 \quad (60)$$

The sum of acceleration contributed by the lateral and angular components may be used to determine the force experienced at each station. In turn, shear forces and bending moments with respect to the tip of the launch vehicle may be determined. These values are shown in Table 42. The corresponding shear force and bending moment diagrams are respectively shown in Figure 116 and Figure 117. In Figure 114, the motor is modeled as being 2620 mm long. The motor mass is only due to the combustion consumables (ie, oxidiser and fuel grain) and so it has a wet mass of 7.87 kg and a dry mass of 0 kg. The length of the motor was calculated such that the location of the CG of the motor (which OpenRocket assumes linear mass distribution) is equal to the CG location of the oxidiser and fuel grain. An oxidiser mass of 6 kg and a fuel grain mass of 0.75 kg was used.

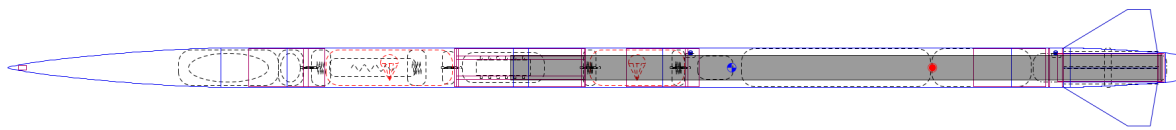


Figure 114: Side Profile of Launch Vehicle.

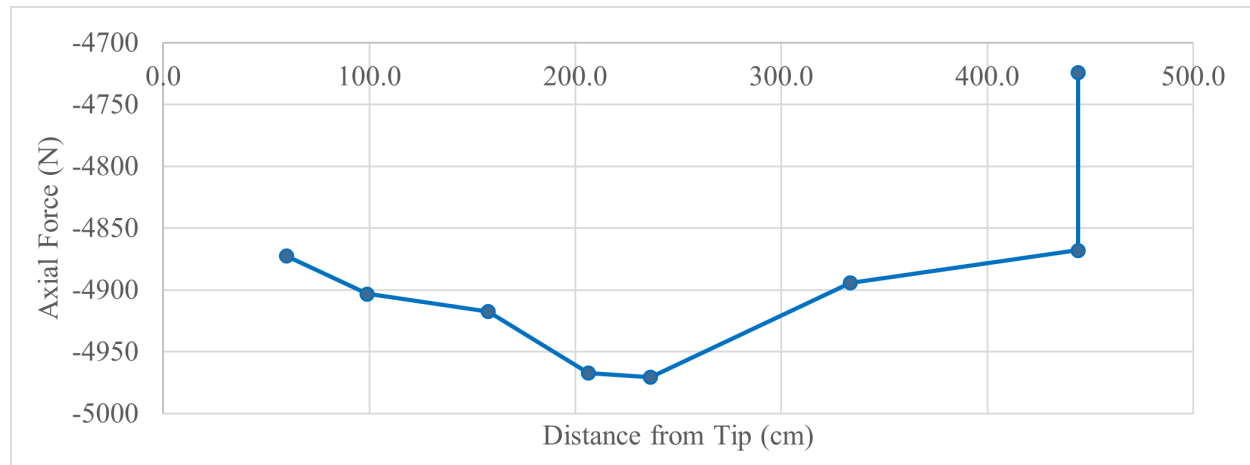


Figure 115: Axial force diagram.

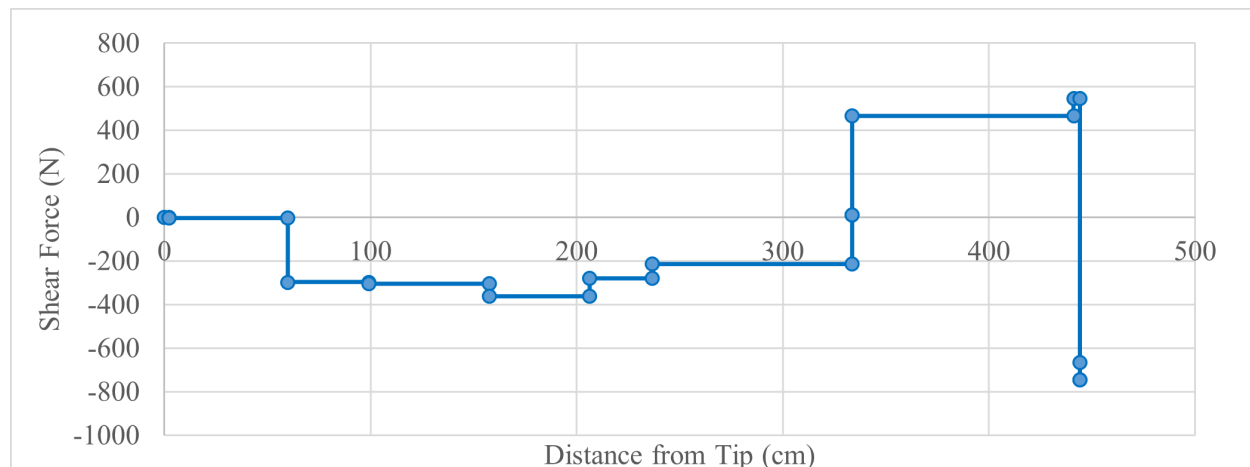


Figure 116: Shear force diagram.

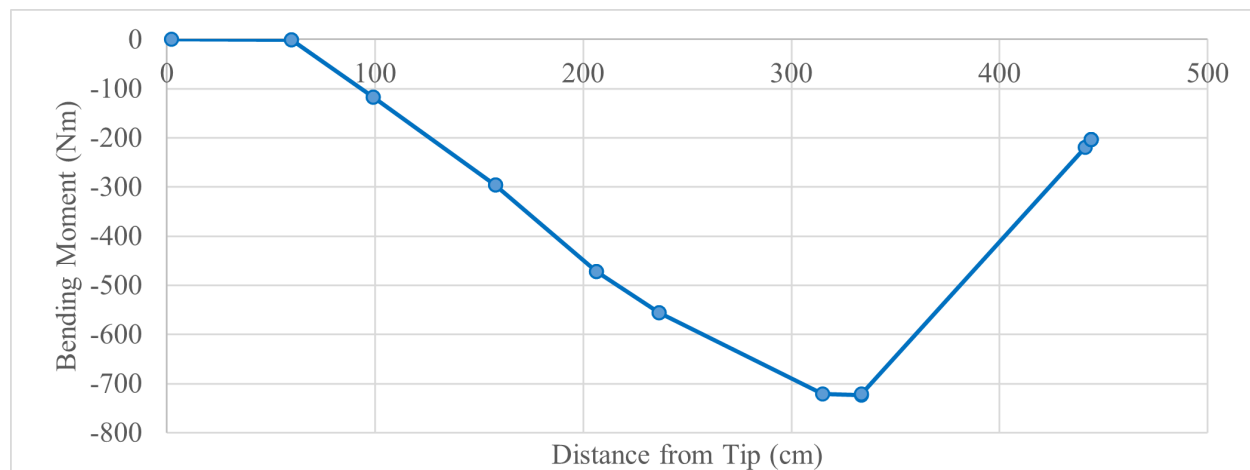


Figure 117: Bending moment diagram.

Table 42: Quantitative Component Analysis Values.

Station	Component	Mass (kg)	x_i (cm)	Acc (m/s ²)	Force (N)	Shear (N)	Moment (Nm)	Inertia (kgm ²)
1	Tip	0.075	2.25	-15.51	-1.164	-1.164	0.000	0.6915
2	NC Normal	0	59.86	0.000	-292.1	-293.3	-0.6703	0.0000
3	NC	0.925	59.86	-4.045	-3.741	-297.0	-0.6703	5.600
4	NC Extension Normal	0	99.05	0.000	-28.72	-325.8	-117.1	0.000
5	Nose Cone Ext	5.818	99.05	3.757	21.86	-303.9	-117.1	24.89
6	FWD Tube Norm	0	157.75	0.000	-98.52	-402.4	-295.5	0.000
7	FWD Tube	2.584	157.75	15.44	39.91	-362.5	-295.5	5.671
8	Switch Band Norm	0	206.38	0.000	-6.882	-369.4	-471.8	0.000
9	Switch Band	3.601	206.38	25.12	90.47	-278.9	-471.8	3.567
10	Center Tube Norm	0	236.55	0.000	-58.53	-337.4	-555.9	0.000
11	Center tube	3.975	236.55	31.13	123.7	-213.7	-555.9	1.912
14	Motor	16.5	315	50.44	832.3	466.8	-721.3	0.618
12	AFT Tube	8.08	333.55	46.75	377.7	12.28	-723.6	0.137
13	AFT Tube Norm	0	333.55	0.000	-151.7	-365.4	-721.3	0.000
15	Phenolic	1.088	441.1	71.85	78.18	545.0	-219.2	1.989
16	Fins Norm	0	444	0.000	-1416	-870.9	-203.4	0.000
17	Fins	1.735	444	72.43	125.7	-745.2	-203.4	3.309
18	Fin Can Norm	0	444	0.000	25.01	-720.2	-203.4	0.000
19	Fin Can	0.736	444	72.43	53.31	-666.9	-203.4	1.404
Total		45.117						49.79

Understanding the interactions of axial and transverse loads on the launch vehicle allows the induced shear and normal stresses to be determined, and hence a suitable design. The maximum transverse shear stress may be determined through the boat tail, shown in Figure 114 at 444 cm from the tip of the launch vehicle:

$$\tau = \frac{VQ}{It} = 2.4248 \text{ MPa} \quad (61)$$

Normal stresses are contributed by the compressive load from thrust (5000 N) and bending moments:

$$\sigma_{Compressive} = \frac{F}{A} = \frac{F}{\frac{\pi}{4}(D^2 - d^2)} = -6.8943 \text{ MPa} \quad (62)$$

$$\sigma_{Bending} = \frac{My}{I} = 26.1810 \text{ MPa} \quad (63)$$

The maximum normal stress experienced is then the summation of magnitudes of compressive and bending stresses:

$$\sigma_{Total} = \sigma_{Compressive} \pm \sigma_{Bending} = -33.075 \text{ MPa} \quad (64)$$

The shear and normal stresses may then be represented using Mohr's circle, shown in Figure 118. They may be decomposed to stresses in the principle planes:

$$\tau_{max} = \sqrt{\tau^2 + (\sigma_{total} - \sigma_{avg})^2} = 16.715 \text{ MPa} \quad (65)$$

$$\sigma_2 = \sigma_{avg} - \tau_{max} = -33.252 \text{ MPa} \quad (66)$$

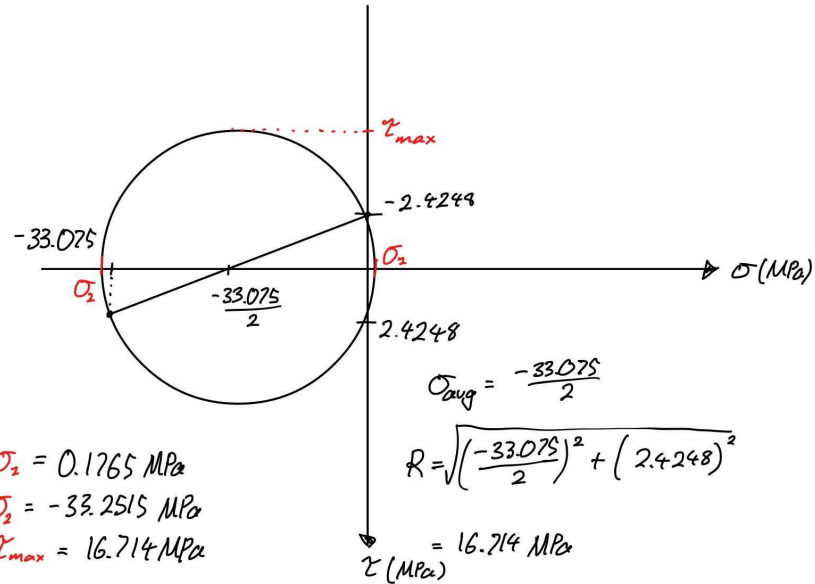


Figure 118: Mohr's Circle for Plane Stress.

9.12.3 Body Tubes

A compression test was conducted on a fibreglass tube sample constructed with five layers of fibreglass, with the maximum sustained compressive load measured to be 77.43 kN. The corresponding compressive stress sustained and MoS may be calculated:

$$\sigma_{Compressive} = \frac{F}{\frac{\pi}{4}(D^2 - d^2)} = 106.8 \text{ MPa} \quad (67)$$

$$MoS = \frac{106.8}{1.5 \times 33.252} - 1 = 1.14 \quad (68)$$

A tube with 6 layers of fiberglass was also tested, and that failed at 84.94 kN. Because of the increased outer diameter (155.4 to 156.0mm), we get the following new theoretical values following the same calculations as Section 9.10.2:

- $\tau = \frac{VQ}{It} = 2.0362 \text{ MPa}$
- $\sigma_{Compressive} = \frac{F_{thrust}}{A} = -5.7341 \text{ MPa}$
- $\sigma_{Bending} = \frac{My}{I} = 21.9418 \text{ MPa}$
- $\sigma_{Total} = \sigma_{Compressive} - \sigma_{Bending} = -27.676 \text{ MPa}$
- $\sigma_{avg} = \frac{\sigma_{Total}}{2} = -13.838 \text{ MPa}$
- $\tau_{max} = \sqrt{\tau^2 + (\sigma_{total} - \sigma_{avg})^2} = 2.0362 \text{ MPa}$
- $\sigma_2 = \sigma_{avg} - \tau_{max} = -27.825 \text{ MPa}$

The actual compressive strength of the tube can be found using:

$$\sigma_{compressive} = \frac{84940}{\frac{\pi}{4}(0.156^2 - 0.1524^2)} = 97.41 \text{ MPa} \quad (69)$$

The new MoS is therefore:

$$MoS = \frac{\sigma_{tested}}{FoS \times \sigma_2} - 1 = \frac{97.41}{1.5 \times 27.825} - 1 = 1.33 \quad (70)$$

This increased MoS comes at the cost of an additional 20% of mass. Since carbon fiber tubes will be used between the AV bay and the boat tail (the area which experiences the highest loadings), five layers will

be used for fiberglass body tubes. It is expected that five layers will also be used for carbon fiber tubes due to its greater strength compared to fiberglass. This value is significantly larger than that sustained by the sample before failure from compressive load. The presence of cracks without lateral deflection signifies failure from compression rather than buckling. Calculations on buckling critical load may be conducted using the experimental Young's Modulus $E = 13.93$ GPa and aft tube length of 1.4 metres:

$$P_{cr} = \frac{\pi^2 EI}{(KL)^2} = 151.3 \text{ kN} \quad (71)$$

The critical load for buckling is much higher than the compressive load at failure, hence is within satisfactory criteria.

9.12.4 Justification of Carbon Fibre Body Tube Strength Prediction

The fibreglass tubes are made from 300 grams per square metre (gsm) fibreglass while the carbon fibre tubes are made from 240gsm carbon fibre. Therefore, while carbon fibre has a higher strength-to-weight ratio than fibreglass, there is doubt regarding the performance of the carbon fibre tube in comparison to the fibreglass tube since the difference in gsm might diminish the strength-to-weight ratio advantage of the carbon fibre tube. Furthermore, the high strength-to-weight ratio of carbon fibre is often derived from tensile tests, not compression tests, and thus the strength-to-weight ratio of carbon fibre must also be validated in a compression setting.

[16] details a research paper that used ASTM: D3410 standardised testing to measure the compressive strength of carbon fibre and fibreglass samples. The results are shown in Figure 119.

Table 2. Compressive properties of the plain and hybrid composite laminates

Composite specimen	(V_f)	Strain (%)	Stress (MPa)	Modulus (GPa)	Specific strength (KNm/kg)	Specific stiffness (MNm/kg)	ρ (g/cc)	(r_h)
GFRP	0.539	1.51 (± 0.11)	430.8 (± 8.36)	28.52	295.061	19.53	1.460	0.00
<i>Group I</i>								
[CG-1:2]	0.430	1.26 (± 0.05)	465.5 (± 10.21)	36.94	351.347	28.87	1.325	0.33
[C1/G2]	0.429	1.25 (± 0.06)	464.1 (± 11.32)	37.13	350.546	28.04	1.324	
<i>Group II</i>								
[CG-1:1]	0.431	0.92 (± 0.04)	491.2 (± 11.32)	54.57	374.398	40.69	1.312	0.50
[C1/G1]	0.433	0.91 (± 0.04)	474.0 (± 10.88)	52.09	359.380	39.49	1.319	
<i>Group III</i>								
[CG-2:2]	0.430	0.93 (± 0.04)	480.8 (± 12.34)	51.69	367.859	39.54	1.307	0.50
[C2/G2]	0.432	0.91 (± 0.03)	470.0 (± 8.98)	51.64	359.061	39.44	1.309	
<i>Group IV</i>								
[CG-3:2]	0.441	0.86 (± 0.04)	527.9 (± 7.89)	61.38	410.799	47.76	1.285	0.60
[C3/G2]	0.438	0.85 (± 0.02)	512.4 (± 8.97)	58.22	397.518	46.73	1.289	
<i>Group V</i>								
[CG-2:1]	0.458	0.83 (± 0.02)	611.4 (± 13.21)	73.66	481.067	57.95	1.271	0.67
[C2/G1]	0.452	0.82 (± 0.04)	583.2 (± 8.87)	71.12	455.633	55.56	1.280	
<i>Group VI</i>								
[CG-3:1]	0.461	0.79 (± 0.04)	676.5 (± 5.65)	85.63	533.533	67.53	1.268	0.75
[C3/G1]	0.469	0.79 (± 0.01)	651.7 (± 8.86)	82.49	505.577	63.99	1.269	
CFRP	0.563	0.7 (± 0.05)	1197 (± 10.89)	171.0	967.671	138.23	1.237	1.00

Figure 119: The comparison of GFRP and CFRP properties during the compression test conducted in [16]

It found that CFRP had $\frac{1197}{430.8} = 2.78$ times the compressive strength of GFRP, as well as $\frac{967.671}{295.061} = 3.28$ times the specific strength (strength-to-weight ratio) of GFRP. While the gsm of the material is not stated, the density (in grams per cubic centimetre (g/cc)) of the fibreglass and carbon fibre are 1.460 and 1.237 respectively, corresponding to an 18% increase in g/cc for the fibreglass. This is comparable to the 25% increase in gsm of the fibreglass (300 gsm) from the carbon fibre (240 gsm) used to make the tubes.

Based on the above information and the comparability of fibre density, it can be concluded that even though carbon fibre has a lower gsm than fibreglass, the difference in compressive stress between them is

so large that it would be reasonable to predict that the carbon fibre tube would be able to hold much more compressive force than the fibreglass tube. This prediction is experimentally verified in subsection 11.6.

9.12.5 FEA of Composite Materials

Composite materials are inherently difficult to model with finite elemental analysis due to them being orthotropic materials. Material processing and manufacturing methods have considerable effects on part integrity so standard operating procedures are put in place to ensure consistency and repeatability. Often a series of mechanical tests on composite parts or coupons are performed to verify strength and stiffness values in various orientations.

To get a ballpark idea of how strong or stiff a composite laminate will be, Classical Laminate Theory can be used for calculating values. Further research is required to develop this skill.

9.12.6 Thread Shear-Out

Calculations were undertaken to determine the required length of thread engagement to significantly reduce the chance that the failure mode of a threaded connection will be thread shear-out. Equations 72 to 76 have been used to determine the required thread length with relevant parameters outlined in Section 9.12.6 [18].

	$d = 0.2489$	in	Maximum major diameter of external thread
	$d_{1min} = 0.2408$	in	Minimum major diameter of external thread
	$d_{2min} = 0.2127$	in	Minimum pitch diameter of external thread
	$D_{1max} = 0.207$	in	Maximum minor diameter of internal thread
	$D_{2max} = 0.2164$	in	Maximum pitch diameter of internal thread
Shear-Out Parameters	$n = 20$		Threads per inch
	$UTS_{external} = 505$	MPa	Ultimate Tensile Strength (UTS) External material
	$UTS_{internal} = 310$	MPa	UTS Internal material
	$A_s = 0.03147$	in^2	Tensile stress area
	$AS_s = 0.06295$	in^2	Minimum thread shear area for external threads
	$AS_n = 0.1012$	in^2	Minimum thread shear area for internal threads
	$LE = 0.1711$	in	Length of thread engagement
	$LE_2 = 0.1734$	in	Length of thread engagement with different strength materials

Shear-Out Relationships

$$A_s = \frac{\pi}{4} \left(d - \frac{0.9743}{n} \right)^2 \quad (72)$$

$$AS_s = \pi \cdot n \cdot LE \cdot D_{1max} \left[\frac{1}{2n} + 0.57735 (d_{2min} - D_{1max}) \right] \quad (73)$$

$$AS_n = \pi \cdot n \cdot LE \cdot d_{1min} \left[\frac{1}{2n} + 0.57735 (d_{1min} - D_{2max}) \right] \quad (74)$$

$$LE = \frac{2 \cdot A_s}{\pi \cdot n \cdot D_{1max} \left[\frac{1}{2n} + 0.57735 (d_{2min} - D_{1max}) \right]} \quad (75)$$

$$LE_2 = LE \cdot \frac{AS_s \cdot UTS_{external}}{AS_n \cdot UTS_{internal}} \quad (76)$$

The results of using these equations are presented in Table 43 considering a FoS of 3. Metric threads used tolerance class 6g and 6H for external and internal threads respectively to obtain the most conservative result. Unless otherwise stated, Al6061 T6 was used as the internal thread material.

Table 43: Tabulated values for required thread lengths.

Thread size	LE_2 (mm)	Required Thread Length FoS=3 (mm)	Final Design Length (mm)
M6x1.0	5.25	16	6
M6x1.0 (Mild Steel)	3.22	10	10
M10x1.25	9.26	28	25
M5x0.8	4.51	14	12
M8x1.25 into 7075T6	3.76	12	-
M8x1.25	6.94	21	21

9.12.7 Tube Shear from Radial Screws

Calculations were undertaken to determine the maximum applied stress on the screws and tubes, allowing for factor of safety calculations.

The shear area is conservatively assumed to the whole diameters. Therefore, the total shear area where the thickness of the wall is 1mm,

$$A = 7.5 \times 1.5 \times 12 = 90 \text{ mm}^2 \quad (77)$$

A hole diameter of 7.5mm is used because of the use of tinnerman washers, which increase the area across which the force is applied to reduce the stress.

To be conservative in calculations the maximum force was applied individually to each bulkhead, to determine the lowest possible factor of safety no matter the force distribution across the bulkheads. Each bulkhead has 12 radial screws, the maximum acceleration used in calculations is 30G and the mass used for calculations is 23.4kg.

The applied screw stress is given by:

$$\tau = \frac{F}{A} = \frac{23.4 \times 30 \times 9.81}{\pi \times 12 \times 1.5^2} = 81.19 \text{ MPa} \quad (78)$$

The applied tube stress is given by:

$$\tau = \frac{F}{A} = \frac{23.4 \times 30 \times 9.81}{90} = 51.01 \text{ MPa} \quad (79)$$

The factor of safety calculations can be completed using the ultimate failure stresses established in previous projects. The carbon tube failure stress is 315 MPa, given in the Bluewren IREC. The fibreglass tube failure stress is 106.7 MPa, given in the Rosella CDR, and the screw failure stress is 152 MPa.

Therefore, the FoS for the screw shear is:

$$FoS_{screws} = \frac{152}{81.19 \times 1.15} = 1.63 \quad (80)$$

The FoS for the carbon tube shear is:

$$FoS_{carbon} = \frac{315}{51.01} = 6.18 \quad (81)$$

The FoS for the fibreglass tube shear is:

$$FoS_{fibreglass} = \frac{106.7}{51.01} = 2.09 \quad (82)$$

10 Recovery Subsystem

10.1 Subsystem Overview

The recovery subsystem is responsible for the controlled descent of the launch vehicle and the relay of telemetry during all stages of flight. The parachutes and rigging components must have sufficient strength and drag to allow for the launch vehicle's safe landing with minimal damage, achieved through the target descent rates in Table 44. The subsystem is responsible for the avionics (Figure 120) required for parachute deployment and transmitting telemetry data during flight. The architecture of the on-board avionics Recovery is also assigned the launch vehicle's on-board cameras, ensuring their safe and reliable operation during flight.

	Descent rate requirements ($m s^{-1}$)	Target Projects	1 Security Insights	Edit	Filling	Simulation	133descent ra
Drogue	20-50		25-30				
Main	<11		5.5-6.5				

Table 44: Parachute Descent Rate Requirements

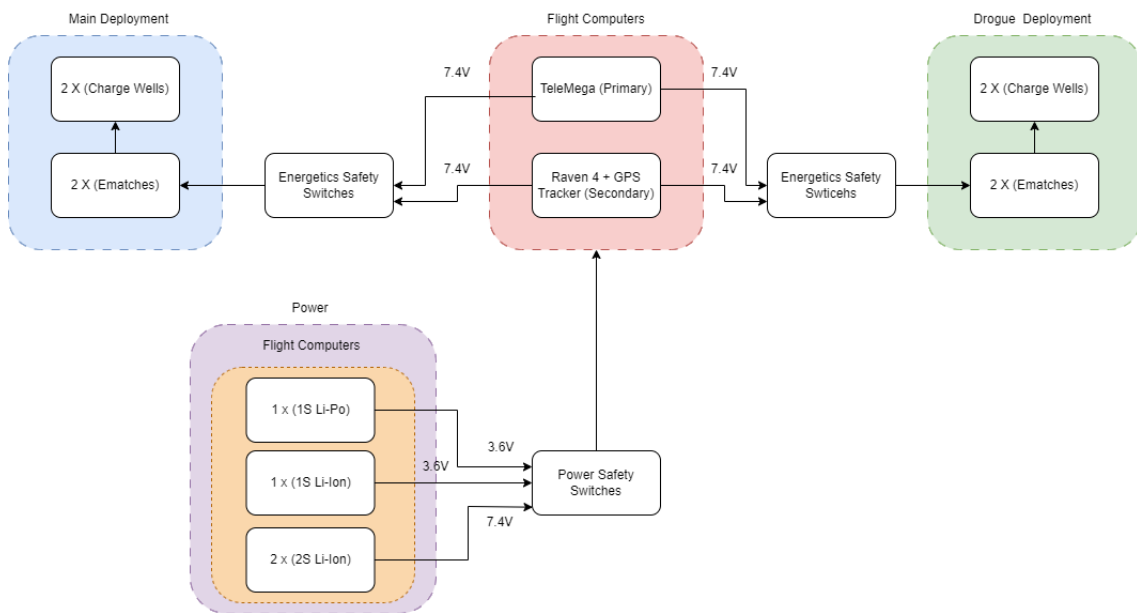


Figure 120: Avionics Functional Diagram

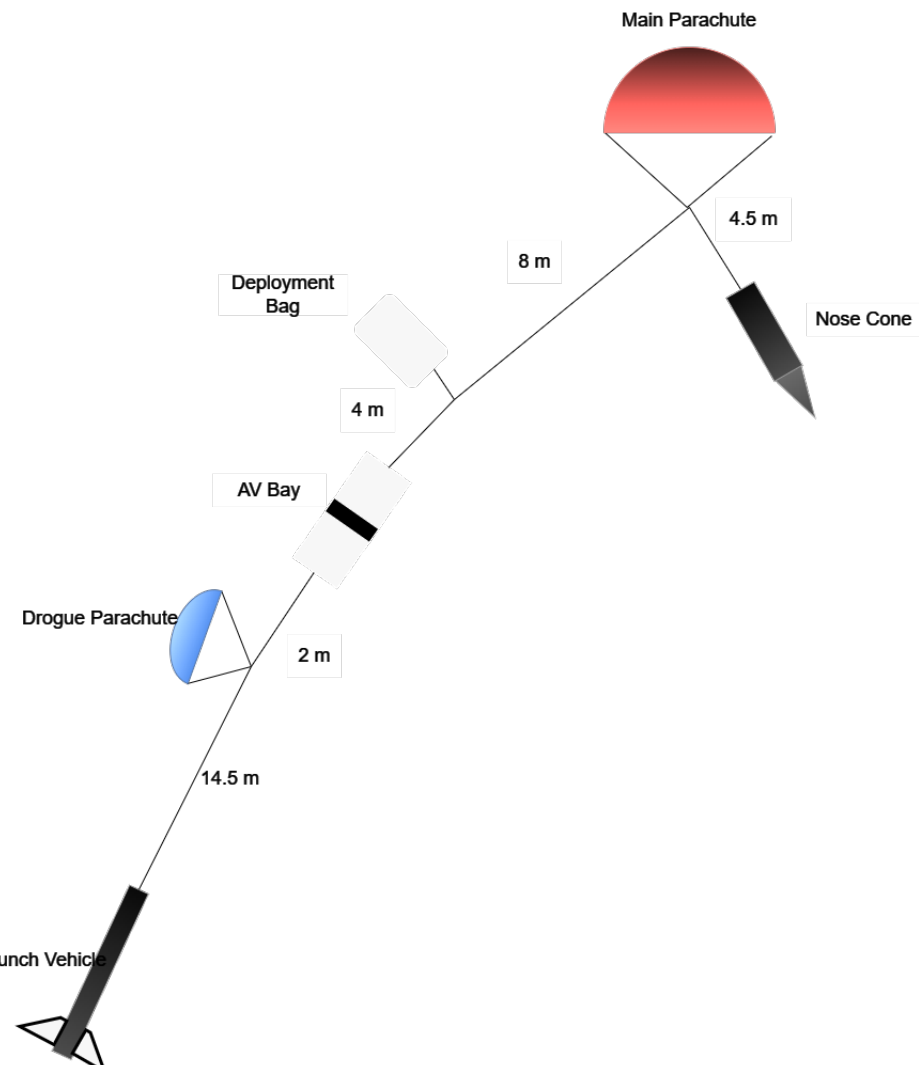


Figure 121: Launch Vehicle Layout after Drogue and Main parachute deployment

10.2 Parachutes

10.2.1 Parachute Profile

Pardalote drogue and main parachutes feature a toroidal canopy profile (Figure 122) for optimal drag characteristics. Toroidal parachutes have outstanding performance to weight ratio, hence reducing material cost and weight [1]. Our team also has significant experience in dealing with toroidal parachutes, allowing us to utilize expertise in regards to parachute manufacturing and calculations related to sizing and loading.

The parachute features a spill hole in its canopy to increase the descent stability. It allows air to exit the parachute evenly, acting as a pressure vent, reducing oscillation. Spill hole diameter will be 20% of the parachute diameter, resulting in approximately a 4% drag area reduction, increasing stability without a significant decrease in drag.

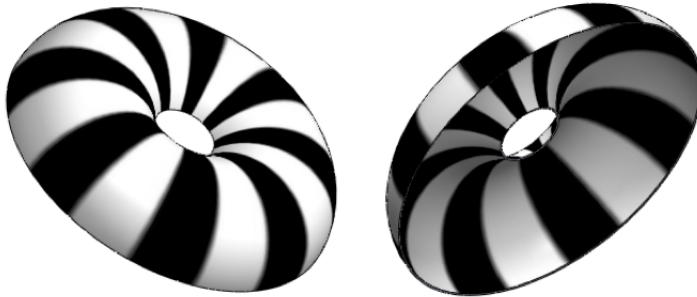


Figure 122: Toroidal canopy profile.

Furthermore, the parachute can achieve a C_d of up to 2.2 using vent reefing - attaching a centre line to the shroud lines inside the canopy vent to pull the spill hole inwards - increasing drag area by up to 30%, decreasing descent rate.

10.2.2 Parachute Sizing

To size the SRAD parachutes, the relationship between descent rate and parachute diameter was graphed across a range of drag coefficients to establish a factor of safety and ensure if the C_d fell below the target of 2.2, the launch vehicle's descent will remain within the required range of $23\text{-}50ms^{-1}$ for drogue and $3\text{-}11ms^{-1}$ for main.

The surface area of the toroidal parachute with the inclusion of a spill hole was determined using equation 83 and plugged into 84 to determine the expected descent rate. Other input parameters into the sizing code included the dry weight and the air density during parachute deployment.

$$A = \frac{(\pi D_m)^2}{4} \quad (83)$$

$$V = \sqrt{\frac{2D}{C_d \rho S}} \quad (84)$$

	Dry Weight(kg)	Density at Deployment(kgm ³)
Main	40	1.15
Drogue	40	0.90

Previous projects sized their parachutes with the assumption that they may be able to achieve a coefficient of drag comparable to its High Performance COTS variants from companies such as Fruity Chutes and Rocketman. Flight data from this previous project suggest that the main parachute had an approximate C_d of 1.9, however the parachute did not fully inflate. Additionally, the uneven length of the shroud lines compromised expected performance. In order to ensure any issues in design or manufacturing do not inhibit the success of all recovery events, for Pardalote the conservative estimate of a 1.9 C_d will be used for both parachutes.

To reach the target speeds outlined in the subsystem overview, the diameter of the drogue parachute was chosen to be 36 inches and the main parachute 150 inches. Figure 123 shows the sizing output for drogue and Figure 124 for main. The chosen diameters are fairly large and due to the 40kg dry weight of Pardalote, both main and drogue will experience significant shock loads upon deployment. This sizing solution also increases the risk of tangling shock cords which can be resolved by selecting heavier and flatter shock cords.

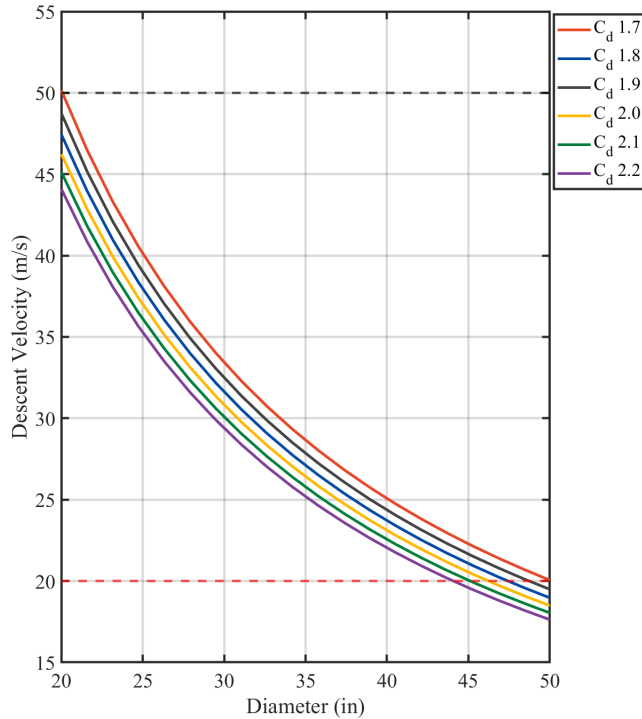


Figure 123: Drogue Parachute Descent Rates against C_d

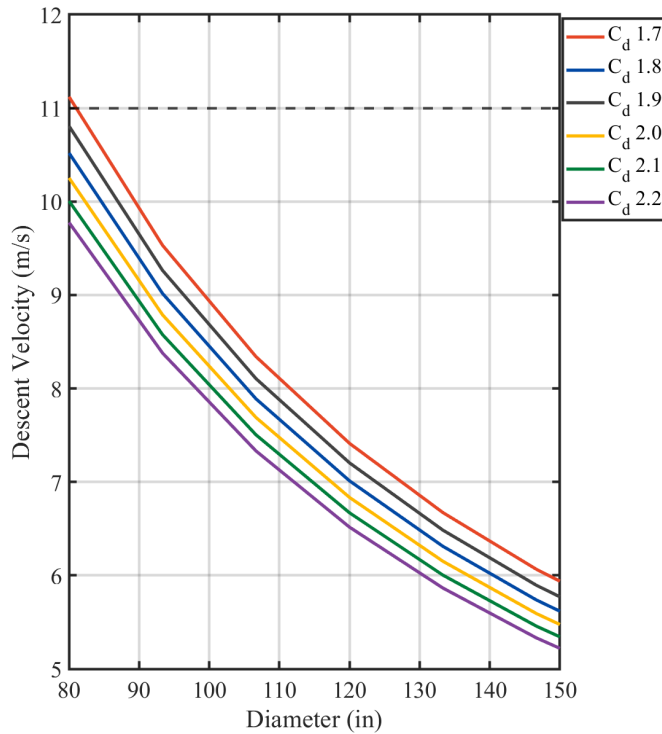


Figure 124: Main Parachute Descent Rates against C_d

10.2.3 Parachute Loading

In order to select components for the recovery system, it is vital to know the maximum shock load when the parachutes open. These maximum shock loads were calculated using the Opening Shock Calculation (OSCALC). OSCALC is a program that estimates the maximum drag force generated during parachute inflation by using basic input variables. The program is based on Equation 85:

$$F_{max} = \left(\frac{1}{2}\rho V_{stretch}^2\right)(SC_D)_{sd}C_k \quad (85)$$

The initial input values for drogue and main can be seen in Table 45 and Table 47 respectively. Using these input parameters, OSCALC returned a range for the shock loads that the parachutes may experience, detailed in Table 46 (drogue) and Table 48 (main). As such, it can be expected that the rocket will experience up to 35G of force during main deployment.

Although the parachute was sized using an assumed Cd of 1.9, shock load calculations will use a more conservative estimate of 2.2. Moreover, to minimise risk during the recovery stages of flight, the materials and rigging hardware will be selected based on the determined upper bound shock loads.

Value	Input	Justification
Atmospheric Density (kg/m^3)	0.9	10000ft (apogee) + 1200ft (launch site height above sea level @ Tolano)
Total Dry Mass (kg)	40	
Estimated Fall Rate at line stretch (m/s)	50	Max allowed descent rate under drogue is 50m/s
Coefficient of Drag	2.2	The target C_d of 2.2 is comparable to the performance of COTS parachutes
Nominal Surface Area (m^2)	0.622	Torus shape \rightarrow 40 inch diameter
Non-dimensional Fill Time	10	Value for reefed (ribbon) based off OSCALC documentation

Table 45: The input values for OSCALC to calculate the maximum shock load for drogue

Lower Bound (N)	Average (N)	Upper Bound (N)
924	1539	2155

Table 46: The calculated opening shock loads for drogue parachute

Value	Input	Justification
Atmospheric Density (kg/m^3)	1.06	1000ft (main deployment) + 1200ft (launch site height above sea level @ Tolano)
Total Mass (kg)	40	
Estimated Fall Rate at line stretch (m/s)	46	Overestimate in case there is damage to drogue from black powder or a rip
Coefficient of Drag	2.2	
Nominal Surface Area (m^2)	11.4	Torus shape \rightarrow 150inchdiameter
Non-dimensional Fill Time	10	Value for reefed (ribbon) based off OSCALC documentation

Table 47: The input values for OSCALC to calculate the maximum shock load for main

Lower Bound (N)	Average (N)	Upper Bound (N)
4577	8392	12206

Table 48: The calculated opening shock loads for main parachute

10.2.4 Parachute Manufacturing

The parachutes will be made of 1.1 oz Mil-Spec calendared rip-stop nylon. This material was selected as it is lightweight and compact while strong and resistant to tearing. Additionally, the performance of the

parachute will be closer to the predicted drag calculations as calendered rip-stop nylon is non-porous as it has been passed through hot rollers.

Both parachutes will have flat shroud lines for ease of manufacturing and to maximise the strength of the shroud line connections. The shroud lines for the drogue parachute will be made of spectra for its excellent strength-to-weight ratio and abrasion resistance. However, spectra is less suitable for the main parachute as its low weight complicates shroud line management. As the main parachute will have more and longer shroud lines than the drogue, its shroud lines will be made from 650 coreless nylon paracord. This is because nylon has a sufficiently high strength-to-weight ratio but is slightly heavier than spectra, which reduces the risk of tangling and makes shroud line management easier. On both parachutes tubular webbing will connect the shroud lines on the spill hole to those on the outside edge. This webbing was chosen as it will take a significant portion of the total shock load and as such must be stronger than the other shroud lines. The webbing used for the drogue is rated to 10.2kN, significantly more than the expected maximum shock load of 2.6kN. Further, the webbing is visually distinct from the other shroud lines which will assist when managing the shroud lines and packing the parachute.

Increasing the length of the shroud lines increases the parachute drag due to less interference from the body wake of the launch vehicle. However, increased slack also increases initial opening shock loads. A shroud line length of 1.15 times the parachute diameter shall balance drag with opening shock loads. Table 49 summarises the final design choices that must be considered for manufacturing.

	Canopy	Shroud Line	Parachute Diameter <i>in</i>	Line Length <i>in (mm)</i>
Drogue	1.1 oz Ripstop Nylon	Spectra Dynamica	35	28.75 (730)
Main	1.1 oz Ripstop Nylon	coreless nylon paracord	150	161 (4089)

Table 49: Parachute Material and Sizing Summary

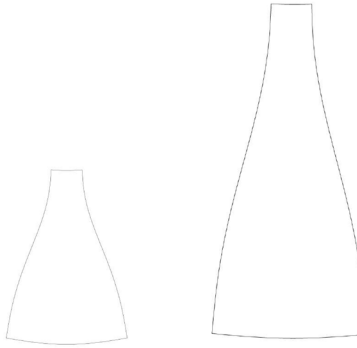


Figure 125: Gore Template for Drogue (left) and Main (right)

Gores, as seen in Figure 125, are identical pieces of material sewn together to form the canopy of a parachute. Curved gores must be used in the manufacturing process to achieve a toroidal profile.

The gores for the drogue parachute will be cut from the material using a laser cutter in order for high precision to be achieved. Additionally, the heat from the laser cutter will seal the edges of the nylon, stopping the material from fraying.

Due to the large size of the gores for the main parachute, they are unable to be cut using the laser cutter. Instead, they will be cut from the rip-stop by tracing the gore template using a hot knife. Similar to using a laser cutter, this will seal the raw edges of the fabric.

A large number of gores allows the parachutes to achieve a more accurate toroidal shape. However, this increases the complexity of the design and the number of weak points, ultimately increasing the risk of

failure. Therefore, the number of gores chosen is eight for the drogue parachute and twelve for the main. This gore selection is also optimal for efficient material usage.

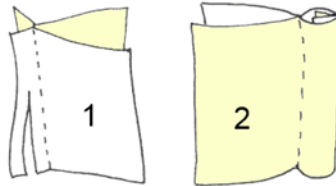


Figure 126: French Seam

The gores will be joined with french seams, as shown in Figure 126. French seams are created by sewing a straight stitch on the edge of the gores with the wrong sides together. The pieces and seam are then flipped. The seam is ironed, and another straight stitch is sewn to conceal the raw edges of the fabric. This creates a flap that will be ironed down and sewn to one side. The sides of each gore will have a 1.5 cm seam allowance to allow for a french seam connection.

10.3 Parachute Deployment

The Drogue parachute will be deployed at apogee and the Main parachute will be deployed at 1,000 ft to ensure the launch vehicle lands safely and with minimal damage. Both deployments will be actuated by black powder. The altitude for drogue ($\approx 10,000$ ft) and main ($\approx 1,000$ ft) will allow for complete black powder combustion to safely ensure the launch vehicle's separation. This deployment system is also lighter and less complex than other systems such as C02 deployment.

Each deployment will function by having two charge wells (Primary and Secondary) with black powder and two e-matches inside each well. The Secondary charge well is filled with 1.5 times more black powder than what is calculated below so that in the event that the primary charge well combustion does not break the shear pins, a larger combustion can increase changes of separation. The secondary charge well combustion will occur independent of the primary charge wells performance to minimise risk and points of failure.

The e-matches are connected to one of the two flight computers such that both flight computers are attached to an e-match in every charge well. The wells will be filled with wadding and sealed using a charge well cap and electrical tape. When the flight computer detects apogee or 1,000 ft altitude, a surge of current will be sent to the e-matches, lighting them and thus causing combustion of the black powder. The resulting pressure will cause the shear pins to break, separating the launch vehicle and thus deploying the parachute.

10.3.1 Black Powder Calculations

The minimum amount of black powder for successful deployment is determined by the force required to break the shear pins holding the body tubes together. Assuming that the products of black powder combustion behave like an ideal gas, using the ideal gas law (Equation 86) we are able to determine how much black powder will be required to generate the necessary pressure and thereby force for deployment.

$$PV = mRT \quad (86)$$

- P = Pressure required for Separation
- V = Volume of Recovery Bay
- m = Mass of Black Powder
- R = Gas Constant for Black Powder
- T = Temperature of Black Powder at Combustion

To maximise the likelihood of successful deployment, a 1.5 Factor of Safety is applied to the mass of black powder for the primary charge wells. The secondary charge wells are given 50% more black powder than

primary. The final masses of black powder for each of the four charge wells is outlined in Table (insert table).

10.3.2 Charge Well Sizing

The charge wells are sized based off the black powder masses calculated in the previous section. Given black powder's density ($0.54134\text{g}/\text{cm}^3$), the volume of black powder and thus the charge wells are determined. An aspect ratio of 1.52 was validated by previous projects as effective sizing.

10.4 Rigging

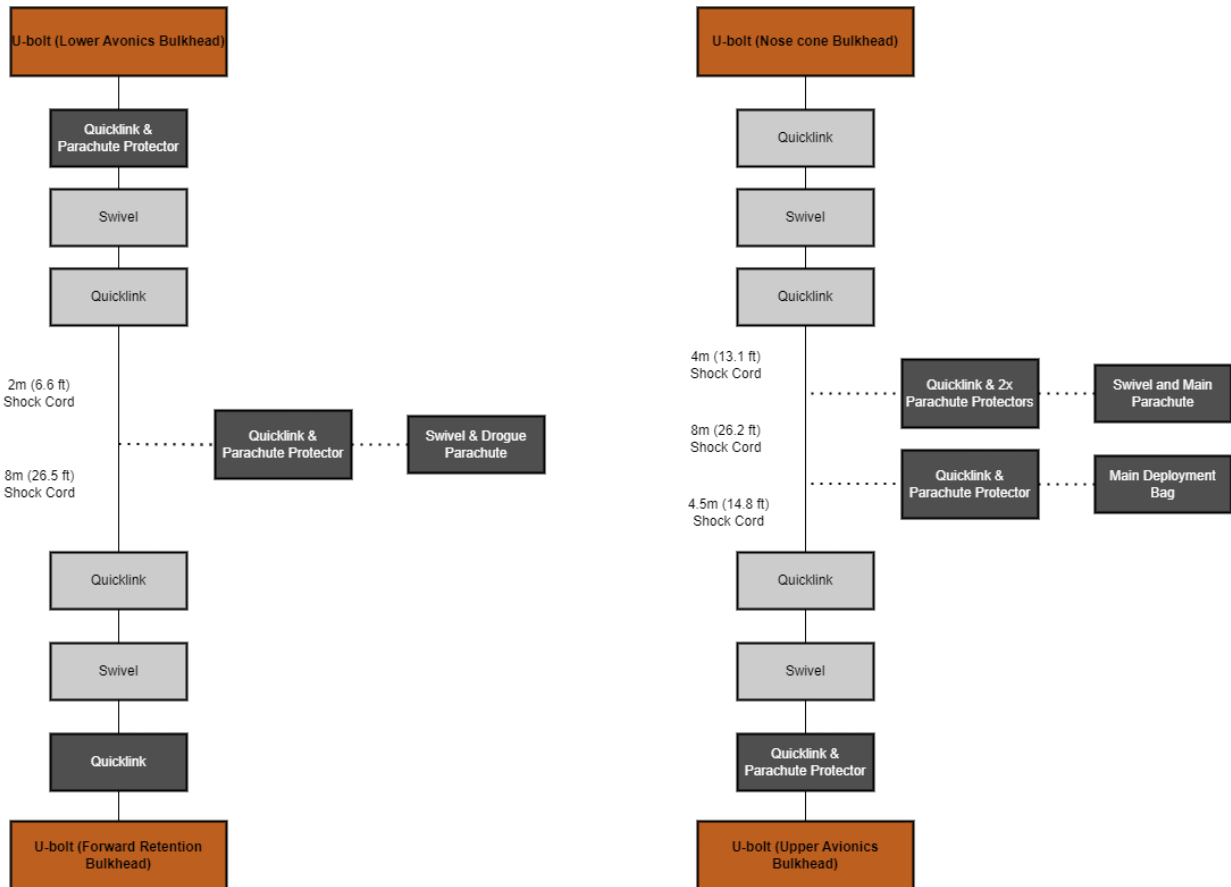


Figure 127: Rigging diagram for Drogue (Left) and Main (Right)

The rigging components selected have been picked to ensure they withstand shock loads, are less susceptible to tangling during deployment and components do not collide with each other during decent under drogue and main. The upper bound shock loads were calculated to be 2155 N from the Drogue parachute and 12206 N from the Main parachute.

10.4.1 Shock Cords

Two 26.7 kN (6,000 lbf) rated braided Kevlar shock cords will be used for the main and drogue parachute. Kevlar is best suited to the requirements over nylon due to its higher strength-to-weight ratio. Additionally, Kevlar has superior thermal properties to Nylon which reduces the chance of component failure from contact with black powder combustion gasses. The maximum shock load experienced by these cords will be the dry mass of the rocket (40 kg) under a 35 G-force during main deployment, distributed evenly over all shock cords to the launch vehicle. Both shock cords will be 16.5 m in length to reduce shock loads as it ensures kinetic energy at separation is properly dissipated.

10.4.2 Swivels and Quick Links

The Main parachute and ends of each shock cord are connected to their respective attachment points using 26.7 kN (6,000 lbf) rated Fruity Chutes stainless steel swivels. This is then connected to another fruity

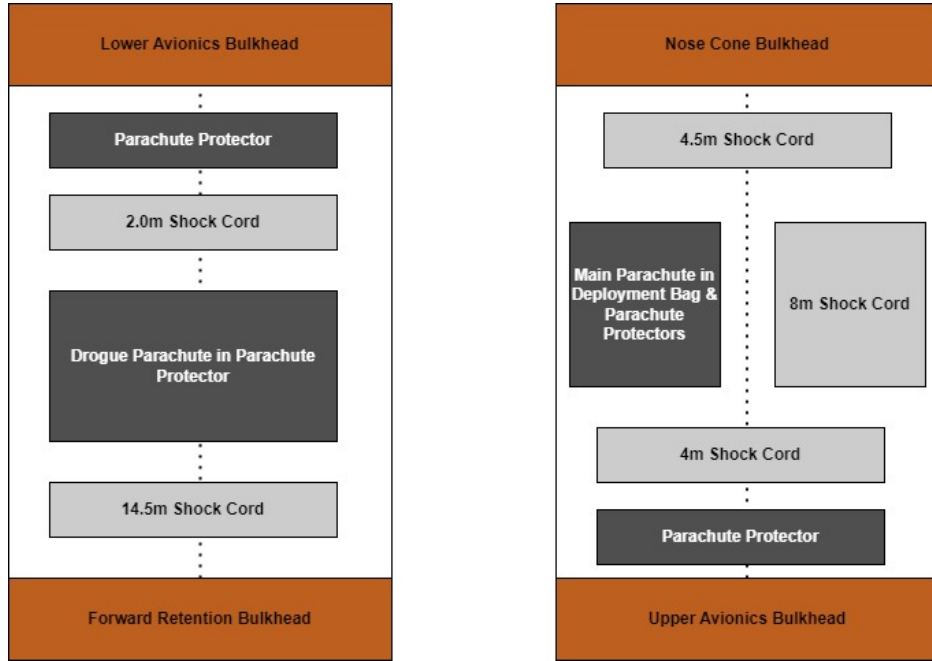


Figure 128: The packing diagrams for Drogue (Left) and Main (Right)

chutes 3/8" stainless steel quick link with a shock load rating of 26.7 kN (6,000 lbf).

The drogue parachute will be attached to the shock cord with a 1/4" Rocketman stainless steel quick link rated for 17.8 kN (4,000 lbf), *and a 13.3 kN (3000 lbf) rated Rosco barrel swivel as shock loads from drogue is significantly less than the main parachute.*

These swivels and quicklinks have been selected to withstand the respective maximum shock loads that drogue and main parachute experience when opening.

10.4.3 Deployment Bag

The 2.4 m (95 in) diameter main parachute will be packed inside a Kevlar-Nomex cloth deployment bag. The shroud lines and attached shock cord will be neatly folded into elastic retainer loops on the outside of the deployment bag. The deployment bag and retainer loops keep the parachute and associated shroud lines firmly in place, preventing them from tangling. This lets them release easily when tension is applied to the shroud lines.

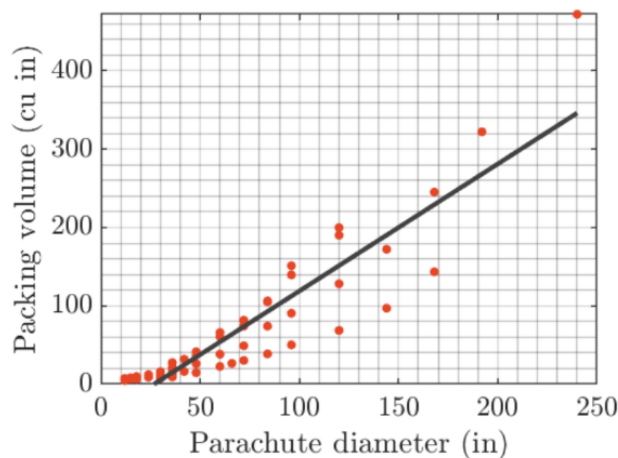


Figure 129: Packing Volume vs COTS Parachute diameter

To size the deployment bag correctly, the packing volume of the main parachute was first estimated using data from existing COTS parachutes from Fruity Chutes as shown in 129. This led to a predicted packing

volume of 190 cu inches for the main parachute.

10.4.4 Parachute Protectors

Four Kevlar-Nomex parachute protectors will be used as it has superior thermal properties and low permeability compared to alternative fabrics. A parachute protector will be used to wrap the drogue and main parachute. Additionally, a parachute protector will form a cup over the drogue and main deployment charges to act as a protective barrier. The protectors feature an extra layer of Nomex fabric in the center for extra protection.

These are vital to protecting the fabric parachutes from heat damage which may be caused by black powder charges. In addition to protecting the parachutes from the black powder charges, the parachute protectors function to pack the parachutes tightly, allowing the pressure from the deployment gases to reliably eject the parachutes. The inclusion of a blanket also has the benefit of preventing the drogue parachute from rubbing on the air frame interior and other rigging hardware, as the drogue parachute is not protected by a deployment bag.

10.4.5 Reefing Ring

By increasing the inflation time of a parachute, the shock loads it experiences will reduce. Due to the significant shock loads experienced by main (12.2kN Upper Bound), a reefing ring will be used to reduce these opening forces.

Upon deployment, as the shroud lines straighten the reefing ring will fall down the lines. The Rocketman 1/4" stainless steel reefing ring will be used because of its durability and low weight of 32 g.

10.4.6 Shock Cord Protectors

The body tubes will rub against the shock cords as the launch vehicle descends. Shock cord protectors will be used to minimize the resulting abrasive damage, preventing the shock cords from breaking. The shock cord protectors will be a tube made from a single piece of Kevlar-Nomex fabric. Additionally, it stops the shock cords from burning when deployment charges go off.

10.4.7 Factor of Safety

Maximum shock load is from main parachute deployment. From the OSCALC simulation, the maximum shock load from the drogue parachute is 2155 N and 12206 N from the main parachute. This will be the working load for all rigging components. Table 50 and Table 51

The factor of safety (FoS) is calculated as follows, where $F_{Applied}$ is the maximum shock load:

$$FoS = \frac{F_{Failure}}{F_{Applied}} - 1$$

An FoS > 0 indicates sufficient strength for the rated load.

	$F_{failure}$ (kN)	$F_{Applied}$ (kN)	FoS
Shock Cords	26.7	12.2	1.18
Quick Links	26.7	12.2	1.18
Swivels	26.7	12.2	1.18

Table 50: Main Factor of Safety

	$F_{failure}$ (kN)	$F_{Applied}$ (kN)	FoS
Shock Cords	26.7	2.2	12.1
Quick Links	17.8	2.2	7.1
Swivels	13.3	2.2	5

Table 51: Drogue Factor of Safety

10.5 Avionics Bay Structure

10.5.1 Switch Plate

The switch plate designed for Pardalote will hold 11 switches and will serve as redundancies for each of the charge wells as well as the flight computers to increase safety when transporting the rocket, additionally preserving charge within the batteries. The switch plate design allows for a total of 12 switches, with the additional housing serving as a reserve.

The design of the entire switch plate will comprise two layers, where the top layer will contain three switches which will serve for each of the flight computers and GPS tracker and will be wired in series with the power supply, as well as containing the reserve switch. The bottom switch plate layer will contain 8 switches which will be wired in series with each of the 8 e-matches. Ultimately, the two-layer design will help visually confirm when flight computers are powered and when e-matches are active from the outside of the rocket. In addition, a numbering system will be used on each safing pin, clarifying the role of each arm on the switch plate.

The switches will be triggered via RBF (Remove Before Flight) pins which, when inserted, will cause open circuits within the system. The RBF pins will be secured via M4 threaded heat inserts located at the centre of the switch plate for each layer. Additionally, the RBF pins will have to provide a 120° clearance to avoid interference with the launch rail. Moreover, the switch plate design ensures that the RBF pins are strategically positioned across the two layers, facilitating easier removal before launch.

The switches that will be implemented within the system are Single Hole Double Throw (SPDT) Micro Lever Switches. When the RBF pins are inserted into the switch plate, they physically actuate the switches, causing discontinuity between power sources and the flight computers and e-matches respectively. As shown in Figure 130, when the RBF pins are removed, the switch will divert to the Normally Closed terminal (NC) and will close the circuit between the battery and the flight computer or energetics. Hence when RBF pins are inserted, the switch will cause an open circuit and there will be no contact between Common (COM) and NC. Ultimately the Normally Opened terminal (NO) will not be wired to anything and therefore for added safety during flight, terminal NO will be heat shrunk to avoid accidental conduction.



Figure 130: Micro Switch Circuit

10.5.2 Integration Structure

The avionics integration structure comprises mainly of the Power Distribution Board (PDB) which holds the flight computers, and the batteries to power the flight computers and trigger the e-matches. The structure rests upon two 12.7mm diameter AV rods that are attached to both upper and lower AV bulkheads. These AV bulkheads are connected to both main and drogue deployment systems in addition to the switch plate.

On one side of the structure is the Battery Bay, which is designed to accommodate five batteries (1x 1S LiPO, 2x 1S Li-ion, and 2x 2S Li-ion). The battery cutouts have been positioned on the top of the structure to permit a smaller overall footprint for the part while making battery wires more accessible. These batteries are held securely in place by a PLA bracket, shown in Figure 134. Furthermore, a cutout was made in the side of the part to allow connections from battery wires to wire extensions to be made in a single secure and

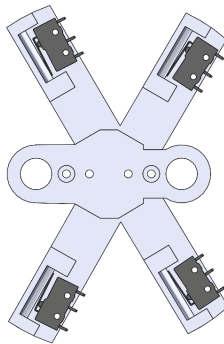


Figure 131: Flight Computer Switch Plate

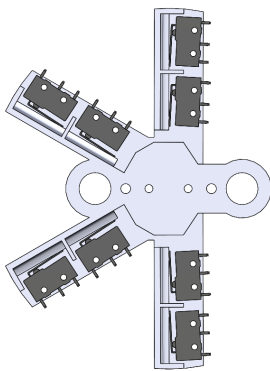


Figure 132: E-match Switch Plate

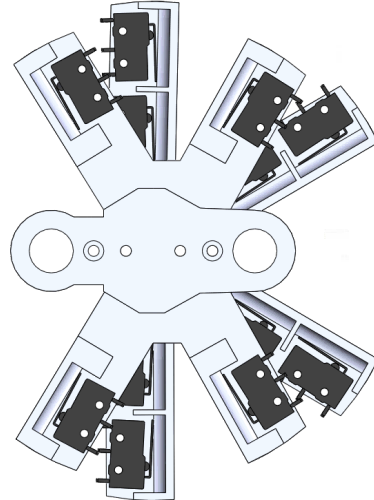


Figure 133: Combined Switch Plate

covered area, ensuring that connections weren't dangling in the AV Bay area. A second PLA bracket was made to cover the wire connections on the side of the battery bay, as seen in Figure 134. Smaller channel cutouts in the Battery Bay structure were made to route wires directly from batteries to the connection area. A large channel was also made with zip-tie holes to route wires from this connection area directly to the corner of the PDB, mounted on the back of the structure, where they would be inserted. Such a design allows for simple and short wiring routes, while also ensuring that all batteries are held firmly in place within a relatively compact and small structure.

PDB Mounting

The opposite side of the structure holds the PDB above the passage illustrated in Figure 136 . Conveniently

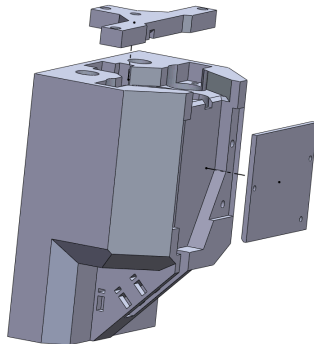


Figure 134: Side Exploded View with Brackets

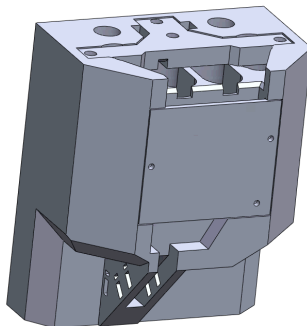


Figure 135: Front View with Brackets

installing the three flight computers. This area is made to be flat, large and parallel to the battery bay side for easy mounting. The PDB is to be mounted with the use of plastic M3 standoffs. To create secure connections, the standoffs screw into knurled inserts set into the structure.

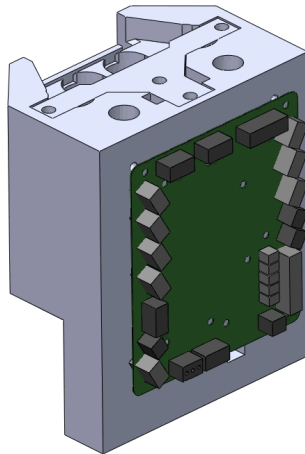


Figure 136: PDB Mounting

Wiring

Each battery features a JST-RCY connector that is then secured to a custom-length 22 AWG wire extension. The other end of these extensions feature a JST-PH connector, which is used to connect these extensions to the PDB, allowing battery power to be routed to the desired flight computer. Additionally, physical wire is used to connect screw terminals on the PDB to each of the eleven used SPDT switches on the switch plate, and from other respective screw terminals to flight computer terminals. All screw terminal connections are crimped with bootlace ferrules to reduce contact resistance and minimise the chance of stray wires causing short circuits. Each wired connection of each switch has been discussed in the switch section. Furthermore, wired connections from the PDB to the barrier blocks on the bulkheads necessitate connections into screw terminals on the board. These connections also employ bootlace ferrules to enhance reliability. Circular connectors are used to facilitate easy connections between the PDB and the barrier blocks, streamlining the

overall wiring process.

10.5.3 Barometric Hole Sizing

Flight computers rely on barometers to translate pressure measurements into altitude values for apogee detection. Therefore, it is crucial for these computers to obtain precise atmospheric pressure readings. Consequently, barometric openings are specifically engineered to allow sufficient pressure to enter the airframe, ensuring accurate altitude recording by the flight computers and the timely deployment of apogee.

10.5.4 Materials

Criterion	Value	ASA	PLA	ABS	PEEK
Strength	7	6	5	7	9
Weather Resistance	6	8	4	6	7
Surface Finish	3	5	5	5	5
Heat Resistance	7	7	4	7	8
Durability	8	8	4	6	9
Cost	9	5	8	6	2
Weight	8	7	9	8	5
Printability	7	8	9	7	5
Total		375	341	364	341

Table 52: Trade-off Table

Table 6 represents the trade-off table for the specific plastic that may be used for printing out the battery bay. The priority of the criterion was based on which material can hold the highest structural integrity while ensuring the manufacturing process of the AV bay would be cost-efficient. Evidently, the ratings above demonstrate that the final AV bay design will be constructed using Acrylonitrile styrene acrylate (ASA). However, during integration and testing of the AV bay design, PLA would be subjected for use as it is a cheaper alternative in comparison to other printing materials, and is a more easily printable design. In which integration and testing would comprise of testing for size and design of the AV Bay to determine if the final product will be suitable for launch.

10.6 Electronics Systems

10.6.1 Flight Computers

The selection of flight computers onboard Pardalote are the Altus Metrum TeleMega and Featherweight Raven 4 with a Featherweight GPS tracker.

TeleMega

The Altus Metrum TeleMega assumes the critical role of primary flight computer within the Pardalote rocket system, with a primary function of transmitting essential telemetry data. This data includes key parameters such as altitude, velocity, and energetics, enabling a comprehensive analysis of the rocket's state, burn time, location, and trajectory throughout its flight. The transmission of telemetry data occurs seamlessly through a direct 433MHz radio link to the TeleDongle, which, in turn, interfaces with a laptop via USB. Additionally, an alternative communication channel is provided by TeleBT, establishing a Bluetooth connection with a mobile device, particularly advantageous during recovery operations. The manufacturer, Altus Metrum, has specified that the flight computer is capable of transmitting signals at altitudes exceeding 40,000 feet, contingent on the use of a 5-element Yagi antenna—well beyond the anticipated apogee for the Pardalote rocket. In a dual capacity, TeleMega also orchestrates the triggering of e-matches, connecting to four charges for the purpose of effecting the rocket's separation during the recovery phase.

Raven 4

The FeatherWeight Altimeter Raven 4 plays a crucial role in the Pardalote rocket system, acting as the secondary flight computer and overseeing parachute deployment during flight. It is intricately connected to four e-matches, akin to TeleMega, with 'APO' terminals designated for drogue parachute deployment and 'Main' terminals for the main parachute. Raven 4 functions autonomously, triggered by its on-board accelerometer detecting the rocket's velocity change at apogee, ensuring precise and timely parachute deployment. Adding an extra layer of reliability, backup terminals '3rd' and '4th' serve as contingency mechanisms for drogue and

main parachutes. Post-flight analysis becomes seamless through computer review, offering valuable insights into trajectory and deployment events. Notably, Raven 4 operates independently, without the need for communication with TeleMega or the ground station. To further enhance accuracy, the on-board accelerometer undergoes meticulous calibration using advanced flight simulation tools. This calibration process ensures optimal performance and reliability in detecting apogee and subsequent deployment events.

Featherweight GPS Tracker

The Featherweight GPS Tracker is designated as the secondary Commercial Off-The-Shelf (COTS) flight computer, with its primary responsibility being the real-time transmission of telemetry data to the ground station. This device establishes a connection with the tracker's ground station, which seamlessly interfaces with an iOS phone application, facilitating communication on the 900MHz frequency band. Noteworthy is the GPS Tracker's capacity to transmit data up to altitudes of 300,000 feet through GPS signals without necessitating a directional antenna, thus presenting a robust solution. This capability ensures the precise determination of the launch vehicle's position and elevation throughout both its ascent and descent phases.

10.6.2 Batteries

To power the various electronic deployment systems, 1s and 2s Li-ion batteries are used with the exception of one 1s LiPo battery used to power Telemega. This is a subsequent change from only using LiPo batteries due to the ruling of SAC to not permit any LiPo batteries be onboard the rocket unless provided by the manufacturer of the component requiring power. Li-ion batteries have an almost comparable energy density to LiPo batteries and therefore will be able to store a significant amount of energy in a compact size. Ensuring sufficient charge being provided to the electronics for longer periods of time. Additionally they charge faster than LiPo batteries and have a slower discharge rate resulting in charge being held for extended periods when not in use. Above all Li-ion batteries have been established as being much safer than LiPo batteries. LiPo batteries are more prone to swelling, overheating, and even catching fire if not properly handled or charged. However these batteries have been used for many projects in the URT where battery issues have rarely encountered thus using a manufacturer recommended LiPo for Telemega is justified.

Three 1s batteries will be used to power the flight computers: Telemega, Raven4, and the Featherweight GPS tracker. For deployment, two 2s batteries are used to supply an adequate amount of current to the J-tek e-matches that have a recommended deployment current of 1.25A. The battery configurations are seen in Table 53

Flight Computer	Power	Deployment
Telemega	1s LiPo	2s Li-ion
Raven4	1s Li-ion	2s Li-ion
Featherweight GPS Tracker	1s Li-ion	N/A

Table 53: Battery Configuration

Testing

To ensure that all batteries deliver adequate voltage and current to the flight computers throughout the required duration, battery drain tests will be conducted. These tests involve using the batteries that are calculated to supply enough current and voltage for each of the flight computers and timing how long it takes until the battery reaches a minimum voltage value. The objective is to measure the time it takes for the battery voltage to drop to a level that is considered too low. This process serves to confirm the expected battery life of each flight computer during both flight and recovery phases, validating the accuracy of the calculated battery lifespan.

10.6.3 Power Distribution Board

The use of a PDB within Pardalote is to keep the wiring of the electronics for the AV bay secure, safe, and clear to trace. The PDB design will house the flight computers: Telemega and Raven 4 with the Featherweight GPS tracker. Figures 137, 138, 139 are circuit diagrams that represent that behaviour of the PDB when all connections are complete. This demonstrates the reduced clutter and increased real estate within the AV Bay afforded by the usage of a PDB.

As shown in Figure 140, the image illustrates terminals being orientated to be pointing in a downward position by approximately 45°. This design aspect reduces the bending radius of the protruding wires so they may avoid making contact with the inner wall of the rocket.

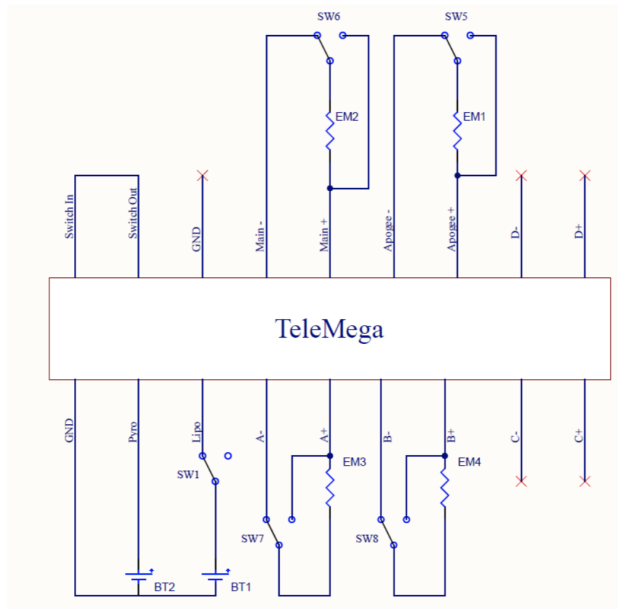


Figure 137: Telemega Wiring Diagram

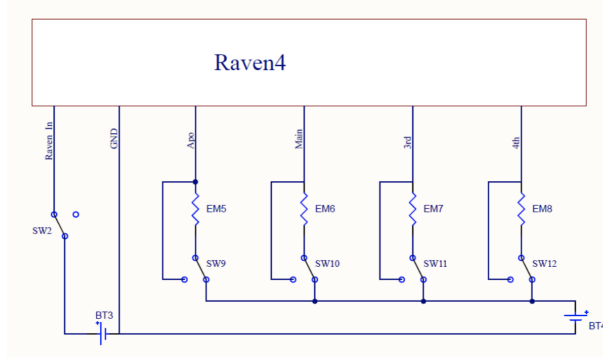


Figure 138: Raven 4 Wiring Diagram

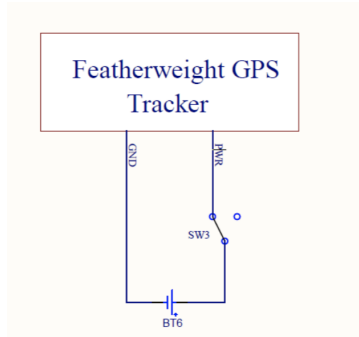


Figure 139: GPS Tracker Wiring Diagram

10.6.4 Wiring and Connections

To maintain secure and reliable connections, all wired connections that use screw terminals on the PDB will have stray wires crimped with bootlace ferrules. The purpose of these ferrules is to prevent any stray wires from causing disruptions and to ensure that the wires within the screw terminals do not accidentally short with other connections on the same terminal. For the screw terminal connections on the flight computers, normal ferrules are employed to fit the smaller screw terminal sizes. On the other hand, bootlace ferrules will be used for all wired connections into the screw terminals on the PDB. This differentiation in ferrule types guarantees compatibility and optimal performance within the respective terminal sizes, ensuring secure

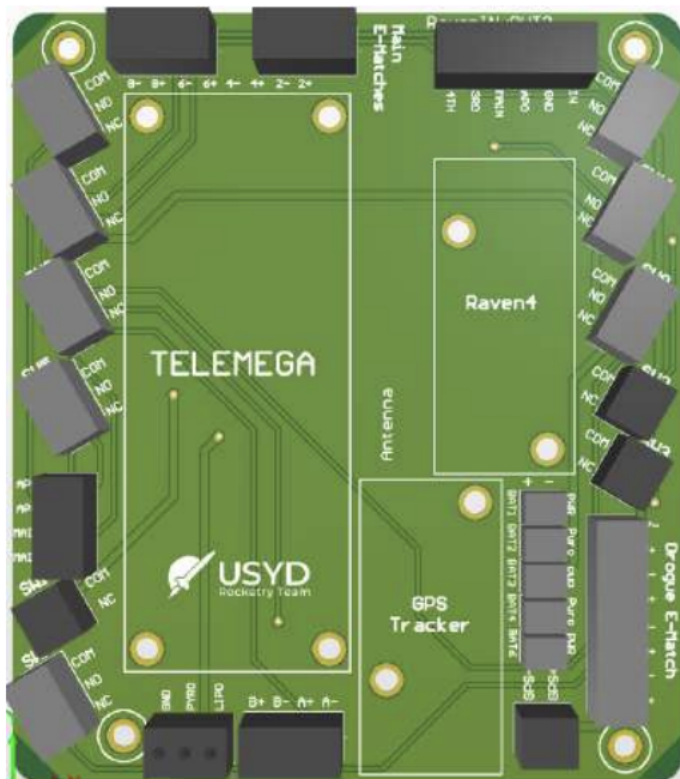


Figure 140: Raven4, TeleMega and Featherweight GPS Tracker PDB Design

connections throughout the system.

Wire Management

To establish physical wiring connections, both red and black 22 AWG wires will be employed throughout the system. These wires will be used for connections between the PDB and flight computers, switch plate, circular connectors, and from another side of the circular connectors to the barrier blocks. The red wire will represent positive connections, while the black wire will indicate negative or ground connections. This colour scheme aids in distinguishing between the different polarities and ensures proper connectivity. To maintain an organised and neat arrangement of the wires, zip ties and velcro straps will be used to group the wires together; preventing any disordered connections. By keeping the connections tidy, it becomes easier to identify and troubleshoot any issues that may arise during the operation of the system.

Circular Connectors

To establish connections between the PDBs and the barrier blocks, 4-pin circular connectors are used. Both female and male circular pin connectors will be used for ease of connection between the board and the barrier blocks. Each barrier block is placed on both bulkheads with each of them having 8 screw terminals. Thus there are two 4-pin circular connectors for each barrier block, where each of the connectors will hold a primary and secondary deployment connection for either drogue or main depending on the bulkhead; which is connected to TeleMega and Raven4 flight computers. Therefore, the two circular connectors at the lower bulkhead will have one circular connector with drogue connections from the flight computers, and the same for the upper bulkhead which is used for main deployment

Barrier Blocks

On both the upper and lower avionics bulkheads, barrier blocks are used to establish connections between the flight computers mounted on the PDBs and the e-matches. These barrier blocks facilitate convenient connections between the e-matches and the circuits for the energetics contained within the PDBs and switches. To ensure consistent contact and secure connections, ring crimp connections are employed on each of the barrier block terminals. These ring crimp connections provide positive retention, maintaining a reliable link between the wired connections and the terminals. The ring crimps fit around the screws on each of the barrier block terminals to secure a connection for the wires.

Each bulkhead feature a pair of 8-pin barrier blocks, enabling both primary and secondary charges from two separate flight computers to trigger the deployment event for either the main or drogue, respectively. Allowing for dual level redundancy. The wired connections from the PDBs connected to the barrier blocks will be connected to e-matches. The e-matches will be securely screwed into the opposite side of the barrier block, establishing a connection between the e-match and the circuit.

Cable Glands

To maintain separation of the black powder and deployment system from all the electronics in the avionics bay, cable glands are used. The cable glands facilitate the passage of the e-matches to the deployment system in both the upper and lower bulkheads. An air-tight gap is maintained to prevent the damage and interference to all electronics during flight.

11 Subsystem Testing

- 11.1 Flight Simulation**
- 11.2 Propulsion - Chamber**
- 11.3 Propulsion - Tank**
- 11.4 Ground Support Equipment**
- 11.5 Ground Control**
- 11.6 Aerostructure**

FIBREGLASS TUBE COMPRESSION TEST

Project	Pardalote	Test Code	PL-T-AER-01			
Subsystem	Aerostructures	Relevant Requirements	PL-R-AER-1, PL-R-AER-2.1			
Date of Test	05/02/2024	Location of Test	The University of Sydney, NSW			
Test Lead	Izaak Cerneaz	Test Oversight	Matthew Spiritosanto			
Attendees	Izaak Cerneaz, Andrew Malysiak, Ethan Englund, Andrian Yasintus					
Aim	To determine the compressive strength advantage of a 6-layer fibreglass body tube as opposed to a 5-layer body tube.					
Expected Outcome	The failure point of the tube should be larger than 77.43kN (the point of catastrophic failure of the 5-layer body tube).					
Success Criteria	<ol style="list-style-type: none"> 1. No yield-type failure of the component below 77.43kN 2. Catastrophic failure occurs at a compressive force that is notably higher than 77.43kN 					
Methodology	<ol style="list-style-type: none"> 1. The sample was placed into the universal testing machine between metal plates 2. The clear protective barrier was positioned in front of the machine 3. The tube was compressed at a rate of 1mm/min. 					
						
Fig. 1 Testing Setup						

Results

The maximum recorded compressive load was 84.94kN, corresponding to a compressive failure stress of:

$$\sigma_c = \frac{F}{A} = \frac{84940}{\frac{\pi}{4} (0.156^2 - 0.1524^2)} = 97.41 \text{ MPa}$$

The deformed test sample and stress-strain behaviour of the fibreglass tube are shown below.



Fig. 2 The deformed test sample

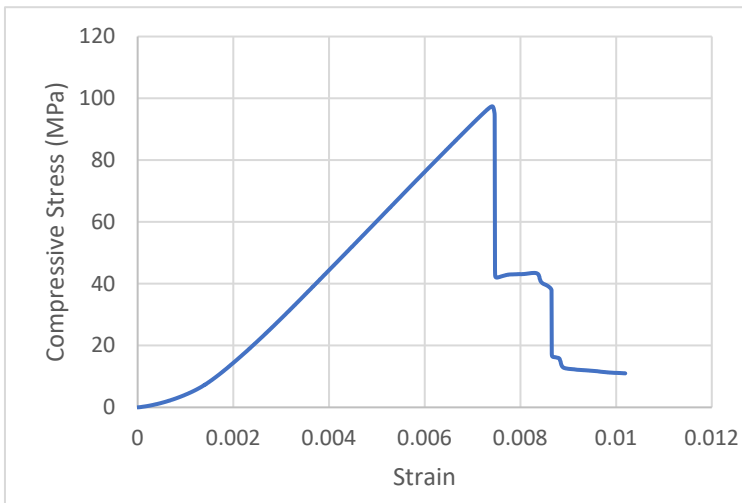


Fig. 3 Stress-strain behaviour of the tube

Overall, the extra layer provided a $\frac{84.94 - 77.43}{77.43} = 9.70\%$ increase in the compression failure point compared to a 5-layer fibreglass body tube.

Conclusion	This was a successful test, with the tube failing at 84.94kN compressive force (97.41MPa of compressive stress). This gives a MoS of 1.33 following consideration of a 1.5 factor of safety.
Future Testing	

Appendix

Risk Analysis

Task	Risk	Mitigation Strategy
Stressing samples	Fragments could strike eyes and other body parts	<ul style="list-style-type: none"> • Wear eye protection • Use the clear protective barrier • Stand back from the machine

Apparatus

- Universal Testing Machine (Instron 3366)
- Fibreglass composite body tube
- Metal loading plate
- Clear protective barrier
- Safety glasses

CARBON FIBRE TUBE COMPRESSION TEST

Project	Pardalote	Test Code	PL-T-AER-02
Subsystem	Aerostructures	Relevant Requirements	PL-R-AER-1, PL-R-AER-2.1
Date of Test		Location of Test	The University of Sydney, NSW
Test Lead	Izaak Cerneaz	Test Oversight	Matthew Spiritosanto
Attendees			
Aim	To determine the compressive strength of a 5-layer carbon fibre body tube and the failure mode.		
Expected Outcome	The failure point of the tube is expected to be significantly larger than 77.43kN (failure point of 5-layer fibreglass tube) with compression as the mode of failure. See Section 9.10.4 for justification.		
Success Criteria	<ol style="list-style-type: none"> Catastrophic failure occurs at a force larger than 71.62kN for the worst-case loading and no yield-type failure below 71.62kN (minimum force requirement for MoS = 1) Catastrophic failure occurs at a force larger than 77.43kN for the worst-case loading and no yield-type failure of the component below 77.43kN (to prove that the carbon fibre tube is stronger than the fibreglass tube) 		
Methodology	<ol style="list-style-type: none"> The sample was placed into the universal testing machine between metal plates The clear protective barrier was positioned in front of the machine The tube was compressed at a rate of 1mm/min. 		

Fig. 1 Testing Setup

Results

Fig. 2 The deformed test sample	Fig. 3 Stress-strain behaviour of the tube
--	---

Conclusion
Future Testing

Appendix

Risk Analysis

Task	Risk	Mitigation Strategy
Stressing samples	Fragments could strike eyes and other body parts	<ul style="list-style-type: none"> Wear eye protection Use the clear protective barrier Stand back from the machine

Apparatus

- Universal Testing Machine (Instron 3366)
- Carbon fibre body tube
- Metal loading plate
- Clear protective barrier
- Safety glasses

AVIONICS BAY ROD TENSILE TEST

Project	Pardalote	Test Code	PL-T-AER-03
Subsystem	Aerostructures	Relevant Requirements	PL-R-AER-1, PL-R-AER-2.1
Date of Test		Location of Test	The University of Sydney, NSW
Test Lead	Izaak Cerneaz	Test Oversight	Matthew Spiritosanto
Attendees			
Aim	To determine the maximum tensile strength of the avionics bay rods and confirm sufficient thread engagement.		
Expected Outcome	The rods are expected to withstand a tensile force of 8.63kN to verify a minimum FoS of 2.44 during flight.		
Success Criteria	1. No catastrophic failure of the component below 8.63kN		
Methodology	1. Two M8 bolts were fastened into the end caps and loaded into the UTM. 2. The rod was loaded in tension at a strain rate of 0.015mm/s until failure.		

Fig. 1 Testing Setup

Results

Fig. 2 The deformed test sample	Fig. 3 Force-displacement behaviour of the tube
--	--

Conclusion
Future Testing

Appendix

Risk Analysis

Task	Risk	Mitigation Strategy
Stressing samples	Fragments could strike eyes and other body parts	<ul style="list-style-type: none"> • Wear eye protection • Use the clear protective barrier • Stand back from the machine

Apparatus

- Universal Testing Machine (Instron 3366)
- 6061 solid bar with M8 threaded end links
- 2x M8 bolts
- Clear protective barrier
- Safety glasses

AVIONICS BAY ROD TENSILE TEST

Project	Pardalote	Test Code	URT-PL-T-AER-04
Subsystem	Aerostructures	Relevant Requirements	PL-R-AER-1, PL-R-AER-2.1
Date of Test	27/05/24	Location of Test	The University of Sydney, NSW
Test Lead	Izaak Cerneaz	Test Oversight	Matthew Spiritosanto
Attendees	Olivia Hayston, Eugenie O'Rourke, Andrian Yasintus		

Aim	To determine the maximum tensile strength of the avionics bay rods and confirm sufficient thread engagement.
Expected Outcome	The rods are expected to withstand a tensile force of 8.63kN to verify a minimum FoS of 1.5 during flight.
Success Criteria	1. No catastrophic failure of the rod below 8.63kN
Methodology	<ol style="list-style-type: none"> Two 80mm pieces of M8 threaded rod were fastened into the 6061 AV rod threaded tube test piece and loaded into the Universal Tensile Testing (UTT) Machine. The rod was loaded in tension at a strain rate of 0.015mm/s until failure.

Results



Fig. 1 Testing Setup UTM

Fig. 2 The deformed test sample

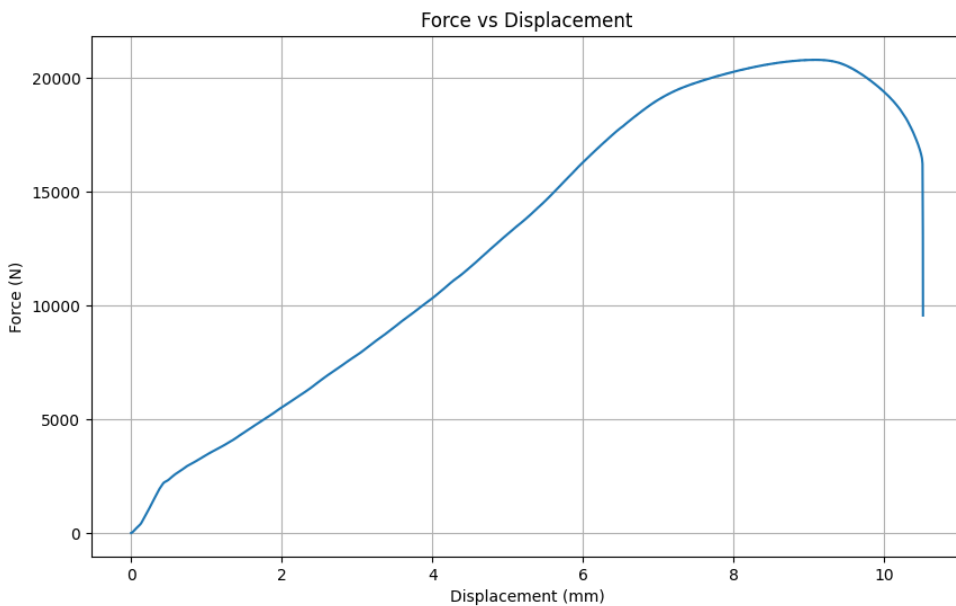


Fig. 3 Force Displacement Behaviour of the AV rod bolt

Conclusion	This was a successful test since it met the success criteria, with the threaded rod and AV rod failing at a tensile force of 18.47kN (yield strength), with an ultimate strength of 20.80kN. Hence no catastrophic failure occurs below 8.63kN. This gives a MoS of 2.14, and an ultimate MoS of 2.41, following consideration of a 1.5 factor of safety.
-------------------	---

Appendix

Risk analysis

Task	Risk	Mitigation Strategy
Stressing sample in UTT Machine	Fragment from testing sample striking eyes or other body parts, causing injury	<ul style="list-style-type: none"> • Wear eye protection • Use the clear protective barrier • Stand back from the machine • Wear steel capped enclosed footwear

Apparatus

- UTT Machine (Instron 3366)
- 6061 AV rod threaded tube test piece
- 2x 80mm pieces of M8 threaded rod
- Clear protective barrier
- Safety glasses

U BOLT TENSILE TEST

Project	Pardalote	Test Code	URT-PL-T-AER-05
Subsystem	Aerostructures	Relevant Requirements	PL-R-AER-1, PL-R-AER-2.1
Date of Test	27/05/24	Location of Test	The University of Sydney, NSW
Test Lead	Izaak Cerneaz	Test Oversight	Matthew Spiritosanto
Attendees	Olivia Hayston, Eugenie O'Rourke, Andrian Yasintus		

Aim	To determine the maximum tensile strength of the U bolts and confirm sufficient thread engagement.
Expected Outcome	The U bolts are expected to withstand a tensile force of 8.63kN to verify a minimum FoS of 1.5 during flight.
Success Criteria	1. No catastrophic failure of the u bolt below 8.63kN
Methodology	<ol style="list-style-type: none"> 1. The U bolt was fastened into a bulkhead and loaded into the Universal Tensile Testing (UTT) Machine. 2. The U bolt was loaded in tension at a strain rate of 0.015mm/s until failure.

Results



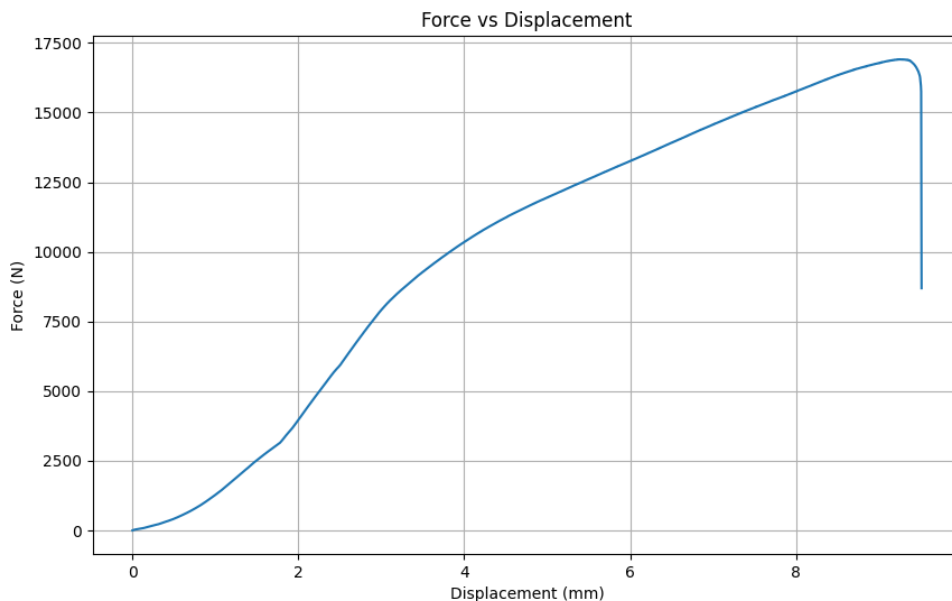


Fig. 3 Force Displacement Behaviour of the U Bolt

Conclusion	This was a successful test since it met the success criteria, with a yield strength somewhere in between 7.5 and 9kN for the U bolt, and an ultimate strength of 16.91kN. Hence no catastrophic failure occurs below 8.63kN. This gives a minimum MoS of 0.87 (conservative) and an ultimate MoS of 1.96, following consideration of a 1.5 factor of safety.
-------------------	--

Appendix

Risk analysis

Task	Risk	Mitigation Strategy
Stressing sample in UTT Machine	Fragment from testing sample striking eyes or other body parts, causing injury	<ul style="list-style-type: none"> • Wear eye protection • Use the clear protective barrier • Stand back from the machine • Wear steel capped enclosed footwear

Apparatus

- UTT Machine (Instron 3366)
- M6 Stainless Steel U Bolt 34mm inside width
- Clear protective barrier
- Safety glasses

11.7 Recovery

The following tests are planned to be conducted:

1. UTM tensile strength test. Strips of 4cm width gradually stretched by UTM machine until failure.
2. Sandbag test. Load canopy with sandbags equivalent to the load the parachute will experience during flight.
3. Inflation test. Drop drogue off of building to gauge inflation. For main, use a leaf blower.

References

- [1] Britting et al. *Selection Criteria for Parachutes of Student-Built Sounding Rockets*. Tech. rep. 4th Symposium on Space Educational Activities, Apr. 2022.
- [2] Anonymous. *Bluewren Preliminary Design Report*. Tech. rep. USYD Rocketry Team, Dec. 2022.
- [3] Engineering Sales Australia. *LOX-8 Catalogue*. <http://www.engineeringsalesaustralia.com.au/fluoramics-sealants--greases.html>. Engineering Sales Australia.
- [4] Sealing Australia. *O-ring Groove Design*. <https://sealingaustralia.com.au/oring-groove-design/>.
- [5] Elmer Franklin Bruhn. *Analysis and design of flight vehicle structures*. Tri-State Offset Co., 1965.
- [6] Allen Chan. "Design Optimisation of HybridPropellant Launch Vehicles". In: (2021).
- [7] AE Components. *AE Components*. <https://aecomponents.com.au/>. AE Components.
- [8] United States of America Department of Defence. *Metallic materials and elements for aerospace vehicle structures*. <http://ssrl-uark.com/MILHDBK5H.pdf>. [Accessed: December 18, 2019]. 1990.
- [9] Department of Defence United States of America. "Design of Aerodynamically Stabilized Free Rockets". In: *Military Handbook* (1990).
- [10] Hobsons Engineering. *Breaking Strength Comparison*. <https://cdn.hobson.com.au/documents/tech-breaking-strength.pdf>. 2021.
- [11] Hobsons Engineering. *Socket Head Cap Screw Tightening Torque*. <https://content.hobson.com.au/category/soko/tech-shcs-129-t-torque.pdf>. 2021.
- [12] Hobsons Engineering. *Socket Head Cap Screw CSK Tightening Torques and Dimensions*. <https://content.hobson.com.au/documents/htd-tigh-torq-scso-220217.pdf>. 2021.
- [13] et all Francesca Heeg. *Design and Test of a Student Hybrid Rocket Engine with an External Carbon Fiber Composite Structure*. https://leopard.tu-braunschweig.de/servlets/MCRFileNodeServlet/dbbs_derivate_00047414/Heeg_aerospace-07-00057.pdf. Institute of Space Systems, Technical University of Braunschweig.
- [14] PHD George Laird. *User guide: FEA of Bolted Joints - A seminar for simulation engineers*. <https://appliedcax.com/support-and-training/technical-online-seminars/seminars/Applied-CAx-User-Guide-FEA-of-Bolted-Joints-Model-Files/Applied-CAx-User-Guide-FEA-of-Bolted-Joints-Rev-0.pdf>. [Accessed: January 28, 2024]. 1990.
- [15] John M. (Tim) Holt. *Structural Alloys Handbook*. Tech. rep. Northrop Services Inc, 1996.
- [16] H. et. al. Iqbal. *Effect of hybrid ratio and laminate geometry on compressive properties of carbon/glass hybrid composites*. Tech. rep. Donghua University, Nov. 2015.
- [17] Industrial Fastener Institute. *Inch Fastener Standards, 7th ed.* 2003.
- [18] Jarrett Linowes. "How to calculate fastener minimum thread engagement length". In: *Omnia MFG* (Oct. 2020). URL: <https://www.omniamfg.com/mechanical/2020/10/3/how-to-calculate-fastener-minimum-thread-engagement-length>.
- [19] AZO Materials. *Carbon - Graphite Materials*. https://www_azom_com/properties.aspx?ArticleID=516. 2024.
- [20] R. McCoy. *Modern Exterior Ballistics: The Launch and Flight Dynamics of Symmetric Projectiles*. A Schiffer design book. Schiffer Publishing, 1999. ISBN: 9780764307201. URL: <https://books.google.com.au/books?id=ay5UPQAACAAJ>.
- [21] Aerospace Specification Metals. *Special Metals Inconel Alloy 718*. <https://asm.matweb.com/search/SpecificMaterial.asp?bassnum=NINC34>. 2024.
- [22] ESPI Metals. *Inconel 718*. <https://www.espmaterials.com/index.php/technical-data/91-Inconel%20718>. 2024.
- [23] Parker. *Parker O-Ring Handbook*. <https://www.parker.com/content/dam/Parker-com/Literature/O-Ring-Division-Literature/ORD-5700.pdf>. Parker.
- [24] Waterloo Rocketry. *Leviathan of the Sky Hybrid Rocket Project Technical Report*. Tech. rep. University of Waterloo, Jan. 2023.
- [25] Wroclaw University of Science and Technology Wroclaw. *Aurora Hybrid Rocket Team 157 Project Technical Report to the 2023 Spaceport America Cup*. 2023.
- [26] AB Seals. *Silicone / AB Seals*. <https://abseals.com.au/products/o-rings/silicone/>. AB Seals.
- [27] EurocodeApplied team. *Table of design properties for metric steel bolts M5 to M39 - eurocode 3*. URL: <https://eurocodeapplied.com/design/en1993/bolt-design-properties>.
- [28] Applied Industrial Technologies. *Applied Industrial Technologies O-Rings*. https://appliedau.com.au/products-list?category_id=558&page_no=1&keyword=&page_size=12. Applied Industrial Technologies.
- [29] URT. *Wattle Critical Design Report*. Tech. rep. USYD Rocketry Team, Jan. 2023.

A Equation Derivations

A.1 Truss Buckling Equation

As seen in ??, each truss member is securely bolted on to the truss rings by 2 bolts, allowing the members to be treated as columns with fixed ends on both sides. Thus, the critical loading for each member is given by:

$$P_{cr} = \frac{4\pi^2 EI}{L^2} \quad (87)$$

where E is the Young's Modulus, I is the second moment of inertia and L is the length of the member. In our calculations, we would also like to include a factor of safety, so that:

$$P_{allow} = \frac{P_{cr}}{\text{FoS}} \quad (88)$$

Combining these two equations gives:

$$P_{allow}(\text{FoS}) = \frac{4\pi^2 EI}{L^2} \implies I = \frac{P_{allow}(\text{FoS})L^2}{4\pi^2 E} \quad (89)$$

Now, the cross-sectional area of the member is formed by removing a sector from a larger sector, both with the same inner angle, as shown in Figure 141. By viewing the member as symmetrical about the x -axis,

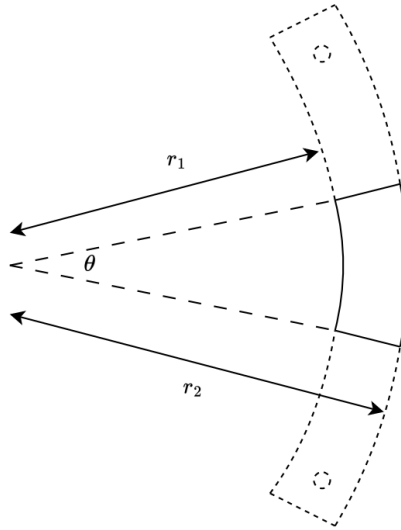


Figure 141: The variables that determine member cross-sectional areas

we can simply subtract the second moment of area of each shape without having to use the parallel-axis theorem. Thus, the second moment of area for the member is:

$$\begin{aligned} I &= (\theta - \sin \theta) \frac{r_2^4}{8} - (\theta - \sin \theta) \frac{r_1^4}{8} \\ &= (\theta - \sin \theta) \frac{r_2^4 - r_1^4}{8} \end{aligned} \quad (90)$$

Setting the second moment of area equations equal to each other, we have:

$$(\theta - \sin \theta) \frac{r_2^4 - r_1^4}{8} = \frac{P_{allow}(\text{FoS})L^2}{4\pi^2 E} \quad (91)$$

$$\theta - \sin \theta = \frac{8P_{allow}(\text{FoS})L^2}{4\pi^2 E(r_2^4 - r_1^4)} \quad (92)$$

This equation allows us to find the truss member angle θ at which buckling will occur. This can then be used to find the minimum cross-sectional area required to prevent buckling.

A.2 Tank Failure Equations

For the following calculations the parameters are as follows

Table 54: Tank Failure Parameter Values

Parameters	Inner Diameter	Outer Diameter	Thickness	Max. Expected Operating Pressure
Units	mm	mm	mm	MPa
Symbol	Di	Do	t	MEOP
Value	133.34	152.34	9.5	6

Parameters	Yeild Stress	Shear Strength	Bearing	Yeild Strength
Units	MPa	MPa	MPa	MPa
Symbol	σ_y	σ_s	σ_b	
Value	240	207	386	

Parameters	Num. of Bolts	Bolt Diameter (Minor)	Bolt Diameter (Major)	Bolt UTS	Edge Distance
Unit		mm	mm	MPa	mm
Symbol	n	D _{bm}	D _{bM}	UTSB	E
Value	12	6	6	700	12

A.2.1 Angle Seat Valve

The Angled-Piston valve is designed to control the flow of Oxidizer while maintaining a constant cross-sectional area of flow in a compact fashion. As seen in figure 142, the valve consists of a housing with a central bore, a piston which actuates linearly and a flange cap which seals the valve. The housing has two 1/2" BSPP ports for Oxidizer in and out; and two 1/8" BSPP ports for Air in and out. The valve is a double acting valve; meaning that it can be actuated "closed" and "open". The valve can be set to a normal position dependent upon the Solenoid Valve setup.

The valve is constructed out of 316 Stainless Steel, has a mass of 1.08kg and a length of 117mm without fittings. FEA is yet to be carried out, however the valve's bore can be modeled as a thick-walled cylindrical pressure vessel using the Lames Equation. This is yet to be carried out however it's noted that the min wall thickness is currently 10.5mm

The valve seals on a male PTFE seat, which is fastened to the piston using an M3 countersunk screw. To seal, the seat presses firmly against the chamfer of the housing with a force of up to 354N depending upon the pressure set. Due to the layout, Nitrous pressure does not impede the valves ability to remain closed during the Fill and Hold stages.

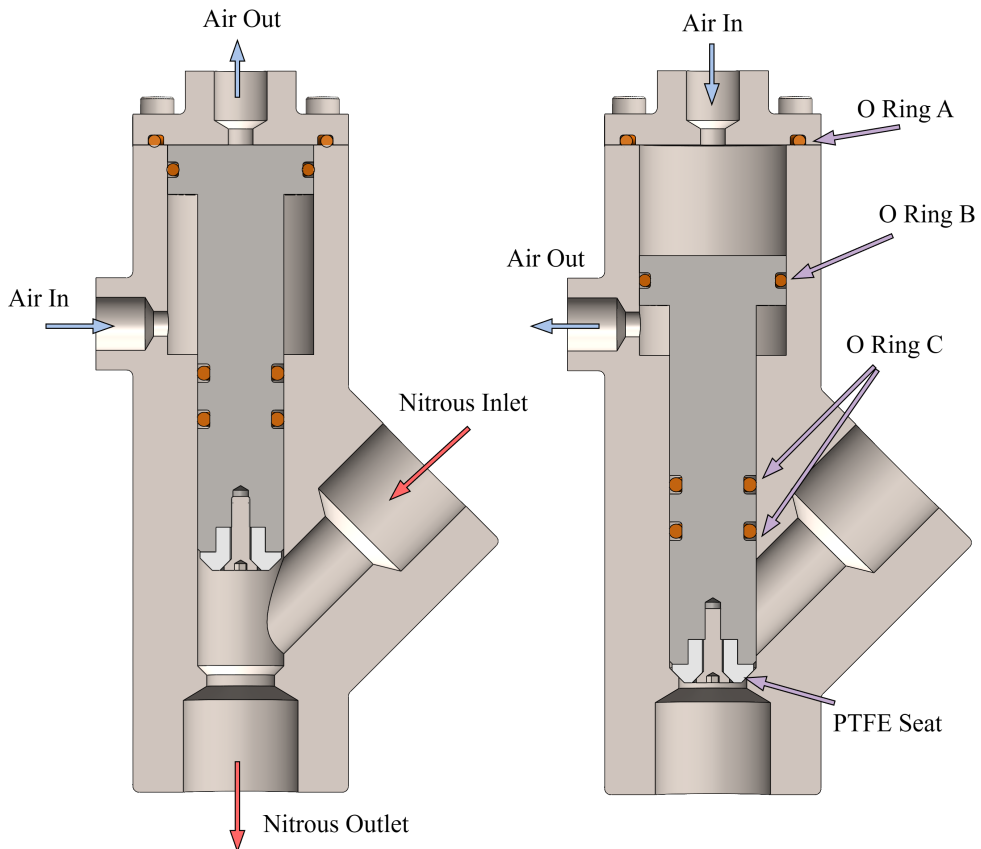


Figure 142: Angled-Piston Valve Cross Section

The piston is sealed through the use of three dynamic O-Rings. O-Rings B and C separate the "open" and "close" air chambers, as well as seal the interface between the compressed air and Oxidizer. Dynamic seals are designed with a certain squeeze % allowing for relatively-friction free motion. According to the Parker O-Ring Handbook [23], the three main considerations to ensure dynamic seals free movement are a low durometer O-Ring, lubrication and low squeeze. The selected O-Rings are Silicone 70 durometer O-Rings from ABSeals [26] and a LOX-8 oxygen-safe Grease will be used for lubrication [3]. The Parker Metric Groove Design Guide was used for sizing O-Ring grooves. The designed size and O-Ring properties can be seen in the table below.

O-Ring	Size	Fit	Squeeze %	Stretch %	Gland Fill %	Quantity
A	MS7-026-2	Face Seal	20	-	78.5	1
B	MS7-020-2	Dynamic	11	1	70.6	1
C	MS7-009.6-2.3	Dynamic	13	4.2	69.2	2

The end-cap seals the air chamber with a face seal O-Ring and 4x M3 socket head cap screws. Face seal O-Rings function differently to a standard seal, to ensure a proper seal a certain compression force is required. The Parker O-Ring Handbook outlines reference graphs for calculating the correct compression force required dependent upon O-Ring duromoter, cross-sectional area and circumference [23]. In addition to the compression force, the end cap must also resist the force of the piston pressing up against it due to the pressure of the Nitrous Oxide flowing through the valve. This pressure was taken at operation 5.6MPa. Calculations for the load on each fastener can be seen below.

O-Ring	Compression Force (N)	Load (N)	# Fasteners	Load / Fastener (N)	Torque (Nm)
A	237.7	1211	4	362.2	2.2

The advantages and disadvantages of the Angled-Piston Valve design can be seen below.

Advantages	Disadvantages
Smaller and lighter than Coaxial	Flow rate reduced due to 45 degree bend + bending in tubing
Constant diameter for flow	Bent tube needed
Dual O-Rings	Potential Deformation to PTFE Seat
Reduced loads due to smaller surface area	

A.2.2 Thin Walled Pressure Vessel Analysis

$$t = \frac{MEOP * D_i}{2\sigma_y - MEOP} \quad (93)$$

A.2.3 Bolt Shear Failure

$$\begin{aligned} \sigma_{\text{bolt shear}} &= \left(\frac{\pi}{4} * D_i^2 * MEOP \right) \left(n * \frac{\pi}{4} * D_{bm} \right) \\ FOS_{\text{bolt shear}} &= \frac{0.75 * UTS_B}{\sigma_{\text{bolt shear}}} \end{aligned} \quad (94)$$

A.2.4 Bolt Tear-out Failure

$$\begin{aligned} F_{\text{bolt}} &= \frac{\frac{\pi}{4} * D_i^2 * MEOP}{n} \\ \sigma_{\text{tear-out}} &= \frac{F_{\text{bolt}}}{E_{\min} * 2t} \\ \text{Where } E_{\min} &= E - \frac{D_{bm}}{2} \\ FOS_{\text{tear-out}} &= \frac{\sigma_s}{\sigma_{\text{tear-out}}} \end{aligned} \quad (95)$$

A.2.5 Casing Tensile Failure

$$\begin{aligned} \sigma_{\text{tensile}} &= \frac{\frac{\pi}{4} * D_i^2 * MEOP}{[(D_o - t) * \pi - n * D_{bM}] * t} \\ FOS_{\text{tensile}} &= \frac{\sigma_y}{\sigma_{\text{tensile}}} \end{aligned} \quad (96)$$

A.2.6 Bearing Stress Failure

$$\begin{aligned} \sigma_{\text{bearing}} &= \frac{F_{\text{bolt}}}{D_{bM} * t} \\ FOS_{\text{bearing}} &= \frac{\sigma_b}{\sigma_{\text{bearing}}} \end{aligned} \quad (97)$$

A.3 Coaxial Valve Failure Equations and Calculations

Table 55: Coaxial Valve Bolt Loading Calculations

Bolt Loading Calculations	Inlet Cap - Inner O-ring	Inlet Cap - Outer O-ring	Outlet Cap O-ring
Squeeze %	22.86	22.86	22.86
Pounds Per Square Inch	40	40	40
Middle Circumference	1.44	2.78	2.15
Cross Section	0.14	0.12	0.14
Pound Force	57.80	111.18	86.14
Force (In Newtons)	257.07	494.33	383.16
Force from Air (N)	499	499	1057.5
Force from N2O (N)	4271	4271	660.84
Total Load (N)	5521.61	5521.61	1718.34
Number of Fasteners	14	14	8
Load per Fastener	394.4	394.4	214.79

A.3.1 Bolt Tension Failure Equation

$$\begin{aligned} N_{tf}^* &= \phi * N_{tf} \\ N_{tf} &= A_s * f_{uf} \end{aligned} \quad (98)$$

Table 56: Coaxial Valve Bolt Loading Values

Bolt Tension Failure	Inlet Cap	Outlet Cap
Minimum tensile strength of bolt f_{uf} (MPa)	700	700
Tensile stress area of bolt A_s (mm^2)	5.03	5.03
Nominal tensile capacity of bolt N_{tf} (N)	3521	3521
Capacity factor ϕ	0.8	0.8
Design tension force N_{tf}^* (N)	394	214
Factor of Safety	7.15	13.16

A.3.2 External Thread Shear Equation

$$\begin{aligned} A_{ts.ext} &= \frac{5}{8} * \pi * d_{p.ext} * L_E \\ \tau_{ts.ext} &= \frac{F_{b.t}}{A_{ts.ext}} \\ FS_{ts.ext} &= \frac{S_{sy}}{\tau_{ts.ext}} \end{aligned} \quad (99)$$

Table 57: Coaxial Valve External Thread Shear

External Shear Out	Inlet Cap	Outlet Cap
Length of thread engagement L_E (mm)	10	10
Pitch diameter $d_{p.ext}$ (mm)	2.675	2.675
Thread shear area $A_{ts.ext}$ (mm^2)	52.5	52.5
Design Tensional Force $F_{b.t}$ (N)	394	214
Shear Stress $\tau_{ts.ext}$ (MPa)	7.50	4.07
Tensile Strength of Bolt S_{sy} (MPa)	700	700
Factor of Safety $FS_{ts.ext}$	93.3	172

A.3.3 Internal Thread Shear Equation

$$\begin{aligned} A_{ts.int} &= \frac{3}{4} * \pi * d_{p.int} * L_E \\ \tau_{ts.int} &= \frac{F_{b.t}}{A_{ts.int}} \\ FS_{ts.int} &= \frac{S_{sy}}{\tau_{ts.int}} \end{aligned} \quad (100)$$

Table 58: Coaxial Valve Internal Thread Shear

Internal Shear Out	Inlet Cap	Outlet Cap
Length of thread engagement L_E (mm)	10	10
Pitch diameter $d_{p.int}$ (mm)	2.675	2.675
Thread shear area $A_{ts.int}$ (mm^2)	63.0	63.0
Design Tensional Force (N)	394	214
Shear Stress $\tau_{ts.int}$ (MPa)	6.25	3.40
Tensile Strength of Aluminium Thread S_{sy} (MPa)	110	110
Factor of Safety $FS_{ts.int}$	17.6	32.4

A.3.4 Hoops Stress

$$\sigma_\theta = \frac{P}{t} D_m^2 \quad (101)$$

Table 59: Coaxial Valve Hoops Stress Calculations and Values

Hoops Stress	Sleeve Part
Internal Pressure P (MPa)	6
Wall Thickness t (mm)	3.91
Radius of Cylinder (mm)	10.5
Mean Diameter D_m (mm)	16.5
Hoops Stress σ_θ	12.38
6061 Aluminium Yield Strength (MPa)	241
Yield Factor of Safety	19.5
6061 Aluminium Ultimate Strength (MPa)	290
Ultimate Factor of Safety	23.4

A.4 Black Powder Calculations

First we calculate the force required for separation.

$$F_{shearpins} = F_{shearrate} \times N_{shearpins}$$

$$F_{shearpins} = 331N \times 5$$

$$F_{shearpins} = 1655N$$

The required pressure to separate the launch vehicle is found by calculating the difference between the force required to shear the shear pins and the pressure differential between the inside and outside of the chamber.

$$P_{main} = \frac{F_{shearpins}}{A - (P_{sl} - P_{main})}$$

$$A = \pi \times \frac{D^2}{4}$$

$$A = 0.0182415m^2$$

$$P_{main} = \frac{1655}{0.0182415 - (101,325 - 97102.31)}$$

$$P_{main} = -0.45807Pa$$